Theory and Application of Thomson Scattering to Particle Transport and Magnetic Field Measurements in Laser-Produced Plasmas

by

Colin Bruulsema

A thesis submitted in partial fulfillment of the requirements for the degree of

Doctor of Philosophy

Department of Physics
University of Alberta

© Colin Bruulsema, 2022

Abstract

The particle transport, plasma currents, and magnetic fields were investigated in laboratory plasmas, both with the Optical Thomson Scattering (OTS) diagnostic and in theory and numerical simulations.

Weibel-unstable plasma was simulated using the OSIRIS particle-in-cell code to examine the capabilities of the OTS diagnostics in counter-streaming plasmas. Synthetic OTS spectra were generated from the simulations, allowing OTS measurement uncertainties to be analyzed. Accurate measurements of current were demonstrated and applied to magnetic field calculations. In experiments at the OMEGA laser facility and MAGPIE pulsed power device, this technique was used successfully to measure magnetic field structures formed in plasma.

In order to understand plasma ablation in Inertial Confinement Fusion (ICF) experiments, metal spheres were shot at the OMEGA laser facility. Ablated plasma was measured with OTS, with basic plasma properties in good agreement with simulations. Heat transport was measured using the ion acoustic wave spectrum, finding heat fluxes consistent with local transport in the second half of the shot duration, but strongly inhibited during the initial laser heating period. Theory and application of the OTS heat transport measurements were supported by Vlasov-Fokker-Planck simulations to determine the electron distribution functions and the resulting OTS spectra.

Preface

Parts of the research conducted in this thesis are components of research collaborations spanning the University of Alberta, Lawrence Livermore National Laboratory (LLNL), Stanford Linear Accelerator Complex (SLAC), Imperial College London, and the Laboratory for Laser Energetics (LLE).

Chapter 2 contains theory that I reviewed and outlined for a publication on Optical Thomson Scattering (OTS) measurement precision, [1] in which I contributed to manuscript edits.

In Chapter 3, I ran Particle-in-Cell (PIC) simulations of the Weibel instability and analyzed the synthetic Thomson scattering effects. I also composed the manuscript analyzing the capability of the OTS diagnostic based on my simulation results [2]. I then analyzed the various experimental measurements of Weibel-unstable plasma included in chapter 3, and assisted in shot planning for the shots at the National Ignition Facility (NIF). I also analyzed the OTS spectra from the magnetic reconnection experiment at the Magpie pulsed power facility. These projects contributed to other publications [3–5], in which I also contributed to manuscript editing.

In Chapter 4, I analyzed the sphere experiments conducted at the OMEGA laser facility by George Swadling. I used simulations run by Mark Sherlock to model the effects of heat transport on the measurements. I was also involved in the planning of the later mid-Z shots. I wrote up the results of this work in our publication on the coronal heat transport measurement [6]. My analysis of these experiments also contributed to other publications [7, 8].

Acknowledgements

Throughout my PhD, I received valuable help and advice from many professors and colleagues at the University of Alberta, and at numerous other conferences, laboratories, and events I have the privilege of attending, especially Lawrence Livermore National Lab (LLNL) and Stanford Linear Accelerator Complex (SLAC).

First of all, I would like to thank my supervisor Wojciech Rozmus for all help and advice I received. He was always available to discuss my projects and connected me with many interesting and productive research opportunities during my studies.

I am very grateful for the introduction to plasma physics and simulations provided to me by Frederico Fiuza and Siegfried Glenzer at the Stanford Linear Accelerator Complex. They also supported my research on field measurements in counter-streaming plasma and welcomed my collaboration in the collisionless shock campaigns.

I would like to thank George Swadling at LLNL for his help and advice on numerous occasions, including sharing data on counter-streaming plasmas, introducing me to experimental plasma physics, and facilitating many of our recent shot campaigns, along with Avram Milder at both the Laboratory for Laser Energetics (LLE) and the University of Alberta. I also learned from and collaborated with Will Farmer and Mark Sherlock at LLNL, as well Jeffery Zielinski and Josh Ludwig at the University of Alberta for simulation support and understanding of heat transport in plasma.

I would also like to thank Lee Suttle, Jack Halliday, and Sergey Lebedev for sharing their magnetic re-connection data, and for their collaboration and advice on our analysis, and Paul-Edouard Masson-Laborde and Sylvie Depierreux for sharing interesting heat transport data and discussing related instabilities and measurement

techniques.

Table of Contents

List of Tables

List of Figures

List of Symbols

λ_{De}	Debye length	$\sqrt{\frac{T_e}{4\pi n_e e^2}}$
ω_{pe}	Electron plasma frequency α	$\sqrt{(4\pi n_e e^2/m_e)}$
ω_{pi}	Ion plasma frequency α	$\sqrt{(4\pi n_i Z^2 e^2/m_i)}$
$\vec{B}$	Magnetic field	
$\vec{E}$	Electric field	
c	speed of light.	$299,792,458\, m/s$
e	electron charge,	$1.06 \times 10^{-19} C$ =4.803×10^{-10} Fr
m_α	mass of particles of species α	
n_α	density of particles of species α	
P_L, ω_L, k_L	power, frequency and wave number of a laser	
P_s, ω_s, k_s	power, frequency and wave number of scattered light	
T_α	Temperature of particles of species α	$\frac{2}{3}$ times the average particle energy
v_e	Mean electron flow velocity	
v_i	Mean ion flow velocity	
$v_{T\alpha}$	Thermal velocity of particles of species α	$\sqrt{\frac{T_\alpha}{m_\alpha}}$
Z	ion charge	q_i/e

Chapter 1

Introduction

This thesis describes analysis, simulations, and experiments conducted in the pursuit of multiple goals in plasma physics research summarized below. These projects are connected by their use of the Optical Thomson Scattering (OTS) systems and its interaction with electric currents, driven by heat flux or plasma instabilities. All these processes are discussed later in this chapter.

I have written and contributed to several publications, in which we initially confirmed that currents in plasma had predictable effects on measured OTS spectra and that these effects could be distinguished from other phenomena present in unstable plasma [2]. We later used this technique to ascertain the magnetic field structure and amplitude in Weibel-unstable plasma [3], and assisted with measurements of collisionless shock formation [4] by quantifying the measurement precision of the OTS system [1]. The current sheet in plasma undergoing magnetic reconnecting was also similarly measured [5].

OTS spectra are affected by currents in plasma and by currents induced by heat transport processes, which are of crucial importance to the modeling of ICF (Inertial Confinement Fusion) plasma evolution. In order to further the understanding of heat transport in these conditions, we analyzed plasma conditions in various ablation plasmas [7, 8] and observed currents caused by heat transport in gold plasma [6]. Return currents in gas-jet plasma were also seen to drive the growth of the ion acoustic

wave [9].

1.1 Laser Plasma Coupling

The primary experimental diagnostic discussed in this work is Optical Thomson Scattering (OTS). In this section, we will outline the process by which the probe laser is scattered from the plasma, as well as the thermal and driven fluctuations which scatter the probe, forming the OTS spectrum.

1.1.1 Thomson Scattering

Photon-electron interactions with free electrons and high-energy photons can be described by Compton scattering. The energy loss of the scattered photon compared to the incident photon $\Delta E_\gamma = -(\frac{m_e c^2}{E_\gamma(1-\cos\theta)} + 1)^{-1} E_\gamma$ [10]. For light in the visible range, the photon energy E_γ is on the order of $\sim 3eV$, leading to $\Delta E_\gamma / E_\gamma \approx 0$. This means we can neglect the momentum imparted on the electron for these laser-plasma scattering events.

When a probe laser propagates through a plasma, the laser field $\vec{E}_L = \vec{E}_0 \cos(\vec{k_L} \cdot \vec{r} - \omega_L t)$, where k_L and ω_L are the laser wave number and frequency, will cause the electrons in the plasma to oscillate in the direction of $\vec{E}_0$. When observing from outside of the plasma in the radiation zone (distances much larger than the electron oscillation radius [11]), the scattered light from one electron is

$$\delta\vec{E}_{se} = -\frac{e}{cR}\left(\frac{\hat{s}\times(\hat{s}-\frac{\vec{v}}{c})\times\frac{\vec{a}}{c}}{(1-\hat{s}\cdot\frac{\vec{v}}{c})^3}\right)_{time=t'} \tag{1.1}$$

where $t' = t - R/c + \hat{s}\cdot\vec{r}/c$ is the retarded time of the electron at position $\vec{r}$ seen from the observer at position $\vec{R}$, in direction $\hat{s}$ [12].

For non-relativistic oscillation of electrons, $|\frac{v}{c}| \ll 1$. The field can be simplified to

$$\delta\vec{E}_{se} = -\frac{e}{cR}\left(\hat{s}\times\hat{s}\times\frac{\vec{a}}{c}\right)_{time=t'} = \frac{e^2}{c^2 R m_e}\cos(\vec{k_L}\cdot\vec{r}-\omega_L t')\left(\hat{s}\times\hat{s}\times\vec{E}_0\right) \tag{1.2}$$

We are interested in the spectrum of light emitted, as observed outside the plasma. This can be found with the Fourier transform of the field in time:

$$\delta\vec{E}_{se}(\omega_s) = \int dt \delta\vec{E}_{se} \exp(i\omega_s t) = \int dt \delta\vec{E}_{se} \exp(i\omega_s(t' - \frac{\hat{s}\cdot\vec{r}}{c} + \frac{R}{c})) \tag{1.3}$$

The electron density in the plasma is also transformed, giving a spectrum in $\vec{k}, \omega$ of fluctuations in the plasma.

$$n_e(\vec{r},t) = \int d^3v F_e = \frac{1}{(2\pi)^3}\sum_{j=1}^{N}\int d\vec{k} n_e(\vec{k},t)\exp(i(\vec{k}\cdot\vec{r}_j - \vec{k}\cdot\vec{v}_j t')) \tag{1.4}$$

where F_e is the discrete electron distribution function $F_e(\vec{r},\vec{v},t') = \sum_{j=1}^{N}\delta(\vec{r}-\vec{r}_j(t'))\delta(\vec{v}-\vec{v}_j(t'))$

This scattered field will be emitted by every electron in the probe beam's path. For N electrons traversed, a field $\vec{E}_s = \int d^3v \int_V d^3r F_e \delta\vec{E}_{se}$ will be emitted, where V is the volume of plasma intersecting the laser. The total field in frequency space can then be written

$$\vec{E}_s(\vec{k},t) = \frac{e^2}{c^2 R m_e}\left(\hat{s}\times\hat{s}\times\vec{E}_0\right) V n_e(\vec{k},t)\frac{1}{2}\sum_{j=1}^{N}(\exp(i\phi_{1j}) + \exp(i\phi_{2j})) \tag{1.5}$$

where

$$\begin{aligned}\phi_{1j} &= \vec{k}\cdot\vec{r}_j - \vec{k}\cdot\vec{v}_j t' + \omega_s t' - \omega_s\frac{\hat{s}\cdot\vec{r}_j}{c} + \omega_s\frac{R}{c} + \vec{k_L}\cdot\vec{r} - \omega_L t' \\ &= \omega_s\frac{R}{c} - t'(\vec{k}\cdot\vec{v}_j - (\omega_s - \omega_L)) + (\vec{k} - (\omega_s\frac{\hat{s}}{c} - \vec{k_L}))\cdot\vec{r}_j\end{aligned} \tag{1.6}$$

$$\begin{aligned}\phi_{2j} &= \vec{k}\cdot\vec{r}_j - \vec{k}\cdot\vec{v}_j t' + \omega_s t' - \omega_s\frac{\hat{s}\cdot\vec{r}_j}{c} + \omega_s\frac{R}{c} - \vec{k_L}\cdot\vec{r}_j + \omega_L t' \\ &= \omega_s\frac{R}{c} - t'(\vec{k}\cdot\vec{v}_j - (\omega_s + \omega_L)) + (\vec{k} - (\omega_s\frac{\hat{s}}{c} + \vec{k_L}))\cdot\vec{r}_j\end{aligned} \tag{1.7}$$

ϕ_{2j} (1.7) is identical to ϕ_{2j} , except with negative values of ω_s. We are interested in the time-average of the squared field to find the scattered power, $< |\vec{E}_s(\vec{k})|^2 >=$

$\lim_{T\to\infty} \frac{1}{T} \int_{-T/2}^{T/2} |\vec{E}_s(\vec{k},t)|^2 dt$. As particles in the plasma are uncorrelated, all phase terms in $< |\vec{E}_s(\vec{k},t)|^2 >$ with different particles will integrate to 0 over the volume V, as $\int dt' \exp\left(i(\phi_{1j} - \phi_{1i})\right) = 0$ for $j \neq i$ [11]. What remains is the incoherent superposition of particle scattering. Therefore, the scattered light will be composed of the auto-correlation of particles, summed over all particles in the distribution. This allows the spectrum of density fluctuations (1.4) to be written using the continuous particle distribution function, f_e, with the discrete list of particle speeds $\vec{k}\cdot\vec{v}_j$ replaced with the scattering frequency ω.

$$\phi_1 = \omega_s \frac{R}{c} - t'(\omega - (\omega_s - \omega_L)) + (\vec{k} - (\omega_s \frac{\hat{s}}{c} - \vec{k_L})) \cdot \vec{r} \tag{1.8}$$

$$\phi_2 = \omega_s \frac{R}{c} - t'(\omega - (\omega_s + \omega_L)) + (\vec{k} - (\omega_s \frac{\hat{s}}{c} + \vec{k_L})) \cdot \vec{r} \tag{1.9}$$

Under time and space integration the phase in ϕ_1 determines the relation between scatted light and perturbations in the plasma density: $\int_{-\infty}^{\infty} dt' \exp\left(-it'(\omega - (\omega_s - \omega_L))\right) = 2\pi\delta(\omega - (\omega_s - \omega_L))$ and $\int_{-\infty}^{\infty} dr \exp\left(i\vec{r} \cdot (\vec{k} - (\omega_s \frac{\hat{s}}{c} - \vec{k_L}))\right) = 2\pi\delta(\vec{k} - (\vec{k}_s - \vec{k}_L))$, where $\vec{k}_s$ is found using the scattered light's dispersion relation in vacuum $\omega_s = k_s c$. As only $\omega = \omega_s - \omega_L$ contributes to scattering, this becomes the wave frequency ω scattering all light at frequency ω_s. This allows the scattered frequency and wave number to be defined:

$$\omega_s = \omega + \omega_L \tag{1.10}$$

$$\vec{k}_s = \vec{k} + \vec{k}_L \tag{1.11}$$

The time-averaged field is replaced with the frequency-averaged field [12]: $\int dt |\vec{E}_s(t)|^2 = \frac{1}{2\pi} \int_{-\infty}^{\infty} |\vec{E}_s(\vec{k},\omega)|^2 d\omega = \frac{1}{\pi} \int_0^{\infty} |\vec{E}_s(\vec{k},\omega)|^2 d\omega$. The term of Eq. (1.5) with phase ϕ_{2j} then completes the spectrum for negative frequencies.

The resulting scattered power spectrum can be seen in the flow of energy in the scattered light, which has energy density $U = U(\vec{E}) + U(\vec{B}) = \frac{\vec{E}_s^2}{4\pi}$. The differential power spectrum $P_s(\vec{k}, \omega)$ can then be defined with the spectrum of the field $\vec{E}_s(\vec{k}, \omega)$, where $\omega = \vec{k} \cdot \vec{v}$:

$$\begin{aligned} P_s(\vec{k}, \omega) &= d\Omega R^2 c \frac{\vec{E}_s^2}{4\pi^2} \\ &= d\Omega c \frac{E_0^2 V}{4\pi^2} \frac{e^4}{c^4 m_e^2} |\hat{s} \times \hat{s} \times \hat{E}_0||n_e(\vec{k}, \omega)|^2 (\frac{1}{4}) \end{aligned} \tag{1.12}$$

With time-averaged probe power $P_L = \frac{cE_0^2}{8\pi} A$, where A is the area of the probe beam,

$$P_s(\vec{k}, \omega) = d\Omega \frac{P_L L_{TS}}{2\pi} \frac{e^4}{c^4 m_e^2} |\hat{s} \times \hat{s} \times \hat{E}_0| n_e S(\vec{k}, \omega) \tag{1.13}$$

where L_{TS} is the length of the Thomson scattering volume in the direction of the probe, and $S(\vec{k}, \omega) = \frac{<|\delta n_e(\vec{k}, \omega)|^2>}{n_e}$ is the dynamical form factor of electrostatic waves in the plasma. The spectrum of this form factor is derived in section 1.1.2.

1.1.2 Fluctuations from Particle Discreteness

When plasma is in thermal equilibrium with no external forces acting on it, the isolated particles in the plasma still produce fluctuations. The discrete nature of particles leads to a level of density fluctuations on different length scales, which evolve according to the electromagnetic susceptibility of the plasma.

Plasma typically consists of two different species: electrons and ions. Electrons move to shield charges at distances greater than the Debye length, and ion fluctuations create similar fluctuations in electron density, which maintains the plasma quasi-neutrality [13].

To quantify the waves that exist in thermal plasma, we supplement the equilibrium distribution of particles f to create a test perturbation distribution $F_{\alpha t}$, approximating the discrete particle distribution $F_\alpha(\vec{r}, \vec{v}, t)$ around $t = 0$. Each particle in $F_{\alpha t}$ is

assumed to be free streaming for the duration of the plasma response. Fluctuations in either of these species have impacts on both species. For a plasma with N_α particles of species α, the perturbation to the plasma is then

$$F_{\alpha t} = \sum_{j=1}^{N_\alpha} \delta(\vec{r} - \vec{r}_{j\alpha} - \vec{v}_{j\alpha} t)\delta(\vec{v} - \vec{v}_j) \tag{1.14}$$

The motion of each test particle also polarizes the rest of the distribution function. The electron distribution function can be split into $F_e = F_{et} + f_{e,(et)} + f_{e,(it)}$: the perturbation distribution due to test particles, the electron polarization response to electron test particles, and the electron polarization response to ion test particles. The ions also respond to electron perturbations, making $F_i = F_{it} + f_{i,(it)} + f_{i,(et)}$.

The Poisson equation for these effects can be written

$$-\nabla^2\Phi = 4\pi \int d^3v(-eF_e + ZeF_i) \tag{1.15}$$

As the Poisson equation is linear in charge density, (1.15) can be split into two potentials: an electron perturbation potential and an ion perturbation potential, which each balance separate polarization distributions in the plasma.

$$-\nabla^2\Phi_e = 4\pi \int d^3v(-eF_{et} - ef_{e,(et)} + Zef_{i,(te)}) \tag{1.16}$$

$$-\nabla^2\Phi_i = 4\pi \int d^3v(ZeF_{it} - ef_{e,(it)} + Zef_{i,(it)}) \tag{1.17}$$

The electron and ion polarization can be related to these potentials using the Vlasov equation:

$$\frac{\partial}{\partial t} f_{e,(et)} + \vec{v} \cdot \nabla f_{e,(et)} - \frac{e}{m_e} \nabla\Phi_e \cdot \frac{\partial F_e}{\partial \vec{v}} = 0 \tag{1.18}$$

$$\frac{\partial}{\partial t} f_{i,(et)} + \vec{v} \cdot \nabla f_{i,(et)} + \frac{Ze}{m_i} \nabla\Phi_e \cdot \frac{\partial F_i}{\partial \vec{v}} = 0 \tag{1.19}$$

$$\frac{\partial}{\partial t} f_{e,(it)} + \vec{v} \cdot \nabla f_{e,(it)} - \frac{e}{m_e} \nabla \Phi_i \cdot \frac{\partial F_e}{\partial \vec{v}} = 0 \tag{1.20}$$

$$\frac{\partial}{\partial t} f_{i,(it)} + \vec{v} \cdot \nabla f_{e,(it)} + \frac{Ze}{m_i} \nabla \Phi_i \cdot \frac{\partial F_i}{\partial \vec{v}} = 0 \tag{1.21}$$

Applying the Fourier transform $\frac{1}{(2\pi)^3} \int d^3r \exp(-i\vec{k} \cdot \vec{r})$ as well as time dependence $\sim \exp(-i\vec{k} \cdot \vec{v}_j t)$ to these the electron polarization equations gives

$$f_{e,(et)}(\vec{k}, \vec{v}, t) = -\frac{e}{m_e} \Phi_e \frac{1}{(\vec{v} \cdot \vec{k} - \vec{v}_j \cdot \vec{k})} \vec{k} \cdot \frac{\partial F_e}{\partial \vec{v}} \tag{1.22}$$

These can be simplified by using the susceptibility function χ_α, with $\omega_j = \vec{v}_j \cdot \vec{k}$:

$$\chi_\alpha = \frac{\omega_{p\alpha}^2}{k^2} \int d^3v \frac{1}{(\omega - \vec{k} \cdot \vec{v})} \vec{k} \cdot \frac{\partial}{\partial \vec{v}} \bar{f}_\alpha(v) \tag{1.23}$$

Where $\alpha = e, i$ and $\bar{f}_\alpha(v) = \frac{f_\alpha(v)}{n_\alpha}$ is the normalized distribution function. $\omega_{pe}^2 = \frac{4\pi e^2 n_e}{m_e}$, so Eq. (1.22) can be simplified to

$$\delta n_{e,(et)}(\vec{k}, t) = \int d^3v f_{e,(et)}(\vec{k}, \omega, v) = \sum_{j=1}^{N_e} -\frac{\Phi_e k^2}{(-e)4\pi} \chi_e(\vec{k}, \vec{k} \cdot \vec{v}_j) \exp(-i\vec{k} \cdot (\vec{r}_{je} + \vec{v}_{je} t)) \tag{1.24}$$

Where $\delta n_{e,(et)}$ is the electron density fluctuation of the plasma in response to an electron density perturbation n_{et}. Similarly, Eq. (1.19) can be solved for the ion response from an electron charge perturbation:

$$\delta n_{i,(et)}(\vec{k}, t) = \int d^3v f_{i,(et)}(\vec{k}, \omega, v) = \sum_{j=1}^{N_e} -\frac{\Phi_e k^2}{(Ze)4\pi} \chi_i(\vec{k}, \vec{k} \cdot \vec{v}_j) \exp(-i\vec{k} \cdot (\vec{r}_{je} + \vec{v}_{je} t)) \tag{1.25}$$

The transformed Poisson equation can then be used to find Φ_e:

$$k^2 \Phi_e(\vec{k}, t) = \sum_{j=1}^{N_e} \exp(-i\vec{k} \cdot (\vec{r}_{je} + \vec{v}_{je} t))(4\pi e) \left(-n_{et} - \int d^3v f_{e,(te)}(\vec{k}, \omega) + Z \int d^3v f_{i,(te)}(\vec{k}, \omega) \right) \tag{1.26}$$

Solving (1.26) for Φ_e also determines $\delta n_{e,(et)}(\vec{k},\vec{v},t)$, the fluctuations in electron density due to the ion an electron response to electron discreteness:

$$\Phi_e(\vec{k},t) = \sum_{j=1}^{N_e} \frac{-4\pi e n_{et} \exp\left(-i\vec{k}\cdot(\vec{r}_{je}+\vec{v}_{je}t)\right)}{k^2(1+\chi_e+\chi_i)} \tag{1.27}$$

$$\delta n_{e,(et)}(\vec{k},\omega) = \sum_{j=1}^{N_e} -n_{et} \exp\left(-i\vec{k}\cdot(\vec{r}_{je}+\vec{v}_{je}t)\right)\frac{\chi_e}{(1+\chi_e+\chi_i)} \tag{1.28}$$

Eqs. (1.20,1.21) can be used similarly to find the electron response to a perturbation in the ion distribution function:

$$\delta n_{e,(it)}(\vec{k},\omega,v) = \sum_{j=1}^{N_i} \exp\left(-i\vec{k}\cdot(\vec{r}_{ji}+\vec{v}_{ji}t)\right)\frac{\chi_e}{(1+\chi_e+\chi_i)} \tag{1.29}$$

The total change in the electron distribution is then $\delta n_e = n_{et} + \delta n_{e,(et)} + \delta n_{e,(it)}$.

$$\begin{aligned}\delta n_e = n_{et}(1-\frac{\chi_e}{1+\chi_e+\chi_i})\sum_{j=1}^{N_e}\exp\left(-i\vec{k}\cdot(\vec{r}_{je}+\vec{v}_{je}t)\right)\\ +n_{it}(-\frac{\chi_e}{1+\chi_e+\chi_i})\sum_{j=1}^{N_i}\exp\left(-i\vec{k}\cdot(\vec{r}_{ji}+\vec{v}_{ji}t)\right)\end{aligned} \tag{1.30}$$

Correlations between particles will contribute to the fluctuation spectrum. As the particle perturbations n_{et} and n_{it} come from free streaming test particles in the electrons and ions respectively, the correlations $< n_{et}n_{it} >= 0$.

When the quantity δn_e^2 is averaged over a volume with $|L| \gg k^{-1}$, terms with non-identical particles in $< n_{et}n_{it} >= 0$ will integrate to 0, as the test particles are uncorrelated and leave a non-zero phase. In each wavelength of a fluctuation with wave number $\vec{k}$, the number of particles that exist of species α is $\frac{2\pi}{k}n_\alpha \bar{f}_\alpha(v=\frac{\omega}{k})$ [12]. The variance of particle fluctuations $< n_{\alpha t}n_{\alpha t} >= |\delta n_\alpha|^2$ is equivalent to the number of particles that can affect a wave of wave number $\vec{k}$.

This allows the definition of the expected fluctuations in stable plasma, $S(\vec{k},\omega)$, defining the frequency $\omega = \vec{k}\cdot\vec{v}_j$:

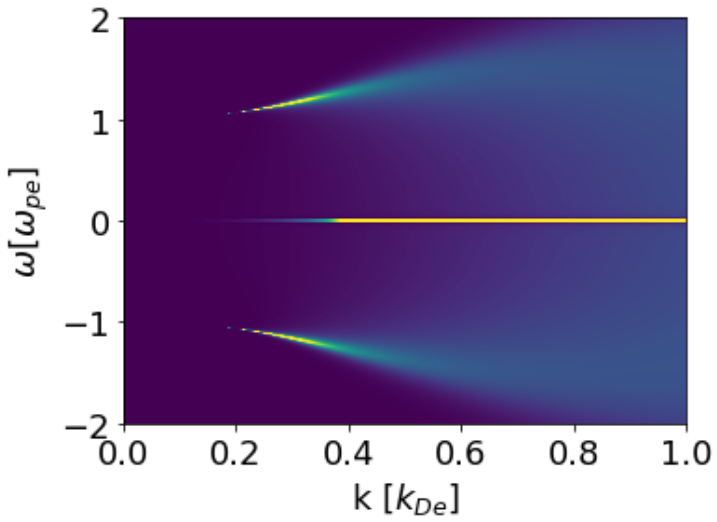

Figure 1.1: Form factor $S(\vec{k},\omega)$ for $T_e = T_i = 1keV$ Neon plasma. Red and blue shifted electron plasma waves (first term, (1.31)) can be seen on the top and bottom, with the ion acoustic wave is constrained to lower phase velocities in the center.

$$S(\vec{k},\omega) = \frac{<|\delta n_e|^2>}{n_e} = \frac{2\pi}{k}\left|1 - \frac{\chi_e}{\epsilon}\right|^2 \bar{f}_e\left(\frac{\omega}{k}\right) + \frac{2\pi}{k}\left|\frac{\chi_e}{\epsilon}\right|^2 Z\bar{f}_i\left(\frac{\omega}{k}\right) \tag{1.31}$$

where $\epsilon = 1 + \chi_e + \chi_i$. Eq. (1.31) is the dynamic form factor of electrostatic waves in electrons, which determines the spectrum of scattered light in OTS (1.13). This determines the OTS scattering spectrum from stable plasma. Typical examples as well as additional effects on the OTS spectrum are included in Ch. 2.

1.1.3 Driven Waves

In addition to fluctuations from particle discreteness, waves in plasma can be driven by external forces. Lasers can exert these forces in plasma, driving waves that can resonate with the plasma response to produce large-scale changes in density. Laser coupling to electrostatic waves in plasma typically occurs via the ponderomotive force, which can be enhanced by plasma and laser properties increasing the oscillation time and amplitude.

Ponderomotive Force

Lasers in plasma initially impact plasma electron density with the ponderomotive force, where the laser field drives electrons in the plasma away from places with higher field intensities.

A stationary particle in a laser field will experience an electric field oscillating with the frequency of the laser, $\vec{E} = \vec{E}_0(x)\cos(\omega t)$. For low-intensity or high-frequency lasers ($\frac{eE_0}{m\omega} \ll c$) [14], the effects of the magnetic field are small and can be neglected. If $E_0(x)$ is non-uniform, it can induce motion in charged particles at two time scales: the short period of the laser $2\pi\omega^{-1}$, and the longer time scale associated with the drift of the particles across the length scale of the laser spot [15],[16].

The motion of charged particles in a laser polarized in the $\hat{x}$ direction can be described as $x = x_0 + x_1$, where x_0 is the slower drift response of the particle and x_1 is the fast motion of the particle at the frequency of the laser. As x_1 is small and changes quickly, $\frac{\partial^2 x_1}{\partial t^2} \gg \frac{\partial^2 x_0}{\partial t^2}$, and $|\vec{E}_0(x_0)| \gg x_1 \frac{dE_0(x_0)}{dx}$. This allows the equation of motion to be split:

$$\frac{d^2x_1}{dt^2} = \frac{q}{m}|\vec{E}_0(x_0)|\cos(\omega t) \tag{1.32}$$

$$\frac{d^2x_0}{dt^2} = \frac{q}{m}\frac{\omega}{2\pi}\int_0^{2\pi/\omega} x_1(\frac{d\vec{E}_0(x)}{dx})|_{x=x_0}\cos(\omega t)dt \tag{1.33}$$

This results in particle trajectories for slow and fast motion:

$$x_1 = -\frac{q}{m}\frac{|\vec{E}_0(x_0)|}{\omega^2}\cos(\omega t) \tag{1.34}$$

$$\frac{d^2x_0}{dt^2} = -\frac{q^2}{m^2}\nabla\frac{|E_0(x_0)^2|}{4\omega^2} \tag{1.35}$$

The factor $\frac{q^2}{m^2}$ indicates that in quasi-neutral plasma, the total force on the ion species will be smaller by a factor of at least 1836 compared to electrons, so the tiny

force on the ions can be ignored. In the $\hat{x}$ direction, the force takes the form of a gradient of E_0^2. This allows the force on electrons $\vec{F}_p$ to be written as the gradient of a potential: $\vec{F}_p = -\nabla U_p$

$$U_p = \frac{e^2 E_0^2}{4 m_e \omega^2} \tag{1.36}$$

Ponderomotive force from the beating of two lasers

When two lasers overlap, they can produce a beat wave in a plasma. This beat drives waves via the ponderomotive force (1.36). The beat frequency and wave number can vary with the laser propagation directions and frequencies. If this beat reaches the phase velocities of electron or ion waves, the plasma response can become much larger for the beating waves than for separate lasers.

The amplitude of the electric field of two lasers can be described as

$$\begin{aligned}\vec{E} &= \vec{E}_{01} \exp\left(i\omega_1 t - i\vec{k}_1 \cdot \vec{r}\right) + i\theta_1 + \vec{E}_{02} \exp\left(i\omega_2 t - i\vec{k}_2 \cdot \vec{r} + i\theta_\right) \\ &= \exp\left(i\frac{\omega_1 + \omega_2}{2} t - i\frac{\vec{k}_1 + \vec{k}_2}{2} \cdot \vec{r}\right) \\ &\left(\vec{E}_{01} \exp\left(i\frac{(\omega_1 - \omega_2)}{2} t - i\frac{\vec{k}_1 - \vec{k}_2}{2} \cdot \vec{r} + i\theta_1\right) + \vec{E}_{02} \exp\left(-i\frac{(\omega_1 - \omega_2)}{2} t + i\frac{\vec{k}_1 - \vec{k}_2}{2} \cdot \vec{r} + i\theta_2\right)\right)\end{aligned} \tag{1.37}$$

where $\vec{E}_{01}, \vec{E}_{01}$ are the amplitudes of the electric fields of the two lasers, and ω_1, ω_2, $\vec{k}_1, \vec{k}_2$ are the respective frequencies and wave numbers of the lasers. θ_1 and θ_2 are the phase shifts of the two lasers.

We see in Eq. (1.37) that this results in a higher frequency of $\frac{\omega_1+\omega_2}{2}$, and a lower frequency $\frac{\omega_1-\omega_2}{2}$ response. For $|\omega_1 - \omega_2| \ll \omega_1 + \omega_2$, the high frequency effect will change the sign of the beat many times during the slower period, making the slow wave's current amplitude act as an envelope of the wave. As the ponderomotive force is proportionate to $|\vec{E}|^2$ the effective frequency of this envelope is doubled to become $|\omega_1 - \omega_2|$, which is known as the beat frequency, ω_b (Fig. 1.2).

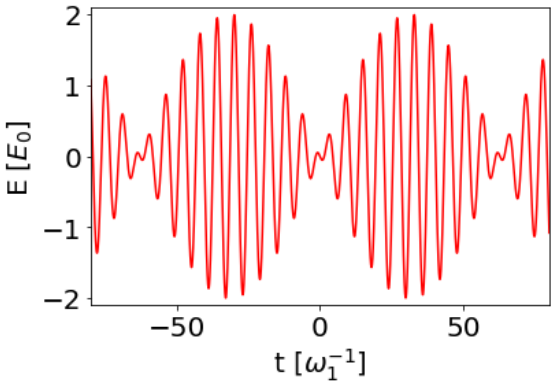

Figure 1.2: Beat wave at a point from two counter-propagating lasers, with $\vec{E}_{01} = \vec{E}_{02}$ and $\omega_2 = 1.1\omega_1$

The beat frequency can be seen in the time dependence of the envelope $E_{env}^2 = |\vec{E}|^2$:

$$E_{env}^2 = (|\vec{E}_{01}|^2 + |\vec{E}_{02}|^2) + 2\vec{E}_{01} \cdot \vec{E}_{02} \cos\left((\omega_1 - \omega_2)t - (\vec{k}_1 - \vec{k_2}) \cdot \vec{r} + (\theta_1 - \theta_2)\right) \tag{1.38}$$

The constant terms in (1.38) are the part of the $\vec{E}$ field with no beat wave, containing only fast oscillations in the $\vec{E}$ field (1.37). These fast oscillations have phase velocities $\omega/k \geq c$, limiting the plasma response they can create. The effect on the plasma would be the same as separate beams would have, so the constant terms in (1.38) can be ignored when investigating resonant plasma response to the beat wave.

The second term in Eq. (1.38) will contain much lower velocity waves for similar frequencies of counter-propagating beams, where $\vec{k}_b = |\vec{k}_1 - \vec{k}_2| \gg |\vec{k}_1|$. These low phase velocity waves follow an amplitude controlled by the angle of the two lasers (1.36):

$$U_p = \frac{2e^2 \vec{E}_{01} \cdot \vec{E}_{02}}{m_e(\omega_1 + \omega_2)^2} \cos\left(\omega_b t - \vec{k}_b \cdot \vec{r} + (\theta_1 - \theta_2)\right) \tag{1.39}$$

This ponderomotive potential forces electrons away from the beating wave but has a negligible effect on ions due to their much larger mass. This results in a charge imbalance, where the change in electron density due to the ponderomotive force δn_e

creates an electric potential $\phi \propto U_p$. The potential can be found with the Poisson equation:

$$-\nabla^2\phi = -4\pi e\delta n_e + 4\pi Ze\delta n_i \tag{1.40}$$

To evaluate the change in density δn_e and δn_i, the Vlasov equation is used:

$$\frac{\partial f_e}{\partial t} + \vec{v}\cdot\nabla f_e + \frac{-\nabla(U_p - e\phi)}{m_e}\frac{\partial f_e}{\partial v} = 0 \tag{1.41}$$

$$\frac{\partial f_i}{\partial t} + \vec{v}\cdot\nabla f_i + \frac{-\nabla(Ze\phi)}{m_i}\frac{\partial f_i}{\partial v} = 0 \tag{1.42}$$

where $f_e = f_e(\vec{r},\vec{v},t)$ and $f_i = f_i(\vec{r},\vec{v},t)$ are the electron and ion distribution functions, respectively. The density perturbation can be found by linearizing the Vlasov equation [17] (1.41), with $f = f_0 + \delta f$, $\delta n = \int \delta f dv^3$. The gradients of the potential ϕ and ponderomotive potential U_p are small, and the terms δf, U_p and ϕ all change in time and space like $\exp(i(\omega_b t - \vec{k}_b\vec{r}))$, leading to the equations

$$\omega_b\delta f_e - \vec{v}\cdot\vec{k}_b\delta f_e - \frac{e\phi - U_p}{m_e}\vec{k}_b\cdot\frac{\partial f_{e0}}{\partial\vec{v}} = 0 \tag{1.43}$$

$$\omega_b\delta f_i - \vec{v}\cdot\vec{k}_b\delta f_i + \frac{Ze\phi}{m_i}\vec{k}_b\cdot\frac{\partial f_{i0}}{\partial\vec{v}} = 0 \tag{1.44}$$

Re-arranging and integrating over velocity gives an expression for δn

$$\delta n_e = \frac{e\phi - U_p}{m_e}\int d^3v\vec{k}_b\cdot\frac{\partial f_{e0}}{\partial\vec{v}}\frac{1}{(\omega_b - \vec{k}_b\cdot\vec{v})} \tag{1.45}$$

$$\delta n_i = \frac{-Ze\phi}{m_i}\int d^3v\vec{k}_b\cdot\frac{\partial f_{i0}}{\partial\vec{v}}\frac{1}{(\omega_b - \vec{k}_b\cdot\vec{v})} \tag{1.46}$$

This density fluctuation level can similarly be combined with the Poisson equation (1.40) to solve for ϕ in terms of U_p.

$$\phi = \frac{U_p}{e} \frac{\chi_e}{1 + \chi_e + \chi_i} \tag{1.47}$$

where χ is the susceptibility (1.23,1.48) (Fig. 1.3):

$$\chi_e = \frac{4\pi e^2}{m_e k^2} \int d^3v \vec{k}_b \cdot \frac{\partial f_e}{\partial \vec{v}} \frac{1}{(\omega_b - \vec{k}_b \cdot \vec{v})} \tag{1.48}$$

$$\chi_i = \frac{4\pi Z^2 e^2}{m_i k^2} \int d^3v \vec{k}_b \cdot \frac{\partial f_i}{\partial \vec{v}} \frac{1}{(\omega_b - \vec{k}_b \cdot \vec{v})} \tag{1.49}$$

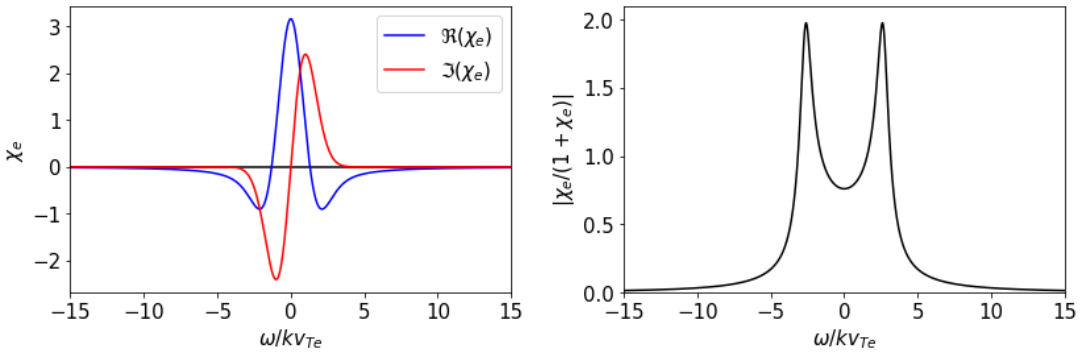

Figure 1.3: Electron susceptibility function for n_e=$10^{20} cm^{-3}$, T_e=1keV, $k = 0.56 k_{De}$. Resonance factor for waves is shown in black, for the high frequency approximation ($\chi_i = 0$). Waves with $\omega/k > 5 v_{Te}$ are strongly suppressed (1.50)

The electron density perturbations are then given by

$$\delta n_e = n_e \frac{-U_p k^2}{m_e \omega_p^2} \frac{\chi_e (1 + \chi_i)}{1 + \chi_e + \chi_i} \tag{1.50}$$

For high frequencies ($\omega_b \gg \omega_{pi}$), these perturbations are primarily dependent on the electron distribution function around the phase speed of the beat, ω_b/k_b. In figure 1.3, we can see that the beat can be strongly enhanced when it coincides with the electron plasma wave's phase velocity [18]. This resonance becomes sharper and more enhanced with increased OTS parameter $\alpha = \frac{1}{k\lambda_{De}}$.

Laser-driven waves in plasma traveling much faster than the thermal electrons have very little impact on the electron density fluctuations (Fig. 1.3). For lasers at very

different frequencies, this makes the effect of counter-propagating lasers generating beating waves much larger than the effects of co-propagating lasers, as the phase velocity of the beat can be much lower than c, coinciding with the EPW resonance. For lasers of very similar frequencies, co-propagating lasers can also have lower phase velocities, as their small differences in $\vec{k}$ can exceed their smaller differences in frequency. In these cases, the driven wave can gain an amplitude larger than that of thermal fluctuations, as seen in sec. 4.5.

1.2 Laser Plasmas Relevant to Astrophysics

Astrophysical plasmas are investigated for their ability to accelerate particles, creating high energy cosmic rays that can be detected on earth [19, 20]. These plasmas of interest typically contain counter-streaming flows, providing the energy necessary to create electromagnetic fields, shocks, and high-energy particles [21]. Similar environments can also be produced in laboratory plasmas, allowing for detailed measurement and analysis of processes that would otherwise be far out of reach.

1.2.1 Weibel Instability

When two expanding plasmas interpenetrate under collisionless conditions, they produce an initially homogeneous plasma containing two distinct sets of particles streaming in opposite directions. This arrangement of plasma is unstable to the formation of separated currents: small fluctuations in current create fields which enhance these currents along the flow directions, driving the growth of stronger magnetic fields. This growth of magnetic fields can eventually lead to turbulence and the formation of a collisionless shock [4] [22] [23].

If a homogeneous counter-streaming plasma has flows with velocity $\pm v_0\hat{x}$, the formation of currents filaments [24] can be found by observing the dynamics of a small transverse fluctuation in the $\hat{y}$ direction with field $\vec{E} = E_1 \exp i(ky - \omega t)\hat{x}$, velocity $\vec{v}_{a,b} = \pm v_0\hat{x} + \vec{v}_1 \exp i(ky - \omega t)\hat{x}$, and a density for each stream of $n_{a,b} =$

$n_0 + n_1 \exp i(ky - \omega t)$ (Fig. 1.4).

The momentum equation for the electron fluid is then

$$\frac{\partial \vec{v}}{\partial t} + (\vec{v} \cdot \nabla)\vec{v} = -\frac{e}{m_e}\vec{E} - \frac{e}{m_e}\frac{\vec{v}}{c} \times \vec{B} \tag{1.51}$$

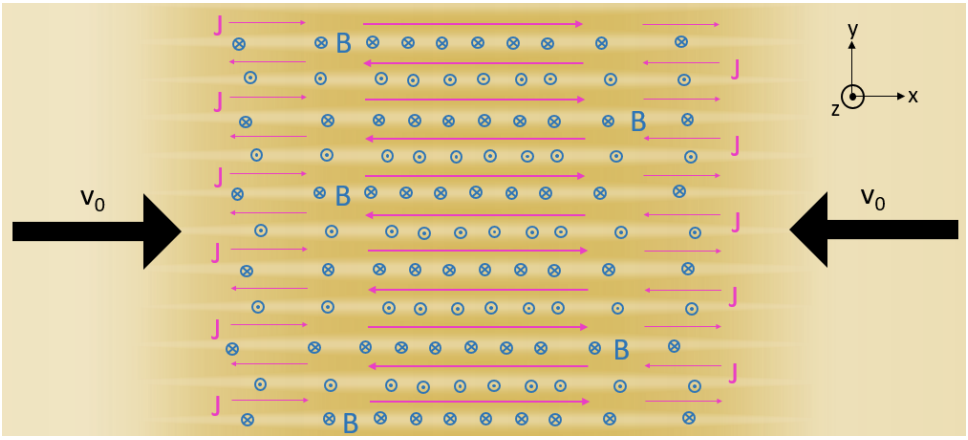

Figure 1.4: Geometry of the Weibel instability

The electromagnetic fluctuations can be described with Faraday's law: $\nabla \times \vec{E} = -\frac{1}{c}\frac{\partial \vec{B}}{\partial t}$. For the fluctuations in $\hat{y}$, this reduces to $\vec{B} = -\hat{z}\frac{kc}{\omega}E_1$. This can be combined with the fluid equation, and the flow velocity can be split into two directions, with $\vec{v_1} = v_{1x}\hat{x} + v_{1y}\hat{y}$. v_{1x} is driven by the $\vec{E}$ field, and v_{1y} is driven by $\vec{v} \times \vec{B}$.

$$v_{1x} = -i\frac{e}{m_e\omega}E_1 \tag{1.52}$$

$$v_{1y} = -i\frac{e}{m_e\omega}E_1(\frac{kv_0}{\omega}) \tag{1.53}$$

To find the current, we must also find the perturbed density of the flows, using the continuity equation:

$$\frac{\partial n}{\partial t} + \nabla \cdot (n\vec{v}) = 0 \tag{1.54}$$

Divergence can only come from the perturbation velocity $\vec{v}_1$. The resulting density perturbation depends on the transverse velocity (1.53):

$$n_1 = n_0 \frac{k v_{1y}}{\omega} = -i n_0 \frac{k^2}{\omega^2} \frac{e v_0}{m_e \omega} E_1 \tag{1.55}$$

Two currents can be calculated, for the streaming direction $\hat{x}$ and the wave direction $\hat{y}$. Current in $\hat{y}$ is linear with v_0, and therefore is canceled in counter-streaming flows. The bulk current $\pm v_0 n_0 e \hat{x}$ is also canceled, leaving the first order perturbations to the current in $\hat{x}$ to be $-2n_1 v_0 e$ and $-2n_0 v_{1x} e$:

$$J_x = 2in_0 \frac{e^2}{m_e \omega} E_1 + n_0 \frac{k^2}{\omega^2} i \frac{e^2 v_0^2}{m_e \omega} E_1 = in_0 \frac{e^2 E_1}{m_e \omega} (1 + \frac{k^2 v_0^2}{\omega^2}) \tag{1.56}$$

We can use this current J_x to find the dispersion relation of the Weibel instability using Maxwell's equations. Since $\nabla \times \nabla \times \vec{E} = k^2 E_1 = i\omega \frac{4\pi}{c^2} J_x + \frac{\omega^2}{c^2} E_1$. Factoring out the initial perturbation field E_1, we have

$$k^2 - \frac{\omega^2}{c^2} = -\frac{4\pi (2n_0) e^2}{m_e c^2} (1 + \frac{k^2 v_0^2}{\omega^2}) \tag{1.57}$$

using $\frac{4\pi (2n_0) e^2}{m_e} = \omega_{pe}$, and $v_0 \ll c$, we can simplify (1.57) to the dispersion relation

$$\omega^2 = -\frac{\omega_{pe}^2 k^2 v_0^2}{\omega^2 + c^2 k^2} \tag{1.58}$$

Eq. (1.58) results in $\gamma = \Im(\omega) > 0$ for the mode perpendicular to the flow, confirming that the perturbation fields and currents will grow in amplitude, creating transversely modulated currents. This process is demonstrated with Particle in Cell simulations in Ch. 3 (Fig. 3.3) and explored in more detail.

1.2.2 Magnetic Reconnection

When counter-streaming plasma is magnetized before it interacts, the magnetic fields can control the evolution of the plasma by their pressure and stored energy [25–27].

Magnetic fields are transported by both plasma flow and magnetic diffusion. These effects are expressed in the non-ideal Magnetohydrodynamics (MHD) equations [13, 28], where the time dependence of the magnetic field is shown as:

$$\frac{\partial \vec{B}}{\partial t} = \nabla \times \vec{v} \times \vec{B} + \frac{c^2}{4\pi\sigma}\nabla^2 \vec{B} \tag{1.59}$$

where $\sigma = \frac{n_e e^2}{m_e \nu_{ei}}$ is the electrical conductivity of the plasma, and ν_{ei} is the collision rate.

The first term in (1.59) controls the advection of magnetic fields due to flows in the plasma, and the second term is caused by the diffusion of fields through the plasma. The ratio of these terms is known as the magnetic Reynolds number, $R_m = VL\frac{4\pi\sigma}{c^2}$, where V and L are the velocity and length scales of the plasma respectively. R_m represents the ratio of field advection to the diffusion of magnetic fields.

In order to carry fields towards each-other, counter-streaming flows must start with high magnetic Reynolds numbers. As the flows reach each other, the length scales can shorten, facilitating diffusion.

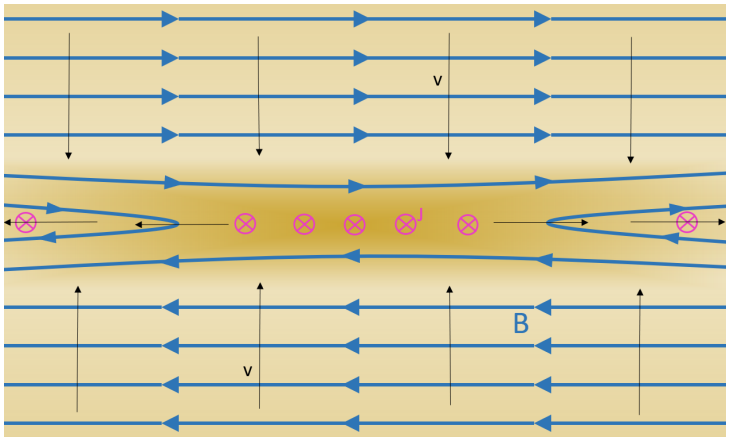

Figure 1.5: Reconnection fields (blue), flow (black) and current (pink)

A counter-streaming plasma that forms a steady state quasi-neutral system has $\nabla \cdot \vec{E} = \nabla \times \vec{E} = 0$, requiring that any electric field be a homogeneous field $\vec{E}_0$. The upstream magnetized plasmas in its own rest frames has electric field $\vec{E} = 0 = \vec{E}_0 + \frac{\vec{v}}{c} \times \vec{B}$, requiring a uniform field of $\vec{E}_0 = -\frac{\vec{v}}{c} \times \vec{B}$.

Between two oppositely directed fields, the magnetic field must reduce to 0 somewhere between the two flows. This point will have $\vec{E} = \vec{E}_0$, driving a current $\vec{J} = \sigma \vec{E}_0$

If the magnetic field changes over a small region of interaction between the two plasma flows, we can expect the slope of the magnetic field $\nabla \times \vec{B}$ to approximate its average value of B_0/L, where B_0 is the upstream field and L is the radius of the current sheet. This allows the scale of the current sheet and the plasma properties to be related:

$$|\vec{J}| = |\frac{c}{4\pi}\nabla \times \vec{B}| \approx \frac{c}{4\pi}(B_0/L) \tag{1.60}$$

$$|\vec{J}| = \sigma E_0 = \sigma \frac{v_0}{c} B_0 \tag{1.61}$$

This allows the magnetic Reynolds number of the current sheet to be found:

$$\frac{4\pi\sigma}{c^2} v_0 L = R_m = 1 \tag{1.62}$$

With $R_m = 1$ on the current sheet scale, the fields can diffuse to reconnect, resulting in energetic outflows of plasma (Fig. 1.5). Empirical measurements of this field structure are explored in section 3.5.

1.2.3 Comparing Plasmas Over Different Scales

As laboratory astrophysics attempts to relate the physics of small, dense, and quickly dissipating laser-ablated plasmas to much larger, lower-density, and longer-lasting astrophysical plasmas, properties observed must be compared across different scales. Simulations using effects relevant to different time and length scales must also be compared to these observables (sec. 3.1). To this end, the causes of plasma evolution and time scales must be understood with respect to characteristic lengths within the plasma. The driving equations can then be transformed into dimensionless equations using these quantities [29].

To fully describe the dynamics of the plasma, we need the election and ion Vlasov equation:

$$\frac{\partial f_\alpha}{\partial t} + \vec{v} \cdot \nabla f_\alpha + \frac{q_\alpha}{m_\alpha}(\vec{E} + \frac{\vec{v}}{c} \times \vec{B}) \cdot \frac{\partial f_\alpha}{\partial v} = 0 \tag{1.63}$$

where $\alpha = e, i$. The evolution of the electric and magnetic fields can be described by

$$\nabla^2 \phi = -4\pi(-en_e + Zen_i) \tag{1.64}$$

$$\nabla^2 \vec{A} = -\frac{4\pi}{c}(-en_e v_e + Zen_i v_i) \tag{1.65}$$

$$\vec{E} = -\nabla\phi - \frac{1}{c}\frac{\partial A}{\partial t} \tag{1.66}$$

$$\vec{B} = \nabla \times \vec{A} \tag{1.67}$$

where $v_{e,i} = \frac{1}{n_{e,i}} \int_{-\infty}^{\infty} f_{e,i} \vec{v} d^3v$ and $n_{e,i} = \int_{-\infty}^{\infty} f_{e,i} d^3v$.

For flowing plasmas, dimensionless equations for ion instabilities can be found using the ion plasma frequency, as well as the characteristic flow speed of the plasma.

Electromagnetic systems

For flowing plasma systems where electromagnetic effects are dominant, $\nabla \cdot \phi$ can be dropped, relying entirely on the vector potential $\vec{A}$ to drive the plasma dynamics. Characteristic scales are then chosen based on the density and flow velocity u (table 1.1)

time	$\frac{c}{u\omega_{pi}}$	$t' = t\frac{u\omega_{pi}}{c}$
length	$\frac{c}{\omega_{pi}}$	$r' = r\frac{\omega_{pi}}{c}$
energy	$\frac{m_i uc}{Ze}$	$\vec{A}' = \vec{A}\frac{Ze}{m_i uc}$
distribution	$\frac{n_\alpha}{u^3}$	$f'_\alpha = f_\alpha \frac{u^3}{n_\alpha}$

Table 1.1: Characteristic lengths used for plasma evolution driven by electromagnetic properties.

The dimensionless Vlasov equation is then reduced to

$$\frac{\partial f'_\alpha}{\partial t'} + \vec{v}' \cdot \nabla' f'_\alpha + \frac{q_\alpha m_i}{q_i m_\alpha}(-\frac{\partial \vec{A}'}{\partial t} + \vec{v}' \times \nabla' \times \vec{A}') \cdot \frac{\partial f'_\alpha}{\partial v'} = 0 \tag{1.68}$$

This contains only one parameter in the electron equation: $\frac{m_i}{Zm_e}$. This implies that two systems with different speeds, densities, lengths, and fields with similar mass to charge ratios for their ions will evolve in the same way, given a similar shape in their initial conditions. The quantities in the two systems can be compared using the scales in table 1.1.

These scaling laws are used in section 3.1 to compare simulations of the Weibel instability to experimental plasmas.

Electrostatic systems

Electrostatic evolution is typically faster than electromagnetic instabilities [29], allowing the short-term evolution of streaming plasmas to be analyzed using exclusively electrostatic equations. For these systems, $\vec{A}$ is dropped, removing magnetic effects. Characteristic scales are chosen based on the speed and density of the plasma (table 1.2)

time	$\frac{1}{\omega_{pi}}$	$t' = t\omega_{pi}$
length	$\frac{u}{\omega_{pi}}$	$r' = r\frac{\omega_{pi}}{u}$
energy	$\frac{m_i u^2}{Ze}$	$\phi' = \phi\frac{Ze}{m_i u^2}$
distribution	$\frac{n_\alpha}{u^3}$	$f'_\alpha = f_\alpha\frac{u^3}{n_\alpha}$

Table 1.2: Characteristic lengths used for plasma evolution driven only by electrostatic properties.

This reduces the Vlasov equation to a similar dimensionless from:

$$\frac{\partial f'_\alpha}{\partial t'} + \vec{v}' \cdot \nabla' f'_\alpha + \frac{q_\alpha m_i}{q_i m_\alpha}(-\nabla'\phi') \cdot \frac{\partial f'_\alpha}{\partial v'} = 0 \tag{1.69}$$

This electrostatic set of equations also has only one parameter controlling plasma evolution: $\frac{Zm_e}{m_i}$. Fixing this quantity allows plasmas across different length, speed, and density scales to be compared, using the scaling relation in table 1.2.

Self-similar plasma expansion

In order to create plasma with similar relative conditions, and therefore identical governing equations (1.68,1.69,1.64,1.65), the plasma conditions must be controlled. The ratios of field energy, kinetic energy, and thermal energy must be equal between two systems in order for them to evolve identically (tables 1.1,1.2).

To control the kinetic energy observed in an ablating plasma, the distance from the plasma source can be used [30]. Once the expanding plasma reaches a scale larger than the Debye length $\lambda_{De} = \sqrt{\frac{T_e}{4\pi n_e e^2}}$, the plasma expands as a quasi-neutral fluid, with electron pressure pulling ions towards the vacuum [31].

The shape of the ion density in the plasma can be understood as a cold fluid. In this case, ion are governed by the continuity and momentum equations:

$$\frac{\partial n_i}{\partial t} + \nabla(v n_i) = 0 \tag{1.70}$$

$$\frac{\partial v}{\partial t} + v\nabla v + \frac{Ze}{m_i}\nabla\phi = 0 \tag{1.71}$$

The electrons have a significant temperature T_e, driving the ions to expand. The electrons are described by a Boltzmann distribution with electrostatic potential ϕ:

$$n_e = Z n_0 \exp\left(\frac{-e\phi}{T_e}\right) \tag{1.72}$$

When considering the 1D expansion of plasma into vacuum and using a sound speed $c_s = \sqrt{\frac{ZT_e}{m_i}}$, these equations can be made dimensionless with the following parameters:

Using quasi-neutrality and the Boltzmann distribution (1.72) we can write the potential as $\Phi = \ln \frac{n_i}{n_0}$ as The continuity and momentum equations (1.70, 1.71) can then be re-written as

$$(u - \epsilon)\frac{d \ln n_i}{d\epsilon} + \frac{du}{d\epsilon} = 0 \tag{1.73}$$

self similar parameter	$\epsilon = \frac{x}{tc_s}$
flow speed	$u = \frac{v}{c_s}$
normalized potential	$\Phi = \frac{e\phi}{T_e}$

Table 1.3: Dimensionless parameters for self-similar expansion

$$(u - \epsilon)\frac{du}{d\epsilon} + \frac{d \ln n_i}{d\epsilon} = 0 \tag{1.74}$$

This can be solved for velocity to $u = \epsilon \pm 1$. Taking the solution that corresponds to out-flowing plasma, we find the self-similar flow velocity v_{ss} of expanding plasma is

$$v_{ss} = \frac{x}{t} + c_s \tag{1.75}$$

This allows for the selection of flow velocities from ablation plasmas by sampling the plasma at the correct distance and time. This self-similar velocity can be seen to match ablated plasma velocities early in plasma evolution (sec. 3.4).

1.3 Kinetic Theory and Particle Transport

When temperature gradients exist in a plasma, energy can be transferred from the hot to the cold regions, driven by the diffusion of high and low energy electrons. This can be described by a heat flux $\vec{q}$ requiring a non-isotropic electron distribution $f_e(\vec{v})$:

$$\vec{q} = \int \frac{m_e v^2}{2} \vec{v} f_e(\vec{v}) d^3v \tag{1.76}$$

In order to describe thermal transport, $f_e(\vec{v})$ is typically expanded into Legendre polynomials, with some characteristic direction $\hat{x}$ aligned with the direction of the temperature gradient in the plasma. The first two terms $f_0(v)$ and $f_1(v)\frac{\vec{v}\cdot\hat{x}}{v}$ describe the temperature and shape of the electron distribution and the majority of the transport, respectively. The shape and size of these distributions is controlled by a balance between transport and particle collisions.

1.3.1 Particle Collisions

When particles are induced to move in plasma by fields or temperature gradients, they quickly reach an equilibrium flux, with the driving thermodynamic forces balanced by friction due to particle collisions. These collisions must be quantified based on particle velocity and plasma properties to determine the equilibrium conditions of a particle transport model.

Coulomb Collisions

To understand collision rates in plasma, the properties of individual coulomb collisions must be quantified. When two particles of mass, charge, and initial momentum m_α, m_β, q_α, q_β, and $p_{i\alpha}, p_{i\beta}$ collide, they follow a trajectory in a 2D plane. In the center of mass frame, the only force between the particles is radial, making their angular momentum constant. Using the particles' reduced mass $m_{\alpha\beta} = \frac{m_\alpha m_\beta}{m_\alpha + m_\beta}$ and relative velocity $\vec{u} = \vec{v}_\alpha - \vec{v}_\beta$, the conserved quantities of energy and angular momentum can be written [32]:

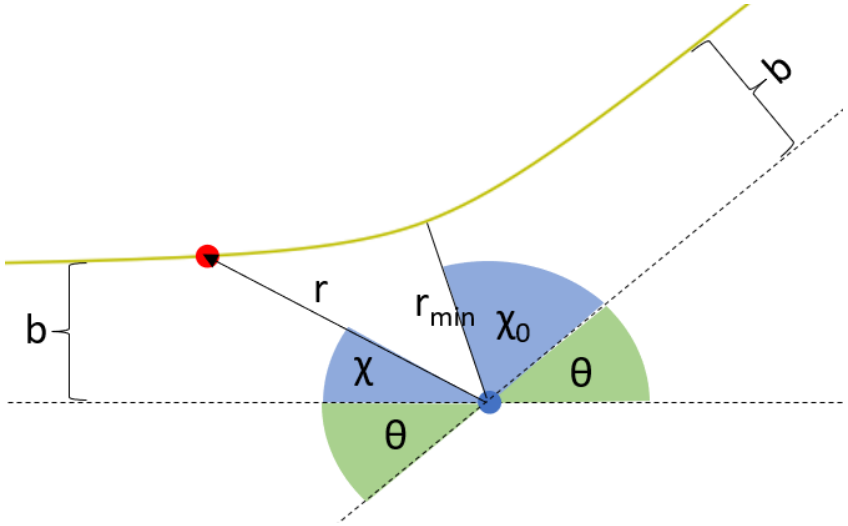

Figure 1.6: Coulomb collision for two charged particles

$$E_0 = \frac{1}{2} m_{\alpha\beta} u_0^2 = \frac{1}{2} m_{\alpha\beta} u(t)^2 + \frac{q_\alpha q_\beta}{r} \tag{1.77}$$

$$L_0 = m_{\alpha\beta} b u_0 = m_{\alpha\beta} r^2 \frac{d\chi}{dt} \tag{1.78}$$

Using $u^2 = (\frac{dr}{dt})^2 + r^2(\frac{d\chi}{dt})^2$, we can use (1.77,1.78) to find the trajectory of the charged particle:

$$\frac{dr}{d\chi} = \frac{r^2}{b}\sqrt{1 - \frac{b^2}{r^2} - \frac{2q_\alpha q_\beta}{r m_{\alpha\beta} u_0^2}} \tag{1.79}$$

At $\frac{dr}{d\chi} = 0$, the closest approach can be found: $r_{min} = \frac{b}{\sqrt{1+\frac{q_\alpha^2 q_\beta^2}{m_{\alpha\beta}^2 u_0^4 b^2}} - \frac{q_\alpha q_\beta}{m_{\alpha\beta} u_0^2 b}}$ (Fig. 1.6). This can then be used with (1.79) to find the angle corresponding to r_{min}:

$$\chi_0 = \int_\infty^{r_{min}} (\frac{dr}{d\chi})^{-1} dr = \int_\infty^{r_{min}} \frac{b}{r^2\sqrt{1 - \frac{b^2}{r^2} - \frac{2q_\alpha q_\beta}{r m_{\alpha\beta} u_0^2}}} dr \tag{1.80}$$

the integral gives

$$\chi_0 = \arcsin\left(\frac{\frac{b}{r_{min}} + \frac{q_\alpha q_\beta}{b m_{\alpha\beta} u_0^2}}{\sqrt{1 + \frac{q_\alpha^2 q_\beta^2}{m_{\alpha\beta}^2 u_0^4 b^2}}}\right) - \arcsin\left(\frac{\frac{q_\alpha q_\beta}{b m_{\alpha\beta} u_0^2}}{\sqrt{1 + \frac{q_\alpha^2 q_\beta^2}{m_{\alpha\beta}^2 u_0^4 b^2}}}\right) = \frac{\pi}{2} - \arctan\frac{q_\alpha q_\beta}{b m_{\alpha\beta} u_0^2} \tag{1.81}$$

From figure 1.6, we see $\chi_0 = \frac{\pi}{2} - \frac{\theta}{2}$, which yields the impact parameter as a function of scattering angle θ:

$$b = \frac{q_\alpha q_\beta}{m_{\alpha\beta} u_0^2 \tan\frac{\theta}{2}} \tag{1.82}$$

Collision Operator

When particles move through a plasma, coulomb collisions (1.82) can occur with any other particle in the plasma. These collisions are limited, however, by the screening of charges: electrons move towards positive charges and away from negative charges. The extent of this screening is determined by the thermal velocity of the particles. This results in Debye screening: the potential from a point charge q is reduced to

$\Phi = \frac{q}{r}\exp(-r/\lambda_{De})$. This means that coulomb collisions will not occur over all angles, but will be restricted to angles where b is smaller than $\sim \lambda_{De}$.

The rate of change of a distribution function $\frac{d}{dt}f_\alpha$ due to collisions ($C_{\alpha\beta}$) is then the rate of collisions resulting in velocity $\vec{v}$ minus the rate starting with velocity $\vec{v}_i$. These terms are equivalent to the phase density of the distribution functions at the required velocities, integrated over the area the particles can stream through and multiplied by the particle speed. When these particle distributions are assumed to be independent, this forms the Boltzmann collision operator:

$$C_{\alpha\beta} = \int d^3v_{i\beta} \int_0^\pi d\phi \int_0^{\lambda_{De}} db(bu)(f_\alpha(\vec{v}_{i\alpha})f_\beta(\vec{v}_{i\beta}) - f_\alpha(\vec{v}_\alpha)f_\beta(\vec{v}_\beta)) \tag{1.83}$$

Using (1.82), we can convert 1.83 to an integral over scattering angles θ. We find $\frac{db}{d\theta} = \frac{-q_\alpha q_\beta}{m_{\alpha\beta}u_0^2}\frac{1}{2\sin\theta/2}$, with a minimum scattering angle $\theta_0 \approx \frac{2q_\alpha q_\beta}{m_{\alpha\beta}u_0^2\lambda_{De}}$. For $u_0 \approx v_{Te}$ and $m_{\alpha\beta} \approx m_e$, this gives a minimum angle $\theta_0 = \frac{2}{\Lambda}$, where $\Lambda = 4\pi n_e \lambda_{De}^3$ is proportionate to the number of electrons within a Debye sphere.

$$C_{\alpha\beta} = \frac{q_\alpha^2 q_\beta^2}{m_{\alpha\beta}^2} \int d^3v_{i\beta} \int_0^{2\pi} d\phi \int_{\theta_0}^\pi d\theta \frac{\cos\theta/2}{\sin^3\theta/2}\frac{1}{2u^3}(f_\alpha(\vec{v}_{i\alpha})f_\beta(\vec{v}_{i\beta}) - f_\alpha(\vec{v}_\alpha)f_\beta(\vec{v}_\beta)) \tag{1.84}$$

If we define the direction of the change in momentum in a given collision $\hat{\zeta} = \frac{\vec{u}_f - \vec{u}_0}{|\vec{u}_f - \vec{u}_0|} = -\sin\frac{\theta}{2}\hat{u_0} + \cos\frac{\theta}{2}\hat{u}_\perp$, this vector can be used to determine the final relative velocity $\vec{u}_f$ after a collision with the initial relative velocity $\vec{u}_0$ (fig. 1.6). The collision can be described by the operator $(I - 2\hat{\zeta}\hat{\zeta})$, or $\vec{u}_f = (I - 2\hat{\zeta}\hat{\zeta})\vec{u}_0$. This operator is its own inverse: $\vec{u}_0 = (I - 2\hat{\zeta}\hat{\zeta})\vec{u}_f$.

The change in velocity during scattering is then

$$\Delta\vec{u} = u\sin\theta\hat{u}_\perp + u(cos\theta - 1)\hat{u}_0 \tag{1.85}$$

This particle species' velocity changes can be expressed as

$$\Delta\vec{v_\alpha} = \frac{\Delta\vec{u}m_{\alpha\beta}}{m_\alpha} \tag{1.86}$$

The difference in the distribution functions can then be approximated by the gradients in the electron distribution function for small changes in velocity Δv:

$$f_e(\vec{v}_{0e}) - f_e(\vec{v}_e) = -\vec{\Delta v} \cdot \nabla_{\vec{v}e} f_e(\vec{v}_e) - \frac{1}{2}(\Delta\vec{v}_e \cdot \nabla_v)^2 f_e(\vec{v}_e) \tag{1.87}$$

Ions similarly can be expanded in terms of $\nabla_v f_i(\vec{v}_i)$, but f_e remains mostly unchanged over the range of $\nabla_v f_i(\vec{v}_i)$ values due to the much higher ion mass, so these terms integrate to 0 for electron-ion collisions, allowing the ion distribution to be separated from the integral.

Because collisions are integrated over 2π in ϕ, all parts of the velocity gradient of f_e perpendicular to $\hat{u}_0$ will cancel in the first order approximation of $f_\alpha(\vec{v}_{0\alpha})$, leaving only the $\hat{v}$ term of (1.85). This term is quadratic in θ for small values of θ, contributing to collisions at a level similar to the perpendicular terms of $(\Delta v)^2$.

This cancellation leaves $f_e(\vec{v}_{0e}) - f_e(\vec{v}_e) \propto \theta^2$. The collision frequency terms in $C_{\alpha\beta}$ are proportionate to θ^{-3} (1.84), leaving a dependence on scatting angle of θ^{-1}. The operator $C_{\alpha\beta}$ is therefore mostly composed of small angle collisions. Expanding the separate gradients from the first and second-order derivatives and using $m_{ei} \approx m_e$ due to the high ion mass, we have

$$C_{ei} \approx \frac{2\pi Z^2 e^4}{m_e^2} \int_{\theta_0}^{\pi} d\theta \frac{4}{\tan(\frac{\theta}{2})} \frac{1}{2u^3}(-\vec{u}_0 \nabla_v f_e + \frac{u^2}{2}(I - \hat{u}_0\hat{u}_0)\nabla_v^2 f_e) \tag{1.88}$$

The integral $\int_{\theta_0}^{\pi} d\theta \frac{1}{\tan(\frac{\theta}{2})} = 2\ln(2/\theta_0) = 2\ln(\Lambda)$ produces the coulomb logarithm: the factor controlling collisions based on the extent of fields in the plasma. Using $\vec{u} \approx \vec{v}$, the collision operator can then be simplified by integration by parts:

$$C_{ei} = \frac{2\pi Z^2 e^4 n_i \ln\Lambda}{m_e^2} \nabla_v \cdot \frac{1}{v}(I - \frac{\vec{v}\vec{v}}{v^2}) \cdot \nabla_v f_e \tag{1.89}$$

This consists of a term $(I - \frac{\vec{v}\vec{v}}{v^2})$ leading to isotropic distributions $\frac{df_e}{d\theta} = 0$ where angular features in the distribution function are removed due to collisions.

1.3.2 Local Transport Theory

In this section, I will summarize the classical, Spitzer-Härm (SH) transport theory [33] by deriving a stationary solution to the kinetic equation assuming that there is zero current in the plasma, in the limit of temperature scale lengths much longer than the collision mean free path of electrons. For large Z, this collision mean free path is dominated by the ion collision rate. In this case, the expansion is characterized by the small parameter

$$\delta_T = \lambda_{ei} \frac{d}{dx} ln(T_e) \tag{1.90}$$

where $\lambda_{ei} = \frac{v_{Te}}{\nu_{ei}}$ is the electron mean free path, and ν_{ei} is the electron-ion collision rate. δ_T is also known as the electron temperature Knudsen number: the ratio of the mean free path of electrons to the scale length of the electron temperature.

A steady-state solution for transport is found when collisions balance the diffusion of particles, leading to a static distribution function. Assuming azimuthal symmetry, we can write Eq. (1.89) in the following form:

$$C_{ei} = \frac{2\pi Z^2 e^4 n_i \ln\Lambda}{m_e^2} \frac{1}{v^3} \frac{1}{\sin\theta} \frac{\partial}{\partial\theta} (\sin\theta \frac{\partial f_e}{\partial\theta}) \tag{1.91}$$

The distribution function is assumed to take the form $f_e = f_0 + \cos\theta f_1$, where f_0 is the Maxwellian distribution $f_0 = (\frac{m_e}{2\pi T_e})^{\frac{3}{2}} \exp(-\frac{v^2 m_e}{2T_e})$, f_1 is the smaller transport distribution, and θ is the angle from the direction of the temperature gradient.

Given the form of $f_e - f_0 \propto \cos\theta$, and the equilibrium under collisions of f_0, the operator $\frac{1}{\sin\theta} \frac{\partial}{\partial\theta} (\sin\theta \frac{\partial}{\partial\theta})$ simplifies to $-2\cos\theta$.

As the electron distribution function for transport should be time-independent, it will follow the steady-state equation:

$$\vec{v} \cdot \nabla f_e - \frac{e}{m_e} \vec{E} \cdot \frac{\partial f_e}{\partial \vec{v}} = C_{ei} \tag{1.92}$$

With a temperature gradient in the $\hat{z}$ direction, $\nabla f_e = \frac{\partial f_e}{\partial z} \hat{z}$. The electric field must also be in the $\hat{z}$ direction, as this is the only direction of asymmetry. Keeping the leading order for each term, (1.92) then becomes

$$v \cos\theta \frac{\partial f_0}{\partial z} + v \cos\theta \frac{eE}{T_e} f_0 = \frac{2\pi Z^2 e^4 n_i \ln\Lambda}{m_e^2} \frac{1}{v^3} (-2\cos\theta) f_1 \tag{1.93}$$

For a Maxwellian f_0, $\frac{\partial f_0}{\partial z} = (-\frac{3}{2} + \frac{1}{2}\frac{v^2}{v_{Te}^2}) f_0 \frac{d \ln T_e}{dz}$. This gives f_1 terms proportionate to $v^4 f_0$ and $v^6 f_0$. To solve for the electric field E, we use the zero current condition: $\int d^3v f_1 \cos\theta \vec{v} = 0$ or equivalently $\int_0^\infty f_1(v) v^3 dv = 0$.

Using the identity $\int_0^\infty v^n \exp(-0.5v^2) dv = \frac{\Gamma(\frac{n+1}{2})}{0.5^{0.5(n-1)}}$, we find $\int_0^\infty v^7 \exp(-0.5\frac{v^2}{v_{Te}^2}) dv = \frac{1}{8}\int_0^\infty v^9 \exp(-0.5\frac{v^2}{v_{Te}^2}) dv$. The electric field caused by transport then must be $E = -\frac{5}{2e}\frac{dTe}{dz}$

The result is the Spitzer-Härm heat transport distribution function:

$$f_1 = \frac{m_e^2 v^4}{2\pi Z^2 e^4 n_i \ln\Lambda} f_0 (4 - \frac{1}{2}\frac{v^2}{v_{Te}^2}) \frac{d \ln T_e}{dz} \tag{1.94}$$

Given a collision rate $\nu_{ei} = \frac{4\sqrt{2\pi} Z^2 e^4 n_i \ln(\Lambda)}{3 T_e^{1.5} \sqrt{m_e}}$ [34], the transport distribution f_1 can be written in terms of the temperature scale length parameter (Knudsen number, (1.90)) δ_T. This shows f_1 is linear with the temperature scale length (1.7):

$$f_1 = \sqrt{\frac{2}{9\pi}} f_0 \frac{v^4}{v_{Te}^4} (4 - \frac{1}{2}\frac{v^2}{v_{Te}^2}) \delta_T \tag{1.95}$$

The contribution of f_1 to the distribution function is $f_1 \cos\theta$, which can be seen in figure 1.8. Heat is transported in high velocity electrons, while the total current is balanced by the reversed return current close to $\vec{v} = 0$.

In the direction of the temperature gradient, this can be integrated to see the shape of the distribution function in one direction of interest (Fig 1.9):

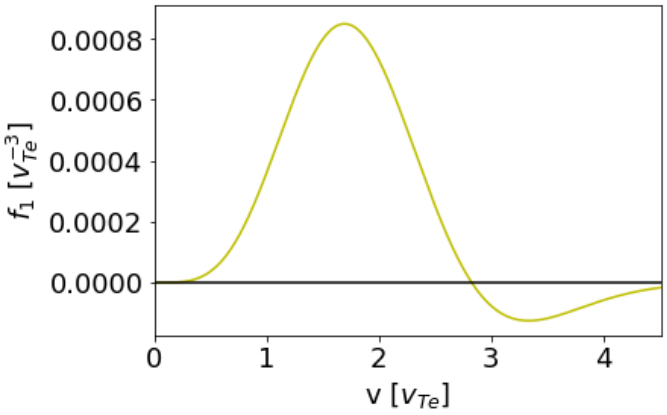

Figure 1.7: Spitzer-Härm f_1 distribution for $\delta_T = 0.01$

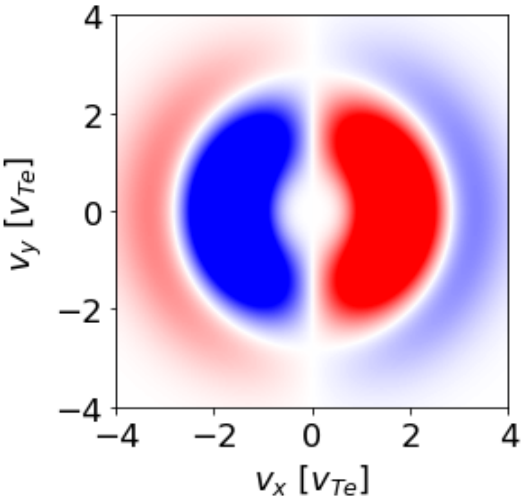

Figure 1.8: Spitzer-Härm f_1 distribution for a temperature gradient in the $\hat{x}$ direction, with positive f_1 in red and negative f_1 in blue

$$f_1(v_x) = \frac{9}{6\sqrt{2\pi}}\frac{v_x}{v_{Te}^2}(1-erf(\frac{|v_x|}{\sqrt{2}v_{Te}}))\delta_T + \frac{v_x|v_x|}{6\pi v_{Te}^3}\exp(-\frac{v_x^2}{2v_{Te}^2})(9+3\frac{v_x^2}{v_{Te}^2}-\frac{v_x^4}{v_{Te}^2})\delta_T \quad (1.96)$$

This distribution has heat flux (1.76) proportionate to the relative temperature gradient:

$$q_{SH} = -\frac{128}{3\pi} n_e m_e v_{Te}^3 \delta_T \quad (1.97)$$

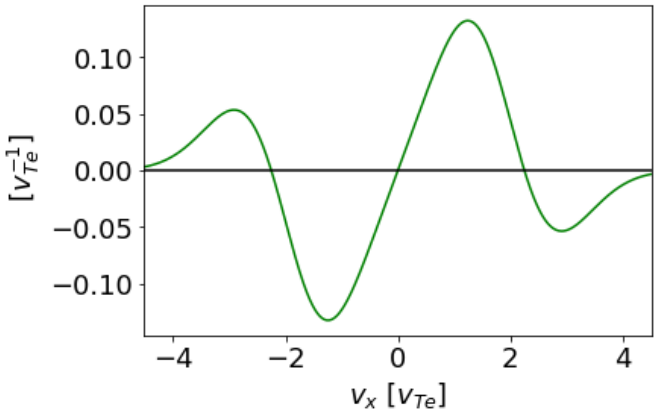

Figure 1.9: Spitzer-Härm f_1 distribution for $\delta_T = 0.01$ projected onto the direction of the temperature gradient.

The SH distribution function (1.95,2.22) is used in section 4.4 to analyze transport based on IAW spectra observed in OTS experiments.

1.3.3 Non-local Transport

Observing the heat flux (1.97) from the Spitzer-Härm distribution (1.94), we see that q_{SH} can be arbitrarily high given a sufficiently large temperature gradient. The electron distribution function at a given temperature, however, has a finite amount of heat flux in any given direction that can be energetically permitted. If all of the thermal energy of the plasma was transmitted in one direction at the speed of the thermal energy for electrons, we would see a heat flux of q_f, the free streaming heat flux:

$$q_f = n_e T_e v_{Te} \tag{1.98}$$

This free streaming heat flux is the maximum theoretical limit of particle heat transport in a hot plasma. q_{sh} is greater than q_f (1.97) for any $\delta_T > 0.0736$. In simulations, heat flux is typically limited to some smaller value $fq_f \sim 0.1q_f$, where the electrons at $\approx 3v_{Te}$ which mediate most of the heat transport have mean free paths similar to the temperature scale length.

Alternatively, non-local approaches can be taken to determine heat transport. These are often more resource-intensive and can require kinetic modeling of the plasma. These models strongly reduce heat transport for plasmas with high heat flux under the local SH model, where $\delta_T > \frac{0.06}{\sqrt{Z}}$ [35] [36] [37], and also pre-heat plasma further from a temperature gradient, as the streaming distance of hot electrons that carry most of the heat can be much longer than the thermal mean free path, and comparable to the temperature scale lengths.

1.4 Plasma Experiments

In order to measure some of the phenomena mentioned above in different conditions, plasmas are created in laboratories by ionizing a target. This ionized plasma then expands due to its pressure, typically in a shape that can initially be approximated by a self-similar expansion (1.75) for high-density targets.

Two main methods of ionizing a target to generate plasma are lasers and electric currents, also known as pulsed power. The MAGPIE pulsed power facility is an example of the latter technique. Here, capacitor banks run 1 TW of power through a wire mesh, creating a magnetized plasma [38]. An experiment at this facility is explored in section 3.5

Laser ablation is used to create plasma in many Inertial Confinement Fusion (ICF) laboratories. ICF involves the compression of a fuel composed of light nuclei by the heating and ablation of a shell of plasma around the fuel. This shell can be heated by lasers directly (Direct Drive, Fig. 1.10) or by laser-produced x-rays (Indirect Drive). The ablating shell exerts pressure on the fuel, driving it to a higher density and enhancing nuclear fusion [39].

Two ICF labs using laser ablation are the National Ignition Facility (NIF) and the OMEGA laser facility. Both use neodymium lasers, with their wavelength converted from 1053 nm to 351 nm before they enter the target chamber. At the time of this writing, NIF is the highest energy laser facility in the world, with shots delivering over

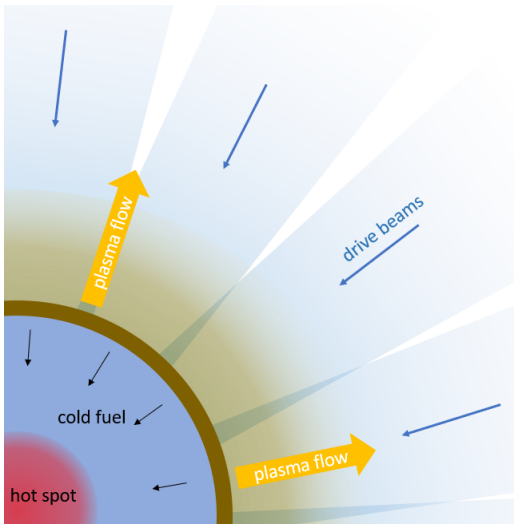

Figure 1.10: Direct Drive Inertial Confinement Fusion (ICF) cross-section. Drive beams heat the ablator (brown), causing it to ablate and flow away from the target. This flow provides an inwards force on the fuel, leading to compression and heating which create fusion.

2 MJ to the target with 192 beams [40]. An experiment on the ion Weibel (section 1.2.1) instability conducted here is examined below (section 3.4)

OMEGA is a smaller facility with a higher shot rate and advanced diagnostic capabilities. It delivers over $30kJ$ per shot with 60 beams [41]. Experiments conducted here are examined in chapters 3 and 4.

Chapter 2

Optical Thomson Scattering

Optical Thomson Scattering (OTS) described in the previous chapter (sec. 1.1) has numerous observables when spectrally resolved. These observables are sensitive to a variety of plasma properties, allowing detailed OTS spectra to diagnose most conditions of interest in a plasma. In this chapter, I review the observables present in the wide band Electron Plasma Wave (EPW, sec. 2.1) and narrow band Ion Acoustic Wave (IAW, sec. 2.2) and their corresponding plasma conditions.

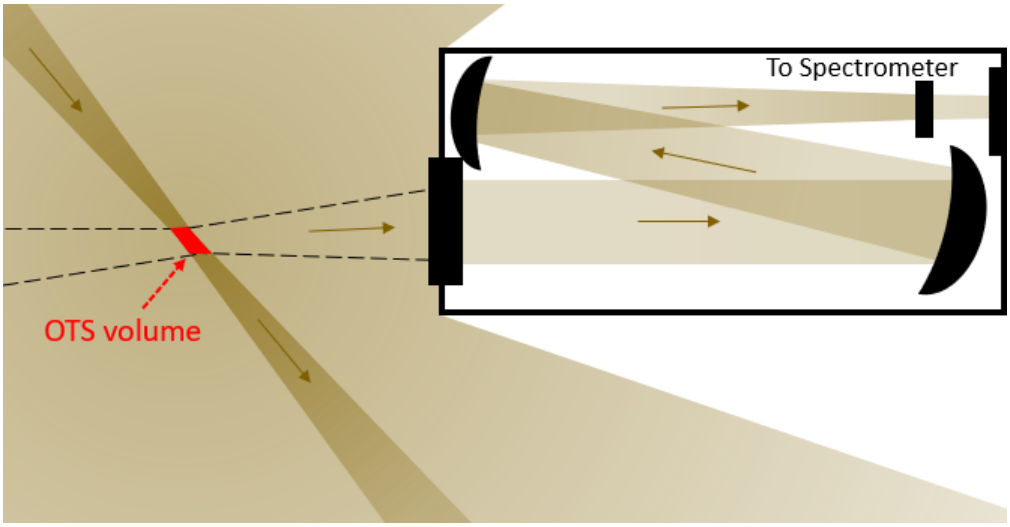

Figure 2.1: A generic OTS telescope. Scattered light is collected and collimated from a scattering location in the plasma and passed into a spectrometer.

To observe OTS spectra, light is first collected in a telescope [42] (Fig. 2.1), then passed through a Czerny-Turner imaging spectrometer [43, 44] (Fig. 2.2) onto a

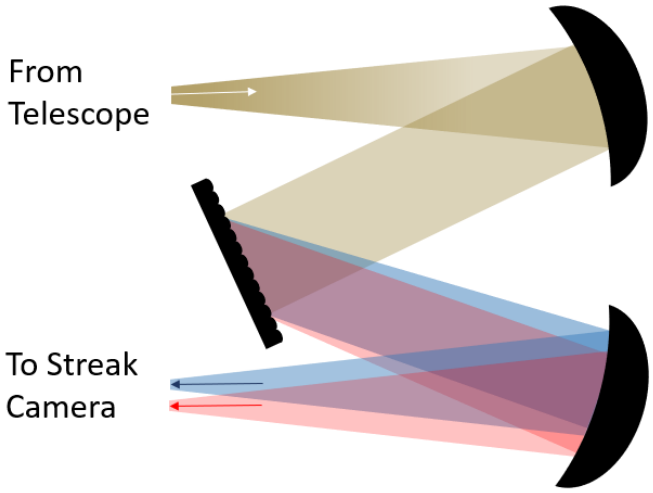

Figure 2.2: A Czerny-Turner spectrometer. Light of different wavelengths is separated in space by a diffraction grating.

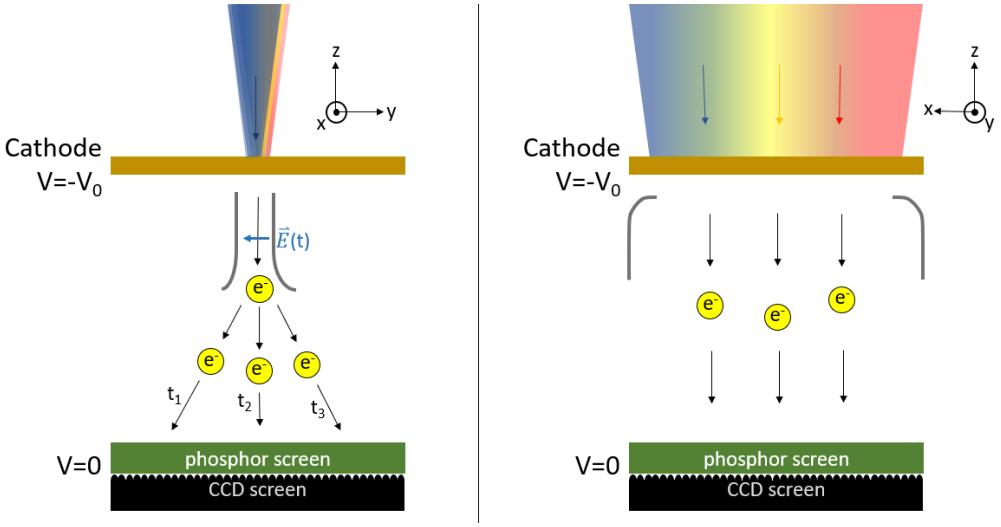

Figure 2.3: A streak camera. Spectrally resolved light from the spectrometer (right) incident on the photo-cathode (yellow) releases electrons, which are accelerated across some voltage difference V_0 towards a phosphor screen (green) connected to CCDs (black). A transverse time-dependent electric field (left, $t_1 < t_2 < t_3$) can be applied to move the electrons perpendicularly to the spectral direction. The CCDs record light released by the phosphor screen, creating the detected image.

streak camera, where time can be resolved with a time-varying transverse electric field moving photo-electrons in the streak tube [45] (Fig. 2.3). The geometry of these processes determines the resolution of the spectrum, as well as the waves sampled

in the plasma (sec. 2.3). The attenuation of light in the telescope and spectrometer affects the shape of the spectrum, and the behavior of the statistical error of the spectrum is controlled by the properties of the streak camera (sec. 2.4). These properties can be accounted for to more accurately infer plasma properties from OTS observables.

2.1 Scattering From Electron Plasma Waves

The electromagnetic waves scattered in the plasma follow the dispersion relation $\omega^2 = \omega_{pe}^2 + k^2c^2$, where ω_{pe} is the plasma frequency in the OTS volume. The light scatters from particles and waves traveling at phase velocity $v_{phase} = \frac{\omega}{k}\hat{k} = \frac{\omega_s - \omega_L}{k_s - k_L}\hat{k}$, where $\hat{k}$ is in the direction of the change in momentum $\vec{k_s} - \vec{k_L}$. Here ω_L and $\vec{k_L}$ are the frequency and wave number of the probe beam, and ω_s and $\vec{k_s}$ are the frequency and wave number of the scattered light.

The quantity of light scattered from the plasma can be described by power P_s [12] per solid angle $d\Omega$ and spectral width $d\omega$ with the scattering $\vec{k}$ determined by the geometry of the telescope (Fig. 2.1):

$$\frac{dP_s}{d\Omega d\omega} = n_e L_{TS} P_L \frac{r_e^2}{2\pi}(1 + \frac{2\omega}{\omega_L})S(\vec{k},\omega)sin^2(\psi) \tag{2.1}$$

Here, $r_e = \frac{e^2}{m_e c^2}$ is the classical radius of an electron, c is the speed of light, P_L is the power of the probe. The angle ψ is the angle between the scattered light and the polarization direction of the probe, which is typically controlled to be 90° to maximize P_s. L_{TS} is the length of OTS volume along the direction of the probe, and $S(\vec{k},\omega)$ is the spectral density function,

$$S(\vec{k},\omega) = \frac{2\pi}{k}\left|1 - \frac{\chi_e}{\epsilon}\right|^2 \bar{f}_e\left(\frac{\omega}{k}\right) + \frac{2\pi}{k}\left|\frac{\chi_e}{\epsilon}\right|^2 Z\bar{f}_i\left(\frac{\omega}{k}\right) \tag{2.2}$$

$$\chi_\alpha = \frac{\omega_{p\alpha}^2}{k^2}\int_{-\infty}^{\infty}\frac{1}{(\omega/k - v)}\frac{d}{dv}\bar{f}_\alpha(v)dv \tag{2.3}$$

where ω is the frequency shift applied to the scattered light, $\epsilon = 1+\chi_e+\chi_i$ is the longitudinal dielectric function, and Z is the ionization state. $\bar{f}_i$ and $\bar{f}_e$ denote the velocity distribution functions of ions and electrons respectively projected onto the direction of $\vec{k}$. This accurately describes the fluctuations in stable plasma, homogeneous at the scale of the scattering volume.

For Maxwellian plasma, these expressions can be used to evaluate the dispersion relation of the plasma waves and scattered light. For $\bar{f}_\alpha(v) = \frac{1}{\sqrt{2\pi}v_{T\alpha}} \exp -\frac{1}{2}(\frac{v^2}{v_{T\alpha}^2})$, with $v_{T\alpha} = \sqrt{\frac{T_\alpha}{m_\alpha}}$, the susceptibility (2.3) can be approximated analytically [12, 32] for $\frac{\omega}{k} \gg v_{T\alpha}$:

$$\chi_\alpha \approx \frac{\omega_{p\alpha}^2}{k^2 v_{T\alpha}^2}\left(-\frac{k^2 v_{T\alpha}^2}{\omega^2} - 3\frac{k^4 v_{T\alpha}^4}{\omega^4}\right) \tag{2.4}$$

To find the dispersion relation for the EPW at long wavelength, $\epsilon = 0 = 1 + \chi_e$ is evaluated for $\omega/k \gg v_{Te}$ resulting in

$$\omega^2 = \omega_{pe}^2 + 3k^2 v_{Te}^2 \tag{2.5}$$

The EPW spectrum must also be multiplied by the wavelength-dependent sensitivity curve, based on the transmission of light in the OTS apparatus (section 2.1.2). Both IAW and EPW spectra are then broadened by convolution with the instrument point spread function to account for the resolution of the measurement.

2.1.1 Scattering Effects of Density Variations

Because the OTS system collects light from finite volumes on the order of 100 μm (Fig. 2.4) with scattering vectors $|\vec{k}| > 1\mu m^{-1}$, the observed OTS spectrum is a sum of a variety of locations in the plasma, with slightly different plasma conditions. Gradients in the plasma can be accounted for by integrating the power spectrum (2.1) over the scattering volume:

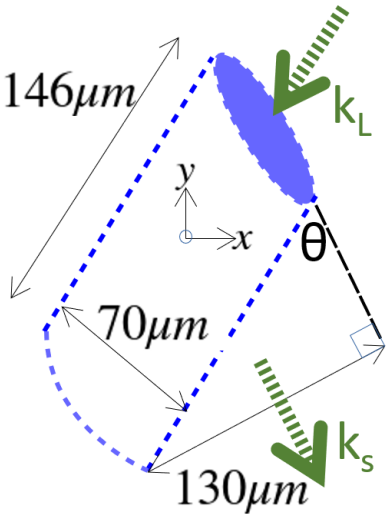

Figure 2.4: OTS volume shape for the two ω system at the OMEGA laser facility [3], $\theta = 60.3°$

$$\frac{dP_s}{d\Omega d\omega} = \frac{r_e^2}{2\pi} \int\int\int n_e I_L (1 + \frac{2\omega}{\omega_L}) S(\vec{k}, \omega) sin^2(\psi) dr^3, \tag{2.6}$$

where $I_L = P_L/A$ is the intensity of the probe beam.

In the corona of ablation plasmas, gradients in density are typically much larger than changes in other plasma properties. These strongly affect the EPW by changing the frequency shift of the Langmuir waves (2.5).

For the EPW, the highly collective response corresponds to $\alpha \gg 1$, where the parameter $\alpha = \frac{1}{k\lambda_{De}}$, and $\lambda_{De} = \sqrt{\frac{T_e}{4\pi n_e e^2}}$ is the Debye length, the scale length of charge screening in the plasma. At high α, the EPW resonance can be very narrow. In this case, local calculations of the spectrum may not match the effect of a continuous density gradient. To fix this, gaussian smoothing and a range of densities can be combined to match the EPW spectra.

The ratio of the OTS volume diameter to the density scale length, L_{TS}/L_{n_e}, where $L_{n_e} = \left|\vec{\nabla} \ln (n_e)\right|^{-1}$ controls the broadening effect on the EPW. If the OTS volume is assumed to be cylindrical, the effective total frequency shift of the resonance will be approximately $\Delta\omega \approx 0.25\omega_{pe} L_{TS}/L_{n_e}$. This is divided between smoothing and

density variation based on the number of points.

Transverse to the probe axis (line of $\vec{k_L}$, Fig. 2.4), the OTS volume has a circular shape of roughly uniform intensity. Density gradients perpendicular to this probe axis will have densities sampled with weighting corresponding to the cord length of the circle: $A(x) = \sqrt{(1-x^2)}$, where x is the distance from the center of the TS volume divided by the radius. This distribution of locations must be sampled at a finite number of points to allow computation. If N points are chosen, OTS spectra are generated at locations $x_n = -1 + n(2/(N+1))$ where n =1 to N. If the density is assigned as with $n_e(x) = n_0 \exp(xL_{TS}/L_{n_e})$, the maximum shift in the plasma frequency (2.5) ω_δ between two adjacent points in this range of densities can be used to estimate the required smoothing. This value ω_δ is then used to determine the portion of the smoothing done with a gaussian filter. A ratio of smoothing to density variation $R = \frac{0.6\omega_\delta}{\Delta\omega}$ appears to be sufficient to smooth contributions from spectra at different densities, creating a similar spectrum to a continuous density variation (Fig. 2.5).

The total smoothing of the EPW peak $\Delta\omega$ is then applied by a mix of smoothing with a gaussian filter and smoothing with a mix of n_e values. Shifts in density are reduced to account for smoothing, with $n_e(x) = n_0 \exp(\sqrt{1/(R^2+1)}xL_{TS}/L_{n_e})$, and gaussian smoothing is applied with a standard deviation of $\omega_{smooth} = \sqrt{R^2/(R^2+1)}0.25\omega_{pe}L_{TS}/L_{n_e}$ (Fig. 2.5).

2.1.2 Background Light and Transmission

The captured image of the EPW typically includes significant self-emission from the hot plasma in addition to the light scattered from Langmuir wave fluctuations. This background must be removed to fit the EPW spectrum.

This can be accomplished with an additional shot with no OTS probe, giving a measurement of the plasma self-emission alone. Alternatively, the self-emission can be approximated with a linear extrapolation from light outside of the region of the

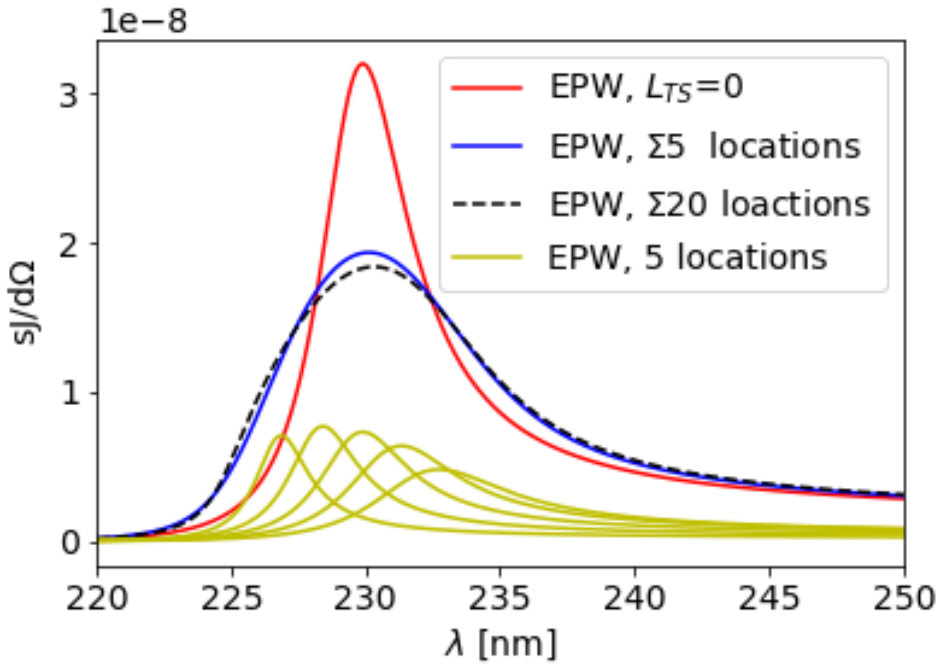

Figure 2.5: EPW for multiple OTS locations across a density gradient. $L_{TS}/L_{ne} = 0.5$, $n_e = 2 \times 10^{20} cm^{-3}$, $T_e = 1keV$

streak camera where the EPW signal is expected (red lines, Fig. 2.6a). Between the horizontal lines, the time dependence of the background radiation is measured, and the region between the vertical lines is used to measure the wavelength dependence. These are assumed to be independent and multiplied to produce a background radiation image which can be subtracted from the raw signal to produce the EPW data, shown in Fig. 2.6b.

The EPW telescope, spectrometer, and photo-cathode may all have large variations in light transmission across the bandwidth of the spectrometer. This transmission function can be calibrated with a known source, but this can become outdated if changes are made to the OTS system. The transmission function can be seen to be out of date if the shape of the transmission function is no longer seen in heavily damped EPW spectra.

To measure an approximate transmission function, the background can be used. If the background is assumed to come from a black-body spectrum emitted from the

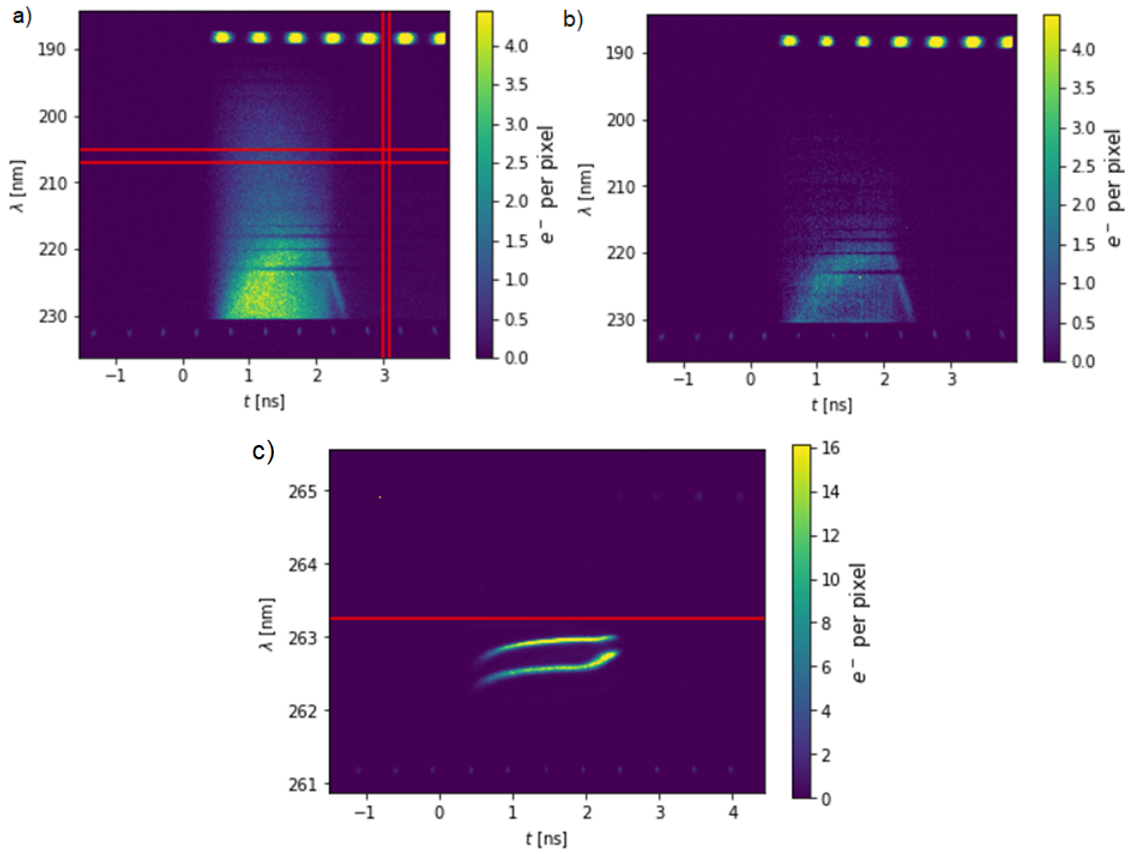

Figure 2.6: Thomson scattering images taken in the radial scattering direction, available at Ref. [46]. a) Raw EPW spectrum, with red lines marking where profiles are taken for background subtraction. b) EPW spectrum after background subtraction. c) Raw IAW spectrum, with a red line denoting the probe wavelength. [From [6], associated dataset available at https://doi.org/10.5281/zenodo.4950679] (Ref. [46]).

hot plasma in the collection volume, the emitted light follows the Planck spectral radiance of $\frac{\omega^2}{2\pi^2 c^3}\frac{\omega\hbar}{exp(\omega\hbar/T_e)-1}$. The transmission function can be found by dividing the observed background spectrum by the black-body spectrum at the temperature of the plasma.

This process has some errors associated with the non-uniformity of the plasma and non-blackbody self-emission spectra but tends to return the approximate shape of the transmission function well (Fig.2.7).

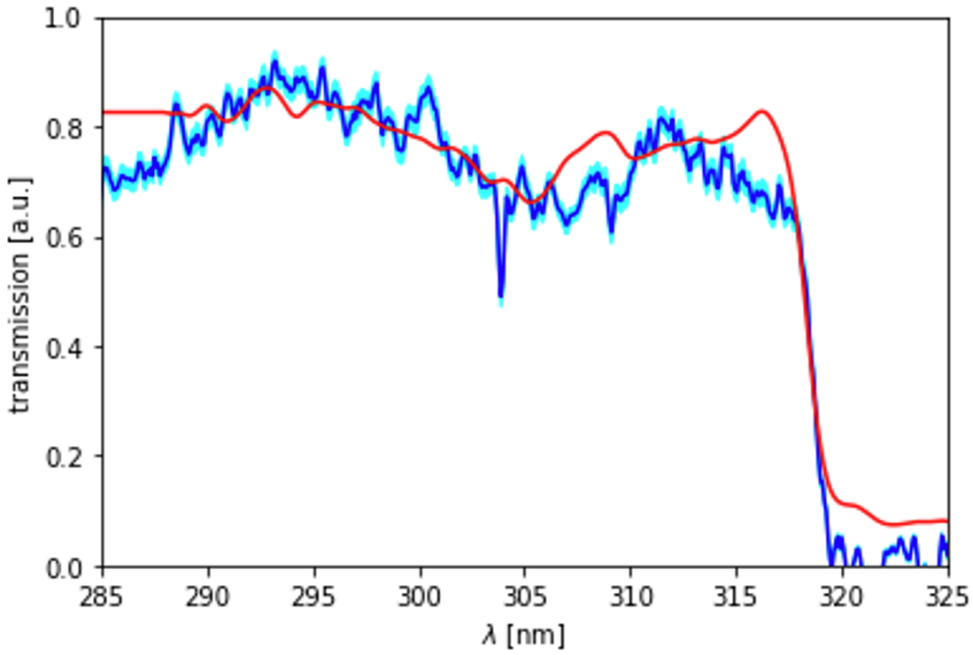

Figure 2.7: Transmission function from calibration (blue) and from black-body spectrum and background (red) for the 3ω OTS at NIF

2.1.3 Magnetized Plasma

When magnetic fields are present in plasma, charged particles begin to gyrate at frequency $\Omega_{ce} = \frac{qB}{mc}$ around the magnetic field lines. Light scattered from scattering vectors perpendicular to these field lines can contain these resonances [12], separated by $\Omega_{ce} = \frac{eB}{m_e c}$, provided the electrons in the plasma are magnetized: $\rho_e = \frac{v_{Te}}{\omega_{ce}} << \lambda_{ei}$

$$S_e(k,\omega) = 2\sqrt{\pi}\left|1 - \frac{H_e}{\epsilon_L}\right|^2 \sum_{l=-\infty}^{+\infty} exp(-k_\perp^2\rho_e^{-2})I_l(-k_\perp^2\rho_e^{-2})exp(-\frac{(\omega - l\Omega_{ce})^2}{2k_\parallel^2 v_{Te}^2})\frac{1}{k_\parallel\sqrt{2}v_{Te}} \tag{2.7}$$

$$H_e(k,\omega) = \alpha^2\left(1 - \sum_l exp(k_\perp^2\rho_e^{-2})I_l(-k_\perp^2\rho_e^{-2})(\frac{\omega}{\omega - l\Omega_{ce}}) \times (2x_{el}exp(-x_{el}^2) \int_0^{x_{el}} exp(p^2)dp + i\sqrt{\pi}x_{el}exp(-x_{el}^2)\right) \tag{2.8}$$

Where $x_{el} = (\omega - l\Omega_e)/k_\parallel\sqrt{2}v_{Te}$, I_l is the modified Bessel function of the first kind.

This results in a spectrum made up of features of spectral width $k_{\|}v_{Te}$, separated by frequency Ω_{ce}. This means it is only possible to observe these effects for $k_{\|}v_{Te} < \Omega_{ce}$ (Fig. 2.8), so only sufficiently large fields change the OTS spectrum.

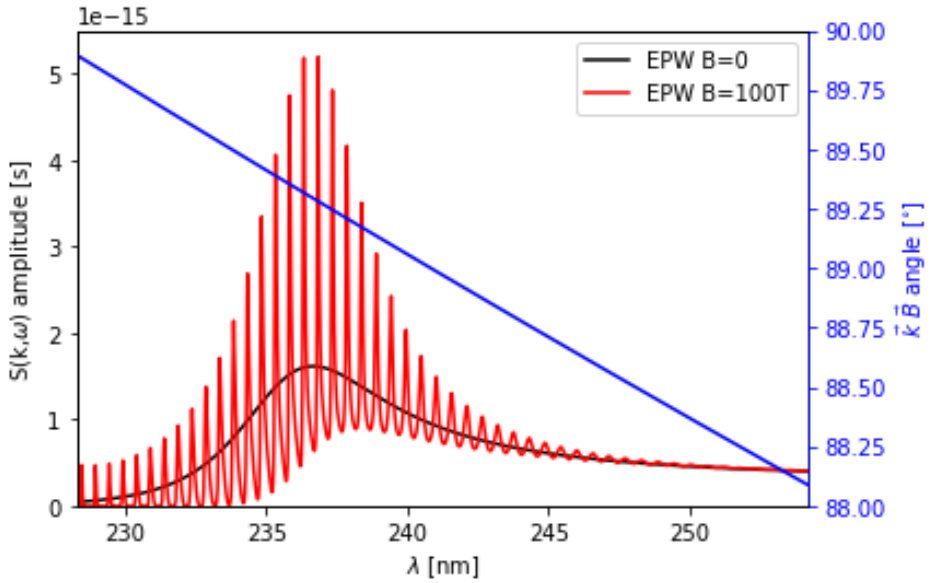

Figure 2.8: Electron plasma wave for magnetized (red) and unmagnetized (blue) plasma, with $n_e = 1 \times 10^{20} cm^{-3}$, $T_e = 800ev$, $B = 100T$. The angle is between the scattering vector and the field changes with wavelength shift and is shown on the right (blue). The EPW from a 263.25 nm probe with the central scattering vector 87.5° from $\vec{B}$ and $\vec{B}$ 70° out of the OTS scattering plane is shown. Here $\Omega_{ce}/kv_{Te} \approx 0.06$

For any magnetized plasma, these conditions are met for a sufficiently small value of $\vec{k} \cdot \hat{B}$. However, OTS images contain a finite range of angles (Fig. 2.21). This limits the observable magnetic field to electron cyclotron frequencies greater than the broadening of the Bernstein waves due to differences in $\vec{k}$ (Fig 2.9).

For typical OTS spectra, the EPW spectrometer (Fig. 2.2) is configured to capture most of the EPW spectrum, or most of the blue-shifted EPW for four-omega OTS. In these cases, it can be difficult to detect the effects of magnetized electrons due to the shape and counting of photo-electrons in the streak camera. This both broadens the resonances of the magnetized EPW and masks the oscillations with random noise

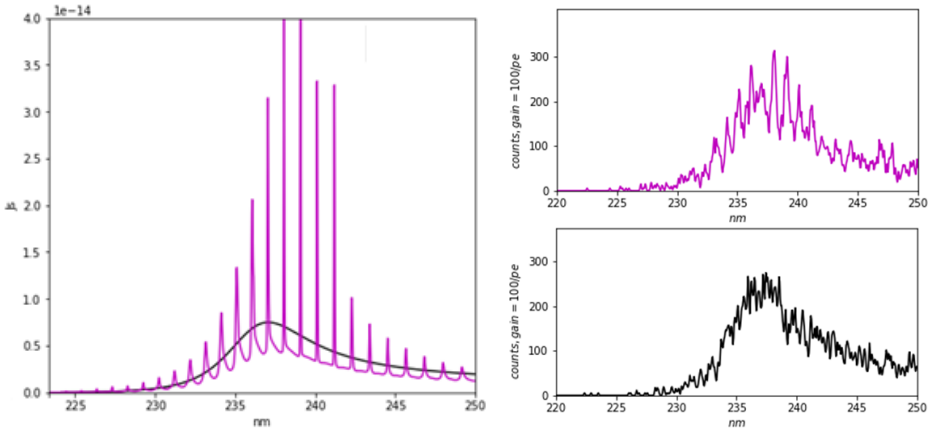

Figure 2.9: Electron plasma wave for magnetized (pink) and unmagnetized (black) plasma, with $n_e = 1 \times 10^{20} cm^{-3}$, $T_e = 0.8keV$, $B = 200T$, integrated over the range of scattering angles in the OMEGA 4ω OTS system (Fig. 2.21). The EPW from a 263.25 nm probe with the central scattering vector 87.5° from $\vec{B}$ and $\vec{B}$ 70° out of the OTS scattering plane is shown. The expected signal on the streak camera is shown on the right.

2.2 Scattering From Ion Acoustic Waves

Ion acoustic waves are electrostatic waves in plasma similar to Langmuir waves with much lower frequencies due to the higher mass of the ions. The dispersion relation for these waves can be found from Eq. 2.4, at $v_{Te} \gg \omega/k \gg v_{Ti}$. This results in the dispersion relation:

$$\omega_{iaw}^2 = \frac{\omega_{pi}^2}{1+\alpha^2} + 3k^2 v_{Ti}^2 \tag{2.9}$$

Ion acoustic waves in plasma also cause fluctuations in the electron density, which can be observed with Thomson Scattering. For low T_i and high α, the dispersion relations can be well approximated by $\omega_{iaw} = \frac{kc_s}{\sqrt{1+k^2\lambda_{De}^2}}$ [47] where $c_s = \sqrt{(ZT_e/m_i)}$. This shows that the electron temperature can be measured from the IAW spectrum due to the separation of the IAW peaks.

Because background subtractions and transmission function measurements are imperfect, the shape of heavily damped EPW spectra can have large errors when determining the temperature of the plasma. Similarly, errors in electron temperature

measurements can be introduced in highly collective EPW spectra if density gradients are modeled incorrectly. To avoid these problems, the IAW separation can more accurately measure T_e as long as the ionization is well understood (Fig. 2.6c).

2.2.1 Damped Ion Acoustic Waves

Like the electron plasma wave, the ion acoustic wave can become heavily damped, corresponding to ion velocities instead of ion thermal acoustic wave phase velocities. Unlike the EPW, however, the IAW is affected by both electron and ion properties, so the transition to heavily damped waves can be caused by a variety of factors.

For Maxwellian ion and electron distribution functions, the IAW damping is affected by ionization (Z), electron and ion temperatures, and the wave number k. We can see from Eq. (2.3) that the relative electron and ion density also affect the damping of the IAW. Plasma is generally neutral, with $Zn_i = n_e$, but for 'beam' plasmas with counter-streaming ions, the sample of ions near a certain velocity may have a lower density n_b than the total ion density n_i, or $Zn_b < n_e$. These ion beams can contain ion acoustic waves identical to thermal plasma, except with a higher effective electron density, neutralized by ions streaming with a very different velocity and therefore not contributing to the beam's waves as shown in figure 2.10. We can take this into account when analyzing IAW damping by including the factor $\frac{n_b}{n_i}$, which is 1 for thermal plasmas.

The transition is affected by the OTS alpha parameter, $\alpha = 1/(k\lambda_{De})$, the ionization and temperature $Z\frac{T_e}{T_i}$, and the ion beam density $\frac{n_b}{n_i}$ representing the fraction of the ion density present in the ion beam of interest.

To determine the state of the IAW resonance shape analytically, the shape of the function at $\omega/k \approx v_i$ where v_i is the mean velocity of the ions, can be examined to determine if it is consistent with resolvable peaks. Taylor expanding the dielectric function (2.3) in small relative phase velocity $v_\phi/v_{Ti} = (\omega/k - v_i)/v_{Ti} \ll 1$, the relevant susceptibilities are given by [12]:

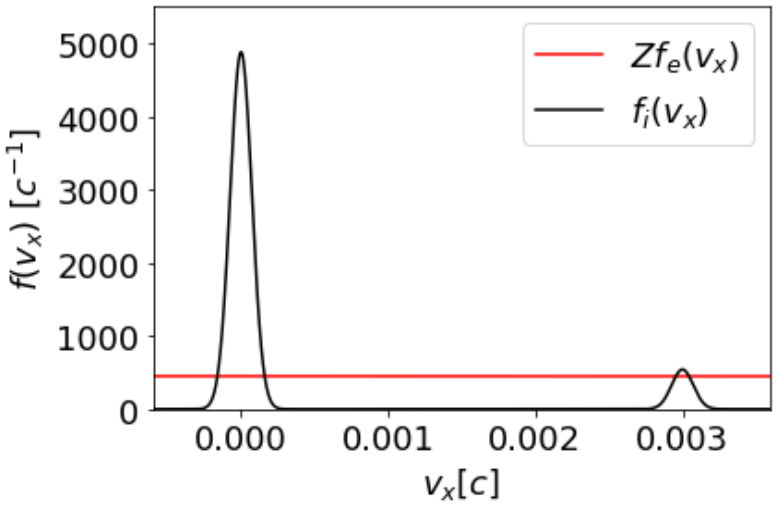

Figure 2.10: Distribution functions for f_e and f_i projected onto one direction for $Z = 50$ gold plasma, $T_e = T_i = 1keV$ for a plasma with an ion beam. The right beam with $n_b/n_i = 0.1$ has ion acoustic waves similar to those of a Maxwellian plasma, except that the electron density is higher than Zn_b, with the charge balanced by the ion around $v = 0$ which do not otherwise contribute to the beam's IAW.

$$\Re(\chi_i) \approx \frac{n_b}{n_i}\frac{ZT_e}{T_i}\frac{\omega_{pe}^2}{k^2 v_{Te}^2}\left(1 - \frac{v_\phi^2}{v_{Ti}^2}\right) \tag{2.10}$$

$$\Im(\chi_i) \approx \frac{n_b}{n_i}\frac{ZT_e}{T_i}\frac{\omega_{pe}^2}{k^2 v_{Te}^2}\frac{v_\phi}{v_{Ti}} \tag{2.11}$$

$$\Re(\chi_e) \approx \frac{\omega_{pe}^2}{k^2 v_{Te}^2} \tag{2.12}$$

The derivatives of χ_e can be neglected as χ_e varies on the scale of $v_{Te} >> v_{Ti}$. The second derivative of S_i can be evaluated at the mean ion population velocity v_i to find the local curvature of the spectrum around $\omega/k = v_i$:

$$\frac{d^2 S_i}{dv_\phi^2}(\vec{k}, v_\phi)|_{v_\phi=0} = \frac{n_b}{n_i}\frac{ZT_e}{T_i}\frac{\chi_e^2 f_i}{\epsilon^2 v_{Ti}^2}(-\pi\frac{\chi_i^2}{\epsilon^2} + 4\frac{\chi_i}{\epsilon} - 1) \tag{2.13}$$

Positive curvature indicates that the feature has the double-peaked mode structure while negative curvature indicates the feature has only a single peak. The threshold for double peak structure to be observed may be written in terms of the ratio of the

ion density of the flow to the total density and the Thomson scattering α parameter as

$$\frac{n_b}{n_i}\frac{ZT_e}{T_i} > \frac{1-\sqrt{4-\pi}}{\pi-3}(1+\alpha^{-2}) \approx 0.519(1+\alpha^{-2}) \tag{2.14}$$

Typically OTS geometry is chosen to create a high α parameter, so IAW peaks are visible unless $T_i >> ZT_e$ or the ion stream fraction is small.

Negative concavity in the center of the IAW can also be seen for $\frac{n_b}{n_i}\frac{ZT_e}{T_i} > \frac{1+\sqrt{4-\pi}}{\pi-3}(1+\alpha^{-2})$. These IAWs still have two resonant peaks, but a local maximum is seen between the peaks at the center of the ion distribution function (Fig. 2.11). This is caused by the value of $\Im(\chi_i)$ increasing damping away from $v_\phi = 0$ and by the peak of the f_i distribution.

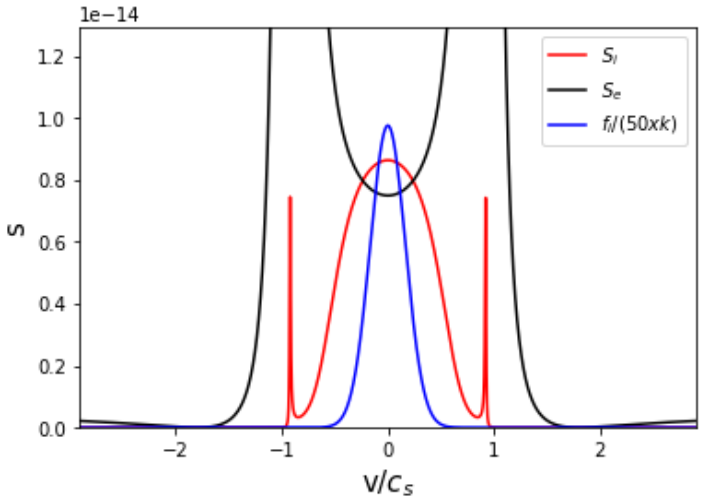

Figure 2.11: S_i and S_e for $ZT_e/T_i = 36$

2.2.2 Electron drift

Ion acoustic waves traveling in plasma experience damping from electrons proportionate to the derivative of the electron distribution function at the phase velocity of the ion acoustic wave. Any asymmetry of the electron flow relative to the ion flow

will result in asymmetric damping of the IAWs, resulting in different amplitudes for the red-shifted and blue-shifted waves.

Asymmetry in the electron distribution function can correspond to a current in the plasma, where the mean electron velocity v_e is different than v_i, or to heat transport, where a return current of slow electrons is required to balance the current of heat-carrying electrons, resulting in a net zero current plasma. For highly collisional plasmas with mild temperature gradients, this follows a current-free Spitzer-Härm (SH) distribution [33] (sec. 1.3.2). This distribution (2.15) diverges from a Maxwellian linearly with $\delta_T = \lambda_{ei}\frac{d}{dx}ln(T_e)$, where λ_{ei} is the electron mean free path for ion collisions.

$$f_{SH}(|\vec{v}|, v_x) = f_M(|\vec{v}|) + \sqrt{\frac{2}{9\pi}}(\frac{|\vec{v}|}{v_{T_e}})^4(4 - \frac{v^2}{2v_{T_e}^2})f_M(|\vec{v}|)\delta_T\frac{v_x}{|\vec{v}|} \tag{2.15}$$

where $f_M(|\vec{v}|)$ is the Maxwell distribution, $v_{T_e} = \sqrt{T_e/m_e}$ and the gradient $\vec{\nabla}T_e$ is anti-parallel to the x-axis.

Since transport and plasma current have equivalent effects on the IAW, we can find the drift velocity $v_d = v_e - v_i$ required to produce the same asymmetry as an electron temperature profile with $\delta_T = \lambda_e\frac{d}{dx}ln(T_e)$, where $\hat{x} = \hat{k}$. To do this, we observe the growth rates γ of Ion Acoustic Wave instabilities in current or return current scenarios.

From [32] p183 Eq6.12, for the ion acoustic wave with phase velocity $\frac{\omega_{iaw}}{k}$, we have

$$\gamma(k) = \frac{\alpha^3}{(1+\alpha^2)^{1.5}}\sqrt{\frac{Z\pi m_e}{8m_i}}k[(v_d - \frac{\omega}{k})\frac{\omega}{\omega_{iaw}} + Z\frac{\omega}{k}\sqrt{\frac{m_iT_e^3}{m_eT_i^3}}exp(-\frac{\alpha^2}{1+\alpha^2}\frac{ZT_e}{2T_i})] \tag{2.16}$$

Where $\omega = \pm\omega_{iaw}$ is the IAW resonance frequency and v_d is the electron drift velocity. With $ZT_e >> T_i$ and long wavelength limit $\alpha \gg 1$ we have

$$\gamma(k) = \sqrt{\frac{Z\pi m_e}{8m_i}}k[v_d - \frac{\omega}{k}]\frac{\omega}{\omega_{iaw}} \tag{2.17}$$

Similarly from [48], Eq 12:

$$\gamma(k) = \sqrt{\frac{\pi}{8}}\frac{\omega_{pi}^2}{\omega_{pe}}\frac{k\lambda_{De}}{(1+k^2\lambda_{De}^2)^2}[\frac{3}{2}cos(\theta)\frac{kv_{Te}}{\omega_{iaw}}\delta_T\frac{\omega}{\omega_{iaw}} - 1] \tag{2.18}$$

Where θ is the angle to the temperature gradient. Using $\sqrt{Z\frac{m_e}{m_i}} = \omega_{pi}/\omega_{pe}$, equation 2.18 becomes

$$\gamma(k) = \sqrt{\frac{Z\pi m_e}{8m_i}}\omega_{pi}\lambda_{De}\frac{k}{(1+k^2\lambda_{De}^2)^2}[\frac{3}{2}cos(\theta)\frac{kv_{Te}}{\omega_{iaw}}\delta_T\frac{\omega}{\omega_{iaw}} - 1] \tag{2.19}$$

Using cold ion limit, $\omega_{iaw} = \frac{\omega_{pi}}{\sqrt{1+k^{-2}\lambda_{De}^{-2}}}$

$$\gamma(k) = \sqrt{\frac{Z\pi m_e}{8m_i}}\frac{k}{(1+k^2\lambda_{De}^2)^{1.5}}[\frac{3}{2}cos(\theta)v_{Te}\delta_T - \frac{\omega}{k}]\frac{\omega}{\omega_{iaw}} \tag{2.20}$$

Taking the long wavelength limit and comparing it to equation 2.17, we can see that

$$v_d = \frac{3}{2}cos(\theta)v_{Te}\delta_T \tag{2.21}$$

This drift velocity produces a slope at $v = v_i$ equivalent to the Spitzer-Harm distribution projected onto the v_x direction (2.22), shown in fig. 2.12.

$$f_{SH}(v_x) = \int f_{SH}(|\vec{v}|, v_x)dv_y dv_z \tag{2.22}$$

We have computed OTS spectra numerically with the Spitzer Harm distribution function [33]. Using Eq. (2.21), the resulting IAW from the Spitzer Harm distribution can be compared to the IAW from the equivalent drifting Maximilian:

$$f_{dM}(v_x) = \sqrt{\frac{m_e}{2\pi T_e}}exp(-\frac{m_e(v_x - v_d)^2}{2T_e}) \tag{2.23}$$

This relation seems to match the IAW shape well for $\delta_T < 0.006$ (Fig. 2.13).

As distinct IAW peaks disappear due to increased ion Landau damping (2.14), asymmetric Landau damping due to electrons has a less significant effect on the IAW amplitude. As S_i/S_e increases, the magnitude of the asymmetry of the IAW can

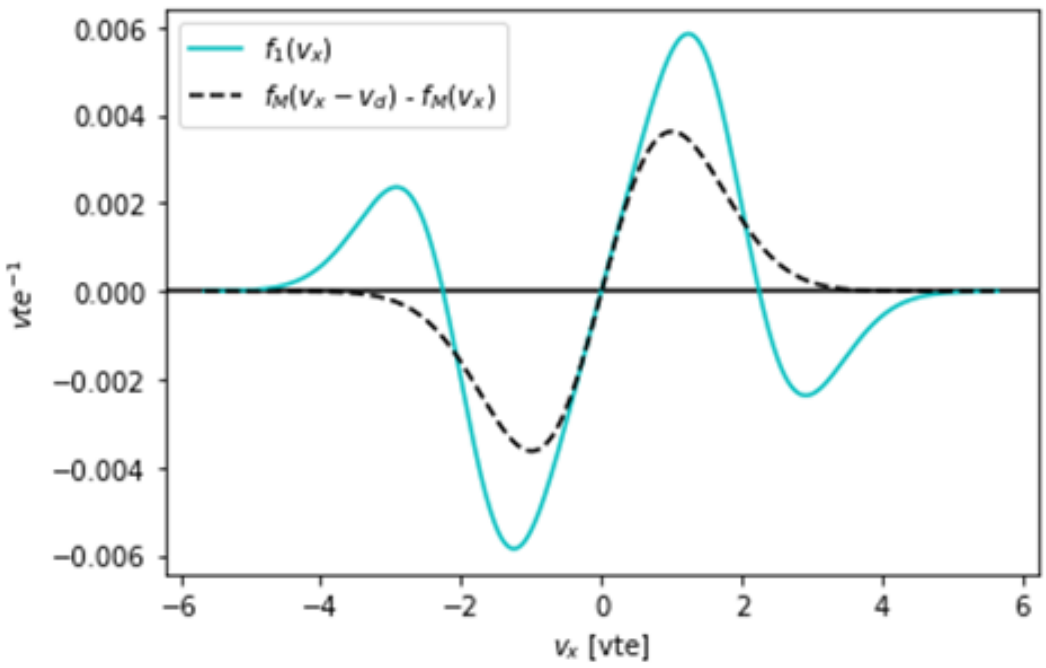

Figure 2.12: Spitzer Harm (blue) and drifting Maxwellian (black) distribution functions with the even part subtracted, with v_d from eq. 2.21. The slopes of the distribution functions at $v = 0$ are equivalent.

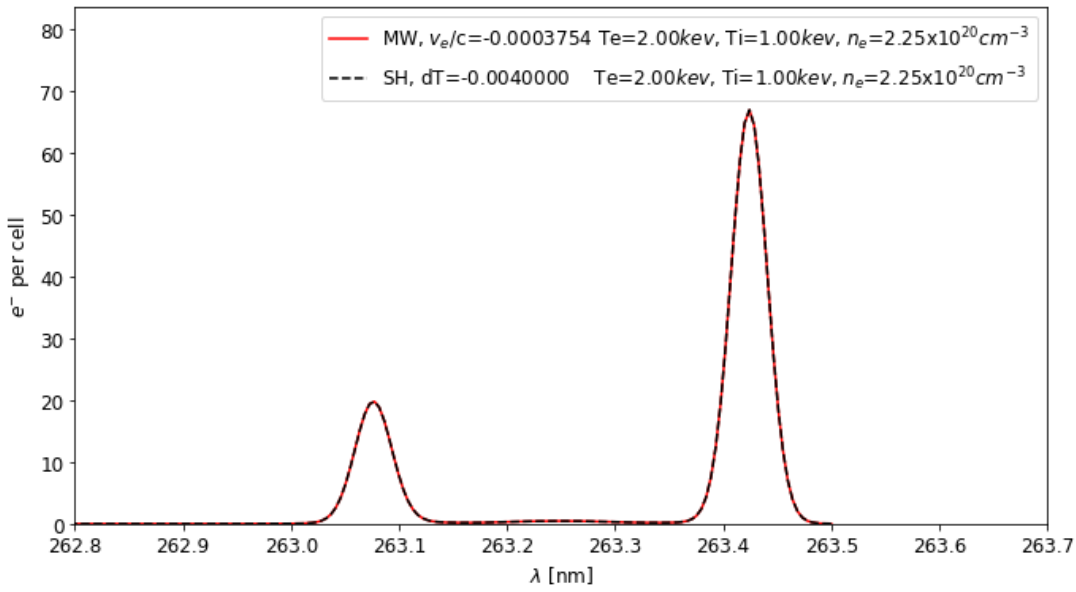

Figure 2.13: Spitzer Harm IAW (black) and drifting Maxwellian IAW (red) for Z=50 Au

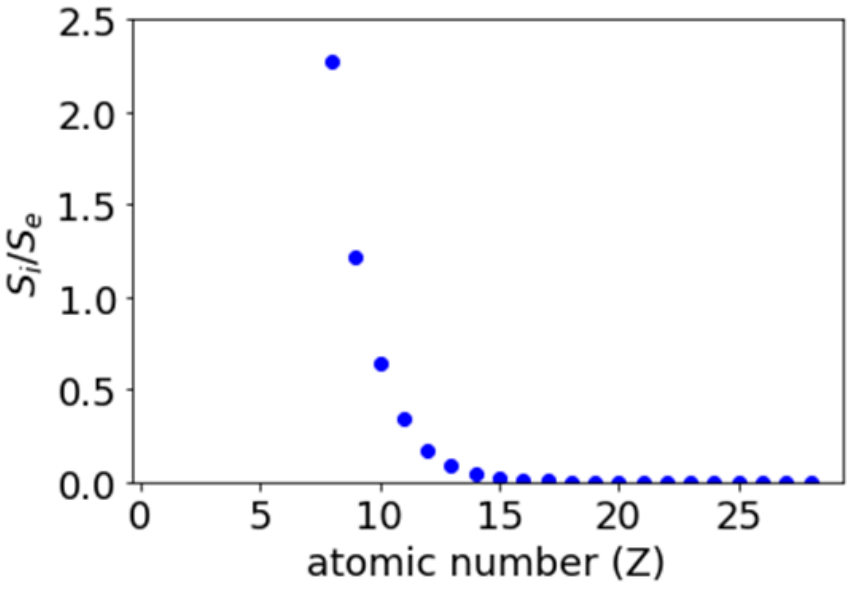

Figure 2.14: Ratio of ion term to electron term in OTS form factor, using T_e=T_i, $\alpha = 2$

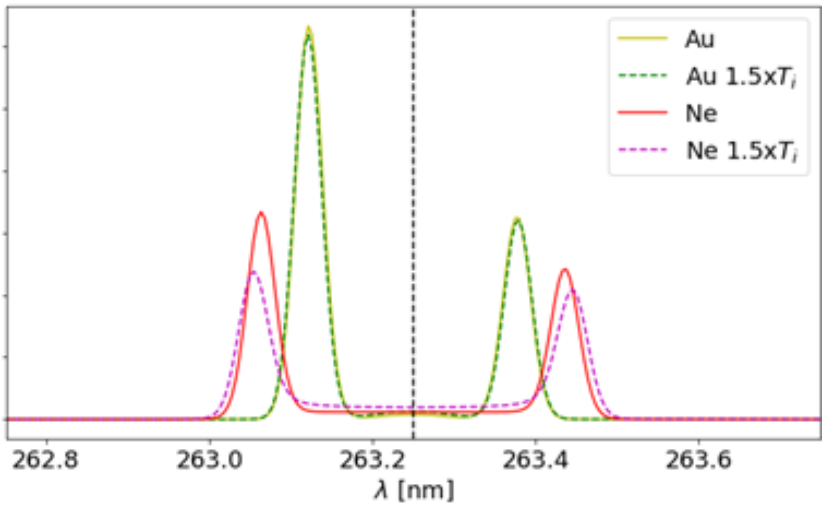

Figure 2.15: Ion acoustic wave change with 50% increase in T_i for Au and Ne plasma. Ion acoustic wave asymmetry from Landau damping is sensitive to temperature for plasma with Z $\lessapprox$ 12

become more sensitive to the ion temperature than the electron drift. (Fig. 2.15) This dependence on the ion temperature appears around $ZT_e/T_i \lessapprox 15$ (Fig. 2.14).

For high ZT_e/T_i, v_d can be determined from the asymmetry of the IAW. The

ion temperature typically cannot be measured, but it does not affect the relative amplitudes of the waves. For $ZT_e/T_i \lessapprox 8$, the ion temperature can be easily measured from the shape of the IAW spectrum, allowing the asymmetry to be analyzed with a known ion temperature. Intermediate Z ions, however, may not determine a unique drift velocity or ion temperature (Fig. 2.15).

2.2.3 Super-Gaussian effects on Ion Acoustic waves

In laser-heated plasmas, the primary process of heat deposition occurs vie Inverse Bremsstrahlung (IB): electrons are accelerated by the laser field and subsequently collide with ions to produce a heated, isotropic electron distribution function[49]. The distribution is driven towards a Maxwellian as electron collision exchange electron energy. However, for sufficiently high laser intensity and electron-ion collisionality can maintain a non-Maxwellian distribution. This occurs when $Z(\frac{v_{osc}}{v_{Te}})^2 > 1$, [50] where $v_{osc} = \frac{e}{\omega_L m_e}\sqrt{\frac{2I}{c\epsilon_0}}$ is the oscillatory velocity of electrons in the electric field of the laser of intensity I.

The extent of the super-Gaussian effect can be seen in the parameter $5 \geq m \geq 2$, [50] controlling the electron distribution function shape:

$$f_{SG0}(|\vec{v}|) = \frac{m}{4\pi\Gamma(3/m)(\sqrt{2}v_m)^3} exp\left(-\left(\frac{|\vec{v}|}{\sqrt{2}v_m}\right)^m\right), \tag{2.24}$$

where, v is the speed of the electrons and $v_m = \sqrt{\frac{3\Gamma(3/m)}{2\Gamma(5/m)}}v_{T_e}$, $v_{T_e} = \sqrt{T_e/m_e}$. From Fokker-Planck simulations in Ref. [50], for homogeneous laser-heated plasma, a practical expression for the exponent $m(\alpha)$ is found:

$$m(\alpha) = 2 + \frac{3}{1 + 1.66\alpha^{-0.724}} \tag{2.25}$$

where $\alpha = Z(v_{osc}/v_{Te})^2$

The modification of the electron distribution function also alters the spectral shape of the Thomson scattered light [51–53]. Although the EPW can be sensitive to many

parts of the distribution function, the IAW is only affected by $f_e(v_x \approx 0)$.

The electron distribution function (2.24) projected onto one spatial dimension (x) is

$$\bar{f}_{SG0}(v_x) = \int_{-\infty}^{\infty}\int_{-\infty}^{\infty} f_{SG0}(|\vec{v}|)dv_y dv_z = \frac{1}{2\sqrt{2}\Gamma(3/m)v_m}\Gamma(2/m, \frac{v_x^m}{(\sqrt{2}v_m)^m}) \quad (2.26)$$

where $\Gamma(a,x) = \int_x^{\infty} t^{a-1}e^{-t}dt$ is the incomplete gamma function. From (2.3,2.26), we can find the susceptibility function for electrons [54] at $\omega/k \approx 0$:

$$\chi_e(\omega = 0) = \frac{\Gamma(1/n)\Gamma(5/n)}{3\Gamma(3/n)^2}\frac{1}{k^2\lambda_{De}^2} \quad (2.27)$$

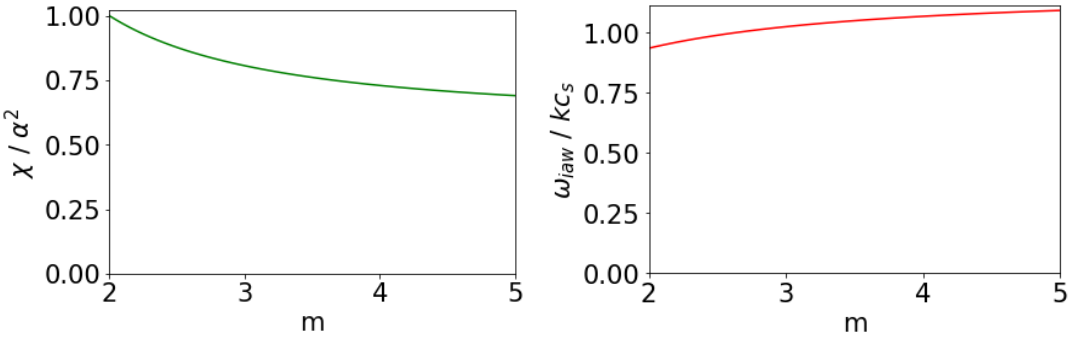

Figure 2.16: Electron susceptibility function (left), (2.3) and ω_{iaw} (right) as a function of super-Gaussian order m, using $T_e = T_i = 1keV$, $n_e = 2 \times 10^{20} cm^{-3}$ in Au plasma, $Z = 50$

We can see that super-Gaussian electron distributions require high Z plasma (2.25), as $v_{osc} \gg v_{Te}$ typically results in unstable plasma and cannot be sustained long [50]. This results in IAW frequency $\omega_{iaw}^2 \approx \frac{\omega_{pi}^2}{1+\chi_e(\omega=0)}$, as seen in figure 2.16. Because $\chi_e(\omega = 0)(2.27)$ is proportionate to $\frac{1}{T_e}$, the IAW spectrum in a super-Gaussian electron distribution is identical to the IAW spectrum from a Maxwellian electron distribution with a higher temperature. A super-Gaussian plasma where the IAW is fit with a Maxwellian electron temperature of T_{e0} will have a true temperature of $T_e = \frac{\Gamma(1/n)\Gamma(5/n)}{3\Gamma(3/n)^2}T_{e0}$

2.2.4 Collision Effects on OTS

Equation (2.2) is valid for electron density fluctuation correlations at the wave vector $\vec{k}$ and frequency ω that evolve according to collisionless Vlasov theory and originate from discrete particle noise. For high-Z plasmas, the evolution of density fluctuations is modified by ion-ion collisions when $k\lambda_{ii} \ll 1$, where the wave number k corresponds to the density fluctuations that are tested in OTS and λ_{ii} is the ion-ion mean free path for thermal ions. At the same time, electron collisions are often negligible in typical laser-produced plasmas because $k\lambda_{ei} \gg 1$ and can be neglected when calculating $S(\vec{k},\omega)$. The ion collisions, however, can change the asymmetry of the IAW peaks and are therefore crucial to the measurement of heat transport in high Z plasma.

Modifications of the IAW spectrum due to damping by ion-ion collisions typically are superseded by spectral resolution and pulse front tilt [43], but collisions are important in determining the relative amplitude of the IAW peaks. At $k\lambda_{ii} \approx 0.1$, typical in high Z coronal plasmas, ion damping is at the cusp of the transition between collisional and collisionless Landau damping (cf. Fig. 3 of Ref. [47]) and therefore a theory of $S(\vec{k},\omega)$ requires proper treatment of the weakly collisional limit usually associated with nonlocal transport. The magnitude of the damping coefficient of the IAW due to ion collisions is small, comparable to electron Landau damping.

The theory of plasma fluctuations is derived in Ref. [55] for arbitrary collision frequencies and particle noise sources. Because only ion-ion collisions are important for the fluctuations tested in OTS measurements of Au plasma, we approximate results of Ref. [55] by keeping collisional ion-ion terms in ion response functions that are evaluated for the ion Maxwell distribution functions. All terms involving electron collisions are dropped and the dynamical form factor is given by the following expression:

$$S^c(\vec{k},\omega) = \frac{2\pi}{k}\left|1-\frac{\chi_e}{\epsilon^c}\right|^2 \bar{f}_e\left(\frac{\omega}{k}\right) + \frac{2}{\omega}\left|\frac{\chi_e}{\epsilon^c}\right|^2 \left(\frac{k}{k_{De}}\right)^2 Im[\chi_i^c]\frac{T_i}{T_e}, \qquad (2.28)$$

where $\epsilon^c = 1 + \chi_e + \chi_i^c$ and $\chi_i^c(\vec{k}, \omega)$ is the ion susceptibility function calculated with the effects of ion-ion collisions and defined by Eq. (28) of Ref. [55]. In the limit of collisionless ions $S^c(\vec{k}, \omega)$ (2.28) takes the form of $S(\vec{k}, \omega)$, Eq. (2.2).

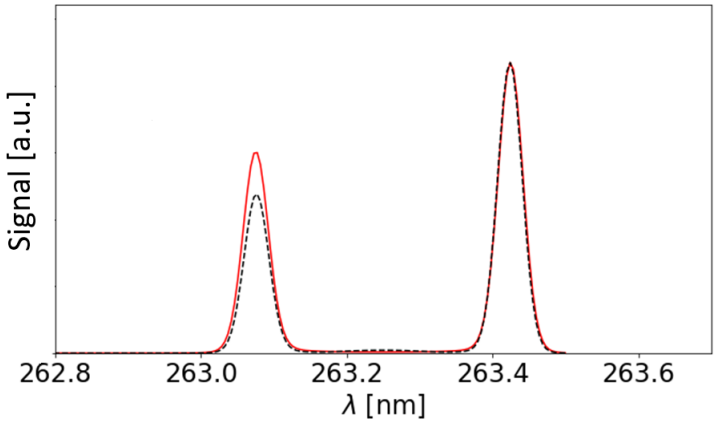

Figure 2.17: IAW spectrum from gold plasma, Z=50, T_e=2 keV, T_i=1 keV, n_e=2.25 × $10^{20} cm^{-3}$ and $v_e = -60 km/s$ ($k\lambda_{ii} \approx 0.1$). The black dotted line shows the spectrum with no ion collisions, and the red line shows the spectrum including the effects of ion collisions, normalized to have the same peak amplitude. (From [6])

Application of $S^c(\vec{k}, \omega)$ (2.28) to the interpretation of the OTS spectra is important for the modeling of the ion peak asymmetry. While ion collisions do not significantly shift the measured wavelengths of IAW peaks or substantially modify their widths, the collisional damping does modify the relative amplitudes of the two peaks. Fig. 2.17 illustrates the effects of including ion-ion collisions on this asymmetry by comparing results with calculations using the collisionless $S(\vec{k}, \omega)$ Eq. (2.2).

2.3 Geometric Effects

OTS systems are composed of many optical components designed to limit the signal observed to a sufficiently small range of scattering vectors to allow isolated features to be identified. However, these restrictions to the observed light must be balanced with light throughput optimization. The scattering cross-section for OTS (2.1) is small and typically scatters on the order of 1×10^{-6} of the probe power, requiring significant

solid angles of acceptance for light collection to transmit a sufficient signal to the streak camera (section 2.4.3). This means the range of directions of light permitted in the telescope (Fig. 2.1) and the optics involved in the spectrometer may result in some changes to the OTS spectrum (2.6).

2.3.1 Range of scattering vectors

When measuring the shape of the IAW spectrum, cf. Fig. 2.6c, it can be important to account for wavelength-dependent broadening caused by the range of angles in the probe beam and collection optics [56]. This has two separable effects: changing the direction of $\vec{k}$ in the plasma, and changing the scattering angle, or equivalently, the size of $|\vec{k}|$ (Fig. 2.18). The measurement of flow velocity v_i is controlled by the direction of $\vec{k}$. When $\vec{k}$ and v_i are parallel, changes in the direction of $\vec{k}$ by a small angle have no significant effect on the spectrum. Changes in $|\vec{k}|$, however, will shift each part of the spectrum, roughly in proportion to its phase velocity. This effect is detailed in [8].

The sets of all accepted probe and collection directions exist as a pair of spherical cones. For either of these cones, and wave vector $\vec{k}'$ permitted through the system must have $\arccos\left(\frac{\vec{k}'\cdot\vec{k}_0}{|k'||k_0|}\right) \leq \delta\theta_{max}$, where $\delta\theta_{max}$ is the half-angle of the cone and $\vec{k}_0$ is the nominal wave vector of the cone (either $\vec{k}_L$ or $\vec{k}_s$).

The angular changes of the wave vectors that affect the OTS spectrum are typically confined to a plane. This could be the $\vec{k}\vec{v_i}$ plane when plasma flow is not aligned with $\vec{k}$, or the OTS plane $\vec{k_L}$ $\vec{k_s}$ when the stretch of k is relevant, or the $\vec{k}$ $\vec{B}$ plane when a strong magnetic field is present. In any case, the deviation of angle in the plane $\delta\theta$ in either the probe or collection cone is of interest for any $\vec{k}'$ in plane with normal $\hat{P}$.

The relevant angle of deviation can be defined as $\delta\theta = \arctan\left((\frac{\vec{k}'}{|k'|} - \frac{\vec{k_0}}{|k_0|})\cdot(1-\hat{P})\right)$ for light scattered at wave vector $\vec{k}'$.

The set of all $\vec{k}'$ with angular deviation $\delta\theta$ in a cone of angle $\delta\theta_{max}$ has a limited range of angles in the $\hat{P}$ direction. If this limit is $\delta\theta_{\perp}$, we have the relation of a circle:

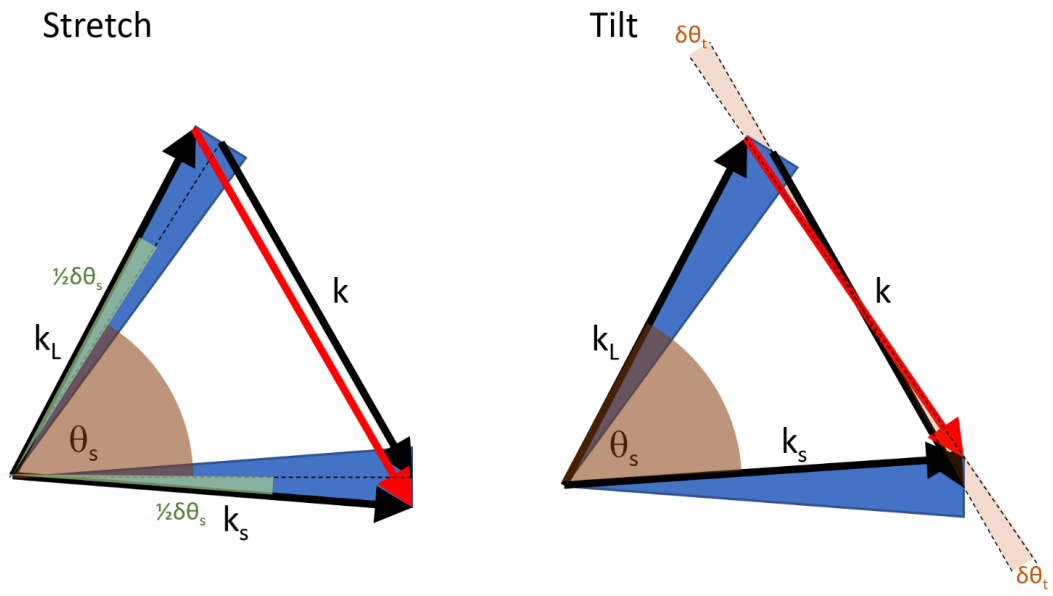

Figure 2.18: OTS angle effects with stretch (left) of angle $\delta\theta_s$ and tilt (right) of angle $\delta\theta_t$ of the scattering vector k. The altered k vector is shown in red, with the nominal scattering k in black. The range of angles permitted in the probe and collection cones are shown in blue.

$\delta\theta^2_{max} = \delta\theta^2 + \delta\theta^2_{\perp}$. Normalizing to find the relative intensity $f(\delta\theta)$ (Fig. 2.19) of transmitted light at angle $\delta\theta$ in the plane of interest, we find

$$f(\delta\theta) = \frac{2}{\pi\delta\theta^2_{max}}\sqrt{\delta\theta^2_{max} - \delta\theta^2} \tag{2.29}$$

The range of OTS scattering angles that determine $|\vec{k}|$ is simply the convolution of the function (2.29) for the probe $f_0(\theta)$ and collection $f_c(\theta)$ (Fig. 2.19):

$$f_s(\delta\theta_s) = \int_{-\infty}^{\infty} f_0(\delta\theta_s - \tau) f_c(\tau) d\tau \tag{2.30}$$

The range of angles in the tilt of $\vec{k}$ depends on the plane of interest. The tilt of $\vec{k}$ in the direction perpendicular to the scattering plane is identical to the range of 'stretch' angles (2.31), but tilt in the OTS plane is more restricted: For changes of stretch and tilt angles $\delta\theta_s$, $\delta\theta_t$ and angular spread functions for probe and collection f_0 and f_c, tilt angles in the OTS plane are distributed

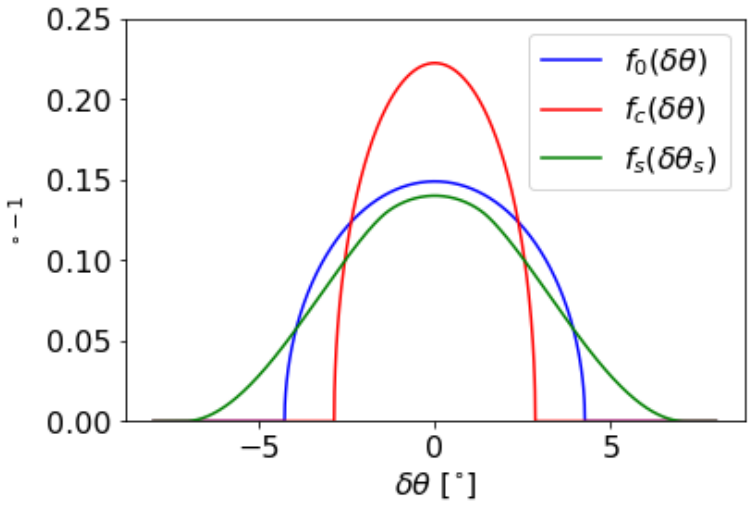

Figure 2.19: Range of angles present in the probe (blue) and collection (red), Eq.(2.29), and the resulting distribution of stretch angles (green), Eq. (2.31) as a function of angular deviation $\delta\theta$ from the normal wave-vector.

$$f_{t\|}(\delta\theta_t) = \int_{-\infty}^{\infty} f_0(0.5\delta\theta_s + \delta\theta_t) f_c(0.5\delta\theta_s - \delta\theta_t) d\delta\theta_s \tag{2.31}$$

where the probe angular deviation is $\delta\theta_0 = 0.5\delta\theta_s + \delta\theta_t$ and the collection angular deviation is $\delta\theta_c = 0.5\delta\theta_s - \delta\theta_t$.

For an arbitrary angle of interest θ_{TS}, (Fig. 2.20) for the relevant tilt direction out of the scattering plane and a $\vec{k}'$ angle out of the OTS plane of θ_p, the relevant tilt angle is $\theta_t = sin(\theta_{TS})\theta_p + cos(\theta_{TS})(\delta\theta_0 - 0.5\theta_s)$. The deviation of $\vec{k}'$ out of the OTS plane can be described as $\theta_p = \theta_a + \theta_b$, where θ_a is the angle the probe strays put of the OTS plane and θ_b is the angle the collection strays out of the OTS plane.

If we then define θ_0 as the angle by which the probe wave vector strays from its nominal value k_L, we can define the deviation of the collection wave vector in the OTS plane as $\theta_c = \theta_s - \theta_0$, where θ_s is the stretch angle, as we see in Eq. (2.31). This allows a full distribution of stretch and tilt angles to be calculated by integrating over all probe angles θ_0:

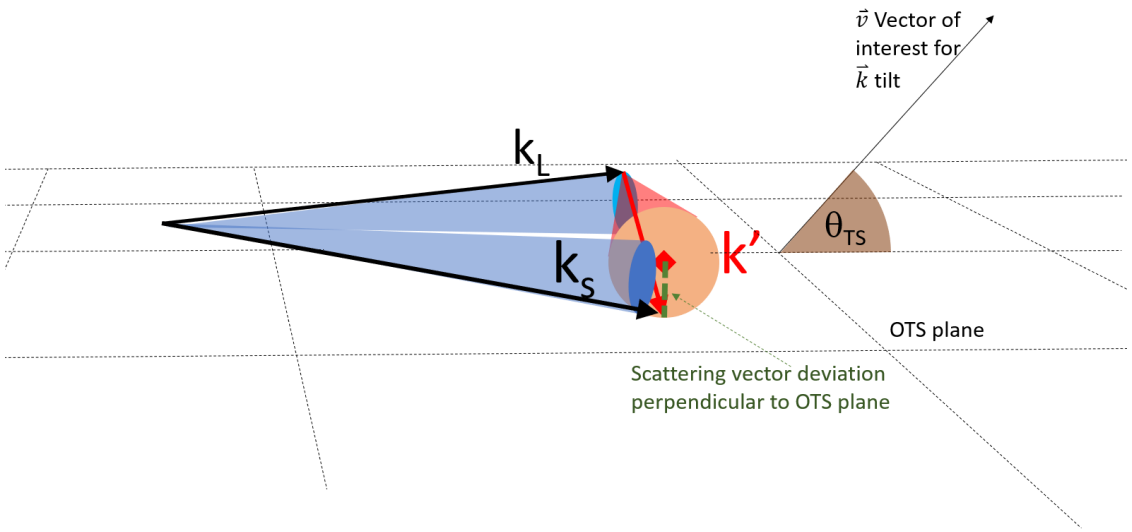

Figure 2.20: OTS wave vectors (also seen in Fig. 2.18) viewed from with the OTS plane. $\vec{v}$ (black, top right) defines the component of the direction of interest in the plasma not captured by $\vec{k}$: $\vec{v} \cdot \vec{k} = 0$. This defines the angle θ_{TS}, the angle between the OTS plane and the $\vec{v}\vec{k}$ plane relevant for tilt (2.32). Deviation of $\vec{k}$ out of the OTS plane is shown in green: this determines the angle θ_p that $\vec{k}'$ points out of plane.

$$f_t(\theta_s, \theta_t) = \int_{-\infty}^{\infty} d\theta_0 \int_{-\sqrt{\delta\theta_{0max}^2 - \theta_0^2}}^{\sqrt{\delta\theta_{0max}^2 - \theta_0^2}} d\theta_a \int_{-\sqrt{\delta\theta_{cmax}^2 - (\theta_s - \theta_0)^2}}^{\sqrt{\delta\theta_{cmax}^2 - (\theta_s - \theta_0)^2}} d\theta_b f_0(\theta_0) f_c(\theta_s - \theta_0) \\ \delta(\theta_t - sin(\theta_{TS})(\theta_a + \theta_b) - cos(\theta_{TS})(\theta_0 - 0.5\theta_s)) \tag{2.32}$$

This displays a distinct shape based on θ_{0max} and θ_{cmax} in the OTS plane, and an isotropic shape when out of plane, seen in figure 2.21.

To reproduce this effect in calculated OTS spectra, (2.1) can be integrated over $f(\theta_s, \theta_t)$ with scattering angle changed by θ_s and projections of v_i changed by θ_t.

2.3.2 Pulse front tilt

The IAW spectrum is also affected by pulse front tilt due to the range of path lengths available to the scattered light in the spectrometer [43], [56]. This range of path lengths causes a measured IAW spectrum to be composed of a range of times up to before or after the nominal time, with weighting falling off with a circular shape:

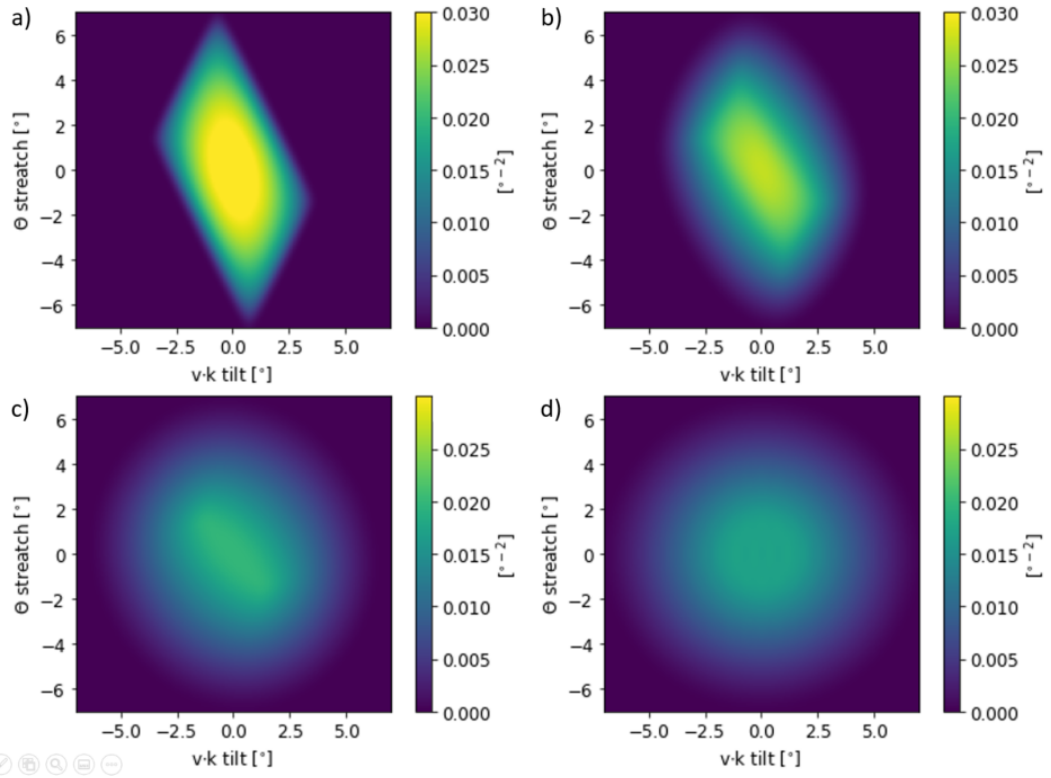

Figure 2.21: Distribution of scattering angles for the OMEGA laser facility, with an f/6.7 probe and f/10 collection. Angles out of plane θ_{TS} are a) 0°, b) 30°, c) 60°, d) 90°

$$f_{pft}(t) = \frac{2}{\pi t_{max}^2}\sqrt{t_{max}^2 - t^2} \tag{2.33}$$

where t_{max} is the maximum extent of the pulse front tilt in time.

The value of t_{max} is determined by the geometry of the IAW spectrometer (Fig. 2.2). Each adjacent groove in the diffraction grating has a light travel time difference of $m\frac{2\pi}{\omega_L}$, where m is the diffraction order. The time difference from the center of the beam to the edge is then

$$t_{max} = \frac{\pi N m}{\omega_L} \tag{2.34}$$

where N is the number of illuminated grating grooves [43].

The short time deviations caused by pulse front tilt primarily affect the IAW spec-

trum by widening the IAW peaks, as slowing flow velocities and cooling temperatures move the location of the resonance on the streak camera. This does not affect the total light captured from each IAW resonance, instead distributing this light to produce a lower, broader peak. This can be matched by adding broadening to the IAW spectrum or by integrating $S(k, \omega)$ over plasma parameters weighted by (2.34).

2.4 Signal, Background and Resolution

When OTS spectra are recorded on a streak camera, the resulting image is mostly a count of photo-electrons hitting the CCD, with some much smaller CCD read noise. These photo-electrons can come from OTS scattering (2.1) or from plasmas self-emission or other non-OTS processes that compose the background of the shot. This background can be subtracted, leaving the original image (Sec. 2.1.2).

When the background signal is large or the OTS scattered light is small, the signal can disappear or be significantly changed by statistical noise in the signal and background. These effects can be quantified to assess potential measurement errors [1].

2.4.1 Scattering Amplitude of the EPW

Scattering cross-sections for OTS are important both for determining the probe power required to make desired measurements of plasma conditions and for analyzing possible driven waves or other features in plasma that can increase scattering cross-sections.

The shape and scale of the EPW spectrum from homogeneous plasma with a Maxwellian electron distribution function are entirely determined by the scattering geometry, electron temperature, and electron density.

The total value of $S(\vec{k}, \omega)$ corresponding to the electron plasma wave can be seen in the first half of (2.2). Integrating this value across all frequencies shows the total scattering form factor S_{EPW}

$$S_{EPW} = \int_{-\infty}^{\infty} S_e(\vec{k},\omega)d\omega = \int_{-\infty}^{\infty} \frac{2\pi}{k} \left|\frac{1}{\epsilon}\right|^2 \bar{f}_e\left(\frac{\omega}{k}\right) d\omega \tag{2.35}$$

the integral of $\int_{-\infty}^{\infty} \left|\frac{1}{\epsilon}\right|^2 d\omega$ at the resonance $\Re(\epsilon) = 0$ can be approximated for linear $\Re(\epsilon)$ as $\int_{-\infty}^{\infty} \frac{1}{\Im(\epsilon)^2+\omega^2(\frac{d}{d\omega}\Re(\epsilon))^2} d\omega$. Since there is a red-shifted and blue-shifted EPW, this is multiplied by 2 for the full spectrum:

$$\int_{-\infty}^{\infty} \left|\frac{1}{\epsilon}\right|^2 d\omega \approx \frac{2\pi}{\Im(\epsilon)\frac{d}{d\omega}\Re(\epsilon)} \tag{2.36}$$

At the EPW resonance, we can write the dielectric functions $\epsilon = 1 + \chi_e$ (2.3) for thermal plasma [12] are

$$\Im(\epsilon) = \alpha^2 \sqrt{\frac{\pi}{2}} \frac{\omega}{k v_{Te}} \exp\left(-0.5 \frac{\omega^2}{k^2 v_{Te}^2}\right) \tag{2.37}$$

$$\Re(\epsilon) = 1 + \alpha^2 - \alpha^2 \left(\frac{\omega}{k v_{Te}} \exp\left(-0.5 \frac{\omega^2}{k^2 v_{Te}^2}\right) \int_0^{\frac{\omega}{k v_{Te}}} \exp\left(-0.5 p^2\right) dp \right) = 0 \tag{2.38}$$

$$\frac{d}{d\omega}\Re(\epsilon) = \frac{1}{k v_{Te}} \left(\frac{\omega}{k v_{Te}} - \frac{k v_{Te}}{\omega}(1+\alpha^2) \right) \tag{2.39}$$

using the EPW shape parameter $\alpha = \frac{\omega_{pe}}{k v_{Te}}$. From these expressions, we can approximate the total form factor as

$$S_{EPW} = \frac{4\pi\alpha^{-2}}{\frac{\omega^2}{k^2 v_{Te}^2} - (1+\alpha^2)} \tag{2.40}$$

using the EPW dispersion relation from Eq. 2.5, this reduces to

$$S_{EPW} = 2\pi\alpha^{-2} \tag{2.41}$$

This expression can be seen to approximate the EPW amplitude well for high α, where the EPW frequency is well-defined. Low α measurements have a more diffuse spectrum that is not as well approximated by a resonance (2.5).

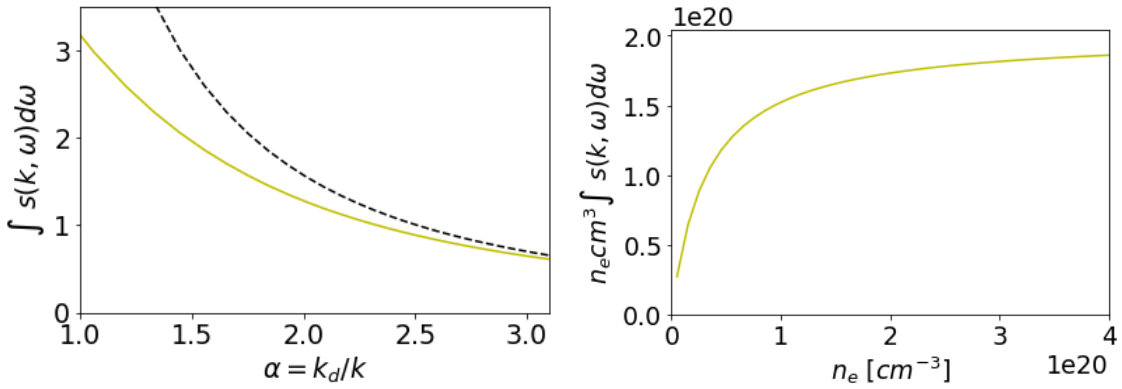

Figure 2.22: Total EPW amplitude $\int_{-\infty}^{\infty} S_e(\vec{k},\omega)d\omega$ as a function of α (left). The approximation $2\pi\alpha^{-2}$ (2.41) is shown in black. On the right the cross-section is shown multiplied by density for $T_e = 1keV$ plasma, making it linear with the scattered power (2.1)

The EPW typically has a different shape than a symmetric resonance, contributing to some discrepancy in amplitude (Fig. 2.22).

While Electron density increases the OTS α parameter, the scattered power is linear with density, so for high α spectra the scattered power approaches a constant with increasing density (Fig. 2.22).

2.4.2 Scattering Amplitude of the IAW

The IAW feature is more commonly enhanced, due to instabilities ([48, 57]) or anomalous collisionality. These effects can be detected if the IAW spectrum is seen to have an amplitude significantly larger than the thermal spectrum.

Similar to the amplitude of the EPW form factor, the IAW amplitude can be found by integrating Eq. 2.2. The IAW spectrum involves contributions from both terms of (2.2), which both contribute the majority of the spectrum in different parameter regimes. These are shown below:

$$S_{(i)IAW} = \int_{-\infty}^{\infty} S_i(\vec{k},\omega)d\omega = \int_{-\infty}^{\infty} \frac{Z2\pi}{k}\left|\frac{\chi_e}{\epsilon}\right|^2 \bar{f}_i\left(\frac{\omega}{k}\right)d\omega \tag{2.42}$$

$$S_{(e)IAW} \approx \int_{-2\omega_{IAW}}^{2\omega_{IAW}} S_e(\vec{k},\omega)d\omega = \int_{-2\omega_{IAW}}^{2\omega_{IAW}} \frac{2\pi}{k} \left|\frac{1+\chi_i}{\epsilon}\right|^2 \bar{f}_e\left(\frac{\omega}{k}\right) d\omega \tag{2.43}$$

the value of $\left|\frac{1}{\epsilon}\right|^2$ at the resonance $\Re(\epsilon) = 0$ is approximated as in (2.36). At the IAW resonance, the dielectric functions $\epsilon = 1 + \chi_e + \chi_i$ (2.3) for thermal plasma [12] are

$$\Im(\epsilon) = \alpha^2\sqrt{\frac{\pi}{2}}\frac{\omega}{kv_{Te}} + \alpha^2\frac{ZT_e}{T_i}\sqrt{\frac{\pi}{2}}\frac{\omega}{kv_{Ti}}\exp\left(-0.5\frac{\omega^2}{k^2v_{Ti}^2}\right) \tag{2.44}$$

$$\Re(\epsilon) = 1 + \alpha^2 + \alpha^2\frac{ZT_e}{T_i} - \alpha^2\frac{ZT_e}{T_i}\left(\frac{\omega}{kv_{Ti}}\exp\left(-0.5\frac{\omega^2}{k^2v_{Ti}^2}\right)\int_0^{\frac{\omega}{kv_{Ti}}}\exp\left(-0.5p^2\right)dp\right) = 0 \tag{2.45}$$

$$\frac{d}{d\omega}\Re(\epsilon) = \frac{1}{kv_{Ti}}\left(\frac{\omega}{kv_{Ti}}(1+\alpha^2) - \frac{kv_{Te}}{\omega}(1+\alpha^2+\alpha^2\frac{ZT_e}{T_i})\right) \tag{2.46}$$

At $\omega/k \ll v_{Te}$, $|\chi_e| \approx \alpha^2$, and at the IAW resonance, $\Re(1+\chi_i) = -\Re(\chi_e) = -\alpha^2$ and $\Im(\chi_i)$ is shown in (2.44). Using ω_{IAW} from (2.9), the two terms of the IAW form factor to be approximated as:

$$S_{(i)IAW} = \frac{2\pi Z\alpha^2}{1+\alpha^2}\frac{1}{\frac{ZT_e}{T_i} + \sqrt{\frac{T_im_e}{T_em_i}}\exp\left(\frac{1}{2}\left(\left(\frac{\alpha^2}{1+\alpha^2}\frac{ZT_e}{T_i}+3\right)\right)\right)} \tag{2.47}$$

$$S_{(e)IAW} = \frac{2\pi\alpha^2}{1+\alpha^2}\frac{1+\frac{\pi}{2}\frac{Z^2T_e^2}{T_i^2}\left(\frac{\alpha^2}{1+\alpha^2}\frac{ZT_e}{T_i}+3\right)\exp\left(-\left(\frac{\alpha^2}{1+\alpha^2}\frac{ZT_e}{T_i}+3\right)\right)}{1+\sqrt{\frac{T_em_i}{T_im_e}}\frac{ZT_e}{T_i}\exp\left(-\frac{1}{2}\left(\frac{\alpha^2}{1+\alpha^2}\frac{ZT_e}{T_i}+3\right)\right)} \tag{2.48}$$

$$S_{IAW} = S_{(e)IAW} + S_{(i)IAW} \tag{2.49}$$

This amplitude matches the IAW scattering cross-section well for high ZT_e/T_i, where the IAW spectrum has a well-defined resonance, as seen in figures 2.23 and 2.24.

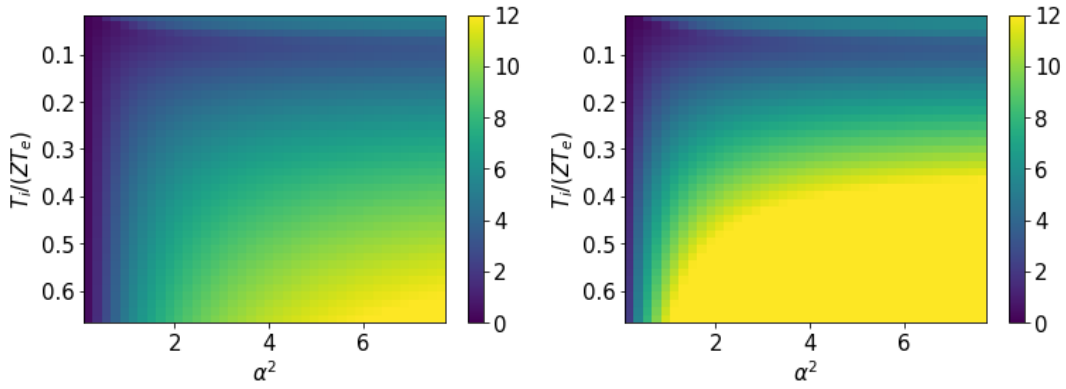

Figure 2.23: S_{IAW} from $S(k,\omega)$ (2.2, left) and from (2.49, right) for Carbon plasma, $T_e = 1keV$.

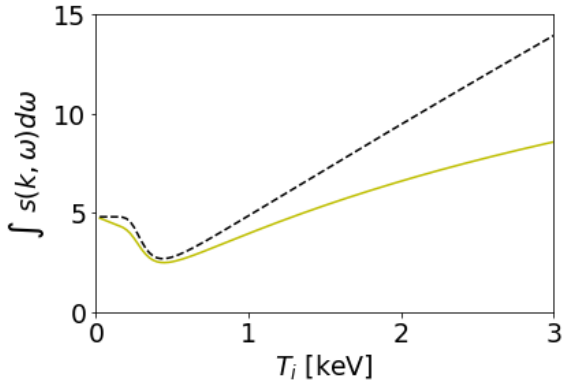

Figure 2.24: S_{IAW} from $S(k,\omega)$ (2.2, yellow) and from (2.49, black) for Carbon plasma, $T_e = 1keV$, $n_e = 1 \times 10^{20} cm^{-3}$.

2.4.3 Photo-electron noise

After light from OTS travels through the spectrometer, photo-electrons are created at the photo-cathode which are pulled through the drift tube to impact the scintillator attached to the CCD screen (Fig. 2.3). However, photo-electrons are not typically confined to one pixel (Fig. 2.25). This causes correlations in adjacent bins of the OTS spectrum and determines the statistical error of the measurement.

To observe the correlation between adjacent CCD pixels, the dark regions of an OTS image can be observed, where individual photo-electrons can be identified (Fig. 2.25). These photo-electrons can be measured for their total integrated signal (G)

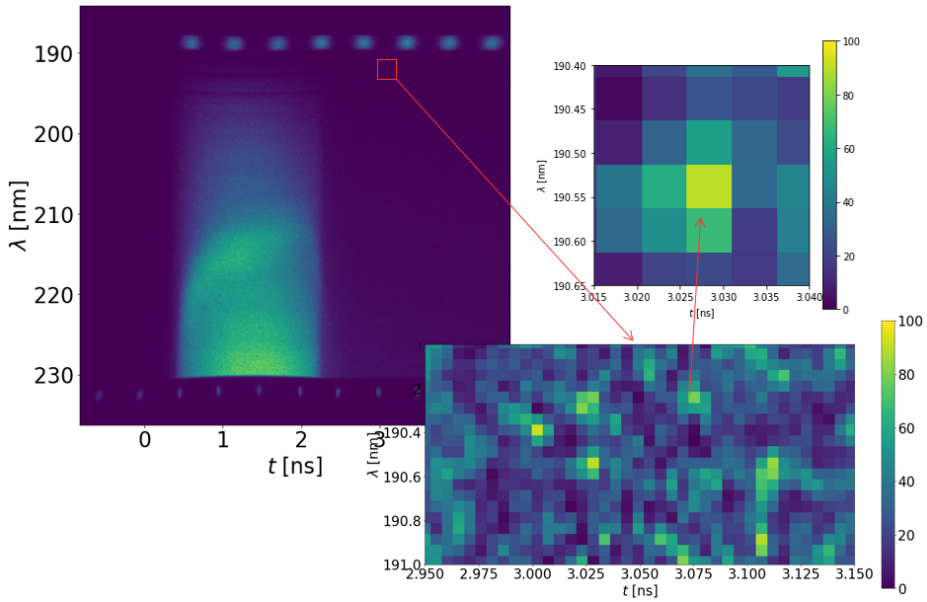

Figure 2.25: In dark regions of OTS spectra, the effects of individual photo-electrons can be identified.

and width (r_{CCD}). Away from any visible photo-electrons, the pixel variance will be the CCD read noise σ_{rn}^2.

Each photo-electron will also have some variability in the total counts deposited. If this has an RMS value of δG, the total variance can be found to be proportionate to the noise factor $F^2 = 1 + \frac{\delta G^2}{G^2}$, which is typically close to 1 [1, 58]. For an OTS image smooth on a larger scale than the CCD reading scale r_{CCD}, the variance of photo-electron signal in a pixel with reading A_i is $\sigma_p^2 = A_i G F^2$.

The OTS image is typically summed over durations comparable to the pulse front tilt time (2.34) to increase signal. If n pixels are summed over and $A_n = \Sigma_{i=1}^{n} A_i$, then

$$\sigma_s^2 = A_n G F^2 \tag{2.50}$$

This spectrum then has a corresponding covariance matrix K composed of the photo-electron signal and the CCD read noise:

$$K = (\mathbf{I}\sigma_s^2) * g + \mathbf{I} n \sigma_{rn}^2 \tag{2.51}$$

where g is the gaussian shape used to match the spread of CCD pixels excited by one photo electron: $g(x) = \frac{1}{\sqrt{2\pi}r_{CCD}} \exp\left(-\frac{x^2}{2r_{CCD}^2}\right)$, where x is the deviation in pixels from the original location.

This covariance matrix can then be used in to fit data and find parameter errors [1]. Once a theoretical spectrum is found to match the data, the quality of the fit can be assessed using the covariance matrix.

Using the range of wavelengths as $\vec{x}$, a vector of wavelength values with each pixel as a dimension, the covariance matrix can be used to normalize the residuals by their expected variance. For a measured spectrum $\vec{y}$ and fit spectrum $\vec{f}$, the residuals are then defined as $\vec{r} = \vec{f} - \vec{y}$. The covariance-normalized sum of the residuals is then:

$$S = \vec{r}^T K^{-1} \vec{r} \tag{2.52}$$

Based on the statistics of the photo-electrons and read noise, this value should follow a chi-squared distribution with degrees of freedom $ndf = L(\vec{r}) - n_{fit}$, where $L(\vec{r})$ is the number of pixels in the spectrum, and n_{fit} is the number of parameters adjusted to fit the data. This can be used to determine the likelihood of the summed residual S being higher than the observed value with a different set of random photo-electron and pixel read noise, determining the set of plausible spectra. This set can be approximated by $S \approx ndf$, the expected value of the chi-squared distribution.

Chapter 3

Counter-Streaming Plasmas

The self-generation and amplification of magnetic fields in high-energy-density (HED) plasmas has attracted significant interest in the last decades due to its importance in inertial confinement fusion (ICF) experiments [59, 60] and for laboratory astrophysics studies [19, 20]. In ICF, magnetic fields impact heat transport and may relax the conditions required for ignition [61]. In laboratory astrophysics, the characterization of magnetic fields produced by plasma instabilities is central to the study of the formation of collisionless shocks [21, 62] and their ability to accelerate particles.

Diagnostics of magnetic fields in HED experiments are typically limited to proton radiography [19, 63, 64] and Faraday rotation [65]. These techniques can only provide line-integrated measurements over the path of the probing protons or laser. Furthermore, proton radiography, the most commonly used diagnostic, cannot easily distinguish between electric and magnetic field deflections. The reconstruction of the path-integrated fields measured by the protons becomes significantly more challenging for strong fields, where caustic structures emerge [66]. In cases where the magnetic field structure is modulated at scales smaller than the scale of the plasma, retrieving the field structure from these diagnostics becomes even more difficult. This is the case for the filamentary magnetic fields produced by the Weibel instability in counter-streaming plasmas [2, 3, 19, 67] or the turbulent fields amplified by small-scale turbulent dynamos [68].

OTS techniques can be used to provide local, model-independent measurements of the ion and electron currents in the plasma, from which the magnetic field can be accurately inferred. The application of this technique to the Weibel instability in counter-streaming plasmas is demonstrated using particle-in-cell (PIC) simulations.

3.1 Theoretical and simulated field growth

The ion Weibel instability is a fundamental plasma instability that drives the formation of current filaments and amplification of magnetic fields due to velocity anisotropy in plasmas [24, 69] (sec. 1.2.1). Here we consider the model of the instability associated with plasma streams counter-propagating and interpenetrating without slowing each other down. In initially homogeneous and unmagnetized plasmas, the instability grows from the random, small-scale fluctuations in the plasma density and velocity, or in the electromagnetic fields. These fluctuations introduce small currents in the plasma along the flow propagation direction. The magnetic fields associated with these currents pinch co-propagating ion streams into filaments with wavevectors transverse to the flow propagation direction, amplifying the initial fluctuations[22]. The amplification of the current filaments enhances the magnetic fields, forming a positive feedback loop that drives the growth of the instability. If a region of the plasma smaller than one of these filaments can be probed, the evolution of the instability can be observed by the characteristics of the filament.

The current growth eventually saturates, after which filaments can merge to form larger structures [70, 71], break due to secondary kink-type instabilities [72], and become turbulent. These instabilities are believed to dominate the formation of collisionless shocks in weakly magnetized environments, such as young supernova remnants and gamma-ray bursts [21]. They are expected to play an important role in the acceleration of charged particles [73] and in their radiative processes in these environments [74, 75].

The astrophysical plasmas associated with the Weibel instability are almost entirely

collisionless. Coulomb collisions in counter-streaming plasma can slow the growth of the Weibel instability [76]. To maintain consistency with the low density astrophysical plasmas, laboratory astrophysics counter-streaming plasma experiments have used large spacing of targets to achieve low densities and high temperatures, similarly mitigating the effects of collisions on the ion Weibel instability [76, 77]. For this reason, we analyse the collisionless form of the Weibel instability here.

Plasma have been observed to undergo ion heating from the ion two-stream instability [13],[78] which is then stabilized by the ion and electron temperature equilibrium. This stabilization allows the ion Weibel instability to grow unimpeded.

For a thermal collisionless plasma streaming at speed v_i, the current filaments form with wavevectors $\vec{k}$ perpendicular to the streaming direction and with the most unstable wavelengths typically around the ion inertial length scale c/ω_{pi}. The amplitude of the current grows as $I \propto e^{\gamma t}$, where γ is the linear growth rate of the instability. It is useful to recast these parameters in dimensionless (sec. 1.2.3) form using

$$\Gamma = \gamma c/(\omega_{pi} v_i) \tag{3.1}$$

and $K = kc/\omega_{pi}$. Assigning coordinates with x in the flow direction and y in the direction of $\vec{k}$, the temperature-dependant instability growth rate can be computed by solving [22]

$$\Gamma = K \frac{\frac{v_i^2+v_{Tix}^2-v_{Tiy}^2}{v_{Tiy}^2} + \frac{m_i}{Zm_e}\frac{v_{se}^2+v_{Tex}^2-v_{Tey}^2}{v_{Tey}^2} - K^2 - \Gamma^2\frac{v_i^2}{c^2}}{D_i + D_e} \tag{3.2}$$

where

$$D_i = \frac{v_i}{v_{Tiy}}\left(\frac{v_i^2+v_{Tix}^2}{v_{Tiy}^2}\right)\sqrt{\frac{\pi}{2}}\exp(\xi_i^2)\mathrm{erfc}(\xi_i) \tag{3.3}$$

$$D_e = \frac{v_i}{v_{Tey}}\frac{m_i}{Zm_e}\left(\frac{v_i^2+v_{Tex}^2}{v_{Tey}^2}\right)\sqrt{\frac{\pi}{2}}\exp(\xi_e^2)\mathrm{erfc}(\xi_e) \tag{3.4}$$

$$\xi_i = \frac{\Gamma v_i}{\sqrt{2}K v_{Tiy}}, \xi_e = \frac{\Gamma v_i}{\sqrt{2}K v_{Tey}} \tag{3.5}$$

here $v_{T\alpha x} = \sqrt{T_{\alpha x}/m_\alpha}$, $v_{T\alpha y} = \sqrt{T_{\alpha y}/m_\alpha}$, where $\alpha = e, i$ and v_{se} is the streaming velocity of the electron population. Equation (3.2) for the growth rate γ, of the Weibel instability is derived [22] for Maxwell distribution functions with nonzero average flow velocities of electrons and ions and with anisotropic temperatures along x (direction of the flows) and y (transverse direction corresponding to the unstable k-vectors).

In typical counter-streaming plasma experiments conducted at OMEGA [3, 78–80], the plasma streams consist of fully ionized beryllium or plastic plasmas with electron and ion temperatures $T_e \approx T_i \approx 1.0$ keV, and flow velocities of $\approx 1000 km/s$ ($v_i/c \approx 0.0033$). Although the electrons initially expand out with the velocities of two interpenetrating ion populations, $v_{se} = v_i$, the electrons are highly collisional and are therefore expected to isotropize quickly [29], with electron-ion collisions on the order of 50 ns^{-1} leading to $v_{se} = 0$. A similar intra-stream ion collision rate works to isotropize the ion temperatures. Using the above equations we calculate for the beryllium plasma case with isotropic temperatures that the fastest growing mode is $K = 0.8$, with a growth rate of $\Gamma = 0.35$ and corresponding $\gamma = 3.2\text{ns}^{-1}$ (similar values are obtained for a carbon plasma). Thomson scattering diagnostics available at HED experimental facilities routinely resolve time scales shorter than 100ps for several nanoseconds, presenting the possibility for direct measurement during the linear phase of the instability.

In order to investigate the evolution of the Weibel instability for the conditions of current HED experiments, two-dimensional (2D) simulations were run with the fully electromagnetic, explicit PIC code, OSIRIS 4.0 [81]·[82]. I modeled a beryllium plasma ($A/Z = 9/4$) using a realistic ion-to-electron mass over charge ratio $m_i/(m_e Z) = 4131$, unlike typical PIC simulations of these HED systems, which tend to use reduced values $m_i/(m_e Z) \lesssim 100$. This allows for a more realistic evolution of the distribution functions.

Both ions and electrons are initialized with drifting Maxwellian distributions streaming at speed v_i in the x direction with $v_{Te} = 13.4 v_i$ and $v_{Ti} = 0.104 v_i$. These relations

are the same as those found in typical double-flow experiments. In these simulations we scale up all flow and thermal velocities by a factor of 10, giving a flow velocity v_i/c=0.03. This is done to reduce the computational cost of the simulations and to improve numerical accuracy. The evolution of purely electromagnetic instabilities in counter-streaming plasmas can be rigorously scaled between systems with different flow velocities (sec. 1.2.3), provided they remain non-relativistic [83]. The nature and characteristics of the instability in our simulations are therefore expected to match those of the experimental conditions, albeit while developing on a faster time scale.

Because the simulation is run at a higher velocity scale, it is possible that electrostatic instabilities may grow at a slower rate relative to electromagnetic instabilities than would be the case in a typical experiment. However, scaled simulations have been seen to accurately capture the evolution of counter-streaming plasmas [67, 77]. For this reason, we expect the simulations to be an adequate tool to test OTS measurement techniques, even though the resulting plasma may differ from experiments due to electrostatic instabilities.

The simulations have a box size of $60c/\omega_{pi}$ in the flow direction and $5c/\omega_{pi}$ in the transverse direction. This domain is resolved with 15360 by 1280 cells, providing 4 grid points per electron skin depth. Each cell is 0.57 Debye lengths, allowing electrostatic interactions to be resolved.

The simulation is run for a duration of $4.45 \times 10^4 \omega_{pe}^{-1}$ in time steps of $0.175\omega_{pe}^{-1}$. The plasma then propagates a length through the counter-streaming plasma a length $L = tv_i$. At the end of the simulations, the plasma flows have propagated a distance $L = 23c/\omega_{pi}$. The length L the plasma has traveled is a useful metric, as it shows the number of growth lengths the plasma has passed through which indicates the progression of instability independent of the velocity scale (3.1). For this reason, we proceed to label times in the simulation with their L value.

Electrons and ions were simulated with 64 particles per cell, in order to have a large enough number of particles to properly resolve the distribution functions locally

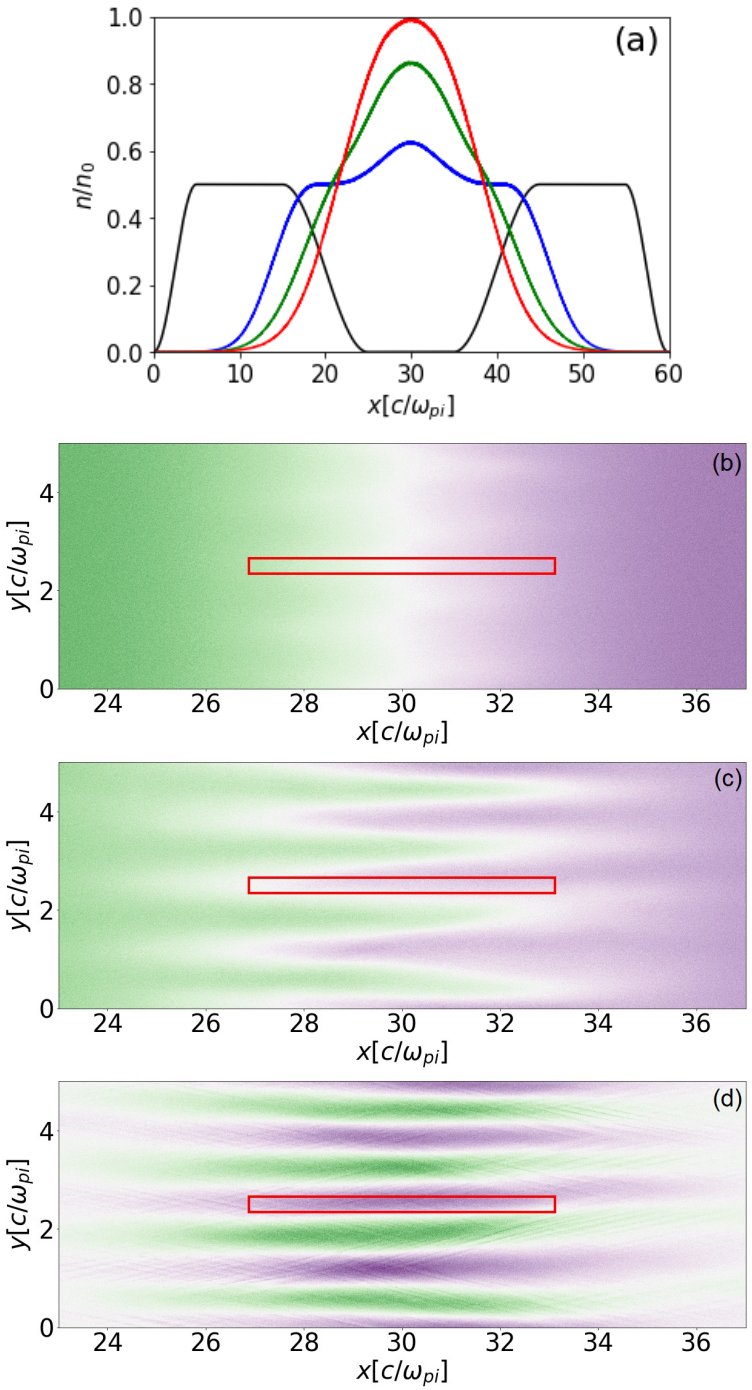

Figure 3.1: Initial ion density at times corresponding to propagation distances of 0 (black), $11c/\omega_{pi}$ (blue), $14c/\omega_{pi}$ (green), and $18c/\omega_{pi}$ (red), (a) and simulated ion current along x for times when the plasma propagation distances is (b) $11c/\omega_{pi}$, (c) $14c/\omega_{pi}$, and (d) $18c/\omega_{pi}$, with green current in the +x direction, and purple in -x. A sample OTS box is shown in red. (From [2])

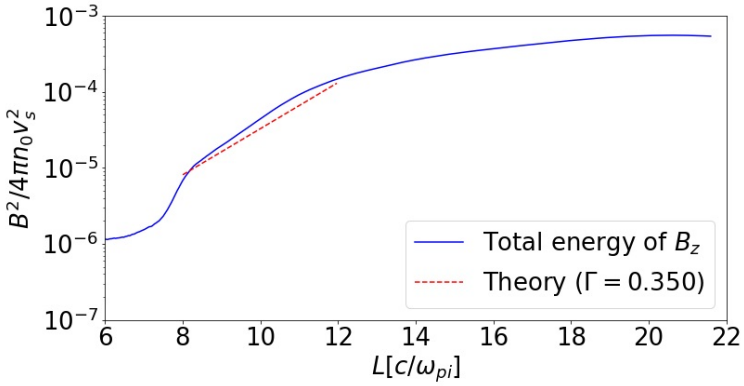

Figure 3.2: Simulated growth of magnetic field energy from the Weibel instability is shown in blue, plotted against the plasma propagation distance (proportionate to the time elapsed). In blue the magnetic energy density within $27c/\omega_{pi} < x < 33c/\omega_{pi}$ is shown. The theoretical growth rate of the magnetic energy is shown in red. (From [2])

in the simulation. Numerical convergence tests indicate that this number of particles is sufficient to provide an accurate description of the evolution of the instability and to produce accurate synthetic OTS spectra which are analyzed below.

The plasma flows are initialized with the simple density profile illustrated in Fig. 3.1 a). The density of each flow ramps up over a length of 10 c/ω_{pi}, remains flat over a further 10 c/ω_{pi}, and finally ramps down over 5 c/ω_{pi}. The initial profile for the species streaming in the $+x$ direction is

$$\frac{n}{n_0} = \begin{cases} 0.25(1-\cos(\pi\frac{x\omega_{pi}}{5c})) & x\omega_{pi}/c \leq 5 \\ 0.5 & 5 < x\omega_{pi}/c \leq 15 \\ 0.25(1+\cos(\pi\frac{x\omega_{pi}/c-15}{10})) & 15 < x\omega_{pi}/c \leq 25 \end{cases} \tag{3.6}$$

The electron and ion species streaming in the $-x$ have a symmetric profile with respect to the center of the simulation box $x = 30c/\omega_{pi}$. The two flows are initially separated by a vacuum region of $10c/\omega_{pi}$ and start interacting at the center of the simulation box, where filamentation develops, as shown in Fig. 3.1 b)-d). The figure illustrates how after a few tens of ion skin depths of interpenetration, current filaments form in the plasmas at the expected wavelength of $\sim c/\omega_{pi}$. After the leading electrons

first stream across the vacuum and the ions begin counter-streaming, the associated magnetic energy grows exponentially with a measured growth rate in good agreement with the theoretical growth rate of (3.2) for the initial parameters of the simulation (Fig. 3.2).

3.2 Validation of OTS Analysis with PIC simulations

In order to validate OTS theory and measurements of the current structure in the plasma, we must also verify that non-equilibrium electrostatic fluctuations do not affect this measurement. The electrostatic ion two-stream instability [78, 84–87] grows faster than the Weibel instability and is observed in PIC simulations. However, this instability saturates at low levels of fluctuations via ion trapping and heating and affects parts of the spectrum of density fluctuations that are not measured by the OTS diagnostic. Figure 3.3 shows the modes produced by the two-stream ion and Weibel instabilities, illustrating how they are well separated in k-space from any density fluctuations measured by Thomson scattering in the k_x direction.

The filamentation of the plasma leads to modulations in the ion current at the ion-inertial length scale. This ion current may simply be viewed as the local difference in the density of the two streams. When the OTS scattering volume is smaller than this length scale the average density of the two streams within the scattering volume cam be different. The density of each ion stream relative to the total density will change based on the location of the Thomson scattering volume in the plasma, as can be seen in Fig. 3.1.

The mean electron velocity will also vary, as electrons are driven in the direction screening the ion current. These changes can be parameterized using the mean electron velocity, v_e, and by n_1/n_i, where $n_i = n_1 + n_2$, with n_1 being the density of ions flowing parallel to $\vec{k}$, and n_2 being the density of ions flowing anti-parallel to $\vec{k}$. Assuming the individual populations are Maxwellian, the ion and electron distribution

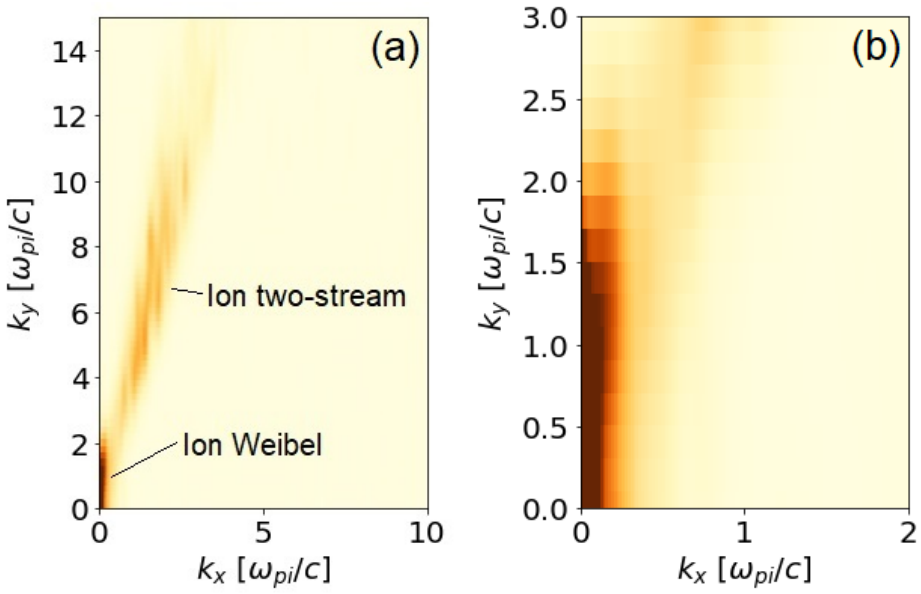

Figure 3.3: Simulated modes in electron density at L=$18c/\omega_{pi}$. In (a) we see that amplitude of modes excited by ion two-stream instability decrease with increasing k, which means that the high-k measurements taken with OTS will not scatter from these modes. OTS samples modes on the order of $k_x \approx k_D = 145\omega_{pi}/c$. (b) shows effects on electron density associated with the ion Weibel instability. (From [2])

functions $f_{i\|}^{fit}(v_x)$ and $f_{e\|}^{fit}(v_x)$ may be written,

$$f_{i\|}^{fit}(v_x) = \frac{1}{v_{Ti}\sqrt{8\pi}}\left(\frac{n_1}{n_i}e^{\frac{-(v_x-v_1)^2}{2v_{Ti}^2}} + \frac{n_2}{n_i}e^{\frac{-(v_x+v_2)^2}{2v_{Ti}^2}}\right) \tag{3.7}$$

$$f_{e\|}^{fit}(v_x) = \frac{1}{v_{Te}\sqrt{2\pi}}e^{\frac{-(v_x-v_e)^2}{2v_{Te}^2}} \tag{3.8}$$

These are parameterized by 6 variables, v_e, n_1/n_i, the ion and electron temperatures T_e and T_i and the flow speeds parallel and anti-parallel to the probed $\vec{k}$, v_1 and v_2.

An example of such a set of distribution functions and the corresponding expected OTS spectrum are displayed in Fig. 3.4, calculated using plasma parameters relevant to our PIC simulations and experimental results [79]. The OTS spectra are plotted as functions of the wavelength of scattered light, $\lambda_s = 2\pi/k_s$, for a probe wavelength $\lambda_0 = 526.5$nm. The one-dimensional distribution functions in Fig. 3.4 are evaluated in terms of phase velocities $v_{ph} = \omega/k$ and plotted as functions of wavelength: $v_{ph} = \omega/k$,

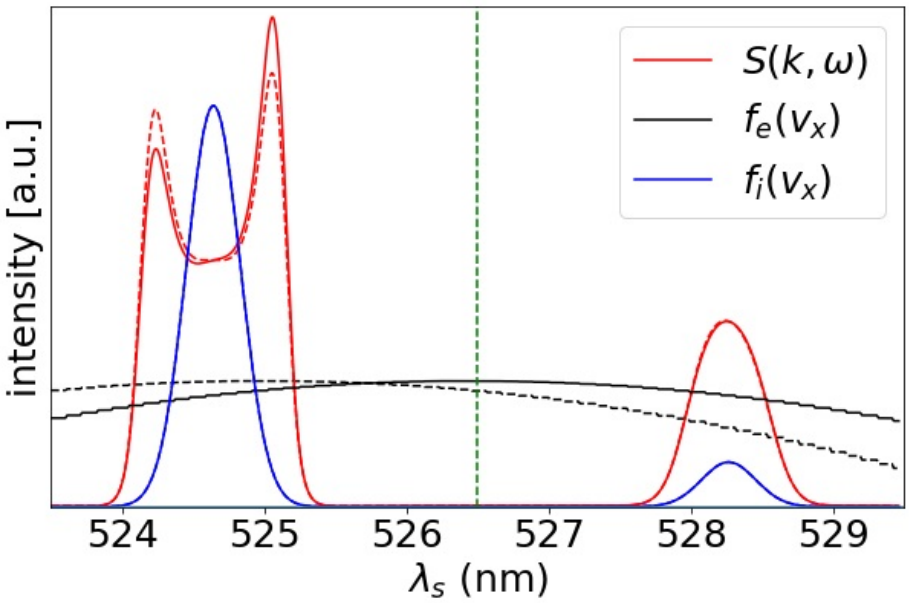

Figure 3.4: Example of IAW OTS spectrum (red) for counter-streaming plasmas with drifting Maxwellian ion distribution $f_i(v_x)$ (blue) with n_1/n_i=0.9. Black curves show electron distribution $f_e(v_x)$ for $v_e = 0$ (solid) and J=0 (dashed). The red curves show the OTS spectra corresponding to both cases, respectively. Spectra are generated with $Z = 4$, $T_e = T_i = 1$ keV, $v_1/c = v_2/c = 0.0033$ and $\lambda_0 = 526.5$ nm (green) (From [2])

$\lambda_s = \lambda_0(1 - v_{ph}/c)$. The typical ion acoustic spectra shown in Fig. 3.4 correspond to two counter-streaming, interpenetrating plasmas: the blue-shifted feature with two distinct ion acoustic peaks for plasma flowing in the $\hat{k}$ direction and the red-shifted feature for plasma flowing in the $-\hat{k}$ direction. The asymmetry between the two features is affected by the relative density of the two streams in the OTS volume, as detailed in section 2.2.1 and Eq. (2.14). In Fig. 3.4, $n_1/n_i = 0.9$ and $n_2/n_i = 0.1$, however, these ratios will depend on the position of the OTS volume with respect to current filaments and therefore assume arbitrary values in the simulations and experiments.

3.2.1 Current features in OTS spectra

Although the ion Weibel instability is electromagnetic and therefore has no direct Thomson Scattering effect, the resulting plasma structures can be measured with OTS. The ion flow density ratio n_1/n_i can be determined based on the relative amplitude of the two features corresponding to oppositely moving flows as seen in figure 3.4. Together with the stream velocities seen in the Doppler shift of the modes, this determines the ion current of the plasma.

For electrons described by a Maxwellian distribution function (3.8), the drift velocity v_e affects the relative amplitudes of the forwards and backward propagating wave within both of the ion streams, as explained in section 2.2.2. In Eq. (2.17), we see the damping of the IAW is proportionate to $(v_e - v_i - \frac{\omega}{k})\frac{\omega}{\omega_{iaw}}$: the difference in speed between the center of the electron distribution function and the phase speed of the IAW. In typical counter-streaming plasma with $v_e < v_i$, this leads to more damping of the outer wave in both the blue-shifted and red-shifted streams, reducing their amplitude and creating asymmetry within each beam's ion acoustic modes.

An electron velocity closer to the velocity of the ion stream will make the ion stream in question more symmetric, as the change in the slope of the electron distribution function between the phase velocities of the red-shifted and blue-shifted modes in the stream will be smaller. This can be seen in the blue-shifted stream in Fig. 3.4.

Together with the ion parameters, this asymmetry feature determines the current per particle along the direction of the scattering vector.

$$\frac{J}{en_e} = \frac{n_1}{n_i}v_1 - \frac{n_2}{n_i}v_2 - v_e \tag{3.9}$$

This current density in the fit distribution functions is then the measured current in the OTS volume of the analysed plasma.

3.2.2 OTS spectra in simulations

To generate an OTS spectrum from a PIC simulation, a small region corresponding to the OTS scattering volume is chosen in the center of the plasma flow interaction, as illustrated in Fig.3.1. This box is extended in the flow direction in order to include more particles in the scattering volume.

An OTS box must be smaller transversely than the current filament width to measure filamentation. The simulated box extends 0.31 c/ω_{pi} in the transverse direction, covering half a filament. Simulated distribution functions $f_{e\|}^{sim}(v_x)$ and $f_{i\|}^{sim}(v_x)$ are constructed by splitting the particles within this OTS volume into velocity bins of $10^{-4}c$ for electrons and $10^{-6}c$ for ions, or 345 bins spanning $2v_{Ti}$. These distribution functions can then be used to calculate synthetic OTS spectra at multiple times throughout the simulation, allowing us to study how the evolution of the plasma influences the scattered light spectrum.

The velocity distribution functions obtained in the simulation are scaled down in velocity by a factor of 10 to correct for the increased simulation velocity, and generate distribution functions comparable to those of the current experiments [83]. To guarantee consistency with the shape of the initial distribution, we replace $f_{e\|}^{fit}(v_x)$ by a Jüttner distribution. We note, however, that in the velocity range of interest for our analysis, near the IAW modes, the Jüttner and Maxwell distributions are equivalent and would yield similar results.

The derivatives of the distribution functions obtained in the simulations are then used to calculate the susceptibility functions χ (2.3). For ions, this derivative is computed numerically, but for $f_{e\|}^{sim}(v_x)$ the derivative around IAW phase velocities is small compared to fluctuation in the distribution function due to noise associated with the limited number of particles present in PIC simulations. To avoid numerical errors in this calculation, the derivative is computed based on a Maxwellian fit to the distribution function.

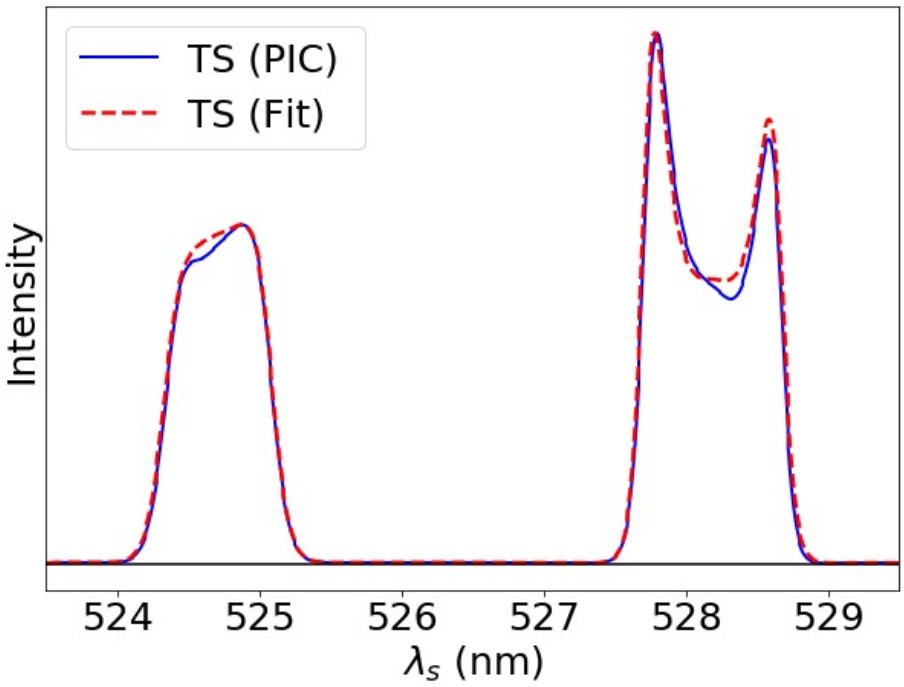

Figure 3.5: Synthetic OTS spectra from PIC at propagation distance L=19c/ω_{pi} with fit OTS spectrum. Mesured conditions are 0.94 keV Be ion, 1.51 kev electrons streaming at 0.0032c with n_1/n_i=0.254 and J=-0.000418 $en_0c\hat{x}$. (From [2])

Having created an OTS spectrum from the simulations, the shape of this spectrum can then be fitted with an OTS spectrum generated using Maxwellian distribution functions of Eqs. (3.7) and (3.8) (cf. Fig. 3.5). We consider an OTS laser probe wavelength of 526.5 nm. The parameters used to fit the spectrum determine the measured current in the direction of the k-vector of the fluctuations based on Eq. (3.9).

The magnetic field corresponding to the current filaments can be estimated from Ampère's law, $\nabla \times B = (4\pi/c)J$, as $B_z \simeq (4\pi/c)J/\Delta_y$, where Δ_y is the size of the OTS volume in the y direction. Note that we have neglected the contribution of the displacement current, which is indeed observed to be negligible in the PIC simulations.

Figure 3.6 shows a comparison of the currents and magnetic field obtained directly from the particle distributions in a PIC simulation with those determined by fitting

the synthetic OTS spectrum generated from the PIC distribution functions with the OTS dynamical form factor, Eq. (2.2), calculated assuming Maxwellian distribution functions, Eqs. (3.7) and (3.8).

The dots in Fig. 3.6 are total and ion currents obtained from the Maxwellian fits to synthetic spectra, as is also done for experimental spectra. The solid lines indicate the parameters as determined through direct integration of the PIC distribution functions. For these calculations, the numerical distribution functions were summed over the OTS scattering volume indicated in Fig. 3.1. The evolution of the plasma current obtained from OTS is in good agreement with the simulation results. The change in the magnetic field is also correctly captured. Our results thus indicate the ability of this novel technique to measure the local evolution of the currents and magnetic field in HED plasmas.

The errors in the estimate of the total current with the OTS technique observed in Fig. 3.6 are primarily due to the development of small non-Maxwellian tails in the ion distribution functions. This is illustrated in Fig. 3.7. When the phase velocities of the ion acoustic resonances in the OTS spectra are well above the thermal ion velocity and the current present in the plasma is small, deviations in the OTS spectrum caused by tails in the ion distribution will affect the peak asymmetry within each flow. This will impact the accuracy of the electron current calculation because v_e is used to control this asymmetry in the fits of the OTS spectra.

The impact of the ion tails on the ion acoustic modes is proportional to their relative phase density at the phase velocity of ion acoustic modes, v_ϕ. For highly supersonic flows, v_ϕ is [88]

$$v_{\phi r} = u_r \pm c_s \sqrt{\frac{n_r}{n_i} \frac{1}{1 + k^2/k_D^2}}, \tag{3.10}$$

where $r = 1, 2$ is the index corresponding to each of the flows, u_j is the fluid velocity of each flow, n_j is the corresponding ion density, and $c_s = \sqrt{ZT_e/m_i}$ is the sound speed in the plasma.

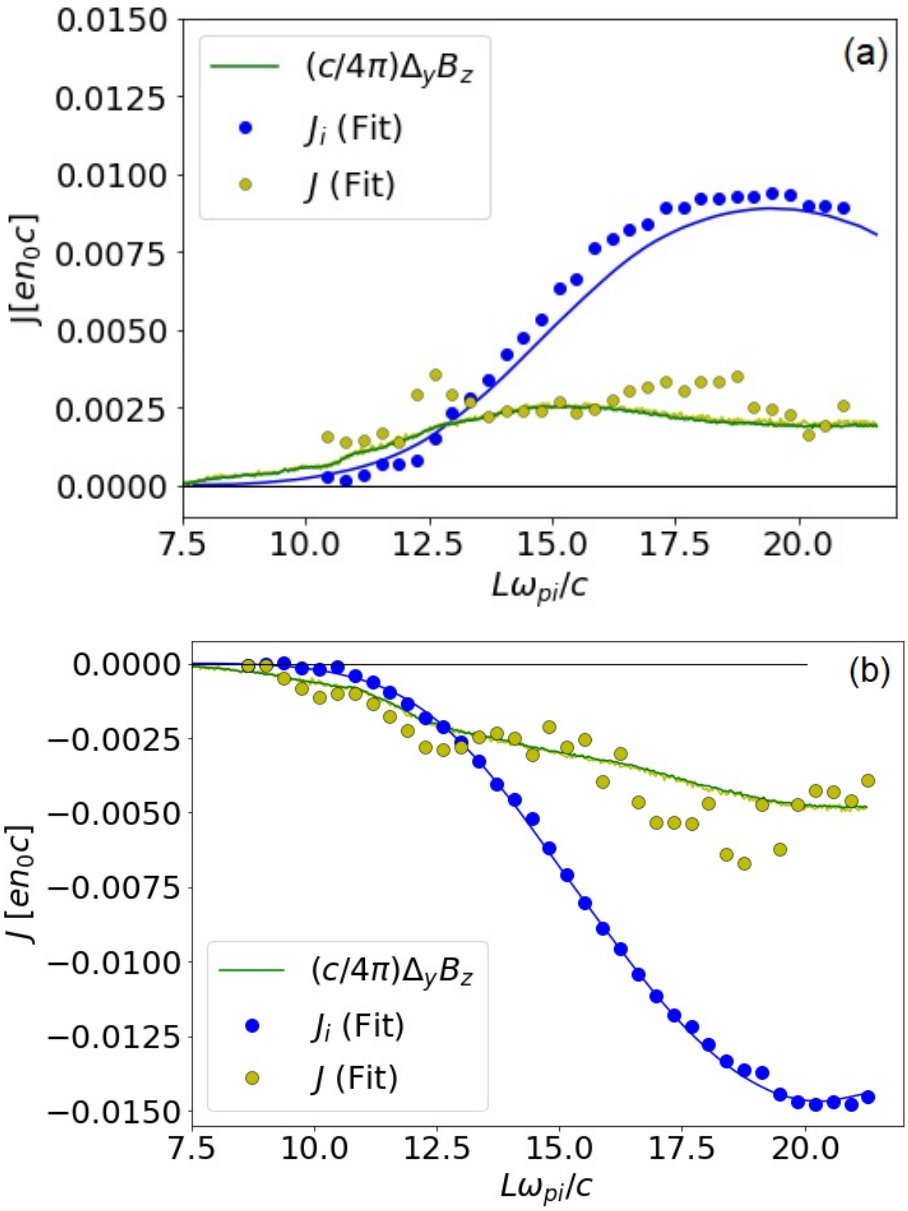

Figure 3.6: Comparison of the currents and magnetic field obtained from fits of synthetic OTS spectra (points) and directly inferred in the PIC simulations (solid curve) at two different locations in the plasma centered on (a) y=3.28 c/ω_{pi} and (b) y=3.88 c/ω_{pi}. (From [2])

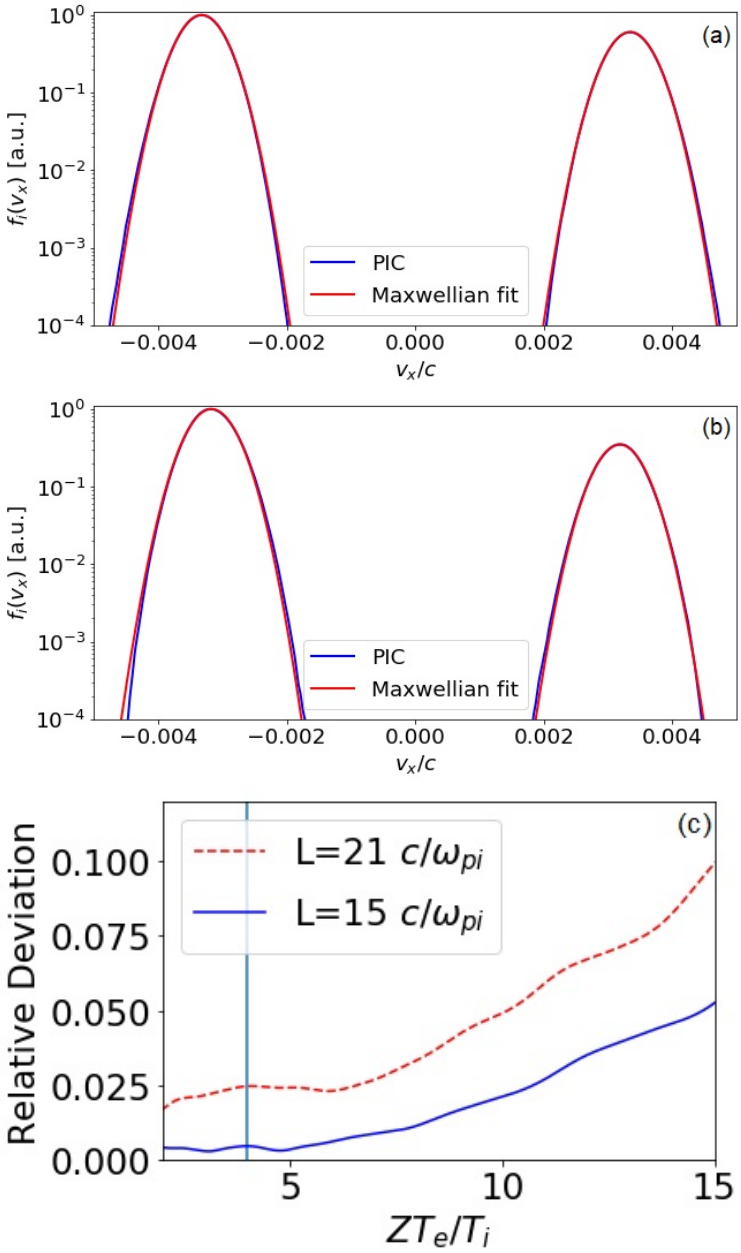

Figure 3.7: Deviation of the ion distribution function in the flow direction from a Maxwellian, at early (a) and late (b) times in the simulation. The relative deviation present in the spectrum at the phase velocity of the IAW is also shown (c). At early times, faster ions arrive earlier, contributing to a tail towards higher velocity, while at later times, the streams begin to slow, creating tails towards lower velocity. (From [2])

In the PIC simulation, we observe that in the time interval $L = 15c/\omega_{pi} - 20c/\omega_{pi}$, centered at $y = 248c/\omega_{pe}$, the ion distribution function develops small deviations from Maxwellian at v_ϕ, which lead to an average asymmetry of 2.4% between the amplitudes of the ion acoustic peaks of each flow. When averaged over both flows, however, the relative asymmetry was only 0.8%, as both flows tended to develop similar tails, either towards higher or lower velocities (Fig. 3.7). This asymmetry corresponds to an error in the electron current of $0.0018en_0c$, which dominates the error observed in Fig. 3.6.

It is important to note that for the typical experimental conditions that we have considered the inter-flow collisionality is very low (meaning that the mean free path for collisions between the two flows is large), but the intra-flow collision frequency (collisions within each flow) can be large[29], on the order of 50 ns^{-1}. This means that Coulomb collisions will act to keep the distribution of each flow approximately Maxwellian and help prevent the development of ion tails described here. The present PIC simulations are collisionless and thus do not take this effect into account. Therefore, the errors observed in the total current estimate are likely overestimated by the ion tails obtained in the collisionless PIC ion distribution simulations.

3.2.3 Simulation growth rate analysis

From a time-resolved measurement of the current in a Weibel unstable plasma, it is possible to measure the growth rate of the instability. As the OTS measurement is local, it is important to evaluate the role that spatial fluctuations in the current will have on the growth rate measurement. In order to investigate the accuracy of the growth rate measurements from a single OTS measurement, we have measured the growth rate from different locations to determine its consistency. The total current and the ion current at each location were fit with exponential growth in time to determine the rate. These measurements were then compared with the growth rate obtained over the entire simulation box, which was shown in Fig. 3.2 to be in good

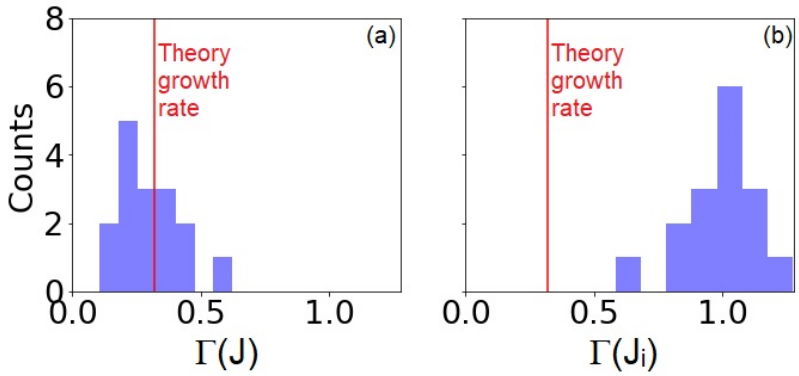

Figure 3.8: Growth rates from total current (a) and ion current (b) seen from a half-ion skin depth box in different locations are $\Gamma = 0.31 \pm 0.13$ for the total current and $\Gamma = 0.98 \pm 0.15$ for the ion current, where as the expected rate is $\Gamma = 0.32$. (From [2])

agreement with theory (3.2). This comparison is shown in Fig. 3.8. The measured growth rate of $\Gamma = 0.31 \pm 0.13$ compares well with the growth of the field averaged over the x direction of the OTS volume of $\Gamma = 0.32$.

As ion currents can be measured more reliably than electron currents in the early phase of the instability (Fig. 3.6), it would be more attainable experimentally to measure the growth of the ion current with high precision. To evaluate the uses of a measured ion current growth, it is useful to evaluate the relative growth between the ion and electron currents. We observe that the growth rate of the ion current is much larger than that of the total current (Fig. 3.8). This is associated with the temporal evolution of the electron current, which is non-monotonic and needs to be considered.

We can see in Fig. 3.9 that the electron current grows first and reverses direction during the growth of the ion current. The initial growth of the electron current is associated with a fast phase of electron Weibel instability. Before the bulk of the ions counter-stream, the electrons are largely collisionless over a very small distance between the plasmas. The fast electrons from each of the flows counter-stream in the interaction region. This leads to the generation of an electron filamentary current and associated magnetic field.

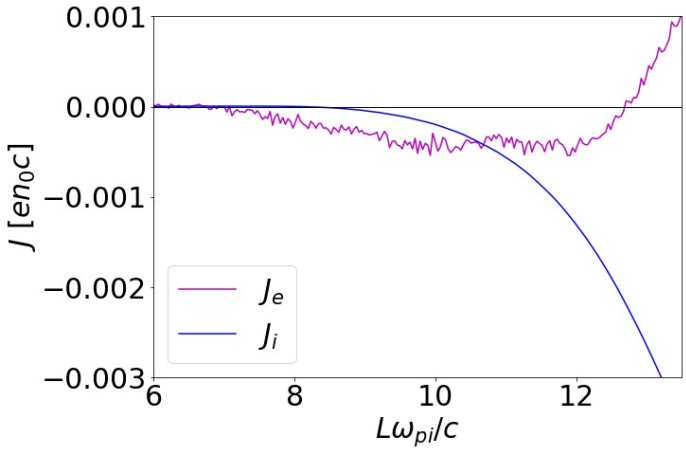

Figure 3.9: Growth of ion and electron J_x in the OTS volume. Electrons start forming current filaments around $L = 7c/\omega_{pi}$. The ions start responding and become unstable around $L = 8c/\omega_{pi}$. As the ion current grows the electrons transition into screening the ion current. During this transition, the ion current grows much faster than the total current. (From [2])

As the ions start to respond and become unstable, this magnetic field can seed the growth of the ion Weibel instability, which will lead to an ion current with the same sign as the initial electron current. However, the further growth of the magnetic field will give rise to an inductive electric field that will try to balance the ion current. This will ultimately lead to the reversal of the electron current in the plasma during the linear phase of the ion Weibel instability. These results indicate the richness of the microscopic dynamics associated with this instability and highlight the importance of measuring both the ion and electron currents to accurately model the evolution of the instability.

3.3 Magnetic Field Measurement from Experimental Data

The technique developed in the previous sections was applied to experimental data obtained at the OMEGA laser facility [3] (sec. 1.4). Two parallel beryllium foil targets separated by 5mm were shot with a 1 ns 3.5 kJ drive laser, as shown in figure

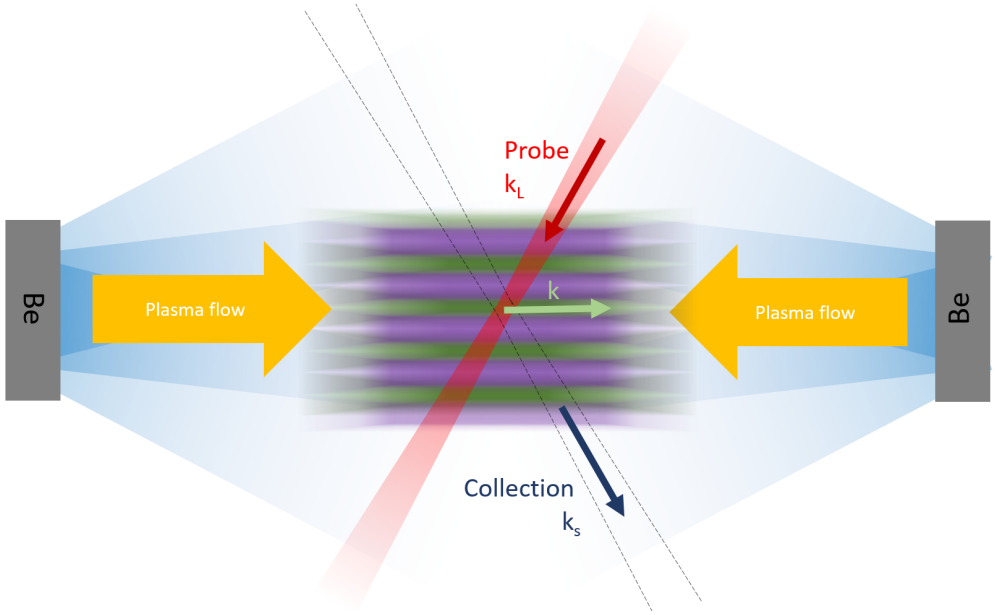

Figure 3.10: Target configuration of counter-streaming plasma experiment. Be foils are illuminated with the 3ω drive, shown in blue. Plasma counter-streams between the two targets, forming current filaments (green and purple). The 2ω OTS probe (red) and collection (black) are arranged to measure a wave vector $\vec{k}$ parallel to the plasma flow.

3.10. In the center of the counter-streaming ablating plasma between the two foils, a 526.5 nm f/6.7 probe beam is focused and collected at 60.3° by an f/10 reflective telescope, resulting in a scattering $\vec{k}$ parallel to the flow.

Experimental ion acoustic spectra [3] (Fig. 3.11) were fitted with the dynamic form factor $S(\vec{k},\omega)$, (2.2), generated assuming Maxwellian electron and ion distributions to determine the average current per particle in the same way as it is done with synthetic spectra in section 3.2. A representative OTS spectrum is shown in Fig. 3.12 at 4.3 ns after the start of the laser drive. The density of the plasma is found by fitting the electron OTS feature, which also provides the electron temperature (cf. Fig. 3.12 a). This temperature is then used when fitting the ion spectra. Together these determine ion and electron temperature, density, and flow velocity as well as the ion and total current.

Because the experimental OTS volume has different widths normal to the direction

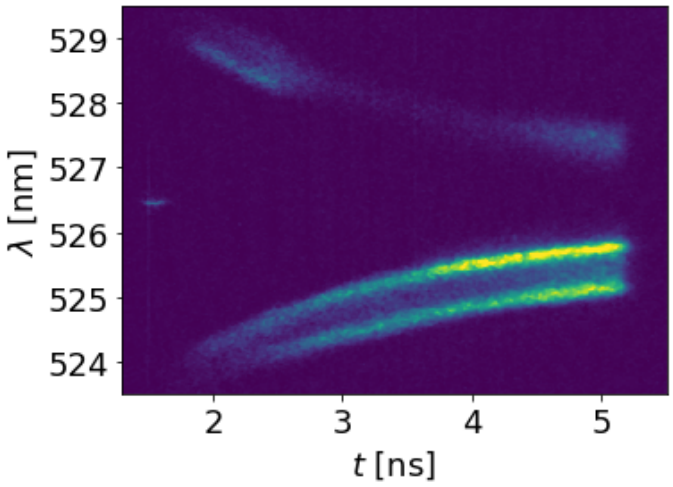

Figure 3.11: IAW spectrum from counter-streaming plasma, with an OTS probe wavelength of 526.5 nm. The blue-shifted feature can be seen to be greatly enhanced above the red-shifted feature for the majority of the shot. (From [2])

of the current, the relation between the field and the current observed in the OTS window depends on the width of the filaments for small filament sizes. We consider a simple current sheet sinusoidal model for the magnetic field with wavelength $2d_f$ given by

$$B_z(y) = B_0 \sin\left(\frac{\pi y}{d_f}\right), \; J_x(y) = \frac{B_0 c}{4 d_f} \cos\left(\frac{\pi y}{d_f}\right). \tag{3.11}$$

We make a conservative estimate of the magnetic field strength by assuming that the OTS volume is centered in y in the middle of a current filament. The current is then numerically integrated over the volume of the OTS volume, which determines the average current measured in the region, $\langle J \rangle_{TS}(d_f) = \int_V d^3 r J_x(y)/V$, where V is the OTS volume as seen in Fig. 2.4. The average value of the current in the whole filament, $\langle J \rangle_f = \int_{-d_f/2}^{d_f/2} dy J_x(y)/d_f$, is also computed. The quantity $J \langle J \rangle_f / \langle J \rangle_{TS}(d_f)$ represents the ratio by which a measured current in an experimental OTS volume must be scaled to accurately measure the average current in a filament.

The magnetic fields of the ion Weibel instability are primarily driven by current. In this case, Ampere's law can be simplified to

$$\nabla \times \vec{B} = 4\pi \vec{J}/c \tag{3.12}$$

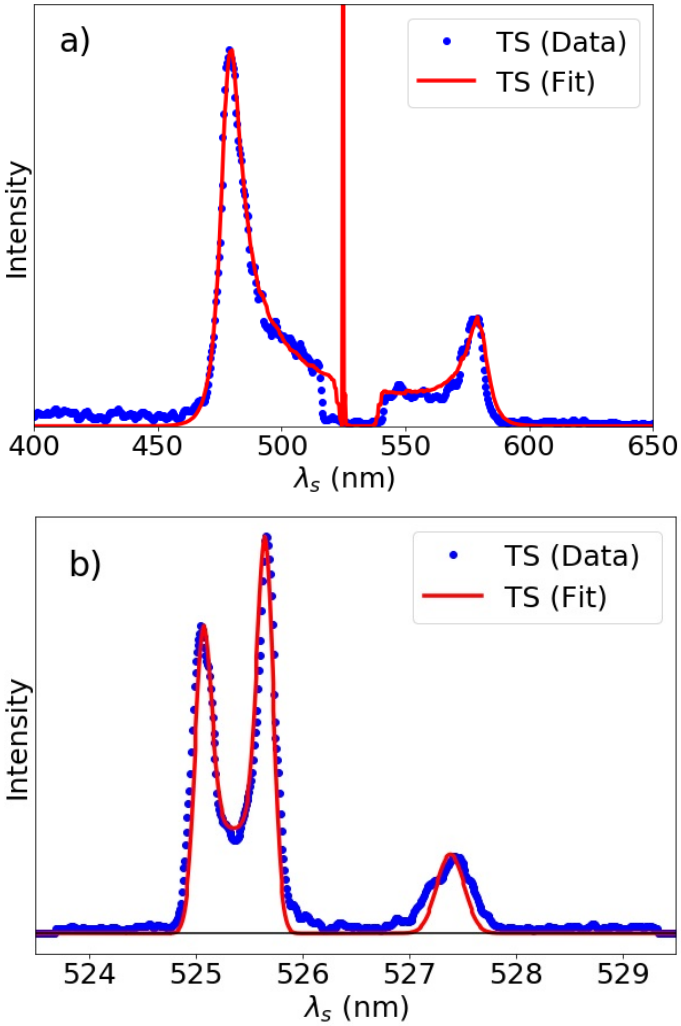

Figure 3.12: (a) Electron/EPW and (b) Ion/IAW OTS spectra (dotted blue) from counter-propagating Be plasmas are shown at 4.3 ns from the start of the drive laser. The corresponding fits of the OTS spectra (solid red) lead to the measurement of $n_e = 1.95 \pm 0.2e19cm^{-3}$, $T_e = 0.53 \pm 0.08keV$, $T_i = 0.26 \pm 0.05keV$, $v_1 = 0.0020 \pm 0.0001c$, $v_2 = 0.0017 \pm 0.0001c$, $n_1/n_i = 0.98 \pm 0.01$, and $v_e = 0.0014 \pm 0.0003c$. (From [2])

In a 2D simulation of the Weibel instability with $\hat{z}$ out of the simulated plane, we can further simplify this to $\frac{dB_z}{dy} = 4\pi\frac{J_x}{c}$. The magnetic field surrounding a symmetric current sheet with total current linear density $I/L_z = \int \vec{J}dy$ would then be $B = \pm\frac{2\pi I}{L_z c}$

In a 3D current, however, the field corresponding to the current (3.12) is spit over the two perpendicular directions. In a cylinder of uniform current density J_x, the field in a given direction changes at a lower rate than a 2D current sheet.

At any radius r, the current will create and an azimuthal magnetic field of strength $|B| = \frac{2\pi Jr}{c}$. If we select an arbitrary vector y, z from the center (defined as $B = 0$), we can observe that $B_z = \frac{2\pi Jy}{c}$ and $B_y = -\frac{2\pi Jz}{c}$. The two terms in (3.12) are equivalent: $\frac{dB_z}{dy} = -\frac{dB_y}{dz}$. This means we can divide Amperes law 3.12 equally for both directions:

$$\frac{dB_z}{dy} = 2\pi\frac{J_x}{c} \tag{3.13}$$

For this reason, a factor of 0.5 is applied to the magnetic field from this current sheet analysis to approximate the field strength in a more complex 3D filament structure.

When calculating the amplitude of the magnetic field, this simplified version of Ampere's law is integrated over the radius of a filament, $d_f/2$. The measured OTS current is used along with the scaling factor $J\left\langle J\right\rangle_f / \left\langle J\right\rangle_{TS}(d_f)$. The measured magnetic field amplitude B_0 from a measured current J is then

$$B_0(d_f) = \frac{2\pi}{c}\frac{d_f}{2}J\frac{\left\langle J\right\rangle_f}{\left\langle J\right\rangle_{TS}(d_f)} \tag{3.14}$$

Between 3.5 and 4.5 ns from the start of the shot, we observe in OTS spectra that the current density is approximately constant and has a value of $(6.0\pm0.6)\times10^{11}A/m^2$ (Fig. 3.13). A sample measurement is shown in Fig. 3.12. For this current density in the OTS window with an unknown filament width, we estimate a minimum magnetic field value at saturation of 0.268 MG (Fig. 3.14), from (3.14).

The capability to measure the current locally using the OTS technique presented here provides a powerful way of estimating the magnetic field directly from exper-

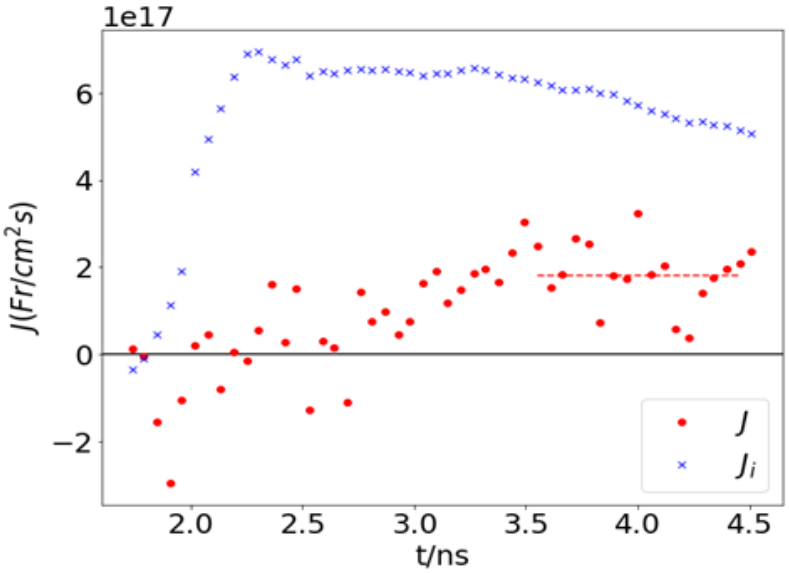

Figure 3.13: Current measured by OTS over the duration of the counter-streaming plasma (IAW seen in figure 3.11). (From [2])

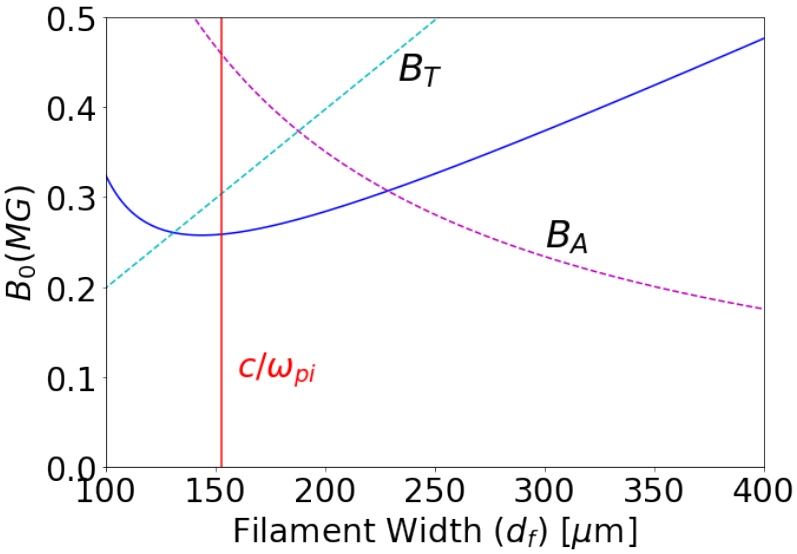

Figure 3.14: Magnetic field amplitude (blue) inferred from the experiment as a function of filament size, based on current density in the OTS region (Fig. 2.4) for cylindrical filaments scaled by the 2D field model (Eq. 3.14). The theoretical Alfvén limit B_A (purple) and magnetic trapping limit B_T (light blue) are also shown. (From [2])

iments without the need to incorporate additional information from simulations to deconvolve path-integrated measurements. Based on these magnetic field measurements, we can for instance benchmark saturation models for the Weibel instability. Different mechanisms have been discussed in the literature, with the most common being the Alfvén limit [23], where the ion gyroradius equals the filament wavelength, $B_A \sim (m_i v_i)/(2Zed_f)$, and magnetic trapping [22], where the bouncing frequency of the ions inside the filaments reaches the growth rate of the Weibel instability, $B_T \sim \frac{m_i v_i}{Ze} \frac{\omega_{pi}^2}{c^2} \frac{d_f}{\pi}$. For the parameters of our experiments with $v_i \approx 600 km/s$, both of these mechanisms are fairly consistent with the measured field for filament widths d_f between 130 and 230 μm (Fig. 3.14).

The measured lower bound of the magnetic field corresponds to a ratio of magnetic energy density to kinetic energy density $\sigma = B_{\text{sat}}^2/(4\pi n_i m_i v_i^2) = 0.011$, which is consistent with previous numerical studies [21] and values inferred from proton radiography and corresponding simulations [77].

Using a different experimental configuration, filament width can be measured simultaneously with the current [3], yielding a specific field measurement. This is accomplished by tilting the foils (Fig. 3.15), causing the counter-streaming plasma to drift in the transverse direction. Arranged in this way, the filaments travel past the OTS volume, leading to many filaments being measured over the course of a shot, as seen in figure 3.16.

The flow speed in the transverse direction can be assumed to be 0.47× the flow speed measured by OTS, since the targets are tilted at 25° out of the counter-streaming direction. This velocity can be integrated over time to determine the y distance the plasma has traveled, revealing the filament width (Fig. 3.17). The magnetic field can be calculated along the path of the OTS volume by integrating the current, assuming a cylindrical current filament geometry (3.13). This results in fields reaching $30T$, also consistent with a magnetic energy density to kinetic energy density ratio $\sigma = B_{\text{sat}}^2/(4\pi n_i m_i v_i^2) \approx 0.01$.

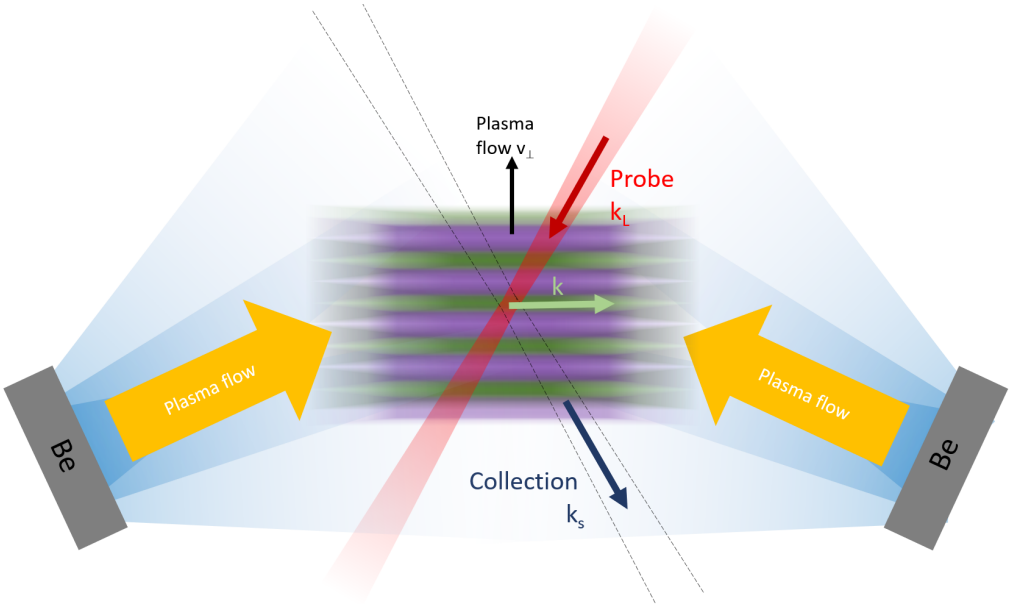

Figure 3.15: Target configuration of tilted counter-streaming plasma experiment [3], with targets tilted 25° in the transverse direction. Be foils are illuminated with the 3ω drive, shown in blue. Plasma counter-streams between the two targets, forming current filaments (green and purple). The OTS probe (red) and collection (black) are arranged to measure a wave vector $\vec{k}$ parallel to the current filaments, while the plasma passes the OTS volume transversely due to the flow induced from the tilt of the targets.

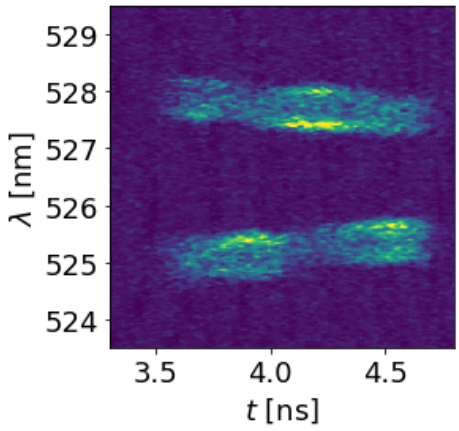

Figure 3.16: IAW spectrum from counter-streaming plasma with tilted targets, causing the OTS volume to pass through multiple filaments over the course of the shot. (From [3])

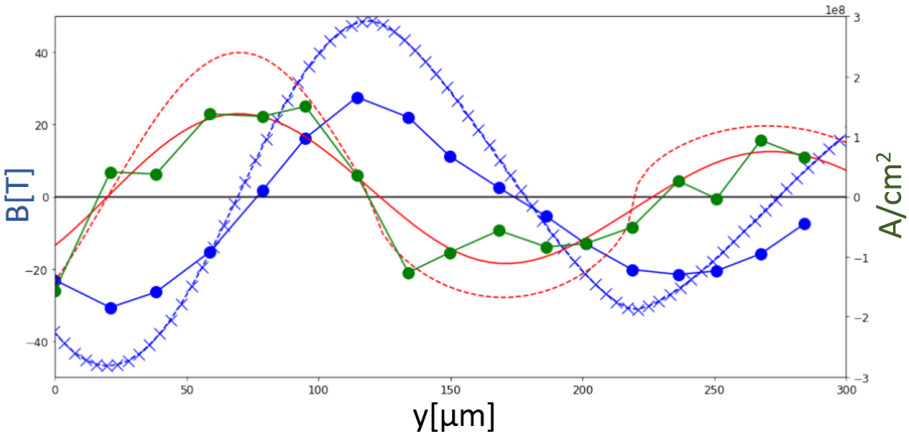

Figure 3.17: Measured parameters in the y direction from OTS data from tilted targets (Fig. 3.13). The measured current is shown in green, with a corresponding field amplitude in blue dots. The red dotted line shows a possible current profile which, when convoluted with the OTS volume shape resulting in the solid red line, matches the measured current fairly well. This current profile produces the field seen in the blue crosses, exceeding $40T$.

Using the profile of current measurements in y, the field measurement can be somewhat improved by noting that the OTS volume will spread out the effects of current on the OTS spectrum in space, which will roughly have the effect of spreading out the measured current. Finding a current density $J(y)$ that convolutes with the OTS volume to approximately match the measured current, we find the peak magnetic field can exceed $40T$, as seen in Fig. 3.17.

3.4 Shock signatures in OTS data

When Weibel-unstable plasma counter-streams over a sufficient interpenetration distance, the magnetic filaments can grow, merging with nearby filaments to increase in size [89]. This can lead to the filaments themselves becoming unstable [72], slowing the counter-streaming plasma without collisions, and leading to the formation of a shock [21, 62]. These shocks are important processes in astrophysics [19, 20] due to their capability to accelerate particles [4].

At NIF, counter-streaming plasma targets were shot in order to generate colli-

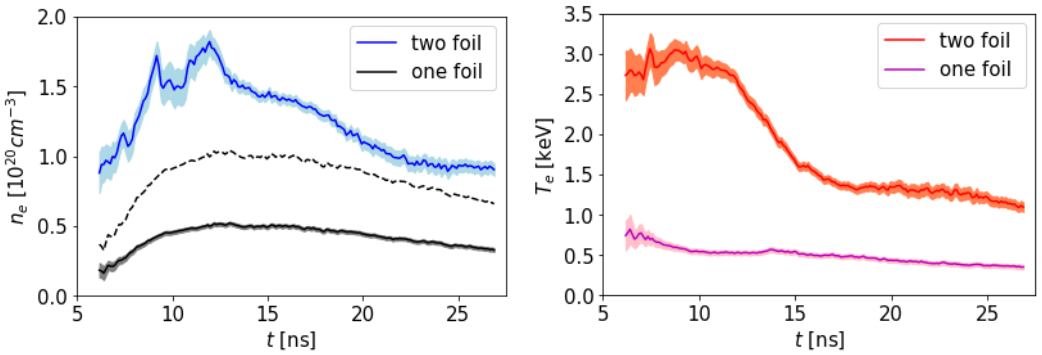

Figure 3.18: Density (left) and temperature (right) as measured from the EPW spectra in the CD2 shots. Density of counter-streaming, non-interacting plasma is also shown with a dotted line at 2× the single stream n_e. Excess density above this value in the two-flow case indicates shock formation.

sionless shocks [4]. These targets were arranged similarly to figure 3.10, but with a separation distance of $25mm$ between foils composed of CH2 or CD2 plastic. Foils were irradiated with $0.455MJ$ of 3ω light to drive the expanding plasmas towards each other.

3.4.1 Shock formation

In a counter-streaming shot conducted at NIF (sec. 1.4) with CD2 foils, the EPW spectra were captured in double-foil and single-foil shots. This allows for a comparison of density between a single flow of plasma and counter-streaming plasma (Fig 3.18). The counter-streaming plasma exceeds 4× the single flow density in the first few ns of the shots, indicating that the plasma compresses.

In the hypothetical plasma conditions of two non-interacting counter-streaming flows, at $8ns$ the plasma would have an ion-ion collision mean free path of $\approx 80cm$. In the real counter-streaming plasma experiment, the plasma is already highly compressed at this time. This compression can only come from collisionless shock formation due to the ion Weibel current filaments [4].

Significant electron heating is also seen in the counter-streaming case (Fig 3.18) corresponding to the time of shock formation. X-ray self-emission from this heated

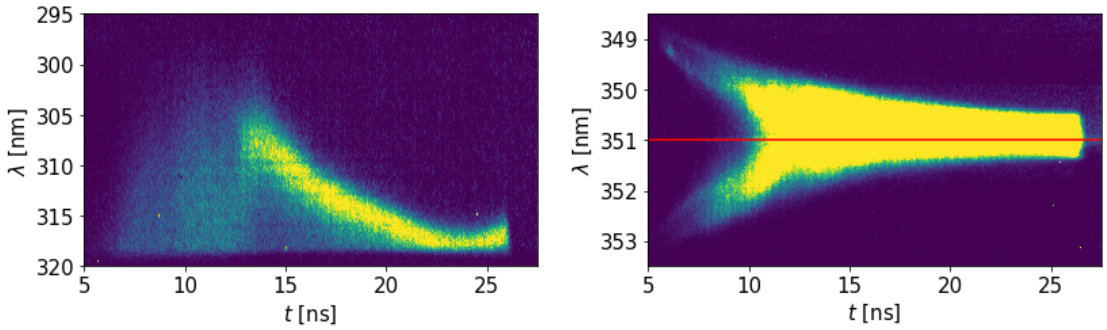

Figure 3.19: EPW (left) and IAW (right) spectra from the CH2 counter-streaming shot. The probe wavelength is shown in red on the IAW spectrum.

region indicates that the shock extended $\approx 5mm$. This scale determines the maximum electron energy that the shock can contain to be $\approx 500keV$, consistent with energies observed in the experiment [4].

3.4.2 Ion Heating

In a counter-streaming shot conducted with CH2 foils, the IAW spectra were captured along with the EPW spectra. The background from the EPW spectra affected both images and was subtracted as shown in section 2.1.2, with a black-body self-emission profile used to estimate transmission. The cleaned EPW and IAW spectra are shown in figure 3.19.

The IAW spectrum allows for the measurement of the ion temperature, as well as flow velocity. As ions can be scattered by turbulent magnetic fields in the plasma, they are strongly heated around shock formation, when much of the kinetic energy in the flow is converted to thermal energy in the ions (Fig. 3.20). This quickly damps the IAW spectrum for all but the first few ns of the shot, which is also moderately damped from the beginning of the shot by the presence of the lower mass hydrogen ions. With the damped IAW spectrum it is not possible to measure current as was done in section 3.3. The flow velocities of the plasma and the temperature of the carbon still appear in the phase velocities of the damped waves.

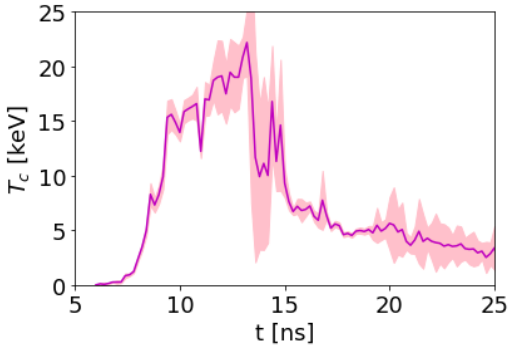

Figure 3.20: Carbon temperatures measured from the CH2 shot IAW spectrum.

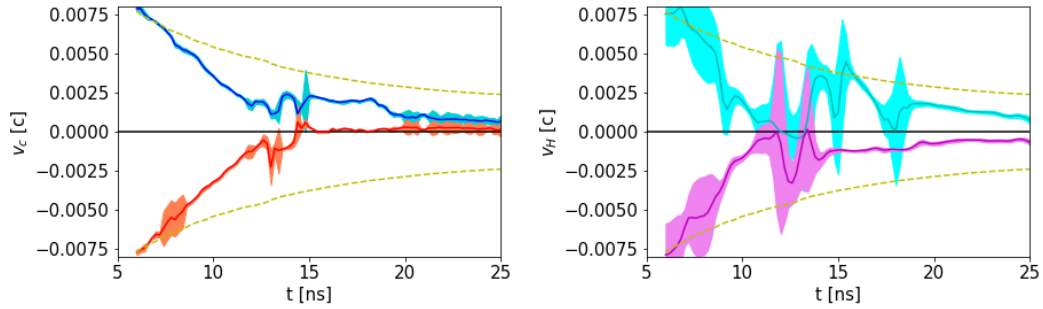

Figure 3.21: Carbon (left) and Hydrogen (right) blue-shifted stream and red-shifted stream flow velocities, measured with the IAW spectrum (Fig. 3.19).

The release of kinetic energy by the flow can be seen in the deviation of the flow velocity from self-similar expansion (1.75). Figure 3.21 shows the self-similar velocity $v_{ss} = L/t + c_s$ of plasma expansion in yellow, which is consistent with the initial speeds observed in the plasma around $6ns$. The flow velocity of the carbon ions slows faster than the self-similar solution as the ions heat (Fig. 3.20).

Hydrogen ions have a smaller contribution to the IAW spectrum than carbon (section 2.4.2) making their properties more difficult to determine among the stronger signal from the carbon ions. However, the flows of hydrogen ions can be seen to slow down earlier than the carbon ions (Fig 3.21) as their higher q/m ratio makes them more susceptible to the forming magnetic shock.

The measured density in the CH2 shot can inform us of other dynamics in the plasma as well. The shot initially has substantially lower densities (Fig. 3.22) than

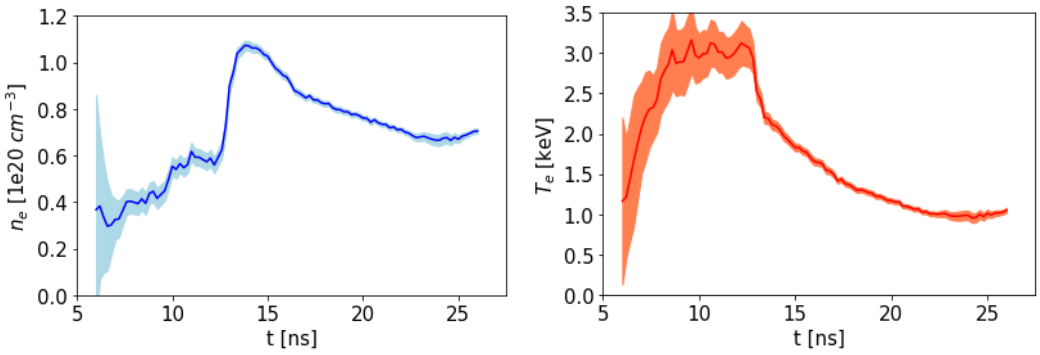

Figure 3.22: Density (left) and temperature (right) as measured from the EPW spectra in the CH2 counter-streaming shot.

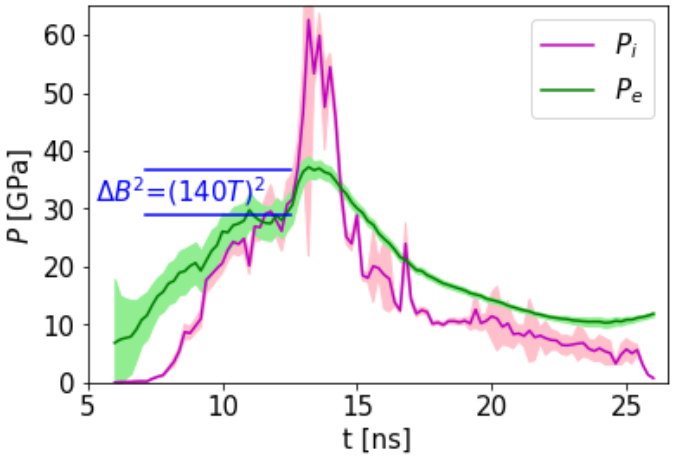

Figure 3.23: Electron (green) and ion (pink) thermal pressure in the CH2 counter-streaming shot. The rapid change in electron pressure at $\approx 13ns$ is equivalent to the magnetic pressure of a $140T$ field.

the CD2 shot (Fig. 3.18) even after electron heating indicates the shock has formed.

Later in the shot at 12.8 ns, we see the density rapidly increase, almost doubling over the course of 1 ns. At the same time, the electron temperature drops much more rapidly than at any time in the CD2 shot.

The thermal pressure of electrons increases sharply as the density increases, despite the falling temperature. The rapid increase in thermal electron pressure $P_e = n_e T_e$ is equivalent to the magnetic pressure $P_B = \frac{B^2}{2\mu_0}$ with $B = 140T$ (Fig. 3.23). This magnetic pressure is consistent with collisionless shock simulations [4].

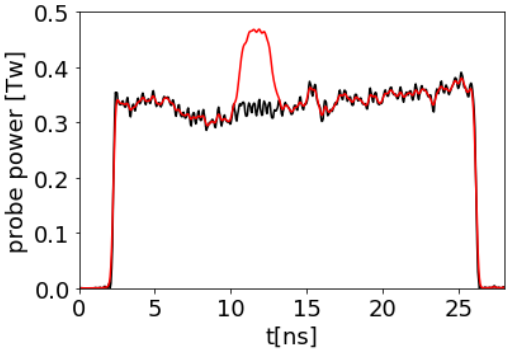

Figure 3.24: Measured probe power (black) and probe power used for IAW fit (red)

These observations are consistent with the OTS volume being traversed by large turbulent structures. A high field region of the turbulent shocked plasma could occupy OTS volume initially, with $B \approx 140T$ balancing the total pressure with the surrounding plasma despite the lower density in the observed region. Turbulent ion dynamics could expand the high-density region, pushing into the OTS volume and causing the rapid increase in density. If this is the case, we see a significantly higher temperature electron population in the high-field region, as the electron temperature rapidly drops when the higher density plasma arrives (Fig. 3.22).

The amplitude of the scattered light observed can indicate the presence of various instabilities. This can be seen when an enhancement of the scattered power appears, despite the power of the OTS probe beam remaining constant (2.1). We can compare the measured power of the probe beam to the change in power needed to match the observed spectra, as seen in figure 3.24. The EPW spectrum is proportional to the input probe energy, but the IAW spectrum significantly increases in power for $\approx 2ns$, ending at 12.8 ns at the same time as the density increase. This may indicate some ion acoustic instability in the highly magnetized region.

3.5 Magnetic Re-Connection

When counter-streaming collisionless plasma is strongly magnetized, counter-streaming can be prevented at large scales by magnetic pressure and subsequent magnetic interactions. If fields of the two colliding plasmas are anti-parallel, this can lead to another kind of current structure, formed by magnetic re-connection. Anti-parallel magnetic fields annihilate and reconnect (Fig. 3.25), releasing energy [25, 26]. This process results in a current sheet separating the two anti-parallel fields, driven by a global $\vec{E}$ field, balanced to $E \approx 0$ outside of the re-connection layer by $\vec{v} \times \vec{B}$ drift.

Reconnection is essential for understanding space plasmas [26]. The converging magnetized plasmas and released energy also contain the capability to accelerate charged particles, making re-connection in astrophysical plasmas a candidate for cosmic rays seen on earth [90, 91].

Models of magnetic re-connections have changed from static arrangements with uniform current sheets to super-alfvenic flows and transient unstable cycles of current sheet formation and plasmoid instability [27, 92]. For these reasons, the structure, formation, and time dependence of the current sheet involved in a reconnecting plasma are necessary to confirm the dynamic nature of re-connection processes.

At the MAGPIE facility, [38] (section 1.4) re-connection experiments were run with a pulsed power plasma, which applies $1MA$ of current over $\approx 0.5\mu s$ [5]. This creates a long-lasting re-connection layer (Fig. 3.25).

Measurements of the IAW spectrum were taken at fourteen locations along the probe. These spectra have resolvable peaks in the center of the plasma, (Fig. 3.26) but the IAW is more heavily damped farther from the current sheet (2.14) due to lower electron temperatures (Fig. 3.27). The peaks in the IAW spectrum allow for the measurement of the current in the $\hat{z}$ direction, via the asymmetric damping of the IAW peaks (section 2.2.2). Ion and electron flow velocities v_i and v_e are measured, with ions in the current sheet flowing in the $+\hat{z}$ direction, and electrons in the $\hat{z}$

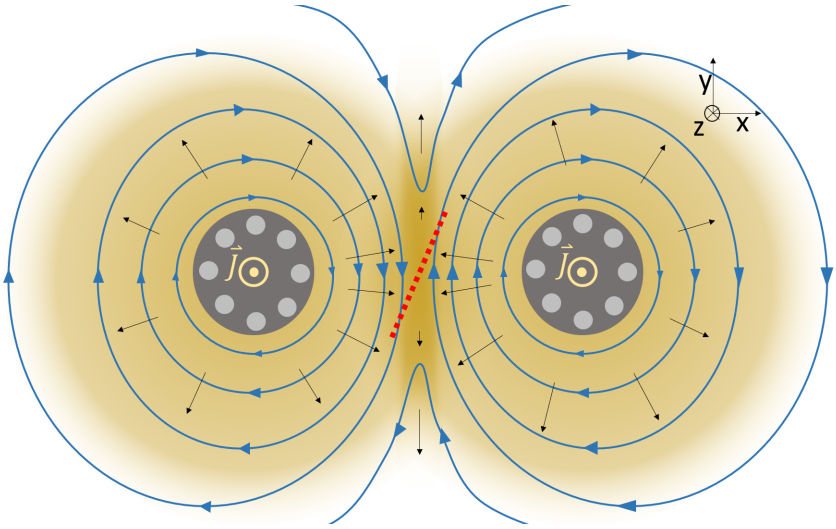

Figure 3.25: Magnetic Re-connection experimental configuration on MAGPIE. Current is run through aluminum wire meshes (grey) in the $-\hat{z}$ direction to produce magnetic fields (blue). The magnetized plasmas collide in the center, causing the anti-parallel magnetic fields to undergo re-connection. The OTS locations are shown in the center, taken with $\vec{k}$ in the $\hat{z}$ direction. [5, 93]

direction (Fig. 3.25). Similarly to (3.9), we calculate $J_z = en_e(v_i - v_e)$ producing $J_z > 0$ as seen in figure 3.28.

The lack of clear peaks in the IAW spectra far from the center of the experiment can lead to large errors when determining the current at $|x| > 0.4mm$, where $x = 0$ is the midpoint of the two wire arrays (Fig. 3.25). To obtain a more robust measurement of the magnetic field, we can use a Harris sheet model [94] to force the majority of the current measurement to be made in the central sheet where the IAW is well resolved. This profile is often used in re-connection environments to model the current sheet, with shape

$$J_z(x) = \frac{cB_0}{\pi L}\frac{\exp(2x/L)}{(\exp(2x/L)+1)^2} \tag{3.15}$$

where B_0 corresponds to the amplitude of the current, and L to its radius. Using Ampere's law with steady state conditions ($\frac{dE}{dt} \ll J$) we have $\frac{dB_y}{dx} = \frac{4\pi}{c}J_z$ with which we can write the corresponding magnetic field as

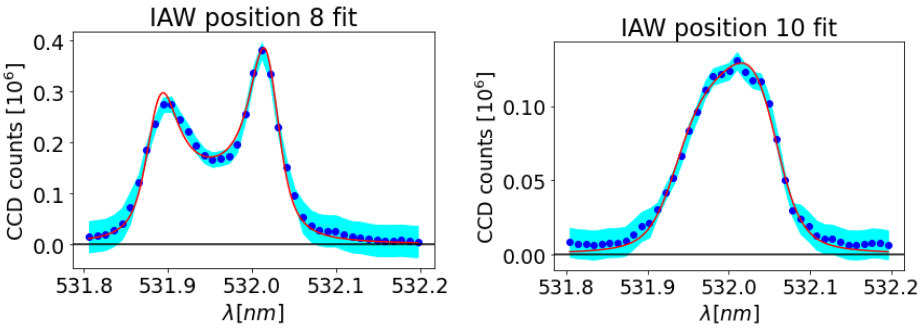

Figure 3.26: IAW data (blue) and fit (red) examples from the 14 positions across the shot, with position 8 (left) at $x = 0.02mm$, within the current sheet, and position 10 at $x = 0.27mm$, close to the edge of the current sheet, where $x = 0$ is the center of the experiment. [5]

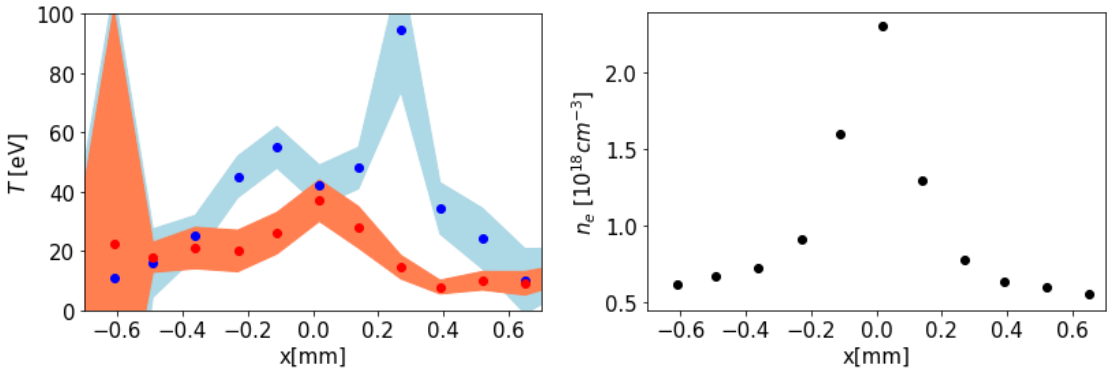

Figure 3.27: Left: Election (red) and Ion (blue) temperatures as measured by IAW spectra. Right: Electron density profile, measured with interferometry.

$$B_y(x) = B_0 \frac{\exp(2x/L) - 1}{\exp(2x/L) + 1} = B_0 \tanh\left(\frac{x}{L}\right) \tag{3.16}$$

The length L can be found via density measurements of the plasma, where the current sheet in the center is $\approx 0.3mm$ in radius [95], restricting most of the current to the well-resolved IAW spectra (3.26). This results in a field strength of $9.2 \pm 0.7T$. The current measurements from OTS can also be integrated directly to determine the field, which is similar to the Harris sheet result (3.28).

This magnetic field is significantly higher than the Faraday rotation measurement of the upstream plasma, which reaches only 4 T. The Faraday probe, however, cannot

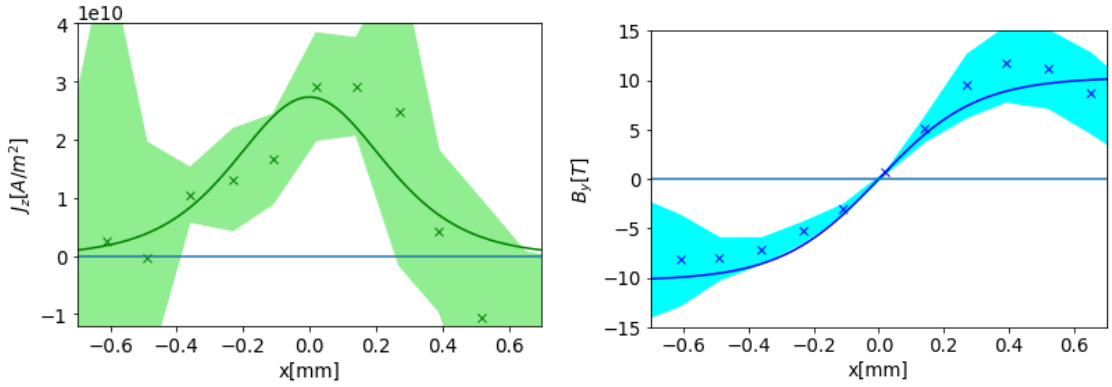

Figure 3.28: Current (green, left) and magnetic field (blue, right) measured from IAW spectra (×) with error shaded in. A Harris current sheet with radius $0.3mm$ is fit to the current (solid lines) with amplitude $B_0 = 9.2 \pm 0.7T$

measure the field near the current sheet due to refraction from the increased density gradient [96]. It is possible, therefore, that the OTS current measurement corresponds to field pile-up, where the magnetized plasma pushes more field to the center faster than the initial re-connection rate [96, 97], causing the field to compress and increase in amplitude.

Chapter 4

Particle Transport

In order to investigate the properties of heat transport and the capability of OTS to directly measure its effects, we investigated laser-ablated Au plasma [6]. Electron heat flux in ICF plasmas is a kinetic process. It remains an outstanding problem, and is the subject of much active research within the ICF field [98].

Improving our understanding of thermal transport under ICF hohlraum-relevant plasma conditions will facilitate the development of predictive models that can be used to design new and better hohlraums via simulations before significant experimental testing is preformed. Here we are able to show some discrepancies between simulations and experimental measurements of heat transport in the corona of ablation plasmas, even while simulations accurately match the plasma conditions. This discrepancy is found early on in the heating process, similar to macroscopic models of hohlraum plasma evolution which have also found the need to artificially lower heat flux early on in laser shots [99, 100].

4.1 Spherical Target Experiments

The plasmas studied in this chapter are produced in directly-driven experiments conducted at the OMEGA laser facility at the Laboratory for Laser Energetics, University of Rochester (sec. 1.4). Targets are metal coated plastic spherical bead targets [7, 8] with a radius of 430 μm.

Electron heat flux can be quantified using measurements of the temperature and density gradients and the particle distribution functions [33, 80, 101–103]. We use a combination of optical Thomson scattering (OTS) measurements and radiation-hydrodynamic simulations of the plasma dynamics to determine the properties and profiles of the coronal plasma. Vlasov-Fokker-Planck (VFP) simulations of the particle kinetics are used to characterize the particle distribution functions. The spectral effects of these distribution functions within the OTS scattering volume are used to measure particle heat flux.

4.1.1 Experimental Setup

This chapter primarily explains the analysis of heat flux in a gold sphere shot, outlined in Ref. [8]. To summarize, the gold target is a 0.86 mm diameter gold coated bead. Its surface is heated using 59 of the OMEGA heater beams (Fig. 4.1); one beam is used to generate the OTS probe. Phase plates are used to shape the beam intensity at the target to produce a smooth intensity distribution over the target surface of $5 \times 10^{14} W/cm^2$ for 2 ns, delivering $21.9kJ$ (Fig. 4.2). The surface of the sphere is ablated and expands rapidly outwards as a hot plasma, which is measured with a Thomson probe.

OTS spectra (seen in Fig. 2.6) were taken in the corona at approximately 735 μm from the sphere center, (305 μm from the surface) at and angle of 160° from the stalk holding the target (Fig. 4.1). This creates a quasi-1D environment around the probe location, as it is nearly opposite the only asymmetry in the spherical target. The probe is pointed at 730 μm, but 5 μm of outwards refraction is expected. The probe is focused at f/6.7, with a wavelength of 263.25 nm. The pulse shape is similar to that of the 2 ns drive, but delayed by roughly 0.4 ns. The probe energy was $96.5J$ with a radius at the focal point of 35 μm.

Light scattered from the probe is collected with a reflective telescope with a focal length of f/10 at 60.3° off the probe axis, and deposited through separate Czerny-

Turner optical spectrometers onto ROSS optical streak cameras [**Katz2012**]. The wave vector observed in this scattering process is $\vec{k} = \vec{k_{out}} - \vec{k_{in}}$, where $\vec{k_{out}}$ is the wave vector of the scattered light and $\vec{k_{in}}$ is the wave vector of the probe. $\vec{k}$ is oriented along the target normal, making the scattered light sensitive to the expansion flow velocity of the plasma.

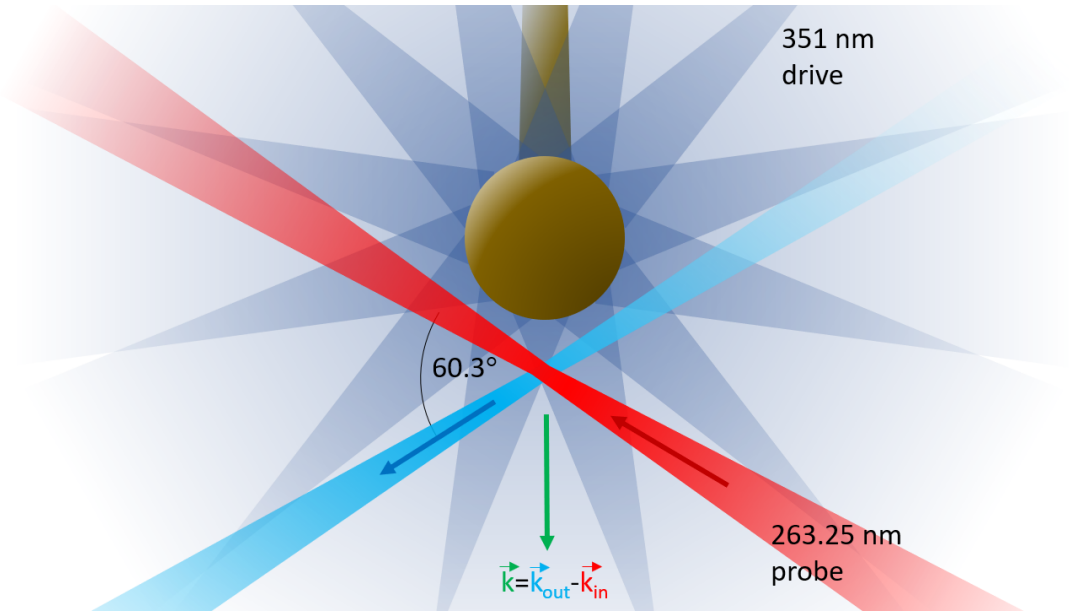

Figure 4.1: Thomsons Scattering probe and collection geometry, observing plasma at 730 μm from the sphere center. The probe beam is shown in red, with the collection volume in light blue and the resulting wave vector probed in green. (From [6])

4.1.2 Applications of the OTS Diagnostic for the measurement of Heat Transport

The OMEGA Thomson scattering system is used to obtain scattering spectra from IAW and EPW fluctuations in the ablated plasma. The red-shifted EPW shares bandwidth with scattering from the 351 nm drive, so the EPW spectrometer observes blue-shifted light in the range of 190 - 230 nm, capturing only the blue-shifted Langmuir waves traveling away from the target surface. These spectra are analyzed to obtain the time evolution of electron temperature and plasma density at the measurement location.

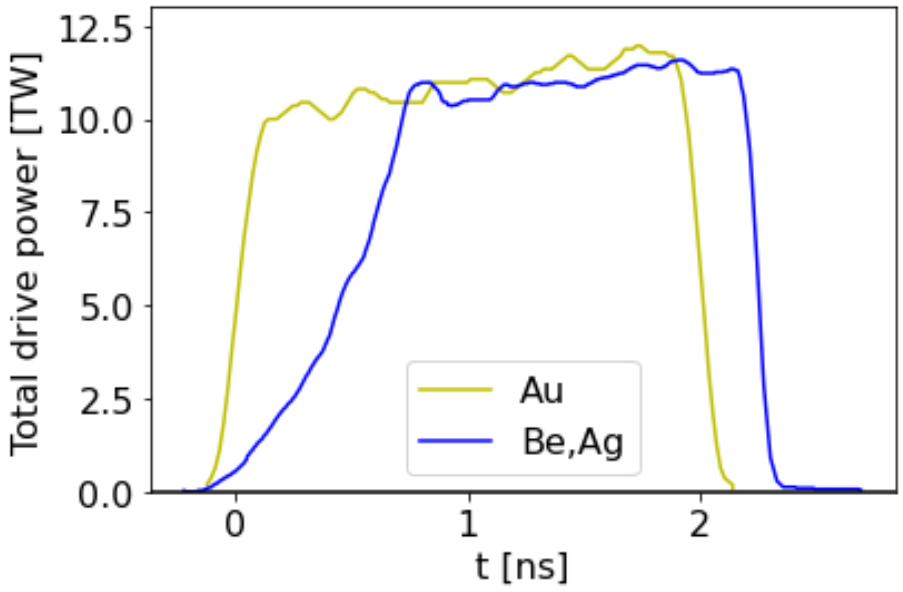

Figure 4.2: Total drive power for the Au sphere shot, as well as the pulse shape for other sphere shots use in section 4.4. These shots reach a peak intensity at the target of $\sim 5 \times 10^{14} w/cm^2$

OTS is a powerful diagnostic technique that can provide uniquely local measurements of plasma parameters in high energy density plasmas. This technique has been applied extensively to make comprehensive studies of the plasma parameters [7, 104], distribution functions [51, 53, 105], magnetic fields and electric currents [2, 3] and thermal transport [80, 106–108] in a variety of laser driven plasmas, including ICF hohlraum plasmas [61]. To properly and accurately fit the OTS spectra, a range of important effects on the spectral shape must be taken into account, based on the details of the measurement geometry and the plasma conditions (Chapter 2).

To infer the basic plasma parameters from the OTS spectra, one relies primarily on the spectral displacements of the resonant peaks in the collective regime of the OTS. Good accuracy is usually achieved in such a procedure without invoking the effects of non-Maxwellian distribution functions and particle collisions in the theory of the dynamical form factor (2.2). Large scale radiation hydrodynamic simulations, which include the effects of non-local thermal transport, are used to calculate the

expected evolution of the electron temperature and plasma density gradients for the analysis of the particle transport. These simulations have been benchmarked against Thomson scattering measurements and have been shown to successfully reproduce the evolution of the electron temperature and plasma density in these conditions [7, 8].

Heat flow can be measured in these spherical target experiments through a more careful analysis of optical Thomson scattering (OTS) data. Diagnosis of the heat flow is achieved via an analysis of its effect on the relative intensity of two ion-acoustic scattering peaks (section 2.2.2). The scattering spectrum can only be sensitive to this effect when the geometry is selected such that the wave vectors of the observed density fluctuations point along the direction of the heat flow, i.e. the radial expansion vector of the plasma for the sphere experiments (Fig. 4.1).

Electron heat flow is dominated by the particles in the tail of the electron distribution, at velocities much greater than the ion acoustic velocity of the plasmas. This flow of electrons in the tail induces an electric field that drives a return current, shifting the bulk of the electron distribution function slightly with respect to the ion flow velocity [33]. The result of this shift is that the velocity gradient of the electron distribution function at the phase velocities of the two counterpointing ion acoustic waves can be different. This leads to a difference in the Landau damping rates and therefore the amplitude of the two peaks. We are therefore able to measure heat flow indirectly through our more direct measurements of this return current.

Analysis of this effect proceeds by accounting first for the instrumental effects in the OTS measurements such as angular spreads of the probe and collection optics, which are particularly important in flowing plasmas (section 2.3), as well as frequency broadening due to pulse front tilt [43]. In addition to these geometric effects, the theory of the dynamical factor, $S(\vec{k},\omega)$ must be expanded beyond the collisionless model that is typically used to include the effect of ion-ion (section 2.2.4) collisions in the highly ionized Au plasmas [47, 55].

Damping of the IAW due to ion-ion collisions is small and comparable with electron Landau damping from the symmetric f_0 electron distribution function, and its effect on spectral broadening is negligible when compared with the instrumental width of IAW peaks in the OTS spectrum. However, in the analysis of the relative intensity of IAW peaks due to the drift velocity of the electrons, electron landau damping is altered and the ion-ion collision effects can become significant when analyzing the relative amplitudes of the IAW.

When analyzing the IAW asymmetry, we are measuring the effects of the non-equilibrium electron distribution functions (EDF). The electron density correlation function and the dynamical form factor are sensitive to the form of the EDF, as the damping rate of each ion acoustic peak is sensitive to the gradient of the EDF at its phase velocity. The non-equilibrium EDFs that are produced by the inverse bremsstrahlung (IB) heating [49] or thermal transport [101] can be measured experimentally through the EPW feature of the OTS spectrum [51] [109] and applied to the calculations of plasma parameters and the heat flux.

Using these measurements of the electron return current, we have found that at late times (t > 1ns after the drive starts, Fig. 4.2) the inferred heat flux is consistent with the nonlocal Schurtz-Nicolai-Busquet (SNB) [37] model and VFP simulations [101]. The spatial profiles of plasma density and electron temperature predicted by the radiation hydrodynamic simulations employing the SNB model disagree with the Spitzer-Härm (SH) local transport theory interpretation of the IAW asymmetry.

The OTS measurements display the change in the direction of the heat flux in response to rapid radiation cooling of the dense plasma near the target surface after the termination of the heating beams. However, a disagreement between measurements of the heat flux and simulation results is seen early in the plasma evolution, $t \leq 1$ ns. We propose that this discrepancy is the result of the combination of two effects: the super-Gaussian form of the symmetric part of the EDF due to IB heating and the presence of steep density gradients at early time [102, 110].

While for most of the simulation and laser pulse duration, modest changes in the exponent of the EDF have a small effect on the transport calculations, at early times the relatively stronger density gradient can reduce the electron heat flux. This is a consequence of the transport relations for the heat flux in non-equilibrium plasmas with super-Gaussian EDFs, which include terms proportional to the density gradients that have negative contributions as compared to the terms proportional to the temperature gradient [102], leading to an observable suppression of thermal transport. This feature of the local transport theory is seen in VFP simulations containing nonlocal effects.

4.2 Radiation hydrodynamic simulations and comparison with the basic OTS results

The experimental measurements and radiation-hydrodynamic simulations that are relevant to the current study were described in a recent paper [8], and form part of an ongoing campaign of experiments on the Omega laser facility that use directly illuminated Be and Au spherical targets [7] to investigate laser coupling, heat transport, and radiation conversion efficiency in order to improve our understanding of ICF hohlraum physics.

We will compare transport in the radiation hydrodynamics simulation with detailed calculations of the observed electron heat flux from the OTS spectra.

4.2.1 Plasma Properties

The radiation hydrodynamic simulations presented here are described in detail in Refs. [7, 8], in which 2D simulations of uniformly illuminated gold spheres at intensities of $5 \times 10^{14} W/cm^2$ for 2 ns duration laser pulses are reported. These simulations predict temperature and density gradients in the plasma, which can be compared to those observed using the OTS signatures of heat transport (section 2.2.2).

Although ICF simulations typically reduce the incident laser power in simulations

to match observables (either observed bang-time, x-ray flux, or scattered light due to laser-plasma-interactions), it was found that using power multipliers to match the measured scattered light did not significantly change the plasma properties at the location of the OTS probe. This allows conclusions regarding transport to be made even with a lack of laser coupling to the target [111]. Temperature and density profiles of the ablating plasma are generated with SNB simulations, shown in Fig. 4.3, with an ionization of $Z \approx 50$ for the gold plasma.

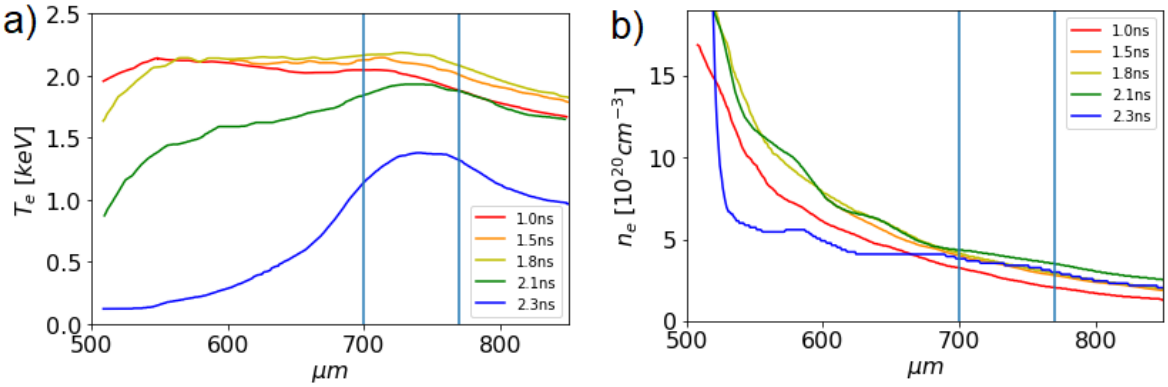

Figure 4.3: Simulated electron temperatures (a) and electron density (b) from the SNB model as a function of the distance from the center of the sphere. Ionization remains near $Z = 50$ over most of the simulated profile. The extent of the probed region is marked by blue vertical lines. [From [6], associated dataset available at https://doi.org/10.5281/zenodo.4951053] (Ref. [46]).

The plasma heating by the Thomson probe is included in the simulations. This is particularly important at the later times after 2 ns when the main drive laser beams are switched off (Fig. 4.2) and dense plasma cools rapidly outside the Thomson scattering volume due to radiation losses as shown in Fig. 4.3a. The profiles of figure 4.3 will later be reproduced by differentiable fits and used in Vlasov-Fokker-Planck simulations of the plasma in the OTS volume in Sec. 4.3. All results of radiation-hydrodynamic simulations have been obtained using the SNB nonlocal transport model.

These results can be compared to experimental data obtained from the OTS spectra

at the probe location at 735 μm from the center of the sphere, between the vertical lines shown in Fig.4.3. These spectra can be fit to the observed IAW and EPW spectra (shown in Fig. 2.6), producing local measurements of the plasma at the probe location (Fig. 4.4). The fits to measured OTS spectra were obtained using OTS theory (2.6)(2.28) with Maxwellian ion distribution functions, and Maxwellian, super-Gaussian (sec. 2.2.3), and VFP-generated electron distribution functions.

4.2.2 Ablation rates

In laser-ablated plasma, the bulk of the drive energy is deposited close to the critical surface, making the conditions of the high-density plasma close to the target crucial for accurate simulations. OTS, however, cannot measure near the critical surface, as refraction from the high-density plasma ruins the pointing precision of the probe. In order to gain information on the high-density plasma, shots were taken to measure the ablation rate caused by the plasma conditions near the target.

Two gold sphere shots similar to the shot seen above (Fig 4.1) but with 0.1 and 0.2 μm of gold on top of plastic were also taken. These shots used OTS data at a radius of 630 μm, with a scattering vector $\vec{k}$ tangential to the sphere surface. The thin gold layers allowed the burn rate of the solid gold target to be measured from the beginning of the shot. As the gold plasma is replaced by plastic and dominated by the charge density of carbon, the sound speed sharply increases with Z/A (Fig. 4.5), increasing the IAW frequency (2.9).

This increase in IAW frequency can be fit by changing the concentration of gold, carbon, and hydrogen ions in the plasma. Allowing these concentrations to vary, we can observe a transition from gold ion waves to carbon-dominated ion acoustic waves around 1.6 ns for the 0.2 μm gold shot (Fig 4.6), where the increase in ω_{iaw} marks the burn-through time. The two shots' burn-through times differ by $0.75ns$, indicating a burn rate of $0.13\mu m/ns$.

In addition to the observable change in ω_{iaw}, the IAW spectra show a shift in their

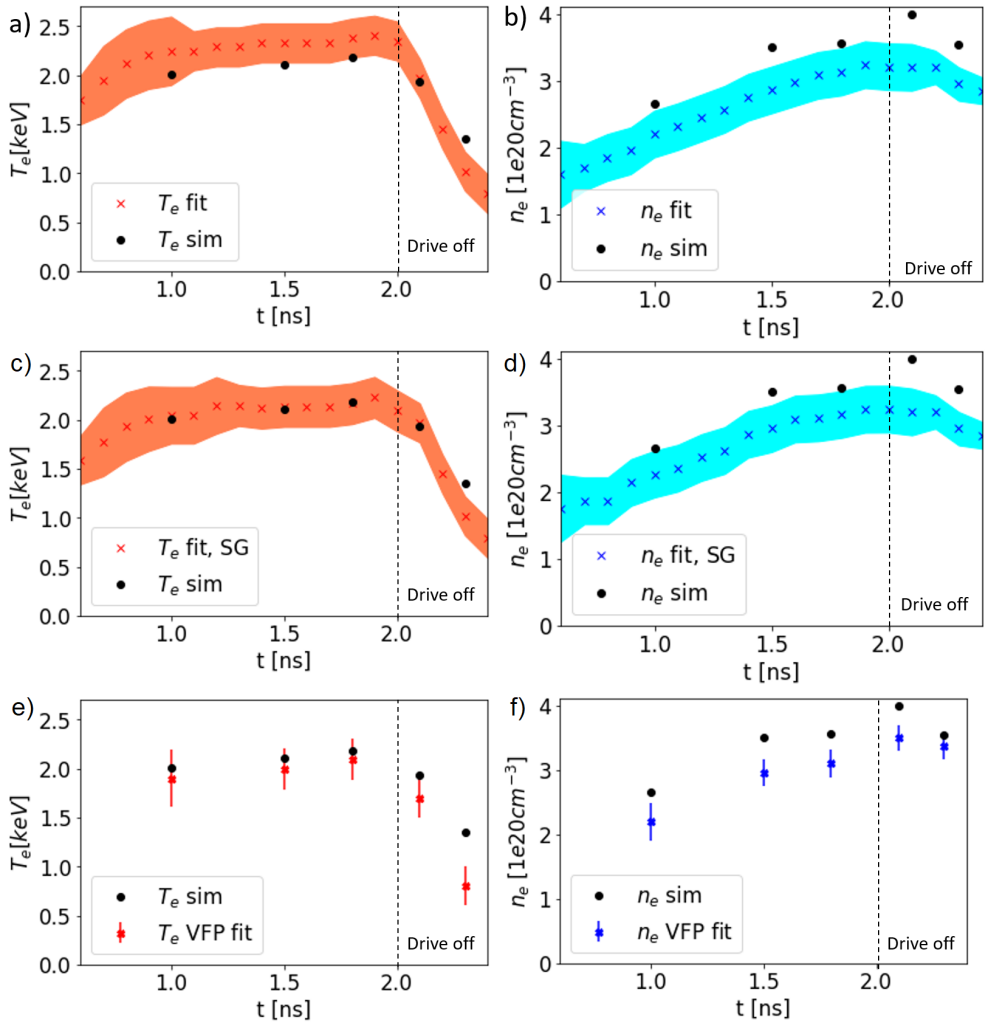

Figure 4.4: Fits to the experimental OTS data (Fig. 2.6) using a Maxwell distribution for electrons (a, b), a super-Gaussian model (2.24) with m = 2.3 (c and d), and using VFP-generated EDF shapes (e and f). Black dots are from radiation hydrodynamic simulations using the SNB transport model. Absorption lines seen in the EPW spectrum may introduce additional uncertainty in the density measurements in the middle of the shot. The faster cooling and lower densities after the drive is off in all OTS fits constitute a significant difference from the simulation. Super-Gaussian distributions are used up to 2 ns in figs. c and d, after which the drive turns off. (From [6])

central wavelength after burn-through. This shift typically corresponds to the flow velocity of the ions. In these thin gold shots, however, OTS spectra are taken with scattering vectors nominally tangential to the surface of the sphere. The expanding plasma in the corona refracts the probe away from the sphere, and light scattered

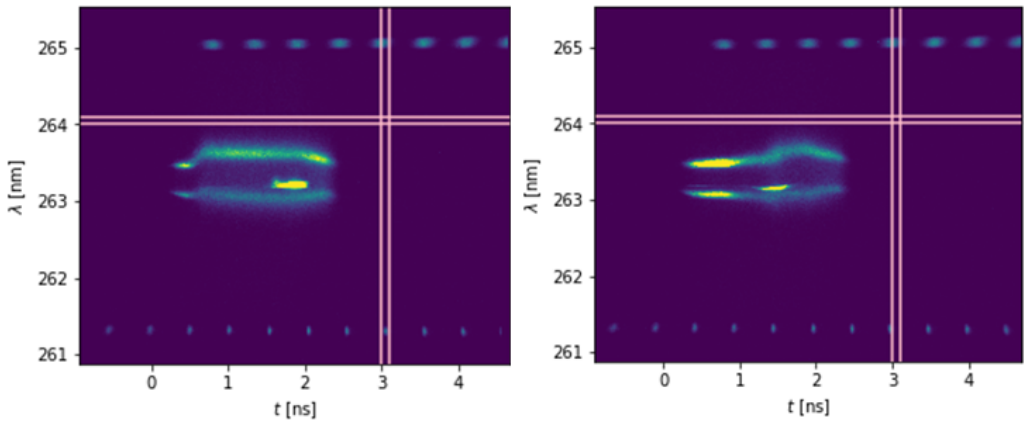

Figure 4.5: IAW spectra from thin gold spheres, with a $0.1\mu m$ (left) and $0.2\mu m$ (right) thick layer of gold on top of plastic. The IAW frequency increasing sharply indicates the burn-through time.

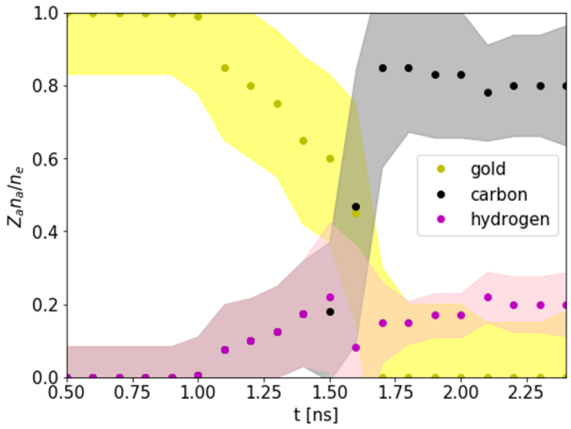

Figure 4.6: Ion change density from OTS fit of thin gold shell spectra (Fig. 4.5, right). Shaded region indicates error.

down towards the target at the same angle is refracted back into the scattering plane, as seen in figure 4.7. This gives the scattering vector a rotation towards the target surface which increases with increasing coronal plasma density.

By comparing the flow velocity observed along the scattering vector in the tangential geometry to the flow velocity of $\sim$700 km/s at 730 μm (Fig. 4.9), we can estimate a refraction angle of a few degrees, assuming flows at 200 and 300 μm from the target are similar to first order. We can see the refraction angle must increase

when the carbon plasma arrives (Fig. 4.8).

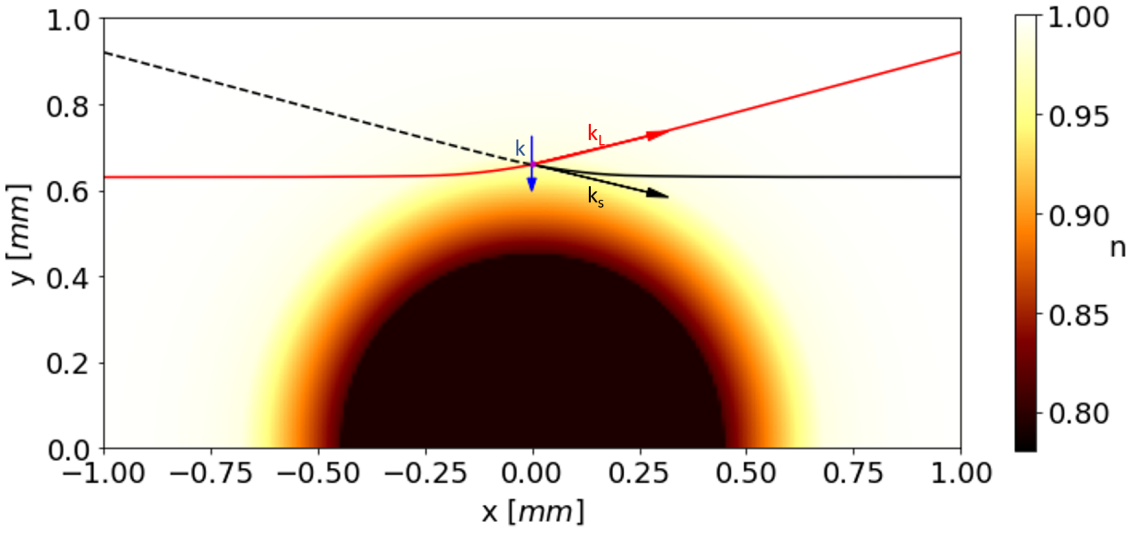

Figure 4.7: Refracted probe beam (red) with refracted collection vector (black) shown with a veiw from inside the nominal OTS scattering plane. The resulting $\vec{k}$ component perpendicular to the original OTS plane is shown in blue, pointing towards the target. The refractive index for 4ω light is shown for a low Z, high-density model of the density gradient.

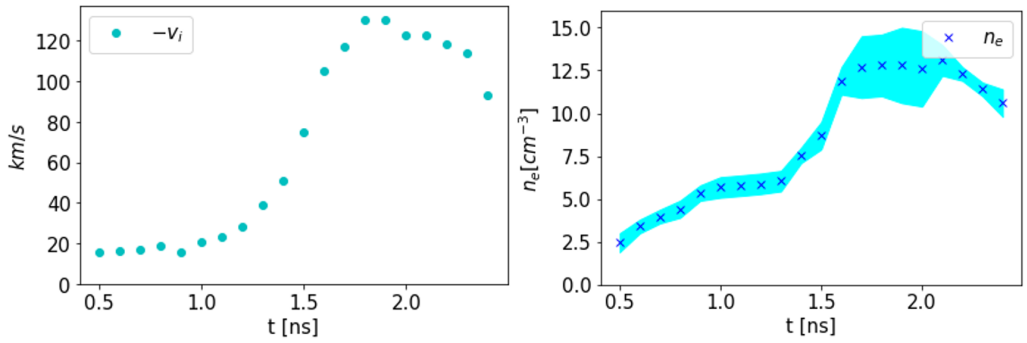

Figure 4.8: Flow velocity in scattering direction and plasma density from OTS fit (Fig. 4.5, right). The scattering vector is nominally tangential to the flow, with velocity proportionate to the refraction angle of the probe beam.

As an alternative to the average burn rate of $0.13\mu m/ns$ measured between the two shots, we can find the target burn depth as a function of time by integrating the observed density (Fig. 4.4) and flow velocity (Fig. 4.9) found in the radial OTS measurement of the thick gold sphere. This determines the rate of mass flow of gold

passing the OTS volume. Given a solid density for gold of $\rho_{Au} = 19.3 g/cm^3$, a ratio of areas of $\pi 730^2 \mu m^2 / \pi 430^2 \mu m^2$, and spherical symmetry from the geometry of the shot, the ablation rate over time can be calculated: (Fig. 4.9).

$$v_{ablation} = \frac{n_e A m_p v_i}{Z \rho_{Au}} \frac{730^2}{430^2} \tag{4.1}$$

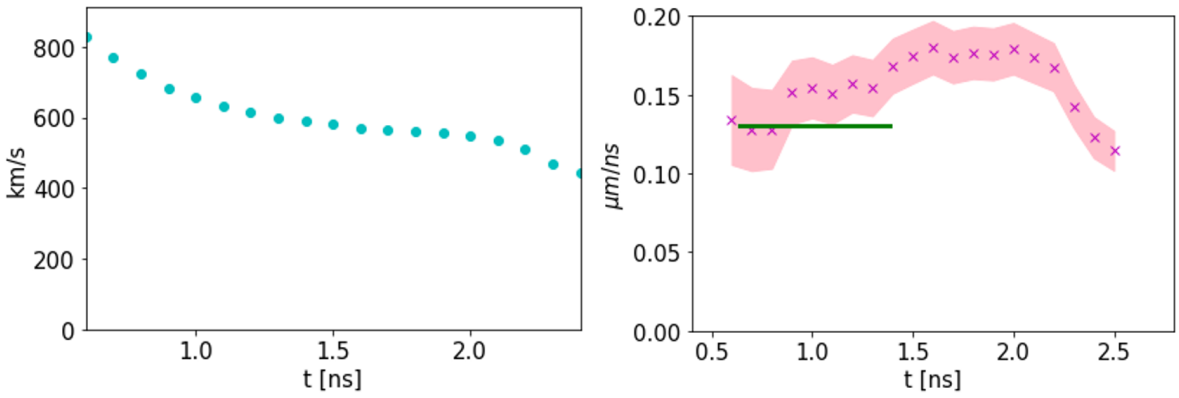

Figure 4.9: Velocity measured in radial gold shot (left) and the ablation rate (right) as measured by radial mass flow rate (pink) and by thin gold shots (green)

The burn rate is mostly consistent with the observed gap in burn-through times for the thin gold shots. This confirms the capability of the thin gold shots to be used to examine burn-through progress occurring before the OTS probe reaches the target and validates the use of the ablation rate to measure extended burn-though. By the end of the probe pulse, the plasma flow indicates $\approx 0.35 \mu m$ of ablation thickness.

4.3 Heat flux models

To measure the heat flow in the gold plasma using the OTS spectrum, we will follow an iterative procedure similar to the approach of Ref. [7]. In the collective regime of the OTS spectra, the location of the IAW peaks is sensitive to electron temperature, flow velocity, and the ion charge (Z). Fitting of the EPW peak shows electron density and can verify electron temperature. Although simultaneous analysis of the results from EPW and IAW spectra can allow for the measurement of Z in the Au plasma

[112], the simulated ionization of Z=50 is used here to reduce dependence on the EPW shape, which is sensitive to background light and density gradients in the OTS volume (2.6). The EPW and IAW are fit together for T_e, n_e, flow velocity v_i, density gradients, and signal amplitude.

The time evolution of these plasma parameters is consistent with radiation-hydrodynamic simulations [8], as seen in Fig. 4.4. They are a starting point for the analysis below where we will examine various non-Maxwellian distribution functions corresponding to different thermal transport models. In this next approximation, different transport models are examined, which take these fit plasma parameters as inputs, in addition to the characteristic spatial profiles found with radiation-hydrodynamic simulations, shown in Fig. 4.3.

Transport models provide the closure relations for hydrodynamic equations, and also their related electron distribution functions [80, 101] for any temperature and density profile. To analyze the discrete time snapshots of the plasma conditions shown in Fig. 4.3, we have used heat transport models that are consistent with these conditions and can be compared with measurements. The perturbed EDFs relate the fast heat-carrying electrons to the resulting return current of slow electrons, which is measurable in ion acoustics wave spectra.

4.3.1 Spitzer-Härm heat flux

The Spitzer-Härm (SH) classical transport model [33] is valid in plasmas dominated by particle collisions and is derived from the Fokker-Planck kinetic equation in a current-free plasma with a temperature gradient, by expansion in the small parameter $\delta_T = \lambda_{ei}/L_T$ where $L_T = (\frac{d}{dx}\ln T_e)^{-1}$ is the signed temperature gradient scale length and λ_{ei} is the electron-ion mean free path. To the leading order in δ_T the electron distribution function is given by the perturbed local Maxwell distribution function:

$$f_{SH}(|\vec{v}|, v_x) = f_M(|\vec{v}|) + \sqrt{\frac{2}{9\pi}}(\frac{|\vec{v}|}{v_{T_e}})^4(4 - \frac{v^2}{2v_{T_e}^2})f_M(|\vec{v}|)\delta_T\frac{v_x}{|\vec{v}|}, \tag{4.2}$$

where $f_M(|\vec{v}|)$ is the Maxwell distribution, $v_{T_e} = \sqrt{T_e/m_e}$ and the gradient $\vec{\nabla} T_e$ is anti-parallel to the x-axis. The small parameter δ_T also determines the heat flux calculated using f_{SH} (4.2)

$$q_{SH} = \frac{m_e}{2} \int d^3v v_x v^2 f_{SH} = -\frac{128}{3\pi} n_e m_e v_{Te}^3 \delta_T \tag{4.3}$$

At $v > 2\sqrt{2} v_{T_e}$, fast heat-carrying electrons enhance the tail of the distribution function in the direction opposite to the temperature gradient (4.2). At lower velocities, the current produced by fast electrons is balanced with a cold return current.

Given any δ_T, a sufficiently high-velocity regime in f_{SH} (4.2) exists which will results in a negative distribution function, indicating that the Spitzer-Härm EDF is non-physical for fast particles, or near thermal particles in environments with long mean free paths. Steep temperature gradients and long mean free paths corresponding to $\delta_T \geq 10^{-2}$ undo the local closure relation (4.3) and must be replaced by non-local heat transport models. For this reason, local hydrodynamic models often use flux-limited SH transport, where $q = min(q_{SH}, f q_f)$, with $q_f = n_e m_e v_{Te}^3$ and $f << 1$ (such a relation is illustrated later on in Fig. 4.16a).

The IAW spectra depend only on the low-velocity electrons in the one-dimensional distribution function which comprise the return current. This flow of electrons changes the damping of the IAW, (2.3) affecting the relative amplitudes of ion-acoustic resonances in the fluctuation spectra. The damping rate of ion acoustic waves due to a return current of electrons is approximately equivalent to the damping rate of a drifting Maxwellian electron distribution function with a velocity v_d linear with transport: $v_d = 1.5 v_{Te} \delta_T$. (Sec. 2.2.2)

Depending on the sign of the phase velocity ω_s/k, the drift velocity v_d increases or decreases the electron Landau damping (2.16) creating asymmetry in the amplitude of the IAW resonances seen in the OTS spectra. In addition to electron damping, these resonances are affected by ion Landau damping proportionate to $\frac{\omega_{iaw}}{k v_{Ti}} exp(-\frac{\omega_{iaw}^2}{2k^2 v_{Ti}^2})$ [12]. This decreases quickly with increasing $\frac{\omega_{iaw}}{k v_{Ti}} \approx \sqrt{Z T_e/T_i}$, causing high Z elements

to be very weakly Landau damped. Collision damping due to ion-ion collisions, however, is still present at high Z. Collisions are included in the calculation of the OTS spectra using $S^c(\vec{k},\omega)$ (2.28).

4.3.2 Non-Maxwellian EDFs due to IB heating and the electron thermal transport

In gold and other high-Z laser-produced plasmas it is common to see evidence of super-Gaussian electron distributions ((2.24) with $m > 2$), altering the spectral shape of the scattered light [51–53]. This super-Gaussian distribution function arises due to competition between IB heating, which evolves the EDF towards the super-Gaussian distribution [49] and electron-electron collisions which thermalize the plasma. The super-gaussian EDF (2.24) was derived in Ref. [50] from the results of Fokker-Planck simulations. For homogeneous laser-heated plasma, Eq.(2.25) approximates the super-Gaussian exponent well for a given laser intensity, frequency, plasma temperature, and average ionization [50].

For our experiment, the super-Gaussian exponent at the OTS probe location is limited to $m \leq 2.3$ by this relation, based on the intensity of the 3 ω drive [50]. For the EPW, this small change in the electron distribution function has an insignificant effect given the noise present in the measured spectrum. The IAW spectrum responds to the shape of the electron distribution function at $|\vec{v}| << v_{Te}$, so larger super-Gaussian coefficients appear to fit OTS spectra with slightly lower electron temperatures (Fig. 2.16). This is illustrated in Fig. 4.4c,d where we compared the time evolution of electron temperature and density from the OTS spectra fitted using EDF $f_{SG0}, m = 2.3$ (2.24) with the radiation-hydrodynamic results.

Successive improvements of the fits to the OTS spectra as we gain a better understanding of the kinetic processes underlining the evolution of the plasma are part of the overall strategy of our OTS experiments. More precise subtraction of the noise in the EPW spectra in planned experiments with background shots will help to identify

the effects of the super-Gaussian distribution functions.

When a super-Gaussian electron distribution function is present, IAW resonance frequencies are increased slightly, and heat transport is significantly affected [102, 103]. The perturbation solution to the Fokker-Planck kinetic equation by expansion in parameters δ_T and $\delta_n = \lambda_{ei}\frac{d}{dx}\ln(n_e)$ about a super-Gaussian background distribution results in the following electron distribution function [49] [102]

$$f_{SG}(|\vec{v}|, v_x) = f_{SG0}(|\vec{v}|) + f_{SG0}(|\vec{v}|)\frac{v_x}{|\vec{v}|}\left(\frac{|\vec{v}|}{\sqrt{2}v_{T_e}}\right)^4 \left(\left(\frac{m}{2}\left(\frac{|\vec{v}|}{\sqrt{2}v_m}\right)^m - \frac{5m}{12}\frac{\Gamma(8/m)}{\Gamma(6/m)}\left(\frac{|\vec{v}|}{\sqrt{2}v_m}\right)^{m-2}\right)\delta_T - \left(\frac{m}{6}\frac{\Gamma(8/m)}{\Gamma(6/m)}\left(\frac{|\vec{v}|}{\sqrt{2}v_m}\right)^{m-2} - 1\right)\delta_n\right), \tag{4.4}$$

which is an equivalent of the SH theory (4.2) for the super-Gaussian distribution. Increasing the super-Gaussian coefficient m reduces the effects of temperature gradients on the heat flux in a plasma [113] (as is shown in Fig. 4.10a) and also results in contributions to the closure relation that are proportional to density gradients [102, 110, 114], with thermal energy flowing towards the higher density region,

$$q/q_f = (q_T + q_n)/q_f = -K_T\delta_{T_e} - K_n\delta_n, \tag{4.5}$$

The transport coefficients K_T and K_n can be written as

$$\begin{aligned} K_T &= \sqrt{\frac{2}{9\pi}}a(7b - 5c) \\ K_n &= \sqrt{\frac{2}{9\pi}}2a(b - c) \end{aligned} \tag{4.6}$$

with $a = \Gamma(3/m)^{5/2}(\frac{3}{\Gamma(5/m)})^{7/2}$, $b = \frac{\Gamma(10/m)}{12}$ and $c = \frac{\Gamma(8/m)^2}{9\Gamma(6/m)}$ [102] [115]. For ablating plasmas where temperature and density gradients both point towards the target, this results in a decreased heat flux when compared to Spitzer-Härm.

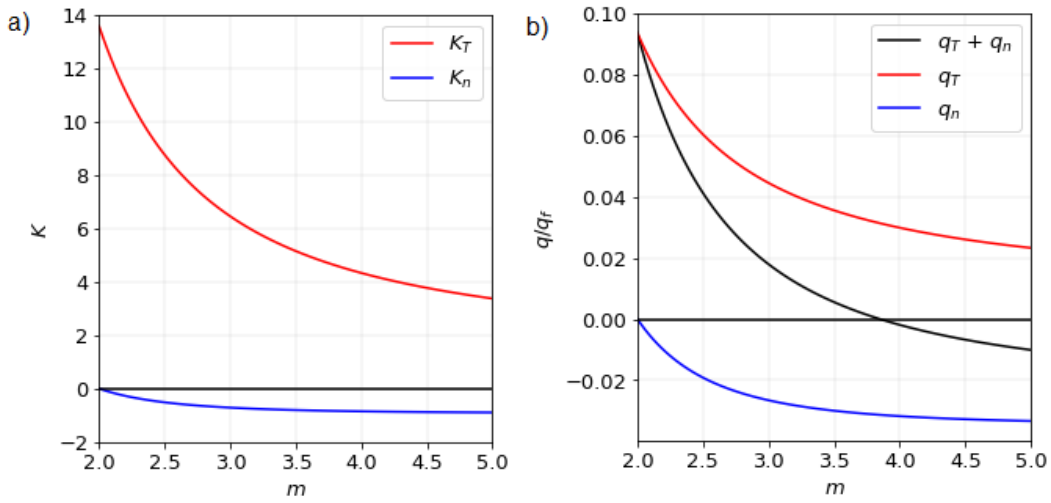

Figure 4.10: a) Heat transport coefficients in super-Gaussian plasma: $q/q_f = -K_T\delta T_e - K_n\delta_n$, (4.6) b) Heat transport due to temperature and density gradients in super-Gaussian plasma found using profiles for t=1ns as seen in Fig. 4.3, shown as a fraction of $q_f = n_e m_e v_{Te}^3$ (From [6])

Transport theory with the super-Gaussian distribution leads to closure relations for the heat flux that involve gradients of density and temperature. This leads to better agreement between theory and experimental measurement (sec. 4.4).

4.3.3 Vlasov-Fokker-Planck simulations

As described above in Sec. 4.3.1 the classical SH transport model can work well in plasmas where the characteristic transport parameter $\delta_T < \frac{0.06}{\sqrt{Z}}$ [35] [36]. For larger temperature gradients it has to be replaced by the kinetic description in terms of Vlasov-Fokker-Planck (VFP) simulations [116] or nonlocal transport models [37]. The nonlocal transport SNB [37] model has been used in the radiation hydrodynamic description of the Au plasma [8] and led to accurate modeling of the electron temperature and density evolution, cf. Fig. 4.4e,f.

We have used density and temperature profiles from the radiation hydrodynamic simulations with SNB transport in VFP simulations with the K2 code [101]. VFP simulations were performed around the relatively small OTS volume and usually quickly

converged to a quasi-stationary solution for the electron distribution function. This has been expected as VFP simulations have been consistent with the SNB model [101] in a broad range of plasma parameters. The density and temperature profiles from the non-local radiation-hydrodynamic simulations [8] are used as input to Vlasov-Fokker-Planck (VFP) simulations with the K2 code [101]. In order to initialize the K2 simulations, we first generate analytic fits to the SNB profiles seen in Fig. 4.3 for electron temperature and density, respectively (Fig. 4.11):

$$\frac{T_e(r)}{keV} = \frac{T_H - T_L}{2}\tanh\left(\frac{r+5\mu m}{75\mu m}\right) + \frac{T_H + T_L}{2} + p_0\tanh\left(\frac{r-p_1\mu m}{p_2\mu m}\right), \tag{4.7}$$

$$\begin{aligned}\frac{n_e(r)}{10^{20}cm^{-3}} = N_H + \frac{q_0}{2}(1+\tanh\left(\frac{r+210\mu m}{7.5\mu m}\right))exp(\frac{-q_1 r}{\mu m}) \\ +(1-0.5(1+\tanh\left(\frac{r+210\mu m}{7.5\mu m}\right)))(N_L - N_H)\end{aligned} \tag{4.8}$$

where T_H, T_L, and $p_i, i = 0, 1, 2$ are fit from the temperature profile and N_H, N_L, and $q_j, j = 0, 1$ are fit from the density profile.

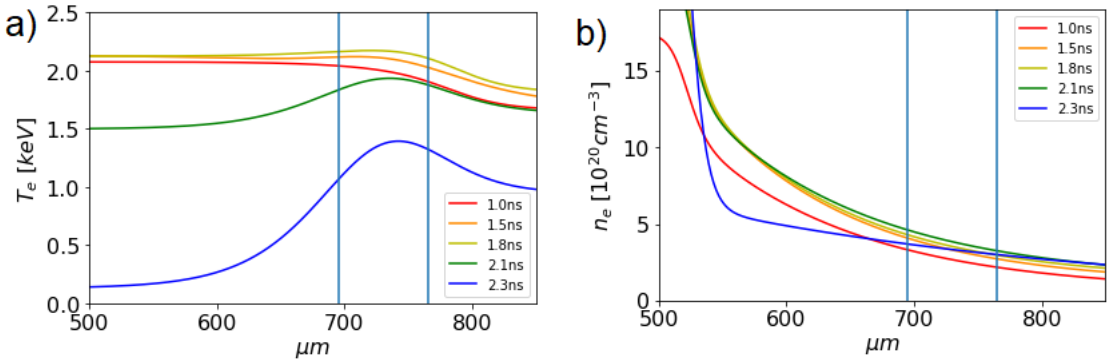

Figure 4.11: Analytical fits (4.7, 4.8) to the simulated temperatures (a) and density (b) profiles seen in Fig. 4.3. Vertical lines show the limits of the OTS volume where the OTS probe beam is pointed, which causes some plasma heating at later times. (From [6])

Once the density and temperature are set, K2 is run iteratively on r=0 to r=1500μm until a steady-state heat flux is produced which is consistent with the profiles. IB

heating is applied from the drive and probe beams, and the initial temperature profile is maintained in K2 by external heating and cooling operators. The electron distribution function is otherwise permitted to evolve self-consistently along with the electric field.

The heating and cooling operators increase or decrease the temperature in a manner that produces a symmetric distribution, f_{0VFP}, with some super-Gaussian characteristics (Fig. 4.12a), with anti-symmetric perturbations, f_{1VFP}, describing heat flux. This f_1 distribution also shows some super-Gaussian effects, including the reversal of the transport direction at low velocities seen in higher exponent super-Gaussians in the presence of density gradients (Fig. 4.12b). The distribution function can be sampled anywhere along the profile to see the resulting form $f_{1VFP}(v)$ of the heat-carrying electrons and the return current. These profiles typically carry heat at velocities lower than the Spitzer-Härm distribution (4.2), resulting in a relatively small ratio of heat flux to return current (seen later in Fig. 4.16).

For the application of VFP simulations to be valid, we are implicitly assuming the temperature profile produced by the SNB model is not too different from the temperature profile that would be generated by a fully self-consistent VFP simulation. Such full VFP simulations are still beyond our modeling capabilities. The heating operator is of the Langdon form [49], which is important to produce the correct super-Gaussian exponent for the symmetric part of the electron distribution [50]. The cooling operator, which accounts for the cooling terms in the radiation hydrodynamic simulations such as radiative cooling and PdV work [117], is a modified Langdon operator that generates a cooler Maxwellian distribution (in the absence of other processes).

The VFP-generated distribution functions can also be used to fit the observed OTS spectra (Fig. 4.4e,f). In this case, the shape of the electron distribution is taken from the simulations, but the width and amplitude are fit to match the OTS spectra. This results in temperatures fairly similar to the simulated temperatures before the drive

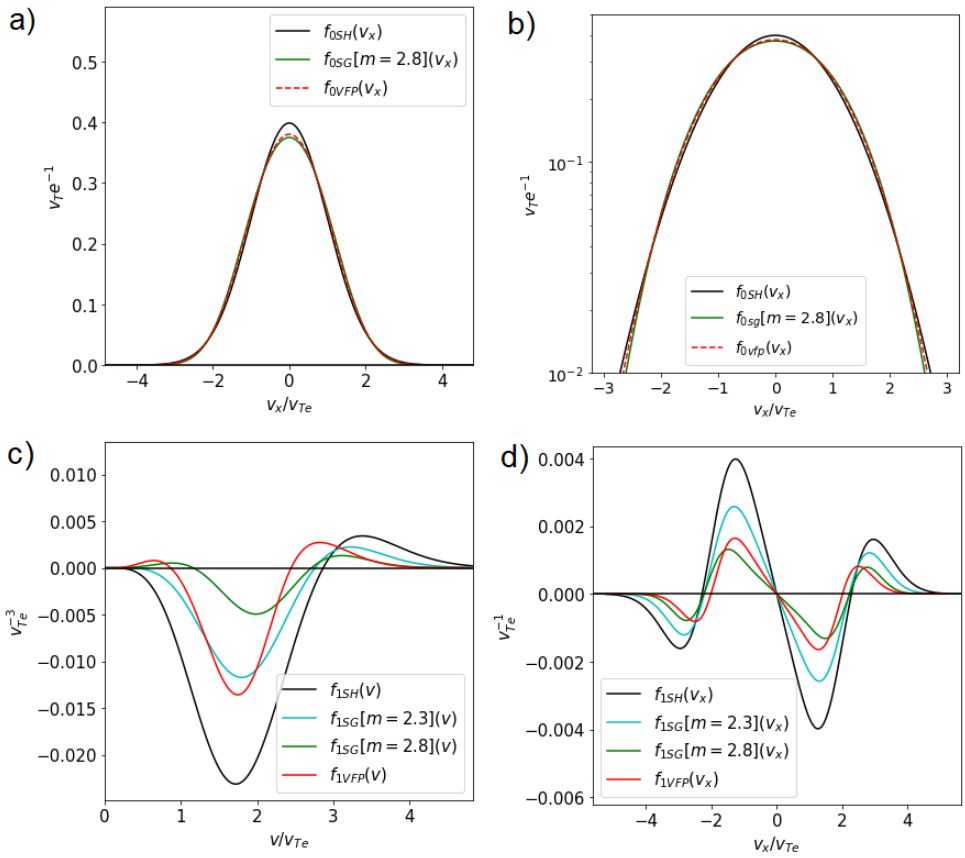

Figure 4.12: Electron distribution functions in the center of the OTS scattering region in the simulated profiles (Fig. 4.3) at 1ns, Te=2.03keV are displayed. f0 is shown in linear (a) and log scale (b), and f1 is displayed in (c) and (d) on $|\vec{v}|$ and projected onto the scattering direction respectively. Spitzer-Härm (black) and VFP (red) as well as the expected super-Gaussian of m=2.3 (blue) and an m=2.8 super-Gaussian (green) are shown. Inversion in the return current due to density gradients can be seen in (c) for the m=2.8 super-Gaussian and the VFP distribution function. (From [6])

is off, with an RMS error of 107eV. This can also be seen in the IAW from unchanged VFP spectra shown at the simulated temperature (Fig. 4.14).

4.4 Heat Flux Measurements

OTS has been established as the routine diagnostic of plasma parameters such as density, temperature, and flow velocity. Additionally, because the dynamical form factors $S(\vec{k},\omega)$ (2.2) and $S^c(\vec{k},\omega)$ (2.28) are expressed in terms of the particle dis-

tribution functions they can be used to study non-equilibrium plasmas characterized by the super-Gaussian or distribution functions with nonzero heat fluxes. Analysis in this section is focused on the asymmetry of the ion-acoustic peaks in the low-frequency OTS spectrum (cf. Figs 2.17, 4.14). This asymmetry is caused by the electron distribution function's particle heat transport [107] (sec. 2.2.2).

Asymmetry in the ion-acoustic resonances can be produced by a current flowing in the plasma [2, 3], (Sec. 2.2.2) or by a return current of low-velocity electrons (shown in Fig. 4.12). A return current is necessary to cancel the current of fast, heat-carrying electrons in a plasma with nonzero heat flux. Both of these electron distribution functions have a similar effect on the observed IAW spectrum (2.21). In our spherically symmetric experiments, the geometry justifies an assumption of no significant magnetization of the plasma outflow. This allows us to restrict ourselves to investigating zero-current distribution functions in order to explain the IAW asymmetry.

Similar experiments to the gold sphere were also undertaken with different materials, allowing us to observe the Z dependence of transport effects (Fig. 4.13). These other spheres also had a different drive rise time, as is shown in figure 4.2. This causes the transport-dependant features in these other experiments to be delayed $\sim 200ps$, but otherwise these shots are largely similar to the description in section 4.1.

4.4.1 Spitzer-Härm Transport Results

We begin by fitting IAW spectra using SH distribution function (4.2) over the full duration of the OTS probe. Results of this fit are displayed in Fig. 4.16a in terms of the electron heat flux (4.3) by black dots within the gray background indicating errors in the measurements. Plasma is assumed to be spherically symmetric, with radial temperature gradient producing the signed Knudsen number $\delta_T = \lambda_{ei} \frac{d}{dx} \ln(T_e)$. This parameter is fit to the asymmetry of the IAW resonances (seen in the raw experimental data of Fig. 2.6 and in Fig. 4.14).

Due to the spherical symmetry of the experiment, the resulting particle heat flux

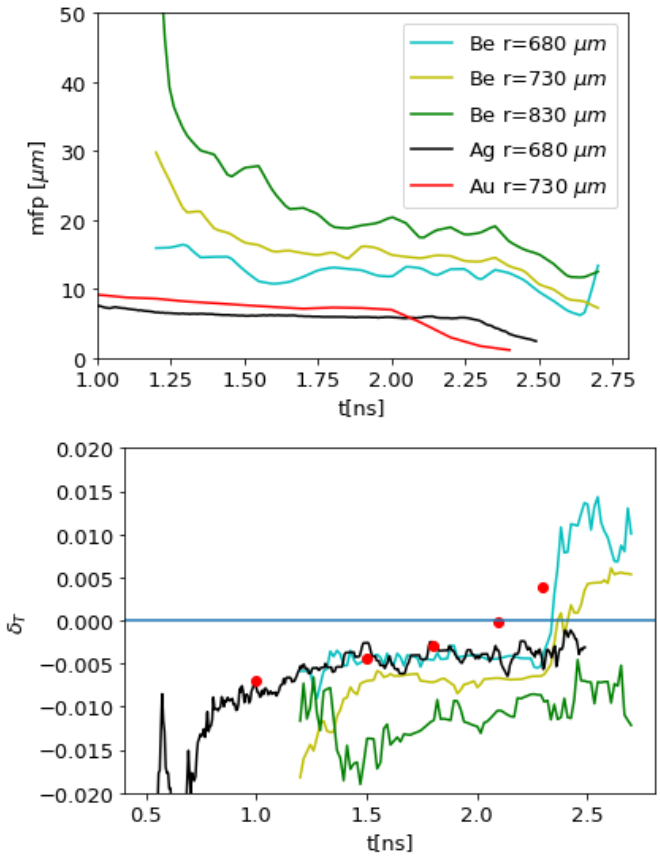

Figure 4.13: Mean free path and $\delta_T = \lambda_{ei} \frac{d}{dx} \ln(T_e)$ from simulations for Au, Ag and Be sphere experiments. Gold δ_T values (red dots) are taken from the simulated profiles (Fig. 4.11) while the other elements use time resolved simulations of T_e at different locations. Higher Z reduces electron mean free path, but also increases temperature and reduces temperature gradients, so increases in locality of heat transport for higher Z plasmas are minimal.

away from the target can be integrated around the spherical shell at the OTS radius of 735μm to find the power of particle transport. The particle heat flux away from the sphere grows from 0 after $\approx$ 1ns, reaching $0.4TW$ before reversing direction at 2ns when the drive is off, cf. Fig. 4.16a.

We have also compared this experimental measurement of the SH heat flux to the results of radiation-hydrodynamic simulation where the SH heat flux is calculated from the gradients given by the analytical fits of the profiles, Eqns. (4.7), (4.8), Fig. 4.11 (section 4.3.1). These gradients are averaged over the probed region, weighting by

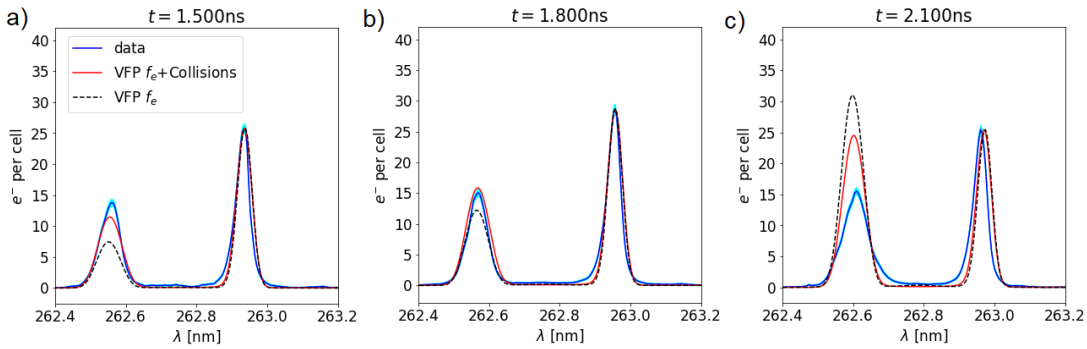

Figure 4.14: IAW data (blue) in photo-electrons produced per CCD cell, and spectra from VFP EDFs with collisions (red) and without collisions (black). Flow velocity is fit to the IAW data while all other parameters are generated from the simulated profiles (Fig. 4.11). Figures a) and b) show good agreement with temperature (Seen in IAW separation) before the drive is turned off at 2ns. (From [6])

laser area and plasma density. The mean free-path over scale lengths from these profiles for $t = (1.0, 1.5, 1.8, 2.1, 2.3)ns$ are $\delta T = (-0.00689, -0.00442, -0.00296, -0.000261, 0.00381)$ and $\delta n = (-0.0373, -0.0320, -0.0291, -0.0205, -0.00744)$ (4.5). The resulting SH heat flux (large red dots, Fig. 4.16a) shows a similar reversal around the drive turn-off, but there are large discrepancies with the experimental SH-based measurement (black), which can be seen in Fig. 4.16a.

The SH model of heat transport is expected to fail for weekly collisional plasmas, where a lack of electron collisions results in limited heat flux at short distances and pre-heat at larger distances as electrons stream past the temperature profile scale length. However, this typically happens around $\delta T \approx \frac{0.06}{\sqrt{Z}}$, significantly higher than the simulated profiles suggest for the gold plasma.

Furthermore, the plasmas with lower collisionality appear to lack some of these discrepancies. Beryllium spheres shot with a similar geometry to the gold sphere experiment [7] were also analyzed for IAW asymmetry. These shots had a significant discrepancy between simulated and measured density but had IAW asymmetries more consistent with simulated temperature gradients (Fig. 4.15).

The expected asymmetry for the beryllium spheres was found using the simulated

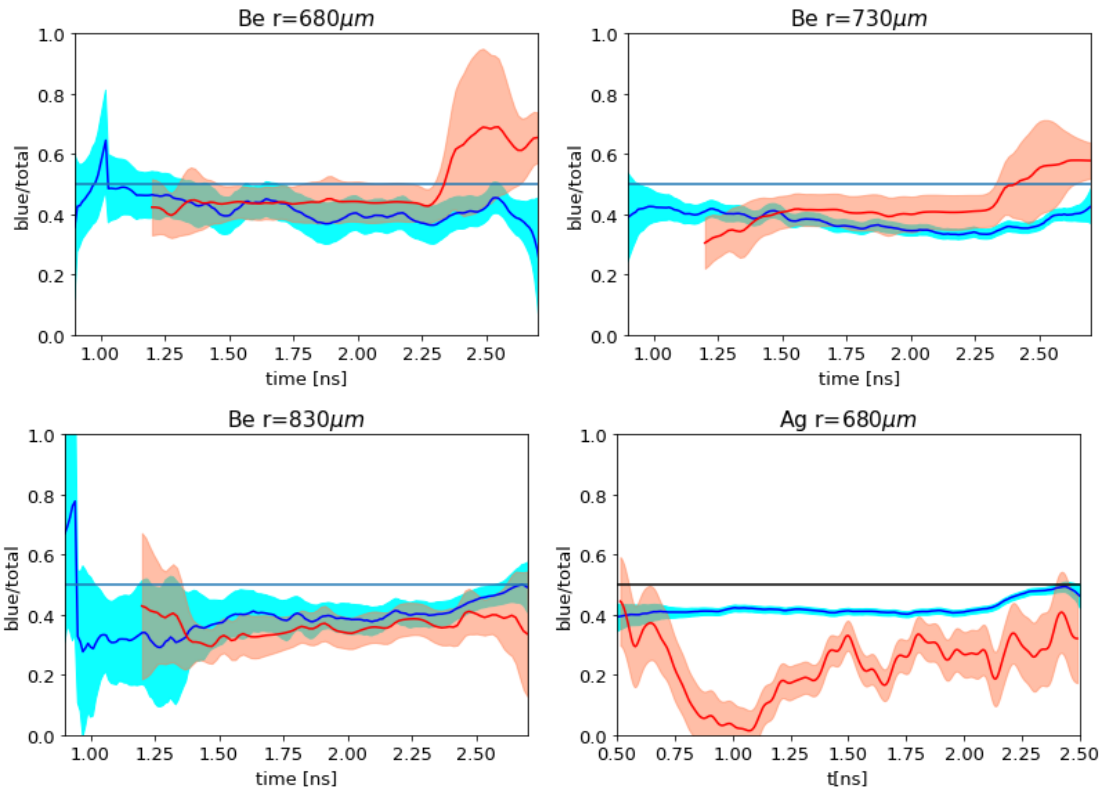

Figure 4.15: Measured IAW asymmetry (blue) and expected (red) observed in Be and Ag sphere shots, with values representing the total integrated signal in the blue-shifted IAW peak divided by the sum of both the blue and red-shifted peaks. Expected asymmetry is calculated from OTS-measured plasma parameters, with temperature scale lengths and uncertainties from SNB simulations.

temperature scale length with the collision frequency and IAW form factor calculated using the OTS-measured plasma conditions. This results in a more non-local plasma for beryllium than gold, with $\delta T \approx 0.01$. However, the asymmetry observed appears to match the asymmetry from SH transport using the simulated temperature scale length in the Be experiments much better than the Au and Ag ones, as seen in figures 4.15. The deviation of the IAW asymmetry away from 0.5 is linear with δ_T for $\delta_T < 0.01$, so this indicates heat flux is modeled fairly well by SH transport in the beryllium corona. The more local silver sphere has a discrepancy in asymmetry at a similar time to the gold shot (Fig. 4.16b). This indicates that the observed inhibition of thermal transport may only occur in high Z plasmas.

Figure 4.16a also includes our main gold sphere theoretical results, with red crosses representing the heat flux calculated using electron distribution functions from the VFP simulations in the OTS volume with the temperature (4.7) and density (4.8) profiles obtained in radiation-hydrodynamic simulations (cf. Figs. 4.3 and 4.11). By comparison to these results, interpretation of the OTS measured heat flux uses temperatures and densities from the basic OTS measurements, Figs. 4.4a,b, and the heat flux is evaluated from the properties of the experimental spectra using the Spitzer-Härm EDF and with no input from the radiation-hydrodynamic simulations.

Other EDFs, however, cannot be compared to this result since similar transport could still produce differing IAW asymmetries. The VFP simulated heat flux displayed in figure 4.16a therefore cannot be compared to an experimental observable directly. The physical processes included in the radiation-hydrodynamic simulations, such as the nonlocal transport model, SNB [37] and the atomic physics, are incompatible with measurements using a simple SH theory of thermal transport.

4.4.2 Thermal Transport Results with Non-Maxwellian Distributions

A more inclusive approach to comparing experimental results and theories is shown in Fig. 4.16b where we plot a ratio of areas under the blue and the red-shifted IAW peaks in the OTS spectra - blue continuous line with the light blue background defining errors inherent in the streak camera's light detection. This allows all the EDF asymmetries to be compared to the observed IAW. These experimental results are well reproduced by the VFP simulations (cf. Figs. 4.14) and the radiation-hydrodynamic generated density and temperature profiles at $t \geq 1.5ns$ and the simulated SH IAW spectra at $t \geq 1.8ns$.

To create the VFP-based IAW spectrum, discussed above, six electron distribution functions from different locations in the OTS volume are used to construct OTS spectra, which are then averaged weighted by probe area (sec. 2.1.1) and electron density.

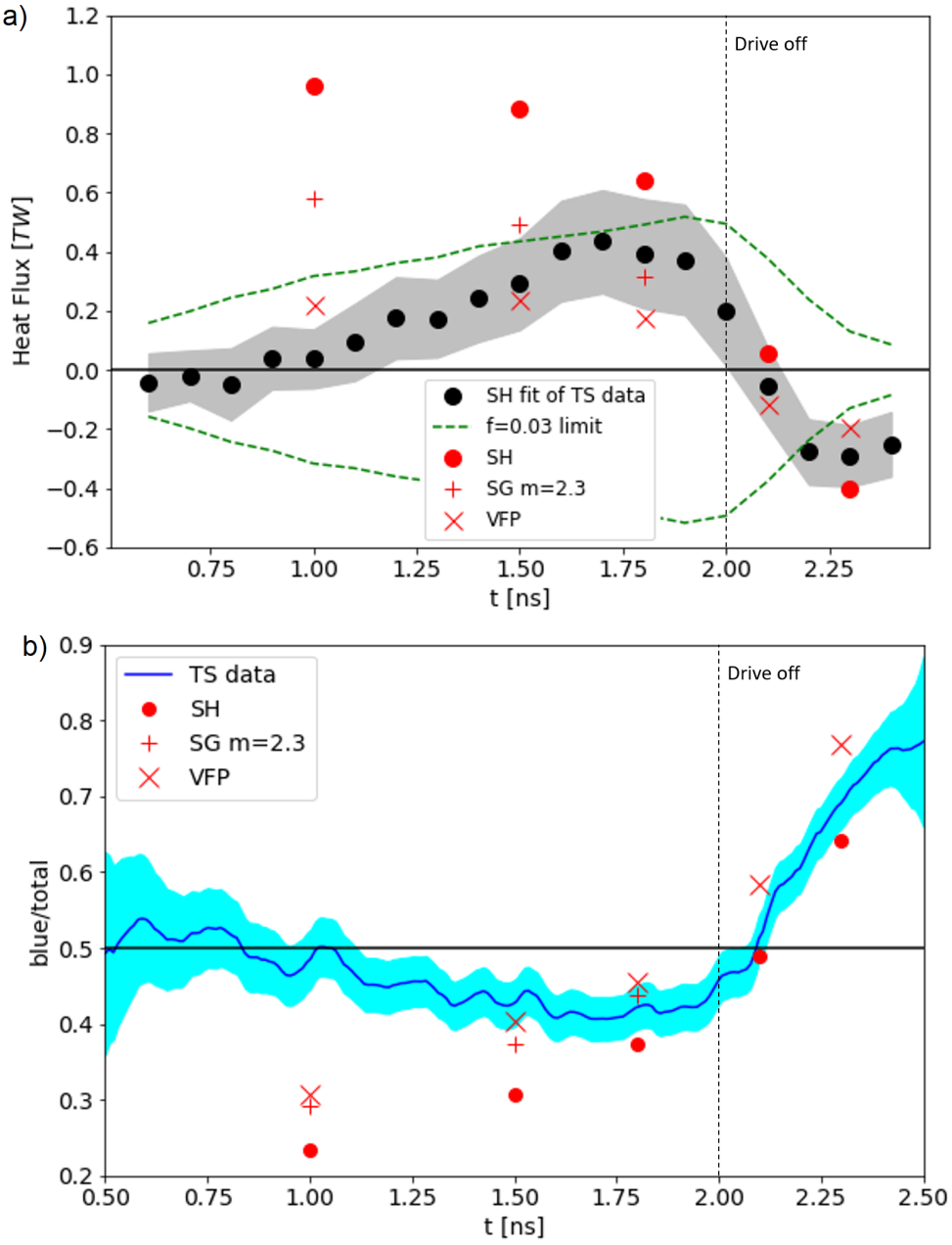

Figure 4.16: Electron heat flux out of the gold spherical target (a) and asymmetry of the ion acoustic wave (b). Various transport models applied to the simulated plasma profiles at the plasma parameters found with OTS measurements (Fig. 4.3) are shown in red. (a) shows heat flux found with SH fits to OTS data in black. A commonly used flux limiter of f=0.03 is shown in green in figure (a) for comparison. (b) shows the asymmetry of the IAW in blue, plotted as the integrated detected signal in the blue-shifted peak divided by the total IAW signal. The shaded error region represents the statistical error of the photoelectrons appearing in each IAW feature. (From [6])

The resulting IAW spectrum has asymmetry corresponding to the heat transport processes in the Vlasov-Fokker-Planck simulation. As shown in Figs. 4.14 and 4.16b, these are mostly consistent with the OTS data, with the exception of t=1ns where no significant asymmetry is detected in the experiment.

The surprising result in Fig. 4.16 is the almost complete disappearance of the heat flux early in time $t \leq 1ns$ in the OTS volume. This is illustrated by the lack of asymmetry in IAW peaks in Fig. 4.16b and in the corresponding blue peak fraction ~ 0.5 in the experimental asymmetry in Fig. 4.16b. Reduction of the heat flux would have to be significantly larger than the limit given by $f = 0.03$ and plotted for comparison in Fig. 4.16a to reproduce these results. The free streaming flux q_f limited by $f = 0.03$ agrees with VFP calculations at t=1 ns but it differs from the experimental measurement of the IAW peak asymmetry at that time. Note, that macroscopic theories of ICF plasmas [99, 100] have identified a need for changing flux inhibitors during plasma evolution to strongly reduced transport early on while the late time evolution was correctly described by the SH model.

The lack of asymmetry in the IAW resonances at 1 ns shows a significant discrepancy with both the SH and VFP electron particle distribution functions. This failure of radiation hydrodynamic simulations in obtaining correct particle transport occurs in spite of a reasonable agreement between measured and simulated temperatures and densities at early times. Closer examination of the time evolution of these parameters, cf. Figs. 8 and 9 in Ref. [8], show different increase rates of electron densities and temperatures early in time. Further observation has been provided by the ongoing campaign in Be plasmas where no such initial disappearance of the heat fluxes has been observed, thus suggesting that some ionization-dependent process specific to high-Z plasmas such as radiation transport or super-Gaussian distributions may be causing this discrepancy.

If high super-Gaussian exponents are used in the fits of the OTS spectra, the disappearance of the heat flux could be explained by the effect of the density gradient

as shown in the local transport theory (4.5), (4.6). To match the early time OTS data using local transport closures, $m \approx 3.8$ is required to eliminate asymmetry in the ion-acoustic resonances and reduce thermal flux to zero, as seen in Fig. 4.10b. However, such a high m-coefficient would significantly alter the results of the OTS fits for temperature and density. Note that f_{SG} (4.4) $m = 2.3$, which is consistent with (2.25), changes $T_e(t)$ and $n_e(t)$ by more than 10% as demonstrated in Figs 4.4c and d, but has a small effect on the heat flux calculations, cf. Fig. 4.16 b. However, calculated super-Gaussian exponents as well as the IB effects in the VFP distributions use a smooth laser intensity in space for the probe and heating beams. It is therefore possible that beam speckles may lead to higher-m super-Gaussian electron distributions, as the OTS signal will disproportionately come from higher intensity speckles in the probe. We can see that the direct effects of such a distribution would be to reduce heat flux and improve the agreement with the data (Fig. 4.16 b), but an analysis of the full effect of this would require large-scale kinetic simulations to justify its existence since the SNB simulations used to construct the temperature and density gradients do not use super-Gaussian effects on heat transport.

4.5 Driven EPW Spectra

Throughout the variety of spherical target shots that were conducted on different materials, resonant features in the EPW spectrum were sometimes seen. This occurred when the spectrum crossed the 210 nm line (Fig. 4.17).

The wavelength of 210 nm corresponds to scattered light with a frequency of 5ω, or 5 times the frequency of the unshifted Neodymium glass laser. A 5ω feature may be observed in OTS if there is a 1ω wave at the vector $\vec{k}$ corresponding to light scattering from the 4ω probe to 5ω collected light. The feature observed in the EPW spectra also disappears when the drive is off (figures 4.17, 4.2). This suggests some effects of the drive could be contributing to a wave that scatters the probe.

In the drive beams, the frequency of the light is firstly doubled to produce 2ω green

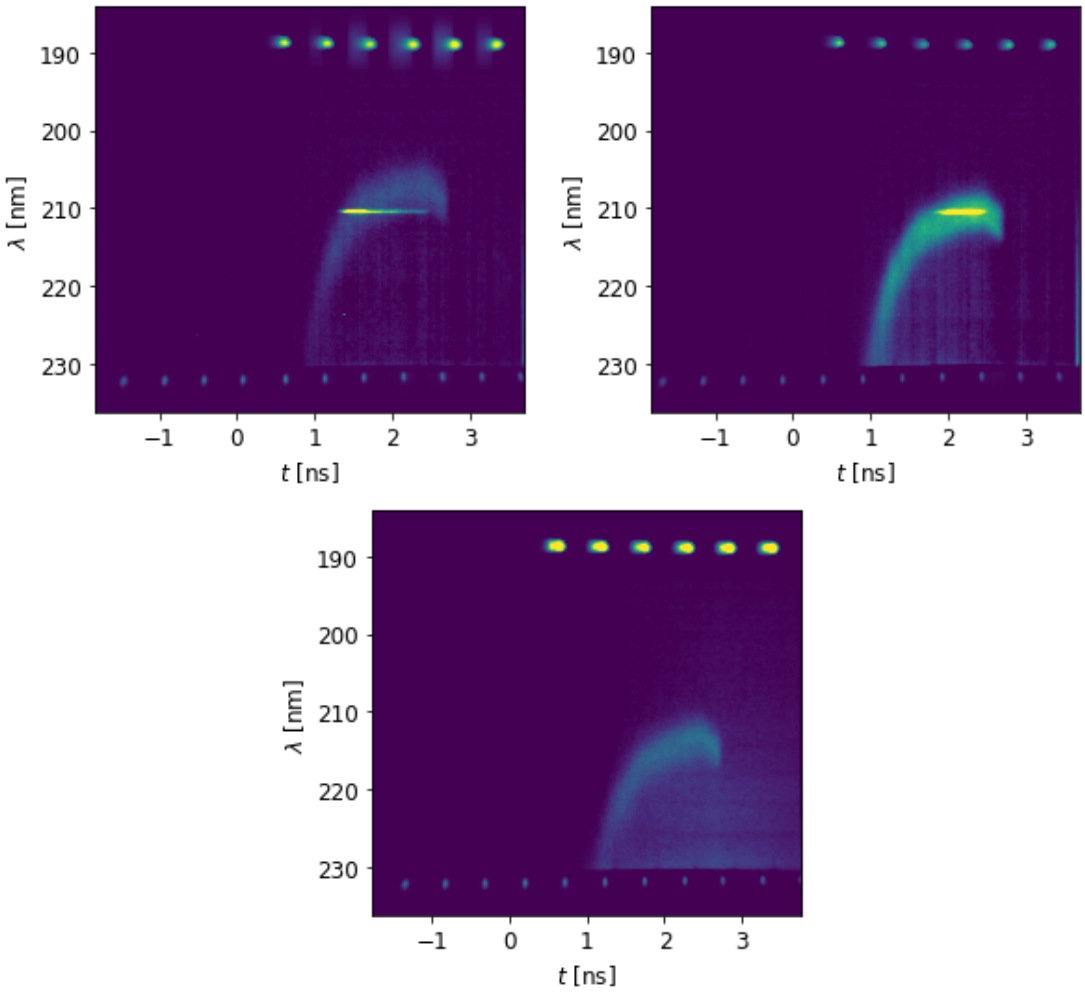

Figure 4.17: EPW spectra from Be sphere shots, pointed at a radius of 680, 730 and 780 μm respectively. A driven wave can be seen when the EPW crosses 210 nm at 680 and 730 μm while the drive laser is still on (Fig. 4.2), but is absent at 780 μm when the EPW never reaches this wavelength.

light, and then further increased to 3ω. Combining the 3ω and 2ω waves can create a beat: at any point where the two beams intersect and interfere, the laser field over time can be seen to be modulated by

$$\vec{E} \propto \cos(2\omega t) + \cos(3\omega t) = 2\cos(2.5\omega t)\cos(0.5\omega t). \tag{4.9}$$

This 0.5ω envelope contains the faster oscillations and flips sign every half wavelength, causing the effective frequency of the laser intensity variations and resulting

ponderomotive forces to be 1ω.

The corresponding wave vector of the beat is is $\vec{k}_{beat} = \vec{k}_{3\omega} - \vec{k}_{2\omega}$. This means the 2ω and 3ω light must be almost anti-parallel to create the required beat. Unconverted 2ω light has a focal spot scale around $1cm$ and comes from every beam, allowing light coming from most directions towards the sphere surface.

Rotating 3ω light to a direction away from the sphere surface can be done via refraction off the sphere surface. Using a simulated density model, a ray from beam number 35 can be found to reach the OTS volume, coming within $33\mu m$ of the nominal scattering location at 730 μm, within 3.6° of the required direction (Fig 4.18). The smallest dimension of the OTS volume has a radius of $35\mu m$ and the range in angles of 2.86° in the f/10 collection cone becomes a change of angle of 7.5° in the 3ω light, meaning that this ray can contribute to the required beat to enhance the 1ω feature.

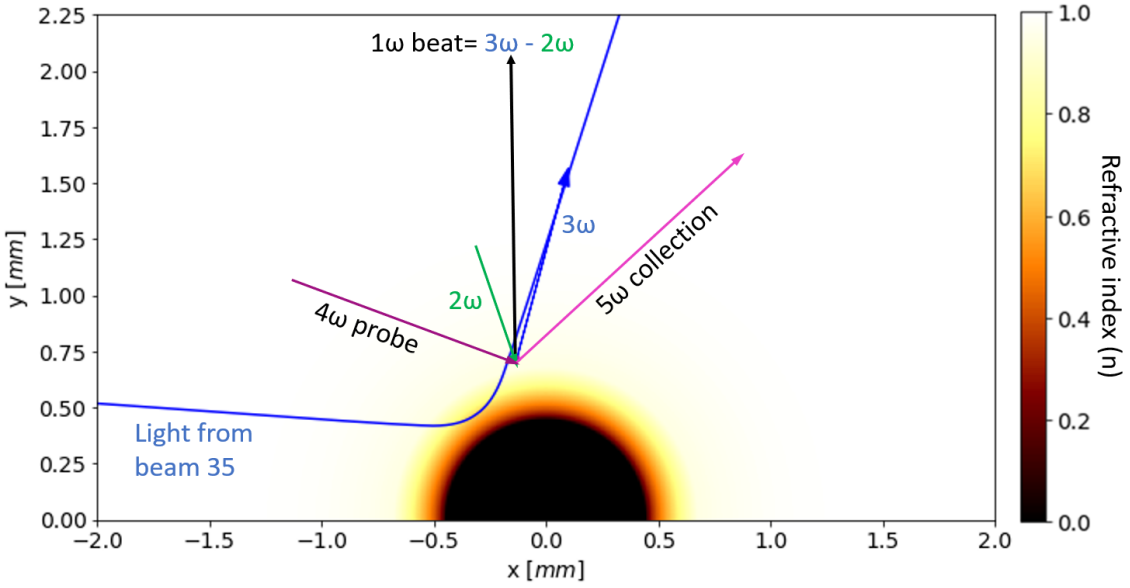

Figure 4.18: Scattering diagram for OTS light and driven beat wave at r=730 μm. The 2ω unconverted light and 3ω refracted drive create a 1ω beat wave with the correct $\vec{k}$ (shown in black) to scatter the 4ω probe to the OTS collection at 5ω (210.6 nm). A sample 3ω ray from beam 35 is shown on the left, with a refracted path reaching within 33 μm of the nominal OTS point, and within 3.6° of the nominal angle to produce the beat wave.

With two counter-propagating lasers, the ponderomotive force of the beat displaces

electrons, creating a beat in electron density (1.50,4.10) with frequency $|\omega_1 - \omega_2|$ and amplitude [17] $\frac{\delta n}{n}$ of

$$\frac{\delta n}{n} = -\frac{k^2 c^2}{\omega_{pe}^2} \frac{\chi_e}{1+\chi_e} \frac{U_p}{m_e c^2} \cos(\theta_{12}) \tag{4.10}$$

where θ_{12} is the angle between the wave vectors of the two beams, and $U_p = \frac{2e^2 |\vec{E}_{01} \cdot \vec{E}_{02}|}{m_e(\omega_1+\omega_2)^2}$. Here $\vec{E}_{1,2}$ and $\omega_{1,2}$ are the maximum laser field and frequency of lasers 1 and 2 respectively, and v_{osc} is the maximum oscillation velocity of electron in the laser field.

In order to compare the amplitude of the resonance observed to the enhancement of amplitude expected by the beating lasers, it is important to make sure the observed signal in the OTS spectrum is far below the saturation intensity of the streak camera. To this end, the visible driven wave below the EPW frequency is chosen, at $r = 680\mu m$ (Fig. 4.17).

The angle between the 3ω and 2ω light in figure 4.18 is 142.7°. The 3ω drive in total has an intensity at the target surface $r = 430\mu m$ of $5 \times 10^{14} W/cm^2$. The unconverted 2ω light is expected to have an intensity at the target around $2 \times 10^9 W/cm^2$.

Both intensities will be lower by a factor of 0.4 above the target at $r = 0.68$. To see the upper bound of the density fluctuations that could be driven, we can use these lowered total intensities as the intensities of the beat waves in their required directions. Assuming parallel polarizations between the 2ω and 3ω light, this gives a normalized ponderomotive potential amplitude of $\frac{U_p}{m_e c^2} = 2.58 \times 10^{-8}$. From the fit density and temperature from the rest of the OTS spectrum 2 ns into the shot, $\frac{\chi_e}{1+\chi_e} = 6.3$ at the 5ω driven wave.

This suggest a driven wave amplitude $\frac{<|\delta n|>}{n} = 2.87 \times 10^{-6}$. To find the signal we expect to scatter from these fluctuations, we can compare the amplitude to the density perturbations from OTS [12]:

$$\frac{<\delta n^2>}{n^2} = -\frac{1}{n_e (2\pi)^4} \int dk^3 \int_{-\infty}^{\infty} S(k,\omega) d\omega \tag{4.11}$$

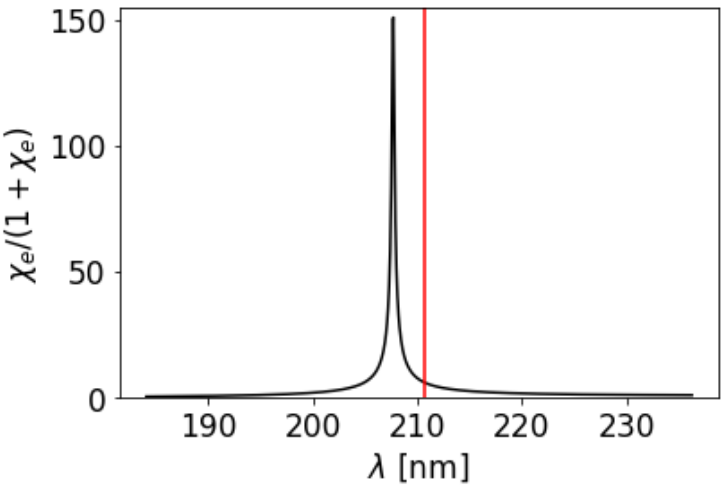

Figure 4.19: EPW resonance factor $\frac{\chi_e}{1+\chi_e}$ for the resonance at $t = 2ns$ for the $680\mu m$ Be sphere shot. The 5ω driven wave is shown in red at 210.6 nm with $\frac{\chi_e}{1+\chi_e} = 6.3$

The integral over dk^3 encompasses all k values contribution to a specific frequency shift, but as these k values only correspond to the collection cone angles (sec. 2.3), $S(k,\omega)$ does not change significantly over these vectors, and the integrals can be separated: $\int dk^3 \approx \delta\theta^2 k^2 \pi (k_{max} - k_{min})$ (Fig. 2.18). For the 680 μm shot, this shows that $\frac{\delta n}{n} = 2.58 \times 10^{-6}$ for the thermal EPW spectrum.

Scattered power is linear with δn^2, so we would expect 24% more scattered light in the driven wave at this point than we have in the EPW spectrum. This would suggest that we would have $\sim$ 307 photo-electrons in the resonance in the $5ps$ pixel duration used to sample the EPW spectrum, which is much more than the observed $\sim$ 50 photoelectrons per time step (Fig. 4.20).

A reduced number of photo-electrons by a factor of $\sim$ 6 is plausible in this case. The laser intensity of the 3ω drive was assumed to be similar to the drive intensity on the target, while this could be altered by focusing or absorption in the plasma. Polarization of the 2ω and 3ω light could also reduce the amplitude of the resulting beat. The 3ω drive is spread over a range of angles and focused on a small radial location. Assessing the magnitude of these effects, however, would require a more precise description of the density gradient in the plasma. The conditions of the beat

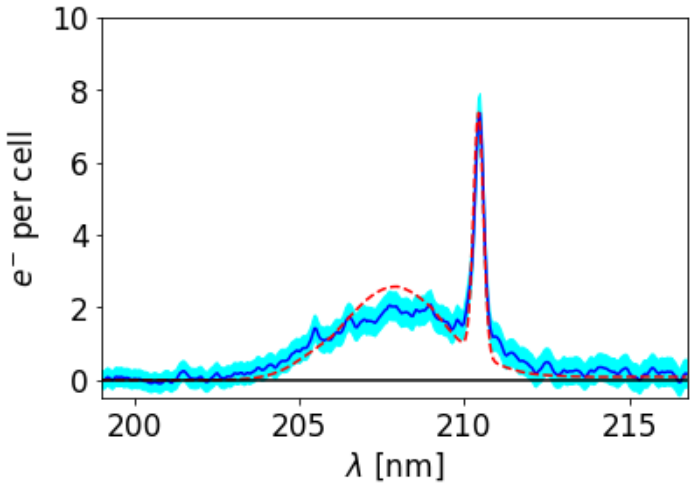

Figure 4.20: EPW and driven wave at 2 ns in the shot with OTS at r=680 μm. The fit of the blue-shifted EPW is shown in red, with the data in blue, averaged over 56 pS. An additional 50 photo-electrons are included at $\lambda = 210.6$, matching the observed driven wave.

also change over the volume of the OTS location, which could limit the available light. These effects could all plausibly explain the discrepancy in the amplitude of the beat.

Although this driven wave is only visible in a small number of shots with high electron densities, the beat is likely present in the plasma in a much larger number of shots. The presence of the OTS probe is not required for this effect, meaning that any location with high plasma density and counter-propagating 2ω and 3ω light could contain this resonant beat. With light from many different drive beams, a variety of $\vec{k}$ vectors are available, meaning each location in the plasma has many samples of the EPW dispersion relation (2.5) increasing the potential to enhance the driven wave. It is possible that this could significantly alter the drive beam's absorption and transmission through the corona.

Chapter 5

Summary and Conclusions

In Chapter 2 we detailed the effects of various plasma conditions on the electron plasma wave and ion acoustic wave spectra. These included magnetized plasma, highly collisional plasma ($\lambda_{ii} \ll k^{-1}$), laser-heated plasma with altered electron distribution functions, and plasma with large temperature or density gradients. The modifications to the spectrum created by the measurement optics including the range of scattering angles and transmission differences are also discussed. The signal and related error expected from optical Thomson scattering is calculated and compared to sources of background.

The techniques developed here will continue to be used in future Thomson scattering experiments. Additionally, we intend to optimize an OTS system to observe the spectral effects of magnetized electrons, providing a highly precise and localized field measurement. The spectral effects of the Thomson scattering optics will also be applied and revised for the new 5ω optical Thomson scattering system currently under development.

In Chapter 3, we explored the capabilities and limitations of optical Thomson scattering in a counter-streaming plasma, and measured the resulting magnetic field structure in Weibel-unstable plasma and in magnetic re-connection. To this end, we generated Thomson scattering spectra from kinetic simulations, validating it's diagnostic capability in experiments. We also measured the formation of collisionless

shocks and the resulting ion heating in counter-streaming plasma.

While the optical Thomson scattering measurements conducted in counter-streaming plasma have provided detailed measurements of the field structure and density evolution, there are still many properties of collisionless shocks left to measure. Ion heating is highly non-isotropic and could be measured at different scattering angles to gain a more complete picture of the energy exchange at shock formation. The plasma density may also have large scale structures, which could be measured with position resolution or large scattering angles. The initial growth rate of the Weibel instability in simulations is sensitive to many plasma conditions, which could be tested for their resulting growth rate of magnetic fields. Finally, the Biermann field has been observed to cause the formation of large structures around the edge of ablating plasmas. We will attempt to use OTS spectra in these features to measure the structure and scale of these fields.

In Chapter 4, we measured heat transport in the ablated plasma from different spherical targets. Agreement between optical Thomson scattering observations and local transport theory was found late in the gold shot, but larger discrepancies were seen early on. This discrepancy was reduced when using Super-Gaussian electron distributions and non-local transport generated with Vlasov-Fokker-Planck simulations, but the measured transport remained significantly smaller than expected.

The discrepancy in transport early on in the sphere shots appears to be more prevalent in high Z plasmas. We are currently investigating this effect across other metal spheres.

Bibliography

[1] G. Swadling, C Bruulsema, W. Rozmus, and J. Katz, "Quantitative assessment of fitting errors associated with streak camera noise in thomson scattering data analysis," *Rev. Sci. Instrum.*, vol. 94, p. 043 503, 2022.

[2] C Bruulsema *et al.*, "On the local measurement of electric currents and magnetic fields using thomson scattering in weibel-unstable plasmas," *Phys. Plasmas*, vol. 27, p. 052 104, 2020.

[3] G. Swadling *et al.*, "Measurement of kinetic-scale current filamentation dynamics and associated magnetic fields in interpenetrating plasmas," *Phys. Rev. Lett.*, vol. 124, p. 215 001, 2020.

[4] F. Fiuza *et al.*, "Electron acceleration in laboratory-produced turbulent collisionless shocks," *Nature Physics*, vol. 16, p. 916, 2020.

[5] L. G. Suttle *et al.*, "Collective optical thomson scattering in pulsed-power driven high energy density physics experiments," *Rev. Sci Instrum.*, vol. 92, p. 033 542, 2021.

[6] C Bruulsema *et al.*, "Characterization of thermal transport and evolution of au plasma in icf experiments by thomson scattering," *Phys. Plasmas*, vol. 29, p. 12 304, 2022.

[7] W. A. Farmer *et al.*, "Validation of heat transport modeling using directly driven beryllium spheres," *Phys. Plasmas*, vol. 27, p. 082 701, 2020.

[8] W. A. Farmer *et al.*, "Investigation of heat transport using directly driven gold spheres," *Phys. Plasmas*, vol. 28, p. 032 707, 2021.

[9] A. Milder *et al.*, "Direct measurement of the return current instability in a laser-produced plasma," *Phys. Rev. Lett.*, vol. 129, p. 115 002, 2022.

[10] A. H Compton, "A quantum theory of the scattering of x-rays by light elements," *Phys. Rev.*, vol. 21, p. 483, 1923.

[11] J. D. Jackson, *Classical electrodynamics*, 3rd ed. New York, NY: Wiley, 1999, ISBN: 9780471309321. [Online]. Available: http://cdsweb.cern.ch/record/490457.

[12] D. H. Froula, S. H. Glenzer, N. C. Luhmann, and J Sheffield, *Plasma Scattering of Electromagnetic Radiation: Theory and Measurement Techniques*. Elsevier, 2011.

[13] D. R. Nicholson, *Introduction to Plasma Theory*. J. Wiley and Sons, New York, 1983.

[14] E. L Lindman and M. A Stroscio, "On the relativistic corrections to the ponderomotive force," *Nucl. Fusion*, vol. 17, p. 619, 1977.

[15] A. V Gaponov and A. M. Miller, "Potential wells for charged particles in a high-frequency electromagnetic field," *Zh. Eksp. Teor. Fiz.*, vol. 34, p. 168, 1958.

[16] W. Kruer, *The Physics Of Laser Plasma Interactions*. CRC Press, 2003.

[17] P. Michel *et al.*, "Saturation of multi-laser beams laser-plasma instabilities from stochastic ion heating," *Phys. Plasmas*, vol. 20, p. 056 308, 2013.

[18] A. Brantov, V. Y. Bychenkov, V. T. Tikhonchuk, W. Rozmus, and V. K. Senecha, "Plasma fluctuations driven by a randomized laser beam," *Phys. Plasmas*, vol. 8, p. 3002, 1999.

[19] C. M. Huntington *et al.*, "Observation of magnetic field generation via the weibel instability in interpenetrating plasma flows," *Nature Physics*, vol. 11, pp. 173–176, 2015.

[20] W. Fox, J. Park, W. Deng, G. Fiksel, A. Spitkovsky, and A. Bhattacharjee, "Electron heating and energy inventory during asymmetric reconnection in a laboratory plasma," *Phys. Plasmas*, vol. 24, 2017.

[21] H. Takabe *et al.*, "High-mach number collisionless shock and photo-ionized non-lte plasma for laboratory astrophysics with intense lasers," *Plasma Phys. Controlled Fusion*, vol. 50, p. 12, 2008.

[22] R. Davidson, D. Hammer, I. Haber, and C. Wagner, "Nonlinear development of electromagnetic instabilities in anisotropic plasmas," *The Physics of Fluids*, vol. 15, p. 317, 1972.

[23] H. Alfvén, "On the motion of cosmic rays in interstellar space," *Phys. Rev.*, vol. 55, p. 425, 1939.

[24] E. S. Weibel, "Spontaneously growing transverse waves in a plasma due to an anisotropic velocity distribution," *Phys. Rev. Lett.*, vol. 2, p. 83, 1959.

[25] P. A. Sweet, "The neutral point theory of solar flares," *Phys. Plasmas*, vol. 13, p. 055 501, 1958.

[26] P. E. N., "Sweet's mechanism for merging magnetic fields in conducting fluids," *J. Geophys. Res.*, vol. 62, p. 509, 1957.

[27] P. H. E., "Magnetic field annihilation," *NASA Spec. Publ.*, vol. 50, p. 425, 1964.

[28] F. F. Chen, *Introduction to Plasma Physics and Controlled Fusion*. Plenum Press, 2016.

[29] D. Ryutov, N. Kugl, H.-S. Park, C. Plechaty, B. Remington, and J. Ross, "Intra-jet shocks in two counter-streaming, weakly collisional plasma jets," *Phys. Plasmas*, vol. 19, p. 074 501, 2012.

[30] P. Mora and R. Pellat, "Self-similar expansion of a plasma into a vacuum," *The Physics of Fluids*, vol. 22, p. 2300, 1979.

[31] A. V. Gurevich, L. V. Pariiskaya, and L. P. Pitaevskii, "Self-similar motion of rarefied plasma," *Soviet Physics JETP*, vol. 22, p. 449, 1966.

[32] S Ichimaru, *Basic Principles of Plasma Physics - A Statistical Approach*. W.A. Benjamin, Reading, 1973.

[33] L. Spitzer and R. Härm, "Transport phenomena in a completely ionized gas," *Phys. Rev.*, vol. 89, p. 977, 1953.

[34] A. S. Richardson, "2019 nrl plasma formulary," *Naval Research Laboratory*, p. 20 375, 2019.

[35] E. M. Epperlein, "Effect of electron collisions on ion-acoustic waves and heat flow," *Phys. Plasmas*, vol. 1, p. 109, 1994.

[36] V. Y. Bychenkov, W. Rozmus, V. T. Tikhonchuk, and A. Brantov, "Nonlocal electron transport in a plasma," *Phys. Rev. Lett.*, vol. 75, p. 4405, 1995.

[37] G. P. Schurtz, P. D. Nicolaï, and M. Busquet, "A nonlocal electron conduction model for multidimensional radiation hydrodynamics codes," *Phys. Plasmas*, vol. 7, no. 10, pp. 4238–4249, 2000.

[38] I. C. London. "Magpie." (2022), [Online]. Available: https://www.imperial.ac.uk/plasma-physics/magpie/ (visited on 12/02/2022).

[39] J. D. Lawson, "Some criteria for a power producing thermonuclear reactor," *Proc. Phys. Soc. B*, vol. 70, p. 6, 1957.

[40] L. L. N. Security. "Nif and photon science." (2022), [Online]. Available: https://lasers.llnl.gov/ (visited on 12/02/2022).

[41] L. for Laser Energetics. "Omega laser facility - laboratory for laser energetics." (2022), [Online]. Available: https://www.lle.rochester.edu/index.php/omega-laser-facility-2/ (visited on 12/02/2022).

[42] P. Datte *et al.*, "The design of the optical thomson scattering diagnostic for the national ignition facility," *Review of Scientific Instruments*, vol. 87, 11E549, 2016.

[43] J. Katz, R. Boni, R. Rivlis, C. Muir, and D. H. Froula, "A pulse-front-tilt–compensated streaked optical spectrometer with high throughput and picosecond time resolution," *Review of Scientific Instruments*, vol. 87, 11E535, 2016.

[44] J. Katz, R. Boni, C. Source, R. Follett, M. J. S. III, and D. H. Froula, "A reflective optical transport system for ultraviolet thomson scattering from electron plasma waves on omega," *Review of Scientific Instruments*, vol. 83, p. 10 349, 2012.

[45] P. Datte, G. James, P. Celliers, D. Kalantar, and G. Vergel de Dios, "Gated photocathode design for the p510 electron tube used in the national ignition facility (nif) optical streak cameras," *Proceedings of the SPIE*, vol. 9591, p. 0D13, 2015.

[46] C Bruulsema *et al.*, *Characterization of thermal transport and evolution of au plasma in icf experiments by thomson scattering - ts data*, https://doi.org/10.5281/zenodo.4951053, 2021.

[47] A. Brantov, V. Y. Bychenkov, and W. Rozmus, "Electrostatic response of a two-component plasma with coulomb collisions," *Phys. Rev. Lett.*, vol. 108, p. 205 001, 2012.

[48] A. Brantov, V. Y. Bychenkov, and W. Rozmus, "Ion acoustic instability driven by a temperature gradient in laser-produced plasmas," *Phys. Plasmas*, vol. 8, p. 3558, 2001.

[49] A. B. Langdon, "Nonlinear inverse bremsstrahlung and heated-electron distributions," *Phys. Rev. Lett.*, vol. 44, no. 9, p. 575, 1980.

[50] J. P Matte *et al.*, "Non-maxwellian electron distributions and continuum x-ray emission in inverse bremsstrahlung heated plasmas," *Plasma Phys. Contr. Fusion*, vol. 30, p. 1665, 1988.

[51] S. H. Glenzer, K. G. Estabrook, R. W Lee, B. J MacGowan, and W. Rozmus, "Detailed characterization of laser plasmas for benchmarking of radiation-hydrodynamic modeling, journal of quantitative spectroscopy and radiative transfer," *JQSRT*, vol. 65, pp. 253 –271, 2000.

[52] E. Fourkal *et al.*, "Electron distribution function in laser heated plasmas," *Phys. Plasma*, vol. 8, pp. 550–556, 2001.

[53] A. L. Milder *et al.*, "Evolution of the electron distribution function in the presence of inverse bremsstrahlung heating and collisional ionization," *Phys. Rev. Lett.*, vol. 124, p. 025 001, 2020.

[54] B. B. Afeyan, A. E. Chou, J. P. Matt, R. Town, and W. Kruer, "Kinetic theory of electron-plasma and ion-acoustic waves in nonuniformly heated laser plasmas," *Phys. Rev. Lett.*, vol. 80, pp. 2322–2325, 1997.

[55] W. Rozmus, A. Brantov, C. Fortmann-Grote, V. Y. Bychenkov, and S. Glenzer, "Electrostatic fluctuations in collisional plasmas," *Phys. Rev. E.*, vol. 96, p. 043 207, 2017.

[56] R. K. Follett *et al.*, "Plasma characterization using ultraviolet thomson scattering from ion-acoustic and electron plasma waves, review of scientific instruments," *Review of Scientific Instruments*, vol. 87, 11E401, 2016.

[57] W. Rozmus, A. V. Brantov, M. Sherlock, and V. Y. Bychenkov, "Return current instability driven by a temperature gradient in icf plasmas," *Plasma Phys. Controlled Fusion*, vol. 60, no. 1, p. 014 004, 2018.

[58] S. Ghosh, R. Boni, and P. A. Jaanimagia, "Optical and x-ray streak camera gain measurements," *Rev. Sci. Instrum.*, vol. 75, p. 043 503, 2004.

[59] C. A. Walsh, J. P. Chittenden, K. McGlinchey, N. P. L. Niasse, and B. D. Appelbe, "Self-generated magnetic fields in the stagnation phase of indirect-drive implosions on the national ignition facility," *Phys. Rev. Letters*, vol. 118, p. 155 001, 2017.

[60] W. A. Farmer *et al.*, "Simulation of self-generated magnetic fields in an inertial fusion environment," *Phys. Plasmas*, vol. 24, p. 052 703, 2017.

[61] S. H. Glenzer *et al.*, "Thomson scattering from laser plasmas," *Phys. Plasmas*, vol. 6, p. 2117, 1999.

[62] J. Ross *et al.*, "Magnetic field production via the weibel instability in interpenetrating plasma flows," *Phys. Rev. Lett.*, vol. 118, p. 185 003, 2017.

[63] M Borghesi *et al.*, "Laser-driven proton acceleration: Source optimization and radiographic applications," *Plasma Phys. Controlled Fusion*, vol. 50, p. 12, 2008.

[64] S. G"ode *et al.*, "Relativistic electron streaming instabilities modulate proton beams accelerated in laser-plasma interactions," *Phys. Rev. Lett.*, vol. 118, p. 194 801, 2017.

[65] J. A. Stamper and B. H. Ripin, "Faraday-rotation measurements of megagauss magnetic fields in laser-produced plasmas," *Phys. Rev. Lett.*, vol. 34, p. 138, 1975.

[66] N. Kugl *et al.*, "Self-organized electromagnetic field structures in laser-produced counter-streaming plasmas," *Nature Physics*, vol. 8, pp. 809–812, 2012.

[67] W. Fox *et al.*, "Filamentation instability of counterstreaming laser-driven plasmas," *Phys. Rev. Lett.*, vol. 111, p. 225 002, 2013.

[68] P. Tzeferacos *et al.*, "Laboratory evidence of dynamo amplification of magnetic fields in a turbulent plasma," *Nat. Comm.*, vol. 9, p. 591, 2018.

[69] B. Fried, "On the mechanism for instability of transverse plasma waves," *Phys. Fluids*, vol. 2, p. 337, 1959.

[70] M. Medvedev, "Weibel turbulence in laboratory experiments and grb/sn shocks," *Astrophys Space Sci*, vol. 307, 245–250, 2007.

[71] C. Ruyer, L. Gremillet, G. Bonnaud, and C. Riconda, "Analytical predictions of field and plasma dynamics during nonlinear weibel-mediated flow collisions," *Phys. Rev. Lett.*, vol. 117, p. 065 001, 2016.

[72] C. Ruyer and F. Fiuza, "Disruption of current filaments and isotropization of the magnetic field in counterstreaming plasmas," *Phys. Rev. Lett.*, vol. 120, p. 245 002, 2018.

[73] A. Spitkovsky, "Particle acceleration in relativistic collisionless shocks: Fermi process at last?" *The Astrophysical Journal Letters*, vol. 682, p. 1, 2008.

[74] M. Medvede and A. Loeb, "Generation of magnetic fields in the relativistic shock of gamma-ray burst sources," *The Astrophysical Journal*, vol. 526, pp. 697–706, 1999.

[75] E. Waxman, "Cosmological gamma-ray bursts and the highest energy cosmic rays," *Phys. Rev. Lett.*, vol. 75, p. 386, 1995.

[76] D. Ryutov, F. Fiuza, C. Huntington, and J. Ross, "Collisional effects in the ion weibel instability for two counter-propagating plasma streams," *Phys. Plasmas*, vol. 21, p. 032 701, 2014.

[77] C. Huntington *et al.*, "Observation of magnetic field generation via the weibel instability in interpenetrating plasma flows," *Phys. Plasmas*, vol. 11, 173–176, 2015.

[78] J. Ross *et al.*, "Collisionless coupling of ion and electron temperatures in counterstreaming plasma flows," *Phys. Rev. Lett.*, vol. 110, p. 145 005, 2013.

[79] J. Ross *et al.*, "Characterizing counter-streaming interpenetrating plasmas relevant to astrophysical collisionless shocks," *Phys. Plasmas*, vol. 19, p. 056 501, 2012.

[80] R. Henchen *et al.*, "Observation of nonlocal heat flux using thomson scattering," *Phys. Rev. Lett.*, vol. 121, p. 125 001, 2018.

[81] R. Fonseca *et al.*, "Osiris: A three-dimensional, fully relativistic particle in cell code for modeling plasma based accelerators," *Plasma Phys. Controlled Fusion*, vol. 2331, 342–351, 2002.

[82] R. Fonseca, S. Martins, L. Silva1, J. Tonge, F. Tsung, and W. Mori, "One-to-one direct modeling of experiments and astrophysical scenarios: Pushing the envelope on kinetic plasma simulations," *Plasma Phys. Controlled Fusion*, vol. 50, p. 124 034, 2008.

[83] D. Ryutov, N. Kugl, H. Park, C. Plechaty, B. Remington, and J. Ross, "Basic scalings for collisionless-shock experiments in a plasma without pre-imposed magnetic field," *Plasma Phys. Controlled Fusion*, vol. 54, p. 105 021, 2012.

[84] C. Ruyer, L. Gremillet, G. Bonnaud, and C. Riconda, "A self-consistent analytical model for the upstream magnetic-field and ion-beam properties in weibel-mediated collisionless shocks," *Phys. Plasmas*, vol. 24, p. 041 409, 2017.

[85] D. W. Forslund and C. R. Shonk, "Formation and structure of electrostatic collisionless shocks," *Phys. Rev. Letters*, vol. 25, p. 1699, 1970.

[86] T. E. Stringer, "Electrostatic instabilities in current-carrying and counterstreaming plasmas," *J. Nucl. Energy C*, vol. 6, p. 267, 1964.

[87] J. B. McBride, E. Ott, J. P. Boris, and J. H. Orens, *Physics of Fluids*, vol. 15, p. 041 409, 1972.

[88] L. V. Powers and R. L. Berger, "Effect of counterstreaming ion flow on ion acoustic modes and stimulated brillouin scattered light," *The Physics of Fluids*, vol. 31, p. 3109, 1988.

[89] M. V. Medvedev, M. Fiore, R. A. Fonseca, L. O. Silva, and W. B. Mori, "Long-time evolution of magnetic felds in relativistic gamma-ray burst shocks," *Astrophys. J.*, vol. 618, p. 75, 2004.

[90] M Hoshino and Y Lyubarsky, "Relativistic reconnection and particle acceleration," *Space Science Reviews*, vol. 173, p. 521, 2012.

[91] S. Totorica, M. Hoshino, T. Abel, and F. Fiuza, "Nonthermal electron and ion acceleration by magnetic reconnection in large laser-driven plasmas," *Phys. Plasmas*, vol. 27, p. 112 111, 2020.

[92] N. L. Loureiro and D. A. Uzdensky, "Magnetic reconnection: From the sweet–parker model to stochastic plasmoid chains," *Plasma Phys. Controlled Fusion*, vol. 62, p. 014 020, 2016.

[93] J. Hare *et al.*, "An experimental platform for pulsed-power driven magnetic reconnection," *Phys. Plasmas*, vol. 25, p. 055 703, 2018.

[94] E. G. Harris, "On a plasma sheath separating regions of oppositely directed magnetic field," *Nuovo Cim*, vol. 23, p. 521, 1962.

[95] L. G. Suttle *et al.*, "Interactions of magnetized plasma flows in pulsedpower driven experiments," *Plasma Phys. Control. Fusion*, vol. 62, p. 014 020, 2020.

[96] L. Suttle *et al.*, "Ion heating and magnetic flux pile-up in a magnetic reconnection experiment with super-alfvénic plasma inflows," *Phys. Plasmas*, vol. 25, p. 042 108, 2018.

[97] S. Lebedev *et al.*, "The structure of bow shocks formed by the interaction of pulsed-power driven magnetised plasma flows with conducting obstacles," *Nuovo Cim*, vol. 23, p. 072 713, 2017.

[98] M. A. Barrios *et al.*, "Developing an experimental basis for understanding transport in nif hohlraum plasmas," *Phys. Rev. Lett.*, vol. 121, p. 095 002, 2018.

[99] M. Rosen *et al.*, "The role of a detailed configuration accounting (dca) atomic physics package in explaining the energy balance in ignition-scale hohlraums," *High Energy Density Physics*, vol. 7, pp. 180–190, 2011.

[100] M. D. Rosen, ""rise shine" and "b good": 2 hypotheses that may unify au sphere and nif hohlraum modeling," *Bull. Am. Phys. Soc. 63 (11), UP11.00107, 60th Annual Meeting of the APS Division of Plasma Physics, Portland, OR.*, 2018.

[101] M. Sherlock, J. P. Brodrick, and C. P. Ridgers, "A comparison of non-local electron transport models for laser plasmas relevant to inertial confinement fusion," *Phys. Plasmas*, vol. 24, p. 082 706, 2017.

[102] P. Mora and H. Yahi, "Thermal heat-flux reduction in laser-produced plasmas," *Phys. Rev. A.*, vol. 26, p. 4, 1982.

[103] S. Brunner and Valeo, "Simulations of electron transport in laser hot spots," *Phys. Plasmas*, vol. 9, p. 923, 2002.

[104] J. Ross *et al.*, "Collisionless coupling of ion and electron temperatures in counterstreaming plasma flows," *Phys. Rev. Lett.*, vol. 110, p. 145 005, 2013.

[105] A. L. Milder *et al.*, "Measurements of non-maxwellian electron distribution functions and their effect on laser heating," *Phys. Rev. Lett.*, vol. 127, p. 015 001, 2021.

[106] G. Gregori *et al.*, "Effect of nonlocal transport on heat-wave propagation," *Phys. Rev. Lett.*, vol. 92, p. 205 006, 2004.

[107] J. Hawreliak *et al.*, "Thomson scattering measurements of heat flow in a laser-produced plasma," *J. Phys B: At. Mol. Opt. Phys.*, vol. 37, p. 1541, 2004.

[108] Q. Z. Yu *et al.*, "Nonlocal heat transport in laser-produced aluminum plasmas," *Physical of Plasma*, vol. 17, p. 043 106, 2010.

[109] D. Turnbull *et al.*, "Impact of the langdon effect on crossed-beam energy transfer," *Nature Physics*, vol. 16, pp. 181–185, 2020.

[110] C. P. Ridgers, A. G. R. Thomas, R. J. Kingham, and A. P. L. Robinson, "Transport in the presence of inverse bremsstrahlung heating and magnetic fields," *Phys. Plasmas*, vol. 15, p. 092 311, 2008.

[111] J. D. Moody *et al.*, "Progress in hohlraum physics for the national ignition facility," *Physical of Plasma*, vol. 21, p. 056 317, 2014.

[112] S. H. Glenzer *et al.*, "Thomson scattering from high z laser produced plasmas.," *Phys. Rev. Lett.*, vol. 82, p. 97, 1999.

[113] A. S. Joglekar, C. P. Ridgers, R. J. Kingham, and A. G. R. Thomas, "Impact of the langdon effect on crossed-beam energy transfer," *Phys. Rev. E.*, vol. 93, p. 043 206, 2016.

[114] J. J. Bissell, C. P. Ridgers, and R. J. Kingham, "Super-gaussian transport theory and the field-generating thermal instability in laser–plasmas," *New Journal of Physics*, vol. 15, p. 025 017, 2013.

[115] A. Brantov, V. Y. Bychenkov, and W. Rozmus, "Relaxation of a thermal perturbation in a collisional plasma," *Plasma Physics Reports*, vol. 32, pp. 337–343, 2006.

[116] A. Bell, R. G. Evans, and D. J. Nicholas, "Electron energy transport in steep temperature gradients in laser-produced plasmas.," *Phys. Rev. Lett.*, vol. 46, p. 243, 1981.

[117] G. Bekefi, *Radiation Processes in Plasmas*. J. Wiley and Sons, New York, 1966.

Appendix A: OTS Program

Code used to generate basic OTS spectra in Python is attached below. Special cases and other updates can be found at: https://github.com/Conotor/OTS.git

A.1 OTSplasma.py

The code below is used to generate electron and ion susceptibility for plasma in thermal equilibrium, as well as plasma with custom distribution functions of other shapes.

```
# helper functions for generating maxwellain OTS spectra
#Created on Fri Sep 2 21:51:32 2022, Colin Bruulsema

import numpy as np
import scipy.special as sps


# from scipy.special import gamma, factorial
# from scipy.special import gammainc
# from scipy.special import gammaincc

from scipy.interpolate import interp1d
# from scipy.interpolate import interp2d


#%%#########################################################################
#    plasma response integral [p106 Froula2011]

# = 1-2zexp(-z^2)\int_0^z exp(p^2)dp
#determines real factor of plasma response for maxwellian plasma species
#inputs: z=phase velocity / sqrt(2T/m)
def plaZre(z): #Rw(x_e)=1-2xexp(-x^2) int0x exp(p^2)dp
    val=0*z
    val=1.0-2.0*z*np.exp(-z**2)*0.5*np.sqrt(np.pi)*sps.erfi(z)
    if(hasattr(val, "__len__")):
```

```
        val[np.isnan(val)]=0
        val[np.isinf(val)]=0
    else:
        if(np.isnan(val) or np.isinf(val)):
            val=0
    return val


# = sqrt(pi) z exp(-z^2)
#determines imaginary factor of plasma response for maxwellian plasma
    species
#inputs: z=phase velocity / sqrt(2T/m)
def plaZim(z): #Rw(x_e)=1-2xexp(-x^2) int0x exp(p^2)dp
    val=0*z
    val=np.sqrt(np.pi)*z*np.exp(-(z**2))
    if(hasattr(val, "__len__")):
        val[np.isnan(val)]=0
        val[np.isinf(val)]=0
    else:
        if(np.isnan(val) or np.isinf(val)):
            val=0
    return val




#coptied to find cust #cbdo check maxv needs
def custZprime(in_xi, makea, maxv):

    maker = np.zeros(len(makea[0]))
    makei = np.zeros(len(makea[0]))
    makex = np.copy(np.real(makea[0])) #cbdo added real
    maker[:] = np.real(makea[1,:])
    makei[:] = np.imag(makea[1,:])
#    print(makea)
#    print(makex)
#    print(maker)
#    print(makei)
    ref = interp1d(makex, maker)
    imf = interp1d(makex, makei)


    length = len(in_xi)
    rout = np.zeros(length)
    iout = np.zeros(length)

    xder=-1.0
```

```
    if(in_xi[-1]>in_xi[0]):
        xder=1.0

    maxfrac=0.99
    ai=-1
    bi=-1
    if(xder>0):
        avec=np.array(np.where(in_xi < -1.00*maxfrac*maxv))
            #find(xi<-10,1,last); #last index where low
        bvec=np.array(np.where(in_xi > 1.00*maxfrac*maxv))
            #find(xi>10,1,first); #first index where high
    elif(xder<0):
        avec=np.array(np.where(in_xi > 1.00*maxfrac*maxv))
            #find(xi<-10,1,last); #last index where low
        bvec=np.array(np.where(in_xi < -1.00*maxfrac*maxv))
            #find(xi>10,1,first); #first index where high
    if len(avec[0])>0:
        ai=avec[0][-1]
    if len(bvec[0])>0:
        bi=bvec[0][0]

    if (ai<0)and(bi<0):
        rout[:] = 1*ref(in_xi[:]) #-1
        iout[:] = imf(in_xi[:])
    elif (ai<0):
        rout[0:bi] = 1*ref(in_xi[0:bi]) #-1
        rout[bi:length] = 0*1.0/(in_xi[bi:length])**(2)
        iout[0:bi] = imf(in_xi[0:bi])
#         iout[bi:length] = 1.0/in_xi[bi:length]**(2)
        iout[bi:length] = 0
    elif (bi<0):
        rout[ai+1:length] = 1*ref(in_xi[ai+1:length]) #1
        rout[0:ai+1] = 0*1.0/(in_xi[0:ai+1])**(2)
        iout[ai+1:length] = imf(in_xi[ai+1:length])
#         iout[0:ai+1] = 1.0/in_xi[0:ai+1]**(2)
        iout[0:ai+1] = 0
    else:
        rout[ai+1:bi] = 1*ref(in_xi[ai+1:bi]) #1
        rout[0:ai+1] = 0*1.0/(in_xi[0:ai+1])**(2)
        rout[bi:length] = 0*1.0/(in_xi[bi:length])**(2)
        iout[ai+1:bi] = imf(in_xi[ai+1:bi])
        iout[0:ai+1] = 0
        iout[bi:length] = 0
    zout = np.zeros([2,length])
    zout[0,:] = rout[:]
    zout[1,:] = iout[:]
    return zout
```

```
#needs 4 vte in each direction to work
def vtabmake(in_dvdist, in_v):
    amaxv=np.max(np.abs(in_v))
    maxv=np.max((in_v))
    minv=np.min((in_v))
    ximin = 1.0*minv #change this to c
    ximax = 1.0*maxv

    minmaxf=0.01

    xi = 1.0*in_v #now in v/c
    L = len(xi)
    N=4 #precision #was 4
    IPV=np.zeros(L)
    RP=np.zeros(L)
    # dvdistf = interp1d(in_v, in_dvdist, fill_value='extrapolate')
    dvdistf = interp1d(in_v, in_dvdist, fill_value=(0,0),
        bounds_error=False)
    for i in range(L):
        phi=(0.01*np.abs(xi[i])+1e-6*maxv) #defining how close to get to
            singularity
        dz=phi/N
        #nonth why this -1 +1
        zm = np.linspace((xi[i]-phi),ximin-minmaxf*amaxv,int(((xi[i]-phi)
        -(ximin-minmaxf*amaxv))/dz) )
        zp =
            np.linspace((xi[i]+phi),ximax+minmaxf*amaxv,int(((ximax+minmaxf*amaxv)
        -(xi[i]+phi))/dz) )

        Ip=0
        Im=0

        Ip=dz*sum(dvdistf(zp)/(zp-xi[i]))
        Im=dz*sum(dvdistf(zm)/(zm-xi[i]))
        IPV[i]=Ip+Im
        #evaluating real pole contribution
        RP[i]=4*phi*xi[i]
    dW = np.array(np.zeros(L), dtype=complex) # fix next line
    dW[:]=(IPV[:]+in_dvdist[:]*(-RP[:]-1j*np.pi))
    dWT = np.array([xi,dW])
    return dWT
```

```
#%%#####################################################################
#    electron and ion susceptibilty [p50 Froula2011]

#chi e
#chi_e= \omega_pe^2/k^2 \int_{-\infty}^{\infty} (k \cdot df/dv) / (w - kv
    -igamma)
#determines plasma response to electron denisty fluctuations
#inputs:
#    omg = wave frequency [rad/s]
#    sa = scattering angle [deg]
#    omgL = probe laser frequency [rad/s]
#    Te = electron temperature [keV]
#    ne = electron density [cm^-3]
#    ve=electron flow speed [c]
def chith_e(omg, sa,omgL,Te,ne,ve):
    c=2.99792458e8 #v light in m/s
    me=511 #kev
    omgpe=56400*np.sqrt(ne) #rad/s
    vte=np.sqrt(Te/me) #c
    kd=omgpe/(vte*c)
    sarad=sa*2*np.pi/360
    kL=np.sqrt(omgL**2-omgpe**2)/c
    omgs=omg+omgL
    ks=np.sqrt(omgs**2-omgpe**2)/c
    k=np.sqrt(kL**2+ks**2-2*ks*kL*np.cos(sarad))
    kkd=k/kd
    xe=((omg/k)-ve*c)/(c*vte*np.sqrt(2.0))
    imxe=(kkd**-2)*plaZim(xe)
    rexe=(kkd**-2)*plaZre(xe)
    return rexe+1j*imxe


#todo remove Te

#chi_i= \omega_pi^2/k^2 \int_{-\infty}^{\infty} (k \cdot df/dv) / (w - kv
    -igamma)
#determines plasma response to electron denisty fluctuations
#inputs:
#    omg = wave frequency [rad/s]
#    sa = scattering angle [deg]
#    omgL = probe laser frequency [rad/s]
#    Te = electron temperature [keV]
#    Ti = ion temperature [keV]
#    Z = ion charge = q/e
#    Ai=ion protons + nuetrons
#    ne = electron density [cm^-3]
```

```
#    vi=ion flow speed [c]
def chith_i(omg, sa,omgL,Te,Ti,Z,Ai,ne,vi):
    c=2.99792458e8 #v light in m/s
    me=511 #kev
    mproton=938300 #kev
    omgpe=56400*np.sqrt(ne) #rad/s
    vte=np.sqrt(Te/me) #c
    vti=np.sqrt(Ti/(mproton*Ai)) #c
    kd=omgpe/(vte*c)
    sarad=sa*2*np.pi/360
    kL=np.sqrt(omgL**2-omgpe**2)/c
    omgs=omg+omgL
    ks=np.sqrt(omgs**2-omgpe**2)/c
    k=np.sqrt(kL**2+ks**2-2*ks*kL*np.cos(sarad))
    kkd=k/kd
    xi=((omg/k)-vi*c)/(c*vti*np.sqrt(2.0))
    imxi=(kkd**-2)*plaZim(xi)*Z*Te/Ti
    rexi=(kkd**-2)*plaZre(xi)*Z*Te/Ti
    return rexi+1j*imxi

#%%#########################################################################


#chi_e= \omega_pe^2/k^2 \int_{-\infty}^{\infty} (k \cdot df/dv) / (w - kv
    -igamma)
#determines plasma response to electron denisty fluctuations, on 2d omega
    k map
#inputs:
#    omg = wave frequency [rad/s]
#    sa = scattering angle [deg]
#    omgL = probe laser frequency [rad/s]
#    Te = electron temperature [keV]
#    ne = electron density [cm^-3]
#    ve=electron flow speed [c]
def chith2D_e(omg, kvals,Te,ne,ve):
    c=2.99792458e8 #v light in m/s
    me=511 #kev
    omgpe=56400*np.sqrt(ne) #rad/s
    vte=np.sqrt(Te/me) #c
    kd=omgpe/(vte*c)
    k=kvals
    kkd=k/kd
    xe=((omg/k)-ve*c)/(c*vte*np.sqrt(2.0))

#    np.array([[1,2], [3, 4], [5, 6]]).flatten().reshape((3, 2))
    xesh=np.shape(xe)
    xefl=(xe).flatten()
```

```
    imxe=(kkd**-2)*plaZim(xefl).reshape(xesh)
    rexe=(kkd**-2)*plaZre(xefl).reshape(xesh)

    return rexe+1j*imxe

#chi_i= \omega_pi^2/k^2 \int_{-\infty}^{\infty} (k \cdot df/dv) / (w - kv
    -igamma)
#determines plasma response to electron denisty fluctuations, on 2d omega
    k map
#inputs:
#    omg = wave frequency [rad/s]
#    sa = scattering angle [deg]
#    omgL = probe laser frequency [rad/s]
#    Te = electron temperature [keV]
#    Ti = ion temperature [keV]
#    Z = ion charge = q/e
#    ne = electron density [cm^-3]
#    vi=ion flow speed [c]
def chith2D_i(omg, kvals,Te,Ti,Z,Ai,ne,vi):
    c=2.99792458e8 #v light in m/s
    me=511 #kev
    mproton=938300 #kev
    omgpe=56400*np.sqrt(ne) #rad/s
    vte=np.sqrt(Te/me) #c
    vti=np.sqrt(Ti/(mproton*Ai)) #c
    kd=omgpe/(vte*c)
    k=kvals
    kkd=k/kd
    xi=((omg/k)-vi*c)/(c*vti*np.sqrt(2.0))

    xish=np.shape(xi)
    xifl=xi.flatten()
    imxi=(kkd**-2)*plaZim(xifl).reshape(xish)*Z*Te/Ti
    rexi=(kkd**-2)*plaZre(xifl).reshape(xish)*Z*Te/Ti
    return rexi+1j*imxi

#%%#########################################################################
#    advanced electron and ion susceptibilty [p50 Froula2011]

#chi_i= \omega_pi^2/k^2 \int_{-\infty}^{\infty} (k \cdot df/dv) / (w - kv
    -igamma)
#determines plasma response to electron denisty fluctuations
#inputs:
#    omg = wave frequency [rad/s]
#    sa = scattering angle [deg]
#    omgL = probe laser frequency [rad/s]
#    dists = distributin functions ########################################
```

```
    todo label how
#    Z = ion charge = q/e
#    Ai=ion protons + nuetrons
#    ne = electron density [cm^-3]
def chicust_i(omg, sa,omgL,dists,ne,Z,Ai): #Te,Ti,Z
    c=2.99792458e8 #v light in m/s
    me=511 #kev
    mproton=938300 #kev
    mi=mproton*Ai
    omgpe=56400*np.sqrt(ne) #rad/s
    omgpi=omgpe*np.sqrt(Z*me/mi)
    sarad=sa*2*np.pi/360
    kL=np.sqrt(omgL**2-omgpe**2)/c
    omgs=omg+omgL
    ks=np.sqrt(omgs**2-omgpe**2)/c
    k=np.sqrt(kL**2+ks**2-2*ks*kL*np.cos(sarad))
    vel=((omg/k)/c) #v/c
    vemax=np.max(np.abs(vel))
    nmakea = vtabmake(dists[1], vel) #cbdo check if binning size changes
        in vtabmake, bad with non uniform vel
    Zpe = custZprime(vel,nmakea, vemax) ###################### numerical
    chiEre= (-(1.0/(c*k[:]/omgpi)**2))*(Zpe[0,:]) #me/mi
    chiEim= (-(1.0/(c*k[:]/omgpi)**2))*(-1j*Zpe[1,:]) #me/mi
    return chiEre+chiEim

#chi e
def chicust_e(omg, sa,omgL,dists,ne):
    c=2.99792458e8 #v light in m/s
    omgpe=56400*np.sqrt(ne) #rad/s
    sarad=sa*2*np.pi/360
    kL=np.sqrt(omgL**2-omgpe**2)/c
    omgs=omg+omgL
    ks=np.sqrt(omgs**2-omgpe**2)/c
    k=np.sqrt(kL**2+ks**2-2*ks*kL*np.cos(sarad))
    vel=((omg/k)/c) #v/c
    vemax=np.max(np.abs(vel))
    nmakea = vtabmake(dists[1], vel) #cbdo check if binning size changes
        in vtabmake, bad with non uniform vel
    Zpe = custZprime(vel,nmakea, vemax) ###################### numerical

    chiEre= (-(1.0/(c*k[:]/omgpe)**2))*(Zpe[0,:])
    chiEim= (-(1.0/(c*k[:]/omgpe)**2))*(-1j*Zpe[1,:])
    return chiEre+chiEim
```

A.2 OTSpower.py

Spectra are generated with the below functions

```
# functions for generating maxwellain OTS spectra
#Created on Fri Sep 2 23:24:44 2022, Colin Bruulsema

import numpy as np
import scipy.special as sps
import scipy.ndimage as spn

from src.OTSplasma import chith_e
from src.OTSplasma import chith_i
from src.OTSplasma import chicust_i

from src.OTSplasma import chith2D_e
from src.OTSplasma import chith2D_i

#%%#########################################################################

#s(k,omega)
#form factor for waves in thermal plasma
#inputs:
#    omg = wave frequency [rad/s]
#    sa = scattering angle [deg]
#    omgL = probe laser frequency [rad/s]
#    Te = electron temperature [keV]
#    Ti = ion temperature [keV]
#    Z = ion charge = q/e
#    Ai=ion protons + nuetrons
#    ne = electron density [cm^-3]
#    ve=electron velocity [c]
#    vi=ion velocity [c]
def skw(omg,sa,omgL,Te,Ti,Z,Ai,ne,ve,vi):
    chie=chith_e(omg, sa,omgL,Te,ne,ve)
    chii=chith_i(omg, sa,omgL,Te,Ti,Z,Ai,ne,vi)
    eps=chie+chii+1.0
    dispe=np.abs((1+chii)/eps)**2
    dispi=np.abs((chie)/eps)**2

    eps=1.0+chie+chii
    c=2.99792458e8 #v light in m/s
    me=511 #kev
    mproton=938300 #kev
    omgpe=56400*np.sqrt(ne) #rad/s
    sarad=sa*2*np.pi/360
    kL=np.sqrt(omgL**2-omgpe**2)/c
```

```
    omgs=omg+omgL
    ks=np.sqrt(omgs**2-omgpe**2)/c
    k=np.sqrt(kL**2+ks**2-2*ks*kL*np.cos(sarad))

    vte=np.sqrt(Te/me) #c
    vti=np.sqrt(Ti/(mproton*Ai)) #c
    fe=np.sqrt(1.0/(2*np.pi*vte**2*c**2))*np.exp(-0.5*((omg/k)-ve*c)**2
    /(vte**2*c**2))
    fi=np.sqrt(1.0/(2*np.pi*vti**2*c**2))
    *np.exp(-0.5*((omg/k)-vi*c)**2/(vti**2*c**2))
    skwe=(2*np.pi/k)*dispe*fe
    skwi=(2*np.pi*Z/k)*dispi*fi
    return (skwe+skwi)



#s(k,omega) #high alpha version of skw
#form factor for waves in thermal plasma
#inputs:
#    omg = wave frequency [rad/s]
#    sa = scattering angle [deg]
#    omgL = probe laser frequency [rad/s]
#    Te = electron temperature [keV]
#    Ti = ion temperature [keV]
#    Z = ion charge = q/e
#    Ai=ion protons + nuetrons
#    ne = electron density [cm^-3]
#    ve=electron velocity [c]
#    vi=ion velocity [c]
def skwha(omg,sa,omgL,Te,Ti,Z,Ai,ne,ve,vi):
    # print('startHA')
    # print(omg)
    chie=chith_e(omg, sa,omgL,Te,ne,ve)
    chii=chith_i(omg, sa,omgL,Te,Ti,Z,Ai,ne,vi)
    eps=chie+chii+1.0
    epse=chie+1.0
    dispe=np.abs((1+chii)/eps)**2
    dispi=np.abs((chie)/eps)**2

    eps=1.0+chie+chii
    c=2.99792458e8 #v light in m/s
    me=511 #kev
    mproton=938300 #kev
    omgpe=56400*np.sqrt(ne) #rad/s
    sarad=sa*2*np.pi/360
    kL=np.sqrt(omgL**2-omgpe**2)/c
```

```
omgs=omg+omgL
ks=np.sqrt(omgs**2-omgpe**2)/c
k=np.sqrt(kL**2+ks**2-2*ks*kL*np.cos(sarad))

# omgpe=56400*np.sqrt(ne) #rad/s
vte=np.sqrt(Te/me) #c
vti=np.sqrt(Ti/(mproton*Ai)) #c
fe=np.sqrt(1.0/(2*np.pi*vte**2*c**2))*np.exp(-0.5*((omg/k)-ve*c)**2
/(vte**2*c**2))
fi=np.sqrt(1.0/(2*np.pi*vti**2*c**2))
*np.exp(-0.5*((omg/k)-vi*c)**2/(vti**2*c**2))
skwe=(2*np.pi/k)*dispe*fe
skwi=(2*np.pi*Z/k)*dispi*fi
specnow=skwe+skwi

kd=omgpe/(vte*c)
#find resonance
negres=np.real(epse)*np.real(np.roll(epse,1))
negres[0]=0
omgres=omg[negres<0]
omgres_e=omgres[np.abs(omgres)>0.99*omgpe]
# print(omgres)
# print(omgres/omgpe)
kres=k[negres<0]
alphares=kd/kres #limit between alpha 3 and 4
# id peak spots
searchlen=1
searchrat=min(0.1*np.abs(omg[0]-omg[-1])/omgpe,0.2) #0.01 #todo make
    prop to omega range
thresh=0.2 #was 0.1
# print(alphares)
if(len(omgres_e)>0):
    if(np.max(alphares)>3.0): #res 3 alpha at 1.2omgpe, omg rat 1.003175
        for res in range(len(omgres_e)):
            res1=omgres_e[res] #todo make this work for arbitarty omg
                array
            argres1=np.argmin(np.abs(omg-res1)) # arg of omg at res. Now
                pick arge range that def has resonance.
            argres1h=np.argmin(np.abs(omg-(res1+searchrat*np.abs(res1))))
            argres1l=np.argmin(np.abs(omg-(res1-searchrat*np.abs(res1))))
            # print(omg)
            # print(res1)
            # print(searchrat)
            # print(argres1l,argres1h)
            domgsign=1
            if(omg[0]>omg[1]):
                domgsign=-1
```

```
                argres1h=int(argres1h+domgsign*searchlen)
                argres1l=int(argres1l-domgsign*searchlen)
                argres1ha=argres1h
                argres1la=argres1l # set in argument orde now to search
                if(omg[0]>omg[1]):
                    argres1ha=argres1l
                    argres1la=argres1h
                # print(argres1la,argres1ha)
                if(skwe[argres1la:argres1ha].size == 0 ):
                    argmaxspec=argres1la
                else:
                    argmaxspec=np.argmax(skwe[argres1la:argres1ha])+argres1la
                if(argres1ha<len(omg) and argres1la<len(omg) and argres1la>0
                    and argres1ha>0): #cbdo test, new condition
                    if(skwe[argmaxspec]-skwe[argmaxspec+1]>thresh*skwe[argmaxspec]
                        or
                        skwe[argmaxspec]-skwe[argmaxspec-1]>thresh*skwe[argmaxspec]
                        ):
                        #too much spikey, try smaller omega
                        omgnew=np.linspace(omg[argres1la],omg[argres1ha],len(omg))
                        specnew=skwha(omgnew,sa,omgL,Te,Ti,Z,Ai,ne,ve,vi)
                        for i in range(argres1la,argres1ha):
                            specnow[i]=0
                        for i in range(len(specnew)):
                            argold=np.argmin(np.abs(omg-omgnew[i]))
                            if(i+1<len(specnew) ):
                                if( (argold+1)<len(omg) ):
                                    jac=(omgnew[i+1]-omgnew[i])
                                    /(omg[argold+1]-omg[argold])
                                else:
                                    jac=(omgnew[i+1]-omgnew[i])/(omg[-1]-omg[-2])
                            specnow[argold]=specnow[argold]+specnew[i]*jac
                                        # was not indent

    return specnow

#s(k,omega) multi Z
#form factor for waves in thermal plasma with two ion species
#inputs:
#    omg = wave frequency [rad/s]
#    sa = scattering angle [deg]
#    omgL = probe laser frequency [rad/s]
#    Te = electron temperature [keV]
#    Ti = ion temperature [keV]
#    Z = ion charge = q/e
#    Ai=ion protons + nuetrons
#    ne = electron density [cm^-3]
```

```
#    ve=electron velocity [c]
#    vi=ion velocity [c]
def skwmz(omg,sa,omgL,Te,Ti1,Ti2,Z1,Z2,Ai1,Ai2,ne,ve,vi1,vi2,zf2):
    chie=chith_e(omg, sa,omgL,Te,ne,ve)
    chii1=chith_i(omg, sa,omgL,Te,Ti1,Z1,Ai1,ne,vi1)*(1.0-zf2)
    chii2=chith_i(omg, sa,omgL,Te,Ti2,Z2,Ai2,ne,vi2)*zf2
    chii=chii1+chii2
    eps=chie+chii+1.0
    dispe=np.abs((1+chii)/eps)**2
    dispi=np.abs((chie)/eps)**2

    eps=1.0+chie+chii
    c=2.99792458e8 #v light in m/s
    me=511 #kev
    mproton=938300 #kev
    omgpe=56400*np.sqrt(ne) #rad/s
    sarad=sa*2*np.pi/360
    kL=np.sqrt(omgL**2-omgpe**2)/c
    omgs=omg+omgL
    ks=np.sqrt(omgs**2-omgpe**2)/c
    k=np.sqrt(kL**2+ks**2-2*ks*kL*np.cos(sarad))

    vte=np.sqrt(Te/me) #c
    vti1=np.sqrt(Ti1/(mproton*Ai1)) #c
    vti2=np.sqrt(Ti2/(mproton*Ai2)) #c
    fe=np.sqrt(1.0/(2*np.pi*vte**2*c**2))
    *np.exp(-0.5*((omg/k)-ve*c)**2/(vte**2*c**2))
    fi1=(1.0-zf2)*np.sqrt(1.0/(2*np.pi*vti1**2*c**2))
    *np.exp(-0.5*((omg/k)-vi1*c)**2/(vti1**2*c**2))
    fi2=zf2*np.sqrt(1.0/(2*np.pi*vti2**2*c**2))
    *np.exp(-0.5*((omg/k)-vi2*c)**2/(vti2**2*c**2))
    skwe=(2*np.pi/k)*dispe*fe
    skwi1=(2*np.pi*Z1/k)*dispi*fi1
    skwi2=(2*np.pi*Z2/k)*dispi*fi2
    skwi=skwi1+skwi2
    return (skwe+skwi)

#s(k,omega) 3 Z
#form factor for waves in thermal plasma with two ion species
#inputs:
#    omg = wave frequency [rad/s]
#    sa = scattering angle [deg]
#    omgL = probe laser frequency [rad/s]
#    Te = electron temperature [keV]
#    Ti = ion temperature [keV]
#    Z = ion charge = q/e
#    Ai=ion protons + nuetrons
```

```
#    ne = electron density [cm^-3]
#    ve=electron velocity [c]
#    vi=ion velocity [c]
def
    skw3z(omg,sa,omgL,Te,Ti1,Ti2,Ti3,Z1,Z2,Z3,Ai1,Ai2,Ai3,ne,ve,vi1,vi2,vi3,zf2,zf3):
    chie=chith_e(omg, sa,omgL,Te,ne,ve)
    chii1=chith_i(omg, sa,omgL,Te,Ti1,Z1,Ai1,ne,vi1)*(1.0-zf2-zf3)
    chii2=chith_i(omg, sa,omgL,Te,Ti2,Z2,Ai2,ne,vi2)*zf2
    chii3=chith_i(omg, sa,omgL,Te,Ti3,Z3,Ai3,ne,vi3)*zf3
    chii=chii1+chii2+chii3
    eps=chie+chii+1.0
    dispe=np.abs((1+chii)/eps)**2
    dispi=np.abs((chie)/eps)**2

    eps=1.0+chie+chii
    c=2.99792458e8 #v light in m/s
    me=511 #kev
    mproton=938300 #kev
    omgpe=56400*np.sqrt(ne) #rad/s
    sarad=sa*2*np.pi/360
    kL=np.sqrt(omgL**2-omgpe**2)/c
    omgs=omg+omgL
    ks=np.sqrt(omgs**2-omgpe**2)/c
    k=np.sqrt(kL**2+ks**2-2*ks*kL*np.cos(sarad))

    vte=np.sqrt(Te/me) #c
    vti1=np.sqrt(Ti1/(mproton*Ai1)) #c
    vti2=np.sqrt(Ti2/(mproton*Ai2)) #c
    vti3=np.sqrt(Ti3/(mproton*Ai3)) #c
    fe=np.sqrt(1.0/(2*np.pi*vte**2*c**2))
    *np.exp(-0.5*((omg/k)-ve*c)**2/(vte**2*c**2))
    fi1=(1.0-zf2-zf3)*np.sqrt(1.0/(2*np.pi*vti1**2*c**2))
    *np.exp(-0.5*((omg/k)-vi1*c)**2/(vti1**2*c**2))
    fi2=zf2*np.sqrt(1.0/(2*np.pi*vti2**2*c**2))
    *np.exp(-0.5*((omg/k)-vi2*c)**2/(vti2**2*c**2))
    fi3=zf3*np.sqrt(1.0/(2*np.pi*vti3**2*c**2))
    *np.exp(-0.5*((omg/k)-vi3*c)**2/(vti3**2*c**2))
    skwe=(2*np.pi/k)*dispe*fe
    skwi1=(2*np.pi*Z1/k)*dispi*fi1
    skwi2=(2*np.pi*Z2/k)*dispi*fi2
    skwi3=(2*np.pi*Z3/k)*dispi*fi3
    skwi=skwi1+skwi2+skwi3
    return (skwe+skwi)


#s(k,omega) density gradient, with hig halpha correction
#inputs:
```

```
#    omg = wave frequency [rad/s]
#    sa = scattering angle [deg]
#    omgL = probe laser frequency [rad/s]
#    Te = electron temperature [keV]
#    Ti = ion temperature [keV]
#    Z = ion charge = q/e
#    Ai=ion protons + nuetrons
#    ne = electron density [cm^-3]
#    ltslne=OTS radius /electron density scale length:
    ne=ne_0*e^(ltslne*r/lts)
#    spots = numper of EPWs of different densities to calculate. Smooting
    inscreases if less spots are used.
#    ve=electron velocity [c]
#    vi=ion velocity [c]
def skwhadnsm(omg, sa, omgL,Te,Ti,Z,Ai,ne,ltslne,spots,ve,vi):
    re=2.8179403227e-13 #cm
    me=511 #kev
    mproton=938300 #kev
    c=2.99792458e8 #v light in m/s
    omgpe=56400*np.sqrt(ne)
    sarad=sa*2*np.pi/360
    mid_ind=int(len(omg)/2)
    domg=np.abs(omg[mid_ind] - omg[mid_ind + 1])
    rtssl=np.linspace(-1.0,1.0,spots+2)
    rtss=rtssl[1:spots+2]
    amps=(1.0/spots)*np.sqrt(1.0-rtss**2)
    amps=amps/np.sum(amps)


    #pre smooth: find ratio of smooth to different n
    reldomgpe=0.25*ltslne #from gradn_integral.py
    domgpesm=omgpe*reldomgpe
    domgdnall=domgpesm
    nesall=ne*np.exp(rtss*ltslne)
    omgpesall=56400*np.sqrt(nesall)
    omgdiffall=(omgpesall-np.roll(omgpesall,1))
    omgdiffall[0]=omgpesall[1]-omgpesall[0]
    omgdiffall[-1]=omgpesall[-1]-omgpesall[-2]
    domgpeall=np.max(np.abs(omgdiffall))
    allrat=0.6*domgpeall/(np.abs(domgdnall)+1e-12*omgpe) #ratio of dn
       omega to sm omega, max about 2, renomred to 1
    #smooth step

    fracdn=np.sqrt(1.0/(allrat**2+1.0))

    nes=ne*np.exp(rtss*ltslne*fracdn) #list of densities to make EWP from
```

```
    omgpes=56400*np.sqrt(nes)
    omgdiff=(omgpes-np.roll(omgpes,1))
    omgdiff[0]=0
    omgdiff[-1]=0
    domgpe=np.max(np.abs(omgdiff))

    reldomgpe=0.25*ltslne #from gradn_integral.py
    domgpesm=omgpe*reldomgpe
    domgdn=domgpesm*np.sqrt(1.0-fracdn**2)

    skom=np.zeros(len(omg))
    for i in range(spots):
        skomnow=skwha(omg, sa, omgL,Te,Ti,Z,Ai,nes[i],ve,vi)*amps[i]
        skom=skom+skomnow
    #find iaw range
    kL=np.sqrt(omgL**2-omgpe**2)/c
    omgs=omg+omgL
    ks=np.sqrt(omgs**2-omgpe**2)/c
    k=np.sqrt(kL**2+ks**2-2*ks*kL*np.cos(sarad))
    mk=np.max(k)*3.0 #1.5
    iawomg=mk*np.sqrt(Te*Z/(Ai*mproton))*c
    # print((domgpe/domgdn)) # about 2 max for good spectrum, this is
        normed to 1 now

    skom_e=np.zeros(len(skom))
    olds=0
    for i in range(len(skom_e)): #spit EPW and IAW spectra so we can
        smooth just the EPW due to density variation
        if (np.abs(omg[i])>iawomg):
            skom_e[i]=skom[i]
            olds=skom[i]
        else:
            skom_e[i]=olds #olds
    skom_i=skom-skom_e
    skom_e=spn.gaussian_filter(skom_e,domgdn/domg, mode='reflect')
        #nearest to ohigh
    skom=skom_e+skom_i
    return skom


#s(k,omega)
#form factor for waves with custom ion distribution
#inputs:
#    omg = wave frequency [rad/s]
#    sa = scattering angle [deg]
#    omgL = probe laser frequency [rad/s]
```

```
#    Z = ion charge = q/e
#    Ai=ion protons + nuetrons
#    ne = electron density [cm^-3]
#    ve=electron velocity [c]
#    dist [1/c] distribution function of ions, at phase velocity omg/k
def skwic(omg,sa,omgL,Te,Z,Ai,ne,ve,dist):
    c=2.99792458e8 #v light in m/s
    me=511 #kev
    omgpe=56400*np.sqrt(ne) #rad/s
    sarad=sa*2*np.pi/360
    kL=np.sqrt(omgL**2-omgpe**2)/c
    omgs=omg+omgL
    ks=np.sqrt(omgs**2-omgpe**2)/c
    k=np.sqrt(kL**2+ks**2-2*ks*kL*np.cos(sarad))

    vte=np.sqrt(Te/me) #c
    fe=np.sqrt(1.0/(2*np.pi*vte**2*c**2))
    *np.exp(-0.5*((omg/k)-ve*c)**2/(vte**2*c**2))

    chie=chith_e(omg, sa,omgL,Te,ne,ve)
    chii=chicust_i(omg, sa,omgL,dist,ne,Z,Ai)

    eps=chie+chii+1.0
    dispe=np.abs((1+chii)/eps)**2
    dispi=np.abs((chie)/eps)**2

    fi=1.0*dist[0]/c

    skwe=(2*np.pi/k)*dispe*fe
    skwi=(2*np.pi*Z/k)*dispi*fi
    return (skwe+skwi)


#s(k,omega)
#form factor for any k, omega (2D map)
#inputs:
#    omg = wave frequency [rad/s] array
#    kvals = wave number [rad/m], array
#    Te = electron temperature [keV]
#    Ti = ion temperature [keV]
#    Z = ion charge = q/e
#    Ai=ion protons + nuetrons
#    ne = electron density [cm^-3]
#    ve=electron velocity [c]
#    vi=ion velocity [c]
def skw2D(omg,kvals,Te,Ti,Z,Ai,ne,ve,vi):
    kmap=np.outer(np.ones(len(omg)),kvals)
```

```
    omap=np.outer(omg,np.ones(len(kvals)))
    chie=chith2D_e(omap, kmap,Te,ne,ve)
    chii=chith2D_i(omap, kmap,Te,Ti,Z,Ai,ne,vi)
    eps=chie+chii+1.0
    dispe=np.abs((1+chii)/eps)**2
    dispi=np.abs((chie)/eps)**2
    eps=1.0+chie+chii
    c=2.99792458e8 #v light in m/s
    me=511 #kev
    mproton=938300 #kev
    k=kvals
    vte=np.sqrt(Te/me) #c
    vti=np.sqrt(Ti/(mproton*Ai)) #c
    fe=np.sqrt(1.0/(2*np.pi*vte**2*c**2))
    *np.exp(-0.5*((omap/kmap)-ve*c)**2/(vte**2*c**2))
    fi=np.sqrt(1.0/(2*np.pi*vti**2*c**2))
    *np.exp(-0.5*((omap/kmap)-vi*c)**2/(vti**2*c**2))
    skwe=(2*np.pi/k)*dispe*fe
    skwi=(2*np.pi*Z/k)*dispi*fi
    return (skwe+skwi)


#s(k,omega) [s] electrons
#form factor for any k, omega (2D map), no ions
#inputs:
#    omg = wave frequency [rad/s] array
#    kvals = wave number [rad/m], array
#    Te = electron temperature [keV]
#    ne = electron density [cm^-3]
#    ve=electron velocity [c]
def skw2De(omg,kvals,Te,ne,ve):
    kmap=np.outer(np.ones(len(omg)),kvals)
    omap=np.outer(omg,np.ones(len(kvals)))
    chie=chith2D_e(omap, kmap,Te,ne,ve)
    eps=chie+1.0
    dispe=np.abs((1.0)/eps)**2
    eps=1.0+chie
    c=2.99792458e8 #v light in m/s
    me=511 #kev
    mproton=938300 #kev
    k=kvals
    vte=np.sqrt(Te/me) #c
    fe=np.sqrt(1.0/(2*np.pi*vte**2*c**2))
    *np.exp(-0.5*((omap/kmap)-ve*c)**2/(vte**2*c**2))
    skwe=(2*np.pi/k)*dispe*fe
    return (skwe)
#%%#########################################################################
```

```
# power


# old way
#inputs:
#    omg = wave frequency [rad/s]
#    sa = scattering angle [deg]
#    omgL = probe laser frequency [rad/s]
#    Te = electron temperature [keV]
#    Ti = ion temperature [keV]
#    Z = ion charge = q/e
#    Ai=ion protons + nuetrons
#    ne = electron density [cm^-3]
#    ve=electron velocity [c]
#    vi=ion velocity [c]
# def TSpwr(Pin,Lts,res_om, omg, sa, omgL,Te,Ti,Z,Ai,ne,ve,vi):
#     re=2.8179403227e-13 #cm
#     skom=skw(omg, sa, omgL,Te,Ti,Z,Ai,ne,ve,vi)
#     mid_ind=int(len(omg)/2)
#     domg=np.abs(omg[mid_ind] - omg[mid_ind + 1])
#     skomres=spn.gaussian_filter(skom,res_om/domg)
#     skompow=skomres*(Pin*re**2*Lts/(2*np.pi))*ne*(1+2*omg/omgL)
#     return skompow

#OTSpwr
#power shape of OTS scattered light in 4pi radians, [w/omega]
# worsk with any skw form factor
#inputs:
#    Pin = input probe power [w]
#    Lts = length of scattering collected [cm]
#    res_om = frequency broadening [s^-1]
#    ne = electron density [cm^-3]
#    omg = wave frequency [rad/s]
#    omgL = probe laser frequency [rad/s]
#    spec = input form factor s(k,omega) [\omega^-1]
def OTSpwr(Pin,Lts,res_om, omg, omgL, ne, spec):
    re=2.8179403227e-13 #cm
    skom=spec #skw(omg, sa, omgL,Te,Ti,Z,Ai,ne,ve,vi)
    mid_ind=int(len(omg)/2)
    domg=np.abs(omg[mid_ind] - omg[mid_ind + 1])
    skomres=spn.gaussian_filter(skom,res_om/domg)
    skompow=skomres*(Pin*re**2*Lts/(2*np.pi))*ne*(1+2*omg/omgL)
    return skompow
```

```
#%%#####################################################################
```

A.3 OTStools.py

Helper functions for generating OTS spectra

```
# common operations using OTS functions
#Created on Fri Sep 9 13:09:10 2022, Colin Bruulsema



import numpy as np
import scipy.special as sps
import scipy.ndimage as spn

# from OTSplasma import chith_e
# from OTSplasma import chith_i

import sys
# sys.path.append("/Users/Colin/OneDrive/EbackMarch2020/OTS/")
    #C:\Users\Colin\OneDrive\EbackMarch2021\OTS
# sys.path.append("/Users/Colin/OneDrive/EbackMarch2020/")


from src.OTSpower import skw




import matplotlib.pyplot as plt
import scipy as sp
#%%%%%%%%%%%%%%%%%%%%%%%%%%%%%%%%%%%%%%%%%%%%%%%%%%%%%%%%%%%%%%%%%%%%%%%
######################### constants
#%%%%%%%%%%%%%%%%%%%%%%%%%%%%%%%%%%%%%%%%%%%%%%%%%%%%%%%%%%%%%%%%%%%%%%%
c=3e8 #m/s
me=511 #kev
mp=938272.0 #keV
#%%%%%%%%%%%%%%%%%%%%%%%%%%%%%%%%%%%%%%%%%%%%%%%%%%%%%%%%%%%%%%%%%%%%%%%
# Spectral shape diagnostics
#%%%%%%%%%%%%%%%%%%%%%%%%%%%%%%%%%%%%%%%%%%%%%%%%%%%%%%%%%%%%%%%%%%%%%%%


#IAW asmmetry from current, maxwellain
```

```
#form factor for waves in thermal plasma
#inputs:
#    omg = wave frequency [rad/s]
#    sa = scattering angle [deg]
#    omgL = probe laser frequency [rad/s]
#    Te = electron temperature [keV]
#    Ti = ion temperature [keV]
#    Z = ion charge = q/e
#    Ai=ion protons + nuetrons
#    ne = electron density [cm^-3]
#    ve=electron velocity [c]
#    vi=ion velocity [c]
def asyiaw_max(sa,omgL,Te,Ti,Z,Ai,ne,ve,vi):
    #find plasuible extent of IAW: omega=2*cs*k
    cs=np.sqrt((Z*Te+3*Ti)/(Ai*mp)) #sound speec/c
    omgpe=56400*np.sqrt(ne) #rad/s
    kL=np.sqrt(omgL**2-omgpe**2)/c
    sarad=sa*2*np.pi/360
    kLa=omgL/c  #approx laser wave number
    ka=np.sqrt(2)*kL*np.sqrt(1.0-1.0*np.cos(sarad)) #approx scattering
        wave number
    omgR=2*cs*c*ka #0.002*omgL
    pix=16001
    omg=np.linspace(-omgR,omgR, pix)
    #make spectrum, find asymmetry
    iaw=skw(omg,sa,omgL,Te,Ti,Z,Ai,ne,ve,vi)
    iawb=np.sum(iaw[omg-vi*c*kL>0])
    iawr=np.sum(iaw[omg-vi*c*kL<0])
    asym=iawb/(iawr+iawb) #####
    return asym

# how to verify above :

# iawcdf=np.zeros(len(iaw))
# for ii in range(1,len(iaw)):
#     iawcdf[ii]=iawcdf[ii-1]+iaw[ii]*(omg[ii]-omg[ii-1])
#
    iawcdfn=np.abs((iawcdf-iawcdf[np.argmin(np.abs(omg-vi*c*kL))])/np.max(iawcdf))
# *np.max(iaw)
# sumiaw=np.max(iawcdf)

# plt.plot(omg,iaw,'r')
# plt.plot(omg,iawcdfn,'m')
# plt.ylim(0,1.1*np.max(iaw))
# plt.title('IAW, asm='+str('{:01.3f}'.format(asym))+'
    sum='+str('{:01.3f}'.format(sumiaw)))
# plt.xlabel('$\omega$ [$s^{-1}$]')
```

```
# plt.show()



#tblueredfind_ind: two-peak finder
#returns bin indicies for each peak
#inputs:
#    spec = IAW spectrum to find peaks in, [any units]
#    res = smoothing to apply to remove noise [bins]
def blueredfind_ind(spec,res=1):
    IAWpf=sp.ndimage.gaussian_filter(spec*1.00,res)
    tops=np.zeros(len(IAWpf))
    for i in range(1,len(IAWpf)-1):
        if(IAWpf[i]-IAWpf[i-1]>=0 and IAWpf[i]-IAWpf[i+1]>=0):
            tops[i]=1
            tops[i-1]=0
    index_blue=0
    val_blue=0
    index_red=0
    val_red=0
    for i in range(1,len(IAWpf)-1):
        if(tops[i]==1):
            # print('top')
            # print(IAWpf[i])
            # print(i)
            if(IAWpf[i]>val_blue and val_red>val_blue):
                val_blue=IAWpf[i]
                index_blue=i
            else:
                if(IAWpf[i]>val_red and val_red<=val_blue):
                    val_red=val_blue
                    index_red=index_blue
                    val_blue=IAWpf[i]
                    index_blue=i
    bluered_ind=np.zeros(2)
    bluered_ind[0]=index_blue
    bluered_ind[1]=index_red
    return bluered_ind

#iawfrqfind: IAW frequency finder
#returns frequncy of IAW
#inputs:
#    wv = wavelength of IAW spec [nm]
#    iawspec = IAW spectrum to find peaks in, [any units]
def iawfrqfind(wv,iawspec,res):
    inds=blueredfind_ind(iawspec,res)
```

```
    wv1=wv[int(inds[0])]
    wv2=wv[int(inds[1])]
    ifrq=np.abs(0.5*(c*2*np.pi/(wv1*1e-9))-0.5*(c*2*np.pi/(wv2*1e-9)))
    return ifrq


#%%%%%%%%%%%%%%%%%%%%%%%%%%%%%%%%%%%%%%%%%%%%%%%%%%%%%%%%%%%%%%%%%%%%%%%%
######################### ots relations
#%%%%%%%%%%%%%%%%%%%%%%%%%%%%%%%%%%%%%%%%%%%%%%%%%%%%%%%%%%%%%%%%%%%%%%%%



#finds phase velocity of waves from frequency input
#inputs:
#    omg = wave frequency [rad/s]
#    sa = scattering angle [deg]
#    omgL = probe laser frequency [rad/s]
#    ne = electron density [cm^-3]
def vfromomg(omg,sa,omgL,ne):
    c=2.99792458e8 #v light in m/s
    me=511 #kev
    omgpe=56400*np.sqrt(ne) #rad/s
    sarad=sa*2*np.pi/360
    kL=np.sqrt(omgL**2-omgpe**2)/c
    omgs=omg+omgL
    ks=np.sqrt(omgs**2-omgpe**2)/c
    k=np.sqrt(kL**2+ks**2-2*ks*kL*np.cos(sarad))
    v=(omg/k)/c
    return (v)

#finds frequency of waves from phase velocity
#inputs:
#    omg = wave frequency [rad/s]
#    sa = scattering angle [deg]
#    omgL = probe laser frequency [rad/s]
#    ne = electron density [cm^-3]
#    steps = umber of iterations to take
def omgfromv(v,sa,omgL,ne,steps):
    c=2.99792458e8 #v light in m/s
    me=511 #kev
    omgpe=56400*np.sqrt(ne) #rad/s
    sarad=sa*2*np.pi/360
    kL=np.sqrt(omgL**2-omgpe**2)/c

    #iterate for k
    k=np.ones(len(v))*np.sqrt(kL**2+kL**2-2*kL*kL*np.cos(sarad)) #starting
        k with no shift
```

```
    for i in range(steps):
        const=(omgL**2-omgpe**2-kL**2*np.cos(sarad)**2*c**2+kL**2
        *np.sin(sarad)**2*c**2)
        rootk=-2*kL*np.cos(sarad)*c**2*np.sqrt(k**2-kL**2*np.sin(sarad)**2)
            #maybe crashes if k gets too small to reach
        ksq=k**2*(v**2-c**2)
        # klin=2*omgL*k*v #will use for lin method
        omg=(-const-rootk-ksq)/(2*omgL) #solv for kv

        #solve 2nd step
        omgs=omg+omgL
        ks=np.sqrt(omgs**2-omgpe**2)/c
        k=np.sqrt(kL**2+ks**2-2*ks*kL*np.cos(sarad))
        omg=k*v*c

    return (omg)

#%%%%%%%%%%%%%%%%%%%%%%%%%%%%%%%%%%%%%%%%%%%%%%%%%%%%%%%%%%%%%%%%%%%%%%%%%%%
######################### dsitribution functions
#%%%%%%%%%%%%%%%%%%%%%%%%%%%%%%%%%%%%%%%%%%%%%%%%%%%%%%%%%%%%%%%%%%%%%%%%%%%


#idistmax: maxwellian distribution, perfect
#generates [fi,dfi/dv]
#   vti is sqrt(Ti/mi) [c],
#   vi[c] is central flow velocity
#   v=aray of all v/c vals
def idistmax(vti, vi,v):
    vdist = np.array(np.zeros(len(v)))
    dvdist = np.array(np.zeros(len(v)))
    vel = 1.0*v
    dvbin=np.zeros(len(v))
    for i in range(1,len(v)-1):
        dvbin[i]=(v[i+1]-v[i-1])/2.0
    dvbin[0]=(v[1]-v[0])/1.0
    dvbin[-1]=(v[-1]-v[-2])/1.0

    supx = ((vel-vi)/vti)
    maxwel=(1.0)*(1.0/(vti*np.sqrt(2*np.pi)))*np.exp(-0.5*(supx)**2)
    fi=maxwel  #ion distribution function on velocity/vti=supx, needs
        \int_-1^1 fitail dv/c =1
    vdist[:] = fi[:]
    vdist=(1.0*vdist)

    #take e derivative
    dvdist = np.array(np.zeros(len(vdist)))
    derlen =int(1) #59
```

```
    for i in range(len(dvdist)-2*derlen):
        dvdist[i+derlen]=0
        for avi in range(derlen):
            dvdist[i+derlen] =
                dvdist[i+derlen]+2*(avi+1)*(vdist[i+derlen+avi+1] -
                vdist[i+derlen-avi-1])/(v[i+derlen+avi+1] -
                v[i+derlen-avi-1])
        dvdist[i+derlen] = dvdist[i+derlen]/(derlen*(derlen+1))
    return vdist, dvdist


#idistHT: hot ion tails
#generates [fi,dfi/dv]
#   vti is sqrt(Ti/mi) [c],
#   vi[c] is central flow velocity
#   hT=T_{tail}/T_i,
#   hf=hot tail fraction
#   v=aray of all v/c vals
def idistHT(vti, vi, hT, hf,v):
    vdist = np.array(np.zeros(len(v)))
    dvdist = np.array(np.zeros(len(v)))
    vel = 1.0*v
    dvbin=np.zeros(len(v))
    for i in range(1,len(v)-1):
        dvbin[i]=(v[i+1]-v[i-1])/2.0
    dvbin[0]=(v[1]-v[0])/1.0
    dvbin[-1]=(v[-1]-v[-2])/1.0

    supx = ((vel-vi)/vti)
    maxwelW=(1.0-hf)*(1.0/(vti*np.sqrt(2*np.pi)))*np.exp(-0.5*(supx)**2)
    maxwelWh=hf*(1.0/(vti*np.sqrt(hT)*np.sqrt(2*np.pi)))
    *np.exp(-0.5*(supx/np.sqrt(hT))**2)
    fitail=maxwelW+maxwelWh  #ion distribution function on
        velocity/vti=supx, needs \int_-1^1 fitail dv/c =1
    vdist[:] = fitail[:]
    vdist=(1.0*vdist)

    #take e derivative
    dvdist = np.array(np.zeros(len(vdist)))
    derlen =int(1) #59
    for i in range(len(dvdist)-2*derlen):
        dvdist[i+derlen]=0
        for avi in range(derlen):
            dvdist[i+derlen] =
                dvdist[i+derlen]+2*(avi+1)*(vdist[i+derlen+avi+1] -
                vdist[i+derlen-avi-1])/(v[i+derlen+avi+1] -
                v[i+derlen-avi-1])
```

```
        dvdist[i+derlen] = dvdist[i+derlen]/(derlen*(derlen+1))
    return vdist, dvdist

#idistmodT: hot ion tail with a tail model
#generates [fi,dfi/dv]
#   vti is sqrt(Ti/mi) [c],
#   vi[c] is central flow velocity
#   hT=T_{tail}/T_i,
#   hf=hot tail fraction
#   v=aray of all v/c vals
def idistmodT(vti, vi, hf,v):
    vdist = np.array(np.zeros(len(v)))
    dvdist = np.array(np.zeros(len(v)))
    vel = 1.0*v
    dvbin=np.zeros(len(v))
    for i in range(1,len(v)-1):
        dvbin[i]=(v[i+1]-v[i-1])/2.0
    dvbin[0]=(v[1]-v[0])/1.0
    dvbin[-1]=(v[-1]-v[-2])/1.0

    supx = ((vel-vi)/vti)
    veld=vel-vi
    veldt=veld+0.91*vti
    maxwelW=(1.0-hf)*(1.0/(vti*np.sqrt(2*np.pi)))*np.exp(-0.5*(supx)**2)
    bs=np.array([3.0,0.4,3.1,0.8])*0.1*vti/0.02569 #*(5e4/3e7)
    # sbs=np.array([0.025,0.004,0.01,0.2])*0.1*vti/0.02569
    sbs=np.array([0.025,0.1,0.01,0.2])*0.1*vti/0.02569
    vexp=0.22*(0.1*vti/0.02569)
    tailturng=(1-0.5*(1+np.tanh((veldt-bs[0])/sbs[0])))
    *(1-0.5*(1+np.tanh((veldt-bs[2])/sbs[2])))
    tailturnh=(0.5*(1+np.tanh((veldt-bs[1])/sbs[1])))
    *(0.5*(1+np.tanh((veldt-bs[3])/sbs[3])))
    tailmax=np.exp(-1.0*(bs[1]/vexp))
    taile=np.exp(-1.0*(veldt/vexp))
    taile[(bs[1]>veldt)]=tailmax*np.ones(len(taile[(bs[1]>veldt)]))
    tail=taile*tailturng*tailturnh
    # tail[0:]
    tailnorm=np.sum(tail*np.abs(dvbin))

    fi1=hf*tail/tailnorm
    # plt.plot(veld/(0.1*vti/0.02569),fi1,'c')
    # plt.plot(veld/(0.1*vti/0.02569),maxwelW,'k')
    # plt.show()


    fitail=maxwelW+fi1   #ion distribution function on velocity/vti=supx,
        needs \int_-1^1 fitail dv/c =1
```

```
    vdist[:] = fitail[:]
    vdist=(1.0*vdist)

    #take e derivative
    dvdist = np.array(np.zeros(len(vdist)))
    derlen =int(1) #59
    for i in range(len(dvdist)-2*derlen):
        dvdist[i+derlen]=0
        for avi in range(derlen):
            dvdist[i+derlen] =
                dvdist[i+derlen]+2*(avi+1)*(vdist[i+derlen+avi+1] -
                vdist[i+derlen-avi-1])/(v[i+derlen+avi+1] -
                v[i+derlen-avi-1])
        dvdist[i+derlen] = dvdist[i+derlen]/(derlen*(derlen+1))
    return vdist, dvdist


#idistmaxp: maxwellian distribution, particles
#generates [fi,dfi/dv]
#   vti is sqrt(Ti/mi) [c],
#   vi[c] is central flow velocity
#   v=aray of all v/c vals
#   part = number of particles in distribution function
def idistmaxp(vti, vi,v,part):
    vdist = np.array(np.zeros(len(v)))
    dvdist = np.array(np.zeros(len(v)))
    vel = 1.0*v
    dvbin=np.zeros(len(v))
    for i in range(1,len(v)-1):
        dvbin[i]=(v[i+1]-v[i-1])/2.0
    dvbin[0]=(v[1]-v[0])/1.0
    dvbin[-1]=(v[-1]-v[-2])/1.0
    dval=np.average(dvbin)
    dmax=int((vti/dval)*0.5) #half len of vti

    supx = ((vel-vi)/vti)
    maxwel=(1.0)*(1.0/(vti*np.sqrt(2*np.pi)))*np.exp(-0.5*(supx)**2)
    maxwelppc=maxwel*np.abs(dvbin)*part
    fi=np.random.poisson(maxwelppc)/(np.abs(dvbin)*part) #ion distribution
        function on velocity/vti=supx, needs \int_-1^1 fitail dv/c =1
    # fierr=np.sqrt(maxwelppc)/(dvbin*part)
    vdist[:] = fi[:]
    vdist=(1.0*vdist)

    #optimize the derivative length
    Dpar=(1.0/(np.sqrt(2)*dvbin**2))*np.sqrt(fi*np.abs(dvbin)/part)
    Gpar=(dvbin**2/vti**4)*(1.0/12.0)*(3-v**2/vti**2)*(fi*v)
```

```
    GD=np.abs(Gpar)/(np.abs(Dpar)+1e-20)
    DG=np.abs(Dpar)/(np.abs(Gpar)+1e-20)
    dapprox=spn.gaussian_filter(np.abs(1.5*DG)**(1.0/3.5),1) # smooth guess

    dlen=np.zeros(len(dapprox),dtype=np.int64)
    for i in range(len(dapprox)):
        gd=np.abs(((3*dapprox[i]+1)/(2*dapprox[i]+1))*(1/np.sqrt(dapprox[i]**3))
        *(1.0/(dapprox[i]+1)**2))
        if(gd>GD[i]):
            dlen[i]=np.ceil(dapprox[i])
        else:
            dlen[i]=np.floor(dapprox[i])
        if(dlen[i]>dmax):
            dlen[i]=dmax
        if(dlen[i]<1):
            dlen[i]=int(1)

    #take v derivative
    dvdist = np.array(np.zeros(len(vdist)))
    derlenmax=int(np.max(dlen))
    for i in range(len(dvdist)-2*derlenmax):
        index=i+derlenmax
        derlen =(dlen[index]) #59
        dvdist[index]=0
        for avi in range(derlen):
            dvdist[index] = dvdist[index]+2*(avi+1)*(vdist[index+avi+1] -
                vdist[index-avi-1])/(v[index+avi+1] - v[index-avi-1])
        dvdist[index] = dvdist[index]/(derlen*(derlen+1))
    return vdist, dvdist



#idistcp: input distribution, particles
#generates [fi,dfi/dv]
#   fiin: input array of f_i(v). Normalized internally
#   v: array of velocity values for f_i(v) [c]
#   part = number of particles in distribution function
def idistcp(fiin, v,part):
    vdist = np.array(np.zeros(len(v)))
    dvdist = np.array(np.zeros(len(v)))
    dvbin=np.zeros(len(v))
    for i in range(1,len(v)-1):
        dvbin[i]=(v[i+1]-v[i-1])/2.0
    dvbin[0]=(v[1]-v[0])/1.0
    dvbin[-1]=(v[-1]-v[-2])/1.0
    dval=np.average(dvbin)
```

```
#find norm and temperature of distribution
normfiin=np.sum(fiin*np.abs(dvbin)) #normaliztoin
vfiin=np.sum(v*(fiin/normfiin)*np.abs(dvbin)) #average velocity
vti=np.sqrt(np.sum((v-vfiin)**2*(fiin/normfiin)*np.abs(dvbin)))
dmax=int((vti/dval)*0.5) #half len of vti

# print('idistcp vti')
# print(vti)


fi=fiin/normfiin #ion distribution function on velocity/vti=supx,
    needs \int_-1^1 fitail dv/c =1
# fippc=fi*dvbin*part #particles per cell in ion distribution, not
    used explicitly here
# fierr=np.sqrt(maxwelppc)/(dvbin*part)
vdist[:] = fi[:]
vdist=(1.0*vdist)

#optimize the derivative length
Dpar=(1.0/(np.sqrt(2)*dvbin**2))*np.sqrt(fi*np.abs(dvbin)/part)
Gpar=(dvbin**2/vti**4)*(1.0/12.0)*(3-v**2/vti**2)*(fi*v)
GD=np.abs(Gpar)/(np.abs(Dpar)+1e-20)
DG=np.abs(Dpar)/(np.abs(Gpar)+1e-20)
dapprox=spn.gaussian_filter(np.abs(1.5*DG)**(1.0/3.5),1) # smooth guess

dlen=np.zeros(len(dapprox),dtype=np.int64)
for i in range(len(dapprox)):
    gd=np.abs(((3*dapprox[i]+1)/(2*dapprox[i]+1))*(1/np.sqrt(dapprox[i]**3))
    *(1.0/(dapprox[i]+1)**2))
    if(gd>GD[i]):
        dlen[i]=np.ceil(dapprox[i])
    else:
        dlen[i]=np.floor(dapprox[i])
    if(dlen[i]>dmax):
        dlen[i]=dmax
    if(dlen[i]<1):
        dlen[i]=int(1)

#take v derivative
dvdist = np.array(np.zeros(len(vdist)))
derlenmax=int(np.max(dlen))
for i in range(len(dvdist)-2*derlenmax):
    index=i+derlenmax
    derlen =(dlen[index]) #59
    dvdist[index]=0
    for avi in range(derlen):
```

```
            dvdist[index] = dvdist[index]+2*(avi+1)*(vdist[index+avi+1] -
                vdist[index-avi-1])/(v[index+avi+1] - v[index-avi-1])
        dvdist[index] = dvdist[index]/(derlen*(derlen+1))
    return vdist, dvdist
```